Applied Bionics and Biomechanics

Autonomous Intelligent Robots in Biomechanics

Lead Guest Editor: Songyuan Zhang
Guest Editors: Qiang Fu, Muye Pang, Haibo Feng, and Qiao Li

Autonomous Intelligent Robots in Biomechanics

Applied Bionics and Biomechanics

Autonomous Intelligent Robots in Biomechanics

Lead Guest Editor: Songyuan Zhang
Guest Editors: Qiang Fu, Muye Pang, Haibo Feng, and Qiao Li

Contents

Hindawi
Applied Bionics and Biomechanics
Volume 2022, Article ID 1751460, 15 pages
https://doi.org/10.1155/2022/1751460

Research Article

A Novel Robotic Exoskeleton for Finger Rehabilitation: Kinematics Analysis

Yong Dai[1], **Junhong Ji**[2], **Guocai Yang**[2] **and Yu Yang**[1]

[1]*School of Mechatronics Engineering, Harbin Institute of Technology, Harbin 150001, China*
[2]*State Key Laboratory of Robotics and Systems, Harbin Institute of Technology, Harbin 150001, China*

Correspondence should be addressed to Junhong Ji; junhong.ji@hit.edu.cn

Received 4 May 2022; Revised 23 August 2022; Accepted 29 August 2022; Published 14 October 2022

Academic Editor: Takahiro Kagawa

A novel robotic exoskeleton for fingers rehabilitation is developed, which is driven by linear motors through Bowden cables. For each finger, in addition to three links acting as phalanxes, two more links acting as knuckles are also implemented. Links are connected through passive joints, by which translational and rotary movements can be realized simultaneously. Either flexion or extension motion is accomplished by one cable of adequate stiffness. This exoskeleton possesses good adaptability to finger length of different subjects and length variations during movement. The exoskeleton's kinematics model is built by the statistics method, and piecewise polynomial functions (PPF) are chosen to describe the relationship between motor displacement and joint variables. Finally, the relationship between motor displacement and the finger's total bending angle is obtained, which can be used for rehabilitation trajectory planning. Experimental results show that this exoskeleton achieves nearly the maximum finger bending angle of a healthy adult person, with the maximum driving force of 68.6 N.

1. Introduction

The human hand is one of the most sophisticated human body parts performing many activities of daily living, so the life quality of patients suffering impairments in hand function is badly affected. Due to the huge amount of patients after stroke or spine injury, the demand for rehabilitation therapy to regain normal hand strength and capabilities is huge [1, 2]. In past, such a rehabilitation process was executed manually by physiotherapists. As technology improves, robot-aided hand rehabilitation or assisting devices have conveyed a lot of interest and have been proven to be good as or even better than conventional therapy because of providing high-intensity and repetitive therapy [3, 4]. With help of robots, patients could practice more easily at their own will and handle functional daily living tasks at ease.

Some prototypes or even commercial products have been developed, which can be categorized into three major types, that is, based on end-effector, exoskeleton, or just a glove, respectively. With the former one, it is usually impossible to control each joint involved in the motion [5], so most current systems are in the form of exoskeleton. The exoskeleton is generally a mechanism that can be placed around a part of the human body to mechanically guide or actuate it without impeding the joint's natural motion [5]. Exoskeletons can be categorized into different types depending on various criteria, comprehensive categorization with respect to exoskeleton is provided in [6]. Major criteria include actuator type, intention sensing method, purpose, and power transmission methods. According to the actuator type, an exoskeleton can be driven by electric motors, pneumatic pistons, pneumatic air chambers, pneumatic artificial rubber muscles (PARMs), series elastic actuators (SEA), shape memory alloy (SMA), and hydraulics for active systems. According to the power transmission method, structures can be driven directly by actuators or with the aid of linkage, belt, cable-driven tendon, or cable with linkages together [4]. Obviously, there are much more combinations than the above-listed categories, for instance, the torque exerted via linkage can be from either an electric motor or SMA.

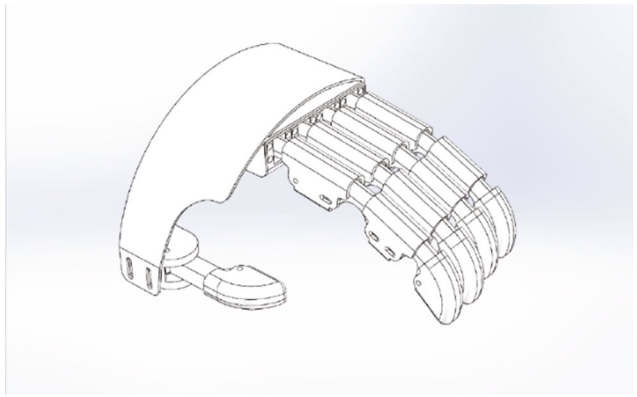

Figure 1: Mechanical structure of the finger rehabilitation exoskeleton.

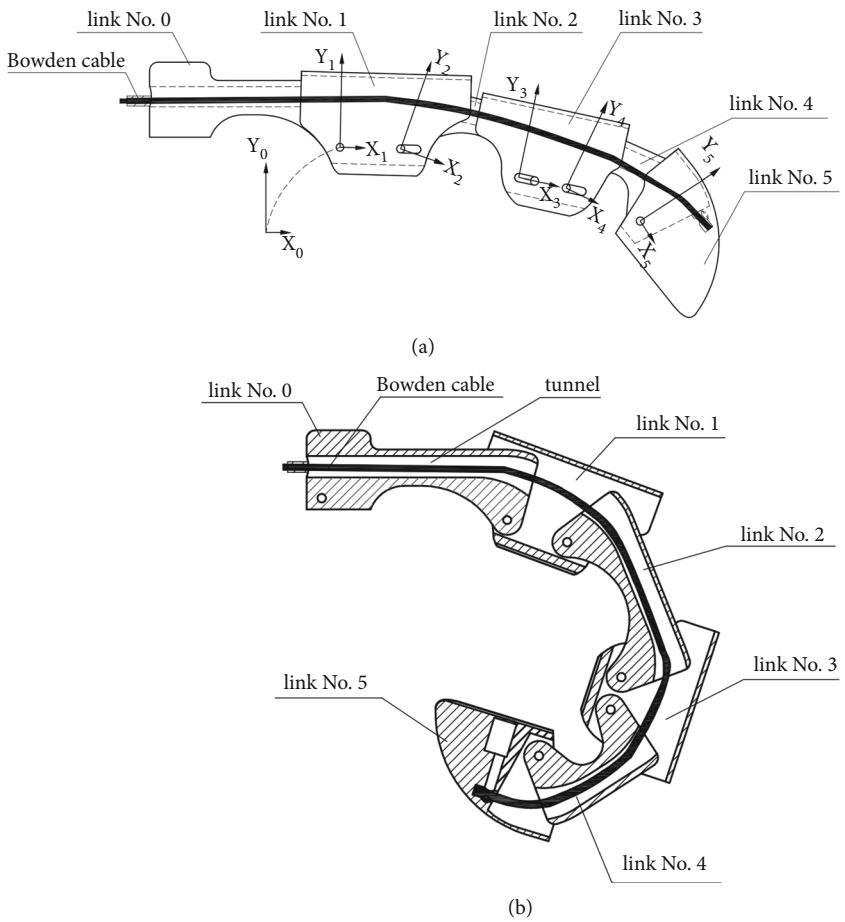

Figure 2: Definition of links and coordinate frames for one finger.

Linkage is the most conventional way consisting an exoskeleton [7–10]. The essential weakness is that the structure is bulky, especially on the dorsal side. To adapt to various finger sizes, a linkage exoskeleton was developed, whose mechanism's active joint axes do not have to coincide with the finger joint axes of human hands [11], with the cost of an extreme bulky mechanical structure.

To modulate mechanic length to adapt finger flexion/extension, a sliding mechanism is adopted. A three-layered sliding spring mechanism is developed to realize large deformation [5]. For each joint, when the inner spring bends, the center and outer springs bend and actively and passively slide, respectively, forming a circular sector. This structure is quite complicated and the stiffness of springs should be chosen carefully. Another common way to adapt different lengths of patients' fingers is implementing passive prismatic joints in addition to active rotary joints [2, 12–15]. Such structure is also helpful to align finger joints and rotary centers.

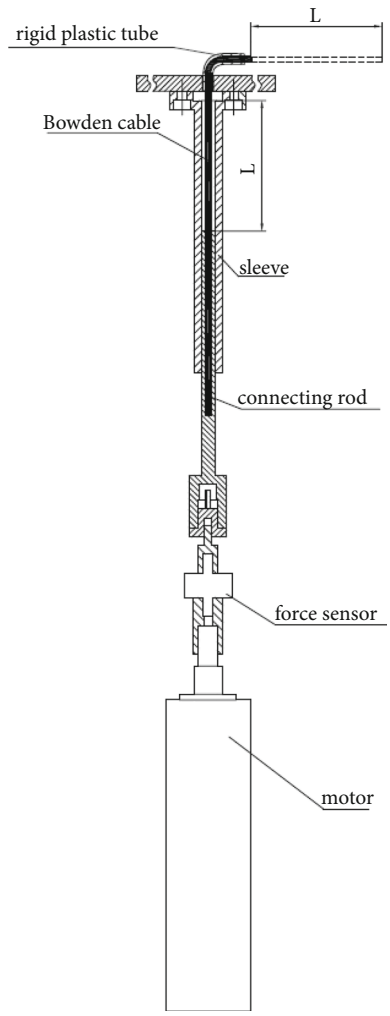

Figure 3: Mechanical structure to guarantee cable stiffness.

A slider-crank-like mechanism is proposed to transmit driving torque onto the metacarpophalangeal (MCP) joint, while proximal interphalangeal (PIP) and distal interphalangeal (DIP) are driven by the Bowden cable. Shell-like structures are fastened on fingers and palms by Velco straps. Two passive translational joints are involved to adapt the finger length of different subjects after manually adjusting such joints are blocked by the screw [2]. A similar linkage structure can be also actuated by SMA instead of electric motors [16].

The principle of remote center of motion (RCM) is another way to fit the mechanical rotation center to human joints. This can be realized by multiparallelogram linkages [17], arc-shaped sliders [18], N-shaped linkages [19], or even more complicated structures consisting of 2 four-bar linkages and 3 five-bar linkages [20]. The common drawback is still that the mechanical structure is bulky and complicated.

Cable is an attractive way of mimicking the tendon's physiological function, while just unidirectional torque can be exerted by one cable [21]. To exert bidirectional torque on one finger, either two independent cables [22] or a pulley is implemented [23]. To replace the pulley, a U-shaped tube can also be implemented to guide wires as tendons for extension and flexion [24], while extension wires are attached to linear springs to generate extension force. The Bowden cable–based series elastic actuation (SEA) is developed allowing bidirectional torque control [1]. Although low reflected inertia is realized to offer minimal resistance to finger motion, the dimension is still big. Sliding joints are implemented as the interface between finger phalanx and exoskeleton links, which can be quickly adjusted, that is, it is still needed adjusting for the individual subject. An exoskeleton driven by cable can cover more than 70% of a healthy hand workspace, and it can achieve forces at the fingertips sufficient for activities of daily living [25]. HX-β, an index finger-thumb exoskeleton is driven by series-elastic actuators via cables, realized robot-user joint alignment, and flexible actuation for users of various hand sizes [26]. In a prototype named "RELab tenoexo," sleek mechanisms are designed, which can generate the four most frequently used grasp motions [27]. A SEA-based prototype is developed which incorporates five passive and two actively actuated joints and provides active control of MCP and PIP joints. But the structure is still bulky; therefore, only the part for index finger is realized [28].

To obtain force feedback in an exoskeleton, whose original purpose is for virtual reality, two cables are implemented, one cable for driving and another one for force feedback [29].

Pneumatic actuators are widespread because of advantages such as high weight–power ratio, compressibility, low heat generation, and clean energy, while a primary drawback is that only unidirectional force/torque can be exerted. A McKibben type pneumatic artificial muscle (PAM) is implemented for actuation [30], to overcome the unidirectional drawback, it is combined with a constant force spring. PARMs are also adopted in grip amplified glove, which achieves power-assist grasping motion [31], but are unhelpful for flexor hypertonia.

Since many patients have flexor hypertonia and finger extensor weakness, a passive exoskeleton, which can exert only unidirectional extension torque, is also developed. Series of elastic cords [32], passive leaf springs, and elastic tension cords [33] are adopted against excessive involuntary flexion torques due to impairments. To apply such a device, offset force should be manually adjusted in advance.

Bio-signals are a way to detect the users' intentions by measuring electrical muscle activity in the forearm or motor functions in the brain. Surface electromyography (SEMG) can be used as a sensor to control the exoskeleton or observe and get feedback from the progress of training. SEMG signals combined with kinematic information from exoskeleton's encoders can be introduced to a torque-controlled hand exoskeleton [34].

The glove is an intuitive and compact embodiment of the wearable device. A polymer-based tendon-driven wearable robotic hand permits adjustment to different hand sizes and ventilation [35].

The soft robot is also an attractive way. A prototype made of molded elastomeric bladders with anisotropic fiber

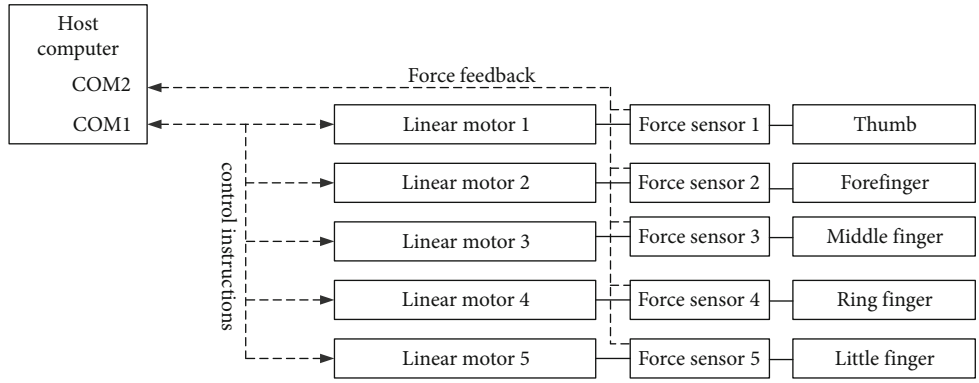

Figure 4: Control system structure.

Table 1: Geometrical parameters corresponding to the forefinger.

	Constant/variable	Value/range	Unit
d_1	Variable	[18.5, 24.5]	mm
d_2	Constant	30	mm
d_3	Variable	[−4, 0.5]	mm
d_4	Variable	[11.5, 16.0]	mm
d_5	Constant	20	mm
θ_1	Variable	[−20, 0]	Degree
θ_2	Variable	[−20, 0]	Degree
θ_3	Variable	[−60, 0]	Degree
θ_4	Variable	[−30, 0]	Degree
θ_5	Variable	[−50, 0]	Degree

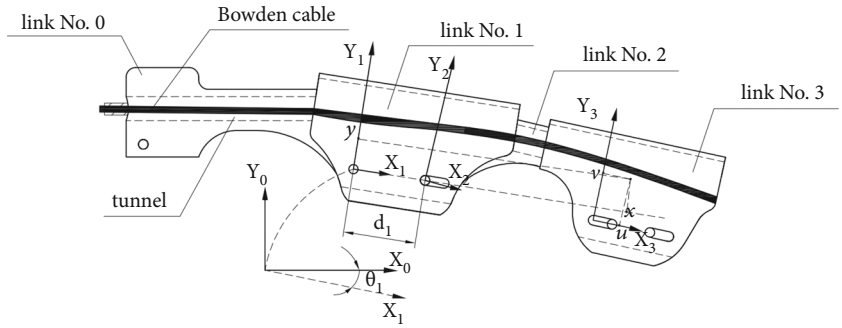

Figure 5: Definition of some kinematics variables.

reinforcement was built, which can produce specific bending, twisting, and extending trajectories upon fluid pressurization [36, 37]. It can be quickly custom-designed to fit the anatomy of individual users, that is, soft actuators were mechanically programmed to match and support the range of motion of individual fingers. Given the condition that soft devices tend to lack well-understood models and traditional rigid devices are always with excessive stiffness, a hybrid soft-rigid exoskeleton (HSRexo) is presented, adopting the simplified three-layered sliding spring (sTLSS) mechanism that combines the intrinsic compliance and comprehensible kinematics [38].

As a common difficulty is that, without correct alignment, the exoskeleton will feel uncomfortable in use, or even unusable [39], a feasible solution is proposed to automatically align exoskeleton axes to human anatomical axes by decoupling joint rotations from translations [40].

In most existing exoskeletons, the adaptability to different patients' fingers is deficient. For some devices, the finger's total bending angle is still inadequate, besides the wearing procedure is a burdensome task, which may last for 30 minutes.

To summarize, there are still several challenges to overcome, that is, an ideal exoskeleton should be:

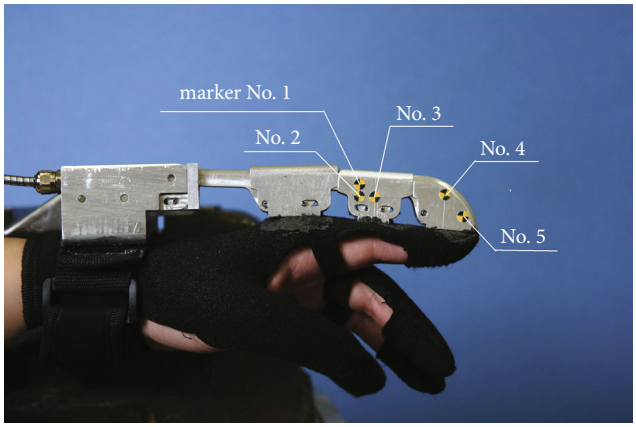

Figure 6: A sample image of the robotic exoskeleton with five markers.

(i) compact in size to minimize the interference between the thumb and fingers

(ii) easy to wear

(iii) adaptable to different patients' finger lengths

(iv) adjustable in length during flexion/extension to minimize the slippage between the finger phalanx and exoskeleton links

To overcome such drawbacks, a novel exoskeleton is developed, for which each finger is driven by an individual linear motor through a Bowden cable. For each finger, two more links are implemented as knuckles. Links are connected by passive joints; therefore, rotational and translational movements can be realized simultaneously. For human knuckles, wrinkles play a vital role to modulate skin tension during movement. In this exoskeleton, knuckle links will lead to adaptability to different subject finger lengths and motion diversity. Compared to the combination of active rotary joint and passive prismatic joint, the designed passive joint can realize rotary and translational movements simultaneously. As a consequence, the mechanical structure is more compact. For this structure, a finger's configuration is described by eight variables. With a cable possessing adequate stiffness, finger flexion/extension is achieved by cable push/pull action. Since there is only one active input, this exoskeleton performs as a typical single input–multiple output system. Theoretically, given a determinate motor displacement, there are infinite possible finger configurations. To build a feasible direct kinematics model for control purposes, the statistic method is implemented. As a consequence, the piecewise polynomial function is adopted to describe the mapping from motor displacement to those variables.

The rest of this article is organized as follows. The hardware structure is introduced in the next section, followed by the kinematics model and parameter estimation process; afterward, experimental results are provided, and finally, the conclusion is given.

2. Hardware Structure

Based on an investigation of patients' demand and feeling, two issues are recognized as important. First, slippage between the finger and exoskeleton during movement should be minimized. Second, the exoskeleton should adopt different patients' finger lengths and length variations during movement. Motivated by those issues, a novel exoskeleton is designed, which consists of a palm platform and five finger assemblies. Then, a textile glove will be adhered to the exoskeleton's bottom side by glue. The exoskeleton mechanism is demonstrated in Figure 1.

2.1. Mechanical Parts. The mechanical structure for one finger is shown in Figure 2, which is consisted of one fixed link (no. 0) and five moveable links. Imitating a human being's hand, moveable links are categorized as phalanxes (no. 1, 3, 5) and knuckles (no. 2, 4). When the finger is totally extended, knuckles locate completely inside adjacent phalanxes. On links no. 1 and 3, one and two slots are milled, respectively. Hinges fixed on adjacent links can move freely inside those slots, either rotating or translating. Due to such structure, the exoskeleton can passively adapt to the patient finger's geometrical variation, both flexing angle and length.

A path for the Bowden cable is formed by tunnels inside links no. 0, 2, and 4 (area without section lines in Figure 2(b)). One end of the cable is connected to a linear motor (see Figure 3), and another end is fixed inside the fingertip. When the cable is pushed or pulled by the motor, the finger will be flexed or extended.

To realize both flexion and extension action by one cable, certain cable stiffness is compulsory. This is ensured by two aspects: on the one hand, a cable with a diameter of 2.5 mm is chosen among cables with different diameters. More importantly, almost the complete cable is constrained by surrounding structures: metal sleeve, rigid plastic tube (see Figure 3), and tunnels mentioned above. The linear motor's shaft is connected to a rod, which moves inside a sleeve. Along the complete cable, the maximum lateral tolerance is about 4 mm, which takes place inside the tunnel. As a consequence, adequate stiffness of the cable is achieved to exert bidirectional torques. A preliminary experiment shows that given the maximum motor displacement of 80 mm, the maximum displacement error due to cable bending is less than 2 mm.

2.2. Electronic Part. Each finger is driven by an individual linear motor, whose displacement is directly controlled, given maximum velocity and acceleration restrictions. During the rehabilitation process, fingers usually move slowly, and the dynamic characteristics of both finger and mechanism are not considered; in other words, it is adequate to control the motor in a displacement way, if the motor's output torque is sufficient.

A dyadic SCN5 series linear motor is adopted, whose driver communicates with a host computer via RS-485 bus according to the dyadic Termi-BUS protocol (see Figure 4). To realize closed-loop control, instructions are sent to motor

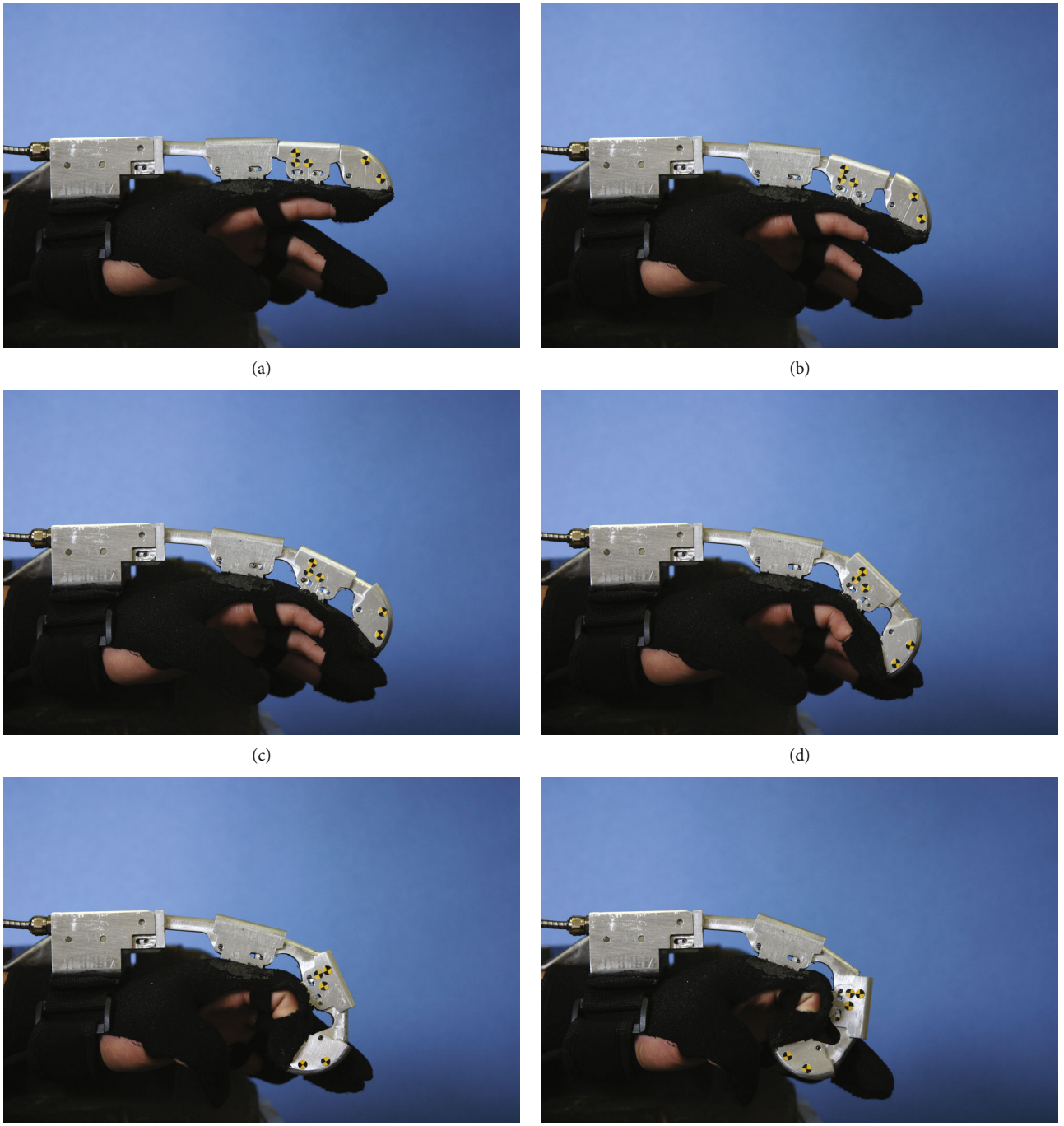

Figure 7: Images series acquired during the model building process.

Table 2: Some information with respect to volunteers.

	Gender		Age, years				Weight (kg)		
	Male	Female	18–30	31–40	41–50	>50	40–55	56–70	>70
Number	14	10	6	6	6	6	7	12	5
Percentage 5%	58%	42%	25%	25%	25%	25%	29%	50%	21%

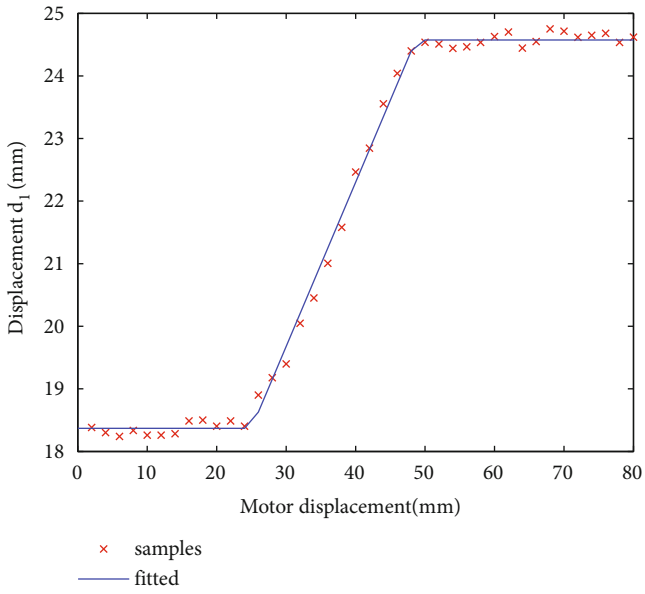

Figure 8: Samples and the fitted curve of displacement d_1 of volunteer 1.

drivers in turn through COM1 port, while the motor position and working status are read through COM2 port.

To monitor force through the Bowden cable, a ZNLBM-VII force sensor (with a resolution of 0.06 N in the range of 0–200 N) is installed between the motor shaft and the connecting rod (see Figure 3). Compared to the solution adopting another cable for force feedback [22], this method is more compact and reliable, since force is measured directly on the drive cable. At the present stage, only motor displacement control is implemented. Cable force will be implemented to realize impedance control in the next step.

3. Kinematics Model

3.1. Definition of Coordinate Frames. Taking the forefinger as an instance, for each link, a local coordinate frame, involving x and y axes, is defined (see Figure 2(a)). At initial configuration, that is, while the finger is totally extended, all frames' x and y axes are toward right and up, respectively. Origins of frames no. 0 and 1 are located at the same position, that is, the hinge connecting them. Origins of frames no. 2, 4, and 5 are located at corresponding proximal hinges. A little attention should be paid to frame no. 3, because there is no hinge fixed on link no. 3. The origin locates at the most proximal position for the distal hinge on link no. 2. Relative orientation and displacement between adjacent frames can be described by two quantities θ_i and d_i (see Table 1). Angle θ_i represents the angle from the axis x_i to axis x_{i-1}, counterclockwise. d_i is the displacement of the origin o_{i+1} along the axis x_i. As instance, θ_1 and d_1 are depicted in Figure 5. Note, d_2 and d_5 are constants, that is, distances between two hinges on link no. 2 and 4, respectively.

According to the definition of θ_i and d_i, the homogeneous transformation matrices between consequent link coordinate frames are given as:

$$T_1^0 = \begin{bmatrix} \cos\theta_1 & -\sin\theta_1 & 0 \\ \sin\theta_1 & \cos\theta_1 & 0 \\ 0 & 0 & 1 \end{bmatrix}, \quad (1)$$

$$T_2^1 = \begin{bmatrix} \cos\theta_2 & -\sin\theta_2 & d_1 \\ \sin\theta_2 & \cos\theta_2 & 0 \\ 0 & 0 & 1 \end{bmatrix}, \quad (2)$$

$$T_3^2 = \begin{bmatrix} \cos\theta_3 & -\sin\theta_3 & d_2 + d_3\cos\theta_3 \\ \sin\theta_3 & \cos\theta_3 & d_3\sin\theta_3 \\ 0 & 0 & 1 \end{bmatrix}, \quad (3)$$

$$T_4^3 = \begin{bmatrix} \cos\theta_4 & -\sin\theta_4 & d_4 \\ \sin\theta_4 & \cos\theta_4 & 0 \\ 0 & 0 & 1 \end{bmatrix}, \quad (4)$$

$$T_5^4 = \begin{bmatrix} \cos\theta_5 & -\sin\theta_5 & d_5 \\ \sin\theta_5 & \cos\theta_5 & 0 \\ 0 & 0 & 1 \end{bmatrix}. \quad (5)$$

3.2. Direct Kinematics Model. Taking the motor's displacement as input, as mentioned above, there are eight output variables, so the finger mechanism acts as a typical single-input multi-outputs system. Theoretically, there are infinite solutions, affected by many factors, for example, the patient finger's dimension, muscular tension, friction, etc. It is extremely difficult to find an analytical solution. Preliminary experiments show that, cooperated with the same subject, the exoskeleton motion's repeatability is quite good, which inspires us implementing statistic characteristics as the direct kinematics model.

To build the statistic kinematics model, images are acquisitioned. Given the linear motor's displacements as inputs, corresponding image series are taken. Five markers have been attached to the exoskeleton, which are denoted by marker no. 1–5 (see Figure 6). Pixel locations corresponding to centers of hinges and markers are read by image editing software. As mentioned early, d_2 is a constant, that is, the distance between two hinges on link no. 2. Knowing the ratio between the pixel distance and real length, another translational displacement can be calculated, for example, d_1 and d_4. Again, a little more attention is paid to d_3, because there is no fixing point on link no. 3 corresponding to the origin of the link coordinate frame no. 3. So, the origin's position is determined with help of markers no. 1 and 2, since marker no. 2 is placed at the midpoint of the line segment connecting marker no. 1 and the origin of frame no. 3. The marker no. 3 acts as a determinate point in frame no. 3. Role of the marker no. 5 is similar to marker no. 3. Displacements d_1, d_3, and d_4 are calculated based on pixel locations of corresponding hinges.

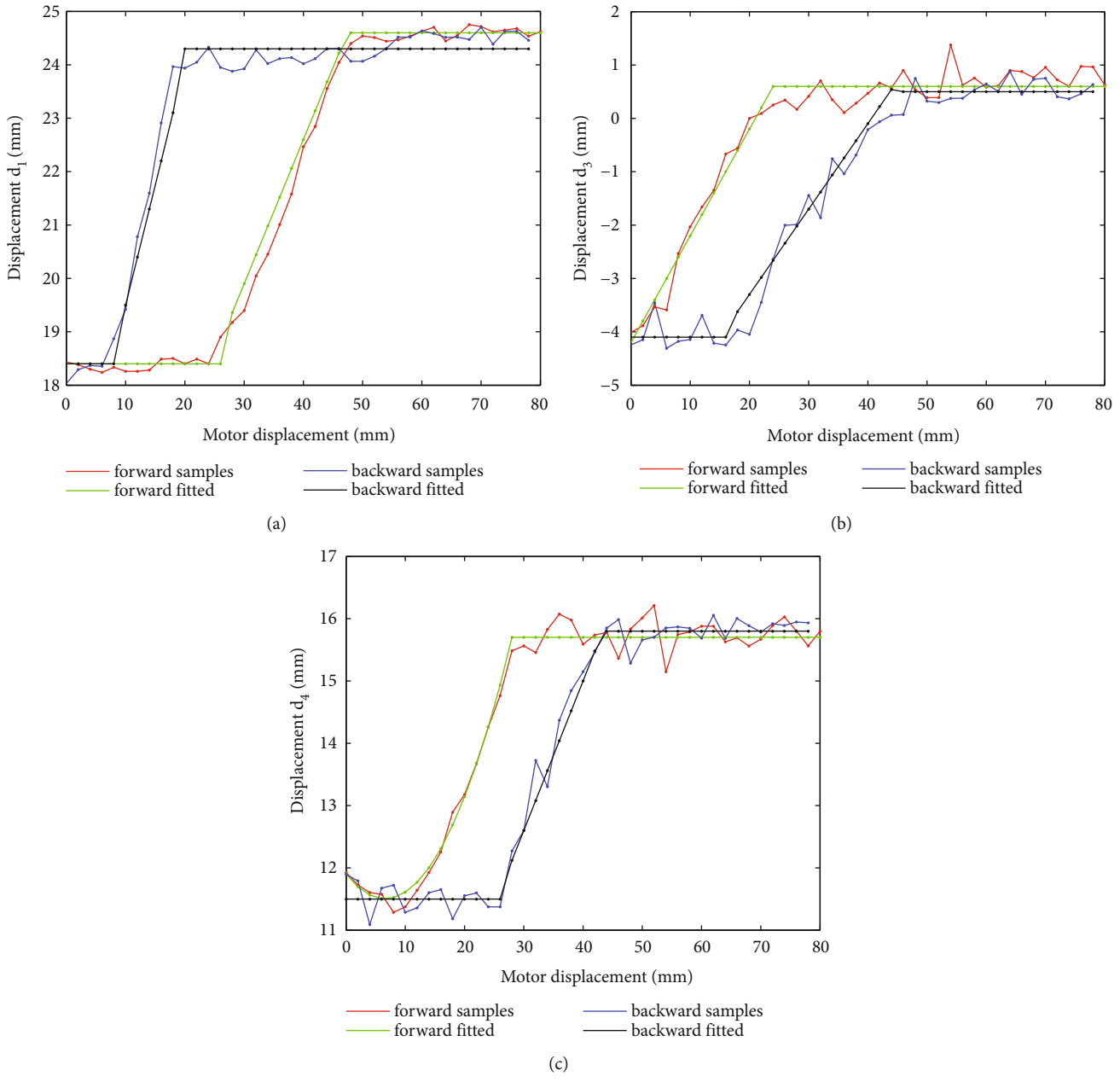

Figure 9: Displacements measured in both forward and backward movements.

By extracting edges corresponding to the upper boundary of links no. 0, 1, and 3, angle θ_1 and sum $\theta_2 + \theta_3$ can be obtained. The orientation of frame no. 5 is determined by markers no. 4 and 5, since there is no straight upper boundary on link no. 5. The orientation of linear segment connecting those two markers is calculated based on markers' pixel location, then the sum $\theta_4 + \theta_5$ can be calculated.

Namely, all angular displacements can be directly extracted. When joints' angles are small, most parts of links no. 2 and 4 are obscured by adjacent links, the extraction precision would be low; therefore, special attention is paid to angles θ_2 and θ_4. Given equations (1)–(5), it is easy to obtain the following transformation matrices by matrices multiplication as:

$$T_3^1 = \begin{bmatrix} c_{23} & -s_{23} & d_1 + d_2 \cos\theta_2 + d_3 c_{23} \\ s_{23} & c_{23} & d_2 \sin\theta_2 + d_3 s_{23} \\ 0 & 0 & 1 \end{bmatrix}, \quad (6)$$

$$T_5^3 = \begin{bmatrix} c_{45} & -s_{45} & d_4 + d_5 \cos\theta_4 \\ s_{45} & c_{45} & d_5 \sin\theta_4 \\ 0 & 0 & 1 \end{bmatrix}, \quad (7)$$

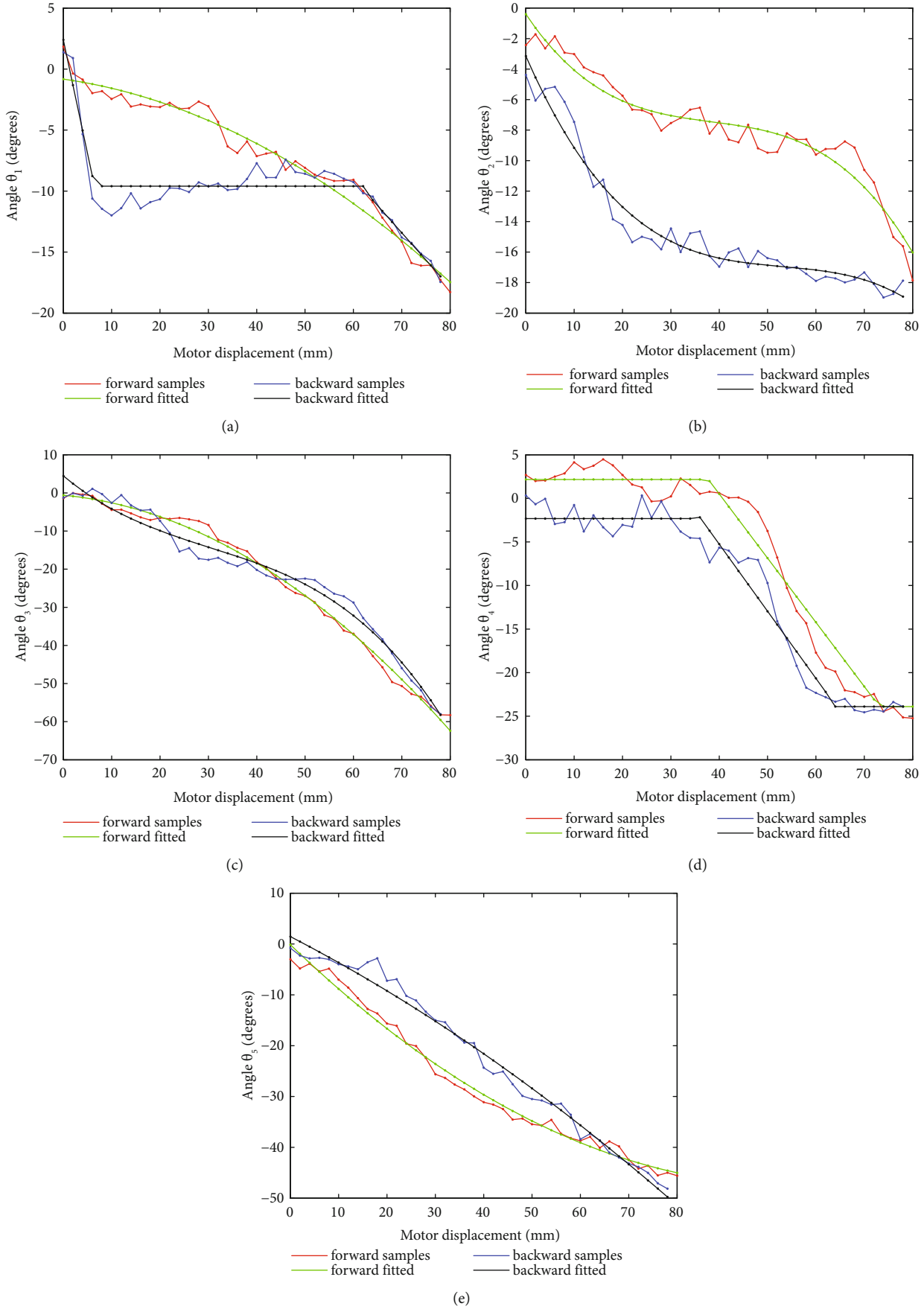

Figure 10: Angular displacements θ_i measured in both forward and backward movements.

Table 3: Expression of fitted joint variables.

	Forward	Backward
d_1	$\begin{cases} 18.4 & 0 < x \le 26 \\ 0.27x + 11.8 & 26 < x \le 46 \\ 24.6 & 46 < x < 80 \end{cases}$	$\begin{cases} 18.4 & 0 < x \le 8 \\ 0.47x + 15 & 8 < x \le 18 \\ 24.3 & 18 < x < 80 \end{cases}$
d_3	$\begin{cases} 0.2x - 4.2 & 0 < x \le 24 \\ 0.6 & 24 < x < 80 \end{cases}$	$\begin{cases} -4.1 & 0 < x \le 16 \\ 0.16x - 6.5 & 16 < x \le 44 \\ 0.5 & 44 < x < 80 \end{cases}$
d_4	$\begin{cases} 0.0091x^2 - 0.12x + 11.9 & 0 < x \le 24 \\ 15.7 & 26 < x < 80 \end{cases}$	$\begin{cases} 11.5 & 0 < x \le 26 \\ 0.24x + 5.4 & 26 < x \le 42 \\ 15.8 & 42 < x < 80 \end{cases}$
θ_1	$-0.0019x^2 - 0.056x - 0.82$	$\begin{cases} -1.86x + 2.4 & 0 < x \le 6 \\ -9.6 & 6 < x \le 62 \\ -0.446x + 17.8 & 62 < x < 80 \end{cases}$
θ_2	$-0.0001x^3 + 0.01x^2 - 0.47x - 0.4$	$-0.0001x^3 + 0.013x^2 - 0.72x - 3.1$
θ_3	$-0.0082x^2 - 0.12x - 0.6$	$-0.0002x^3 + 0.02x^2 - 1.05x + 4.5$
θ_4	$\begin{cases} 2.0 & 0 < x \le 40 \\ -0.97x + 42.5 & 40 < x \le 64 \\ -23.8 & 64 < x < 80 \end{cases}$	$\begin{cases} -2.3 & 0 < x \le 34 \\ -0.77x + 25.6 & 34 < x \le 62 \\ -23.9 & 62 < x < 80 \end{cases}$
θ_5	$0.0044x^2 - 0.91x - 0.1$	$-0.0021x^2 - 0.49x + 1.5$

where c_{23} and s_{23} are the abbreviations of terms $\cos(\theta_2 + \theta_3)$ and $\sin(\theta_2 + \theta_3)$, and other terms possess similar meaning.

Taking matrix T_3^1 as an instance, coordinates of a distinct point in frames no. 3 and 1 are denoted by u, v, x, and y, respectively (see Figure 5). The relationship between those quantities can be expressed as:

$$\begin{bmatrix} x \\ y \end{bmatrix} = T_3^1 \bullet \begin{bmatrix} u \\ v \end{bmatrix}. \tag{8}$$

More explicitly,

$$x = c_{23}u - s_{23}v + d_1 + d_2 \cos\theta_2 + d_3 c_{23}, \tag{9}$$

$$y = -s_{23}u + c_{23}v + d_2 \sin\theta_2 + d_3 s_{23}, \tag{10}$$

where u, v, and d_2 are known, variables x, y, d_1, and d_3 can be directly read from the image, the sum $\theta_2 + \theta_3$ also can be extracted with adequate accuracy, then s_{23} and c_{23} can be calculated. Finally, θ_2 can be obtained as:

$$\theta_2 = \arctan\left(\frac{y + s_{23}u - c_{23}v - d_3 s_{23}}{x - c_{23}u + s_{23}v - d_1 - d_3 c_{23}}\right). \tag{11}$$

Due to mechanical constraints, θ_2 is valid only in the fourth quadrant, so there is a distinct solution of the function $arctan()$ with only one argument.

Similarly, θ_4 can be solved as:

$$\theta_4 = \arctan\left(\frac{y + s_{45}u - c_{45}v}{x - c_{45}u + s_{45}v - d_4}\right), \tag{12}$$

where u and v are constants defined in the fifth link coordinate frame, and x and y are expressed in the third link frame.

3.3. Data Fitting Function. Analytical expressions of variables should be obtained by fitting sample data. Based on preliminary experiments, piecewise polynomial functions are chosen. First, switching points are determined intuitively by observing the data curve, then, in each segment, the degree and corresponding parameters are obtained by the nonlinear least square method (LSM) [41]. For the same data set, a polynomial of degrees from 0 to 3 are implemented as the desired model, then the polynomial with the minimum squared error is adopted. This will be explained with examples in the next section.

4. Experimental Results

4.1. Experimental Setup. During the modeling process, the exoskeleton's palm is steadily fixed onto a test table, and the camera is supported by a tripod, so the relative pose between the camera and the exoskeleton palm is kept invariant. The motor's step length is 4 mm, so there are 20 samples

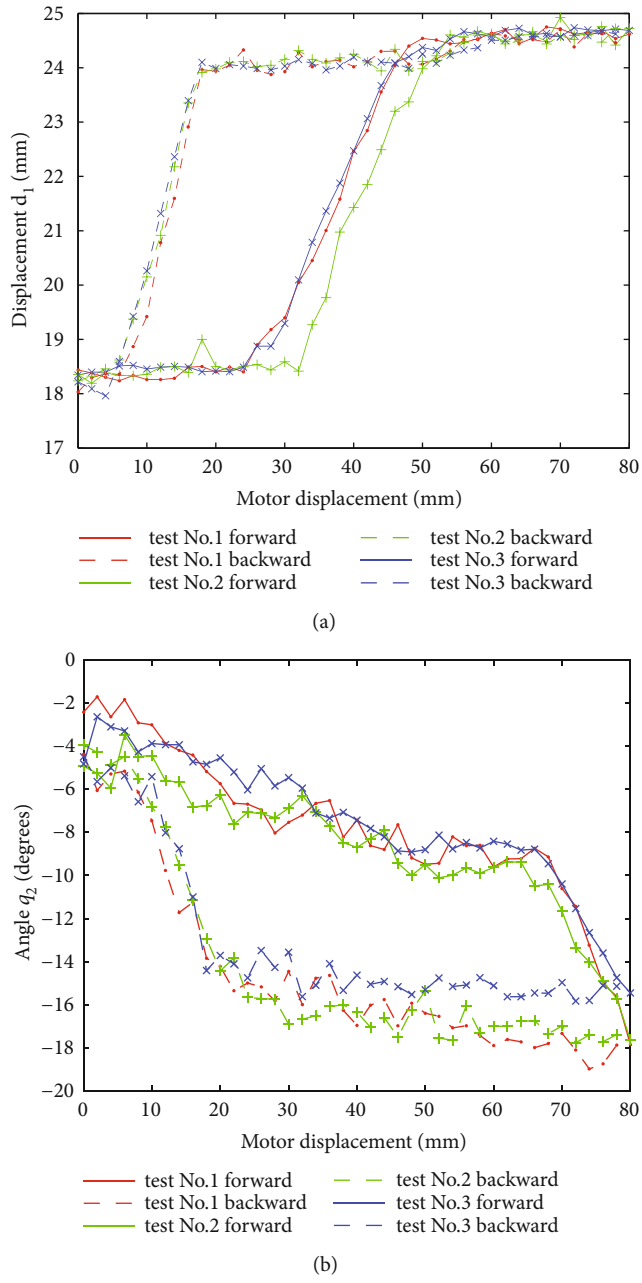

Figure 11: Repeatability with respect to movement of volunteer no. 1.

for one-way inside a total motion range of 80 mm. Six sample images are shown in Figure 7.

Twenty-four healthy Asian volunteers are recruited, who are required to keep the forefinger relaxed to follow exoskeleton's movement. For each volunteer, complete motion series including forward and backward stages are executed three times. More information about volunteers is listed in Table 2.

It is quite easy to wear the glove because of a semiopen form for the finger part, that is, Velco is implemented to fasten (see Figure 6). For a healthy volunteer, it consumes less than 1 minute to wear with help of others.

4.2. Original Data and Fitting Functions. The curve of d_1 of volunteer 1 during a forward movement is shown in Figure 8. The expression is consisted of three parts, with a form of constant, linear function and constant, respectively.

An interesting phenomenon is observed that for all configuration variables, there are obvious differences between forward and backward movements, either shift or shape deformation. To demonstrate this, the original data set and fitted curves for all eight configuration variables of volunteer 1 are drawn in Figures 9–10. Corresponding expressions are listed in Table 3, where the argument x represents the motor displacement. It is observed that for translational

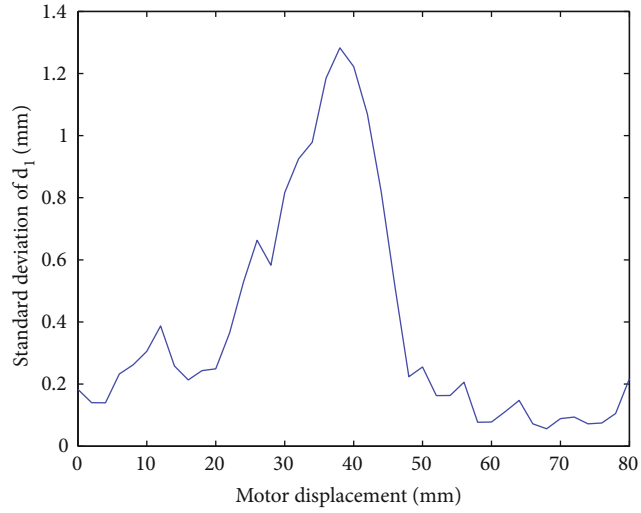

(a)

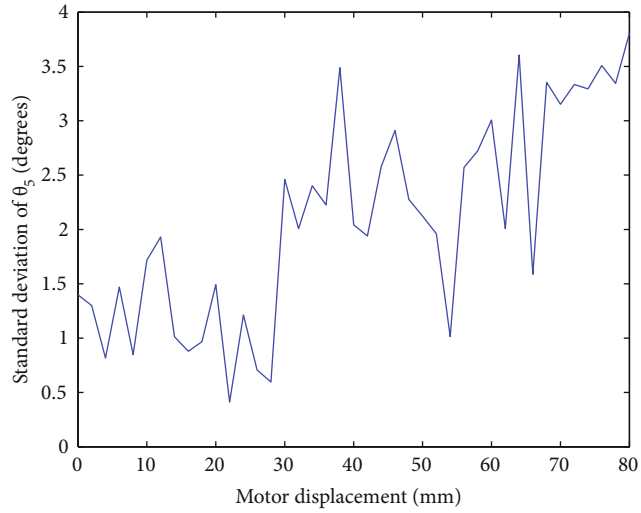

(b)

Figure 12: Standard deviation of variables d_1 and θ_5 of all volunteers.

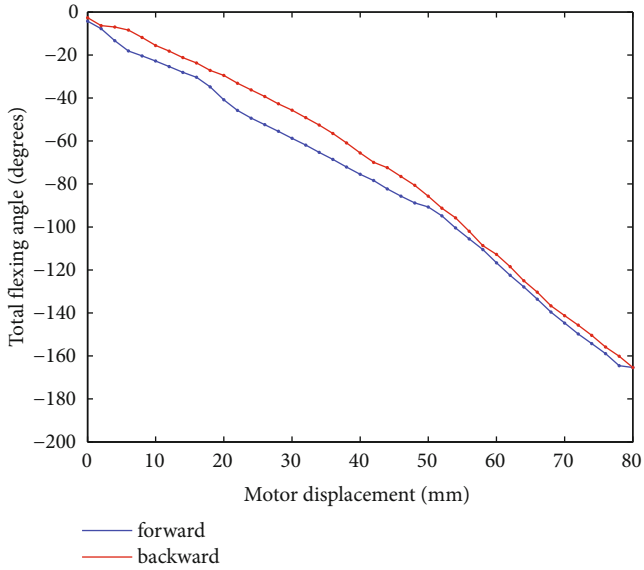

Figure 13: Finger's total flexing angle of volunteer 1.

displacements d_1, d_3, and d_4, differences are with the form of relative regular hysteresis. For angular variables, situation is more complicated. For θ_1, shapes corresponding to two ways are totally different, so do the corresponding expressions. For θ_3, expressions even possess different degrees.

Then, the repeatability for an individual volunteer is verified. As instances, d_1 and θ_2 of the volunteer 1 are shown in Figure 11. A similar phenomenon appears for other variables and volunteers. It can be seen that the repeatability is quite good, that is, data can be fitted by similar expressions.

Difference between volunteers is also analyzed. As an instance, the standard deviation of d_1 and θ_5 are shown in Figure 12. It can be found that the maximum for d_1 takes place in the middle part, which is mainly caused by shift (see Figure 11(a)). And the standard deviation of θ_5 increases with it. A similar phenomenon appears in rest variables. If necessary, the model for different volunteers can be described by the same type of expressions with different parameter values.

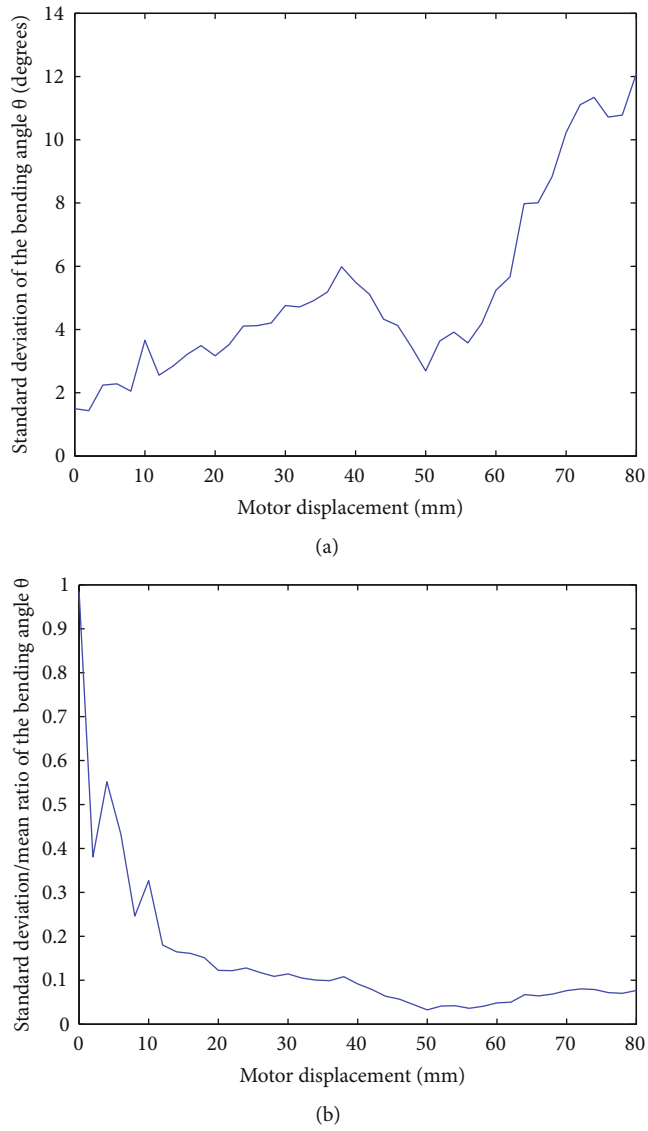

Figure 14: Finger's total flexing angle of all volunteers.

The relationship between the motor's displacement and the total flexing angle of the exoskeleton for volunteer 1 is shown in Figure 13. It can be observed that the nonlinearity is obviously weaker than relationships between motor displacement and most intermediate variables, and so does the difference between forward and backward movements. By LSM, the relationship can be described by:

$$\theta(x) = \begin{cases} -0.013x^2 - 1.05x - 3.14, & \text{forward} \\ -0.0083x^2 - 1.33x - 8.52, & \text{backward} \end{cases}, \quad (13)$$

where the total flexing angle is denoted by θ. Equation (13) can be employed as a kinematics model for rehabilitation trajectory generation or control purposes.

The standard deviation of $\theta(x)$ for all volunteers is shown in Figure 14. Similar to an individual angle, the standard deviation increased with $\theta(x)$, and the maximum reaches about 12 degrees, while the bending angle is nearly −160 degrees (see Figure 7). The ratio between standard deviation and the bending angle itself is shown in Figure 14(b). In the beginning, a big ratio is due to that the bending angle itself is small; therefore, the influence of noise is significant. With increasing $\theta(x)$, this ratio convergence to low level, that is, about 0.1. This phenomenon demonstrates that the exoskeleton possesses a good generality to volunteers. From a hardware point of view, it adapts to different finger lengths and length variations during movement. From a software point of view, it will be easy to "customize" a distinct finger model by calibration.

5. Conclusion

A robotic exoskeleton for fingers rehabilitation is introduced, which possesses the following characteristics:

(i) two links mimicking knuckles are implemented

(ii) links are connected by passive joints

(iii) bidirectional torque is exerted by one Bowden cable with help of a sleeve

(iv) the maximum bending angle approaches nearly −160 degrees

Because of those characteristics, it possesses good adaptability to finger length of different subjects and length variation during movement while keeping the structure compact. Piecewise polynomial functions are chosen as the direct kinematics model. Experimental results show that this robot possesses adaptability to different subjects and has achieved nearly the maximum finger bending angle of a healthy adult person. It will be easy to customize a distinct finger model by calibration for the individual patient, individual finger, or during different therapy stages, to satisfy rehabilitation requirements.

Data Availability

The data used to support the findings of this study are available from the corresponding author.

Conflicts of Interest

The authors declare that there is no conflict of interest regarding the publication of this paper.

Acknowledgments

The authors would like to thank all volunteers for their kind helps to test the exoskeleton prototype. The work was supported by the Foundation for Innovative Research Groups of Natural Science Foundation of China (Grant Number 51521003) and Self-topic Fund of the State Key Laboratory of Robotics and Systems (Grant Number SKLRS201705A).

References

[1] P. Agarwal, J. Fox, Y. Yun, M. K. O'Malley, and A. D. Deshpande, "An index finger exoskeleton with series elastic actuation for rehabilitation: design, control and performance characterization," *International Journal of Robotics Research*, vol. 34, no. 14, pp. 1747–1772, 2015.

[2] A. Chiri, N. Vitiello, F. Giovacchini, S. Roccella, F. Vecchi, and M. C. Carrozza, "Mechatronic design and characterization of the index finger module of a hand exoskeleton for post-stroke rehabilitation," *IEEE/AMSE Transactions on Mechatronics*, vol. 17, no. 5, pp. 884–894, 2012.

[3] G. Kwakkel, B. Kollen, and H. Krebs, "Effects of robot-assisted therapy on upper limb recovery after stroke: a systematic review," *Neurorehabilitation and Neural Repair*, vol. 22, no. 2, pp. 111–121, 2008.

[4] T. du Plessis, K. Djouani, and C. Oosthuizen, "A review of active hand exoskeletons for rehabilitation and assistance," *Robotics*, vol. 10, no. 1, pp. 40–82, 2021.

[5] J. Arata, K. Ohmoto, R. Gassert, O. Lambercy, H. Fujimoto, and I. Wada, "A new hand exoskeleton device for rehabilitation using a three-layered sliding spring mechanism," *Proceedings of the IEEE International Conference on Robotics and Automation (ICRA)*, pp. 3902–3907, Karlsruhe, Germany, 2013.

[6] P. Heo, G. Gu, S. Lee, K. Rhee, and J. Kim, "Current hand exoskeleton technologies for rehabilitation and assistive engineering," *International Journal of Precision Engineering and Manufacture*, vol. 13, no. 5, pp. 807–824, 2012.

[7] T. Tang, D. Zhang, T. Xie, and X. Zhu, "An exoskeleton system for hand rehabilitation driven by shape memory alloy," *Proceedings of the IEEE International Conference on Robotics and Biomimetics (ROBIO)*, pp. 756–761, Shenzhen, People's Republic of China, 2013.

[8] W. Wei, S. Guo, F. Zhang, J. Guo, Y. Ji, and Y. Wang, "A novel upper limb rehabilitation system with hand exoskeleton mechanism," *Proceedings of the IEEE International Conference on Mechatronics and Automation (ICMA)*, pp. 285–290, Takamatsu, Japan, 2013.

[9] S. Kim, J. Lee, and J. Bae, "Analysis of finger muscular forces using a wearable hand exoskeleton system," *Journal of Bionic Engineering*, vol. 14, no. 4, pp. 680–691, 2017.

[10] A. Lince, N. Celadon, A. Battezzato et al., "Design and testing of an under-actuated surface EMG-driven hand exoskeleton," *Proceedings of IEEE International Conference on Rehabilitation Robotics (ICORR)*, pp. 670–675, London, UK, 2017.

[11] S. Ueki, H. Kawasaki, S. Ito et al., "Development of a hand-assist robot with multi-degrees-of-freedom for rehabilitation therapy," *IEEE/AMSE Transactions on Mechatronics*, vol. 17, no. 1, pp. 136–146, 2012.

[12] M. Cempini, S. M. M. De Rossi, T. Lenzi et al., "Kinematics and design of a portable and wearable exoskeleton for hand rehabilitation," *Proceedings of the IEEE International Conference on Rehabilitation Robotics (ICORR)*, pp. 1–6, Seattle, WA, USA, 2013.

[13] L. Cui, A. Phan, and G. Allison, "Design and fabrication of a three dimensional printable non-assembly articulated hand exoskeleton for rehabilitation," *Proceedings of the 37th Annual International Conference of the IEEE Engineering in Medicine and Biology Society (EMBC)*, pp. 4627–4630, Milan, Italy, 2015.

[14] O. Sandoval-Gonzalez, J. M. Jacinto-Villegas, I. Herrera-Aguilar et al., "Design and development of a hand exoskeleton robot for active and passive rehabilitation," *International Journal of Advanced Robotic Systems*, vol. 13, no. 2, p. 66, 2016.

[15] D. Wang, Q. Meng, Q. Meng, X. Li, and H. Yu, "Design and development of a portable exoskeleton for hand rehabilitation," *IEEE Transactions on Neural Systems and Rehabilitation Engineering*, vol. 26, no. 12, pp. 2376–2386, 2018.

[16] A. H. A. Rahim, A. Lachmann, C. Y. Low, and A. T. M. Amin, "SMA actuated finger exoskeleton device for rehabilitation of acute paresis patient," *Applied Mechanics and Materials*, vol. 773–774, pp. 883–887, 2015.

[17] M. Fontana, S. Fabio, S. Marcheschi, and M. Bergamasco, "Haptic hand exoskeleton for precision grasp simulation," *Journal of Mechanisms and Robotics - Transactions of the ASME*, vol. 5, no. 4, pp. 1–9, 2013.

[18] N. S. K. Ho, K. Y. Tong, X. L. Hu, W. Rong, E. A. Susanto, and S. K. Ho, "An EMG-driven exoskeleton hand robotic training device on chronic stroke subjects," *Proceedings of IEEE International Conference on Rehabilitation Robotics (ICORR)*, pp. 1–5, Zurich, Switzerland, 2011.

[19] T. Hsu, Y. Chiang, W. Chan, and S.-J. Chen, "A finger exoskeleton robot for finger movement rehabilitation," *Inventions*, vol. 2, no. 3, pp. 1–8, 2017.

[20] I. Jo and J. Bae, "Design and control of a wearable and force-controllable hand exoskeleton system," *Mechatronics*, vol. 41, pp. 90–101, 2017.

[21] P. Weiss, L. Heyer, T. F. Muente, M. Heldmann, A. Schweikard, and E. Maehle, "Towards a parameterizable exoskeleton for training of hand function after stroke," *Proceedings of IEEE International Conference on Rehabilitation Robotics (ICORR)*, pp. 1–6, Seattle, WA, USA, 2013.

[22] A. Wege and G. Hommel, "Development and control of a hand exoskeleton for rehabilitation of hand injuries," *Proceedings of 2005 IEEE/RSJ International Conference on Intelligent Robots and Systems (IROS)*, pp. 3046–3051, Edmonton, Canada, 2005.

[23] C. L. Jones, F. Wang, R. Morrison, N. Sarkar, and D. G. Kamper, "Design and development of the cable actuated finger exoskeleton for hand rehabilitation following stroke," *IEEE/AMSE Transactions on Mechatronics*, vol. 19, no. 1, pp. 131–140, 2014.

[24] H. In, K. Cho, K. Kim, and B. Lee, "Jointless structure and under-actuation mechanism for compact hand exoskeleton," *Proceedings of IEEE International Conference on Rehabilitation Robotics (ICORR)*, pp. 1–6, Zurich, Switzerland, 2011.

[25] L. Randazzo, I. Iturrate, S. Perdikis, and J. R. Millan, "Mano: a wearable hand exoskeleton for activities of daily living and neurorehabilitation," *IEEE Robotics and Automation Letters*, vol. 3, no. 1, pp. 500–507, 2018.

[26] D. Marconi, A. Baldoni, Z. McKinney, M. Cempini, S. Crea, and N. Vitiello, "A novel hand exoskeleton with series elastic actuation for modulated torque transfer," *Mechatronics*, vol. 61, pp. 69–82, 2019.

[27] T. Bützer, O. Lambercy, J. Arata, and R. Gassert, "Fully wearable actuated soft exoskeleton for grasping assistance in everyday activities," *Soft Robot*, vol. 8, no. 2, pp. 128–143, 2021.

[28] H. Talat, H. Munawar, H. Hussain, and U. Azam, "Design, modeling and control of an index finger exoskeleton for rehabilitation," *Robotica*, pp. 1–25, 2022.

[29] Y. Park, I. Jo, J. Lee, and J. Bae, "A dual-cable hand exoskeleton system for virtual reality," *Mechatronics*, vol. 49, pp. 177–186, 2018.

[30] P. Heo, S. J. Kim, and J. Kim, "Powered finger exoskeleton having partially open fingerpad for flexion force assistance," *Proceedings of IEEE/ASME International Conference on Advanced Intelligent Mechatronics (AIM)*, pp. 182–187, Wollongong, NSW, Australia, 2013.

[31] K. Tadano, M. Akai, K. Kadota, and K. Kawashima, "Development of grip amplified glove using bi-articular mechanism with pneumatic artificial rubber muscle," *Proceedings of the IEEE International Conference on Robotics and Automation (ICRA)*, pp. 2363–2368, Anchorage, AK, USA, 2010.

[32] E. B. Brokaw, I. Black, R. J. Holley, and P. S. Lum, "Hand spring operated movement enhancer (HandSOME): a portable, passive hand exoskeleton for stroke rehabilitation," *IEEE Transactions on Neural Systems and Rehabilitation Engineering*, vol. 19, no. 4, pp. 391–399, 2011.

[33] S. Ates, J. Lobo-Prat, P. Lammertse, H. van der Kooij, and A. H. A. Stienen, "SCRIPT passive orthosis: design and technical evaluation of the wrist and hand orthosis for rehabilitation training at home," *Proceedings of IEEE International Conference on Rehabilitation Robotics (ICORR)*, pp. 1–6, Seattle, WA, USA, 2013.

[34] E. Capotorti, E. Trigili, Z. McKinney et al., "A novel torque-controlled hand exoskeleton to decode hand movements combining SEMG and fingers kinematics: a feasibility study," *IEEE Robotics and Automation Letters*, vol. 7, no. 1, pp. 239–246, 2022.

[35] B. B. Kang, H. Lee, H. In, and K.-J. Cho, "Development of a polymer-based tendon-driven wearable robotic hand," *Proceedings of the IEEE International Conference on Robotics and Automation (ICRA)*, pp. 3750–3755, Stockholm, Sweden, 2016.

[36] P. Polygerinos, K. C. Galloway, E. Savage, M. Herman, K. O'Donnell, and C. J. Walsh, "Soft robotic glove for hand rehabilitation and task specific training," *Proceedings of the IEEE International Conference on Robotics and Automation (ICRA)*, pp. 2913–2919, Seattle, WA, USA, 2015.

[37] P. Polygerinos, Z. Wang, K. C. Galloway, R. J. Wood, and C. J. Walsh, "Soft robotic glove for combined assistance and at-home rehabilitation," *Robotics and Autonomous Systems*, vol. 73, p. 135, 2015.

[38] L. Lin, F. Zhang, L. Yang, and Y. Fu, "Design and modeling of a hybrid soft-rigid hand exoskeleton for poststroke rehabilitation," *International Journal of Mechanical Sciences*, vol. 212, pp. 106831–106841, 2021.

[39] A. Schiele and F. van der Helm, "Kinematic design to improve ergonomics in human machine interaction," *IEEE Transactions on Neural Systems and Rehabilitation Engineering*, vol. 14, no. 4, pp. 456–469, 2006.

[40] A. H. A. Stienen, E. E. G. Hekman, F. C. T. van der Helm, and H. van der Kooij, "Self-Aligning exoskeleton axes through decoupling of joint rotations and translations," *IEEE Transactions on Robotics*, vol. 25, no. 3, pp. 628–633, 2009.

[41] T. F. Coleman and Y. Li, "An Interior trust region approach for nonlinear minimization subject to bounds," *SIAM Journal on Optimization*, vol. 6, no. 2, pp. 418–445, 1996.

Hindawi
Applied Bionics and Biomechanics
Volume 2022, Article ID 2166082, 14 pages
https://doi.org/10.1155/2022/2166082

Research Article

Short-Term Load Forecasting Based on EEMD-WOA-LSTM Combination Model

Lei Shao[1], **Quanjie Guo**[1], **Chao Li**[1], **Ji Li**[1] and **Huilong Yan**[2]

[1]*School of Electrical Engineering and Automation, Tianjin University of Technology, Tianjin 300384, China*
[2]*School of Precision Instrument and Opto-Electronics Engineering, Tianjin University, Tianjin 300384, China*

Correspondence should be addressed to Chao Li; liton@email.tjut.edu.cn and Ji Li; liji0606@163.com

Received 22 June 2022; Accepted 8 August 2022; Published 24 August 2022

Academic Editor: Muye Pang

The purpose of this study was to better apply artificial intelligence algorithm to load forecasting and effectively improve the forecasting accuracy. Based on the long short-term memory neural networks, a combined model based on whale bionic optimization is proposed for short-term load forecasting. The whale bionic algorithm is used to solve the problem that the long short-term memory neural networks are easy to fall into local optimization and improve the accuracy of parameter optimization. The original signal is decomposed into multiple characteristic components by set empirical mode decomposition. Each feature component is input into the bionic optimized combination model for prediction. Finally, get the load forecasting results. Compared with the prediction results of EEMD-ARMA model, RNN model, LSTM model, and WOA-LSTM model, the combined prediction model optimized by whale bionics has less prediction error and higher prediction accuracy.

1. Introduction

Due to the intelligence and progressiveness of artificial intelligence technology, artificial intelligence technology has been applied in aerospace, medical and health, power system, and many other fields. The application of artificial intelligence technology in power system and power enterprises can optimize the stability and security of power system. Due to the increasing complexity of power system load, power load forecasting has become a key technology for the stable operation of the system. The development of short-term load forecasting has also changed from basic mathematical methods to artificial intelligence forecasting. The prediction accuracy is improved by combining artificial intelligence algorithm.

There are three kinds of short-term power load forecasting methods: traditional forecasting method, modern forecasting method, and combined forecasting model method. Traditional prediction methods include regression prediction method [1], exponential smoothing method, [2], and time series method [3]. The prediction accuracy of regression prediction method is low, but the fitting speed is fast. It is a basic prediction model. Exponential smoothing method can get the contribution of all data to the prediction data through different weights. Exponential smoothing method has poor ability to judge the turning point of data. The advantage of time series method is that it can eliminate random fluctuations. The disadvantage is that the time series method is greatly affected by the original data, and the fitting accuracy is poor when the amount of data is large.

Modern prediction methods include grey prediction method, fuzzy prediction method, and neural network method. Jin et al. [4] proposed a new grey relational competition model for short-term power load forecasting. When the amount of data of load series increases and the degree of dispersion increases, the prediction accuracy of grey prediction method will decrease. Cevik and Cunkas [5] proposed a short-term load forecasting model based on fuzzy logic and adaptive neuro fuzzy inference system (ANFIS). The fuzzy control algorithm based on fuzzy logic and fuzzy mathematics in fuzzy theory is often used in the field of power load. However, this method has high dependence on experience, poor adaptive learning ability, and poor prediction effect on nonlinear data. Neural networks (NNs) are

the most widely used prediction methods [6–8], and build a multifunctional computing model. In neural network model, radial basis function and error back propagation algorithm are widely used. Various neural network structures have been proposed to improve the prediction effect [9–11]. With the rapid development of artificial intelligence, many experts and scholars have proposed deep neural network. Compared with traditional neural network, deep neural network (DNN) [12] has multiple hidden layers, which enhances the sensitivity to the correlation of temporal data.

Typical deep neural networks include convolutional neural network (CNN), deep confidence network, and recurrent neural network (RNN). RNN is proposed to better process sequence information [13]. LSTM evolved from RNN [14] and was first developed by Hochreiter [15], which solves the problems of gradient disappearance and gradient explosion that are easy to occur in RNN and can retain short-term and long-term memory in the network [16]. LSTM has also been successfully applied in many research fields [17], such as phoneme classification [18], traffic prediction [19], language subtitles [20], and action recognition [21]. LSTM can effectively learn the law information in the historical sequence information. In the above research fields, LSTM model has achieved high accuracy, and it is a very efficient neural network model.

A single neural network prediction algorithm is easy to fall into local optimization during testing. The complexity of power load also leads to the fact that a single prediction method cannot ensure the accuracy of prediction. Combined prediction model is proposed to solve the problem of prediction accuracy. The combination of different types of artificial neural network models is a research hotspot to solve the problem of short-term power load forecasting. Santra and Lin [22] proposed a combined model of genetic algorithm (GA) and long-term and short-term memory (LSTM). GA is used to optimize the parameters of LSTM to improve the robustness of short-term load forecasting. However, at present, the selection of parameters of genetic algorithm mostly depends on experience, such as crossover rate and mutation rate. And the genetic algorithm is slow to deal with the feedback information of the network, and the search speed of the algorithm is slow. Hong et al. [23] proposed a short-term load forecasting model based on deep neural network and iterative ResBlock to learn the correlation between different power consumption behaviors. Compared with the traditional convolutional neural network, iterative ResBlock can transmit low-level information and make the network training deeper. But the deeper network structure needs better GPU to train, and the requirements for hardware are higher. Moradzadeh et al. [24] proposed a combined model of improved support vector regression (SVR) and long-term and short-term memory (LSTM), which achieved good prediction results. However, support vector regression is not suitable for large data sets. When the number of features of each data point exceeds the number of training data samples, support vector regression performs poorly. And when the data set is noisy, it is easy to cause the target classes to overlap. He et al. [25] proposed a combined prediction model based on variational modal decomposition and long-term and short-term memory networks. The original input signal is processed by variational modal decomposition, which reduces the interference of noise. However, the parameter selection of LSTM will affect the prediction accuracy of the whole combined model. Meng et al. [26] proposed a long-term and short-term memory neural network model combining empirical mode decomposition and attention mechanism. The performance of LSTM neural network is optimized. However, empirical mode decomposition (EMD) has a serious mode aliasing phenomenon, which requires high requirements for the original data. Set empirical mode decomposition (EEMD) is proposed to solve the mode aliasing phenomenon in EMD.

To sum up, consider the raw data processing and parameter selection. The set empirical mode decomposition is used to process the original signal to overcome the phenomenon of modal aliasing. The whale bionic optimization algorithm is used to optimize the parameters. In this paper, we propose an LSTM neural network model optimized by whale bionic algorithm for short-term load forecasting. The model combines bionic algorithm with artificial intelligence algorithm. The data is decomposed into modal components of different scales as the input of the model through set empirical mode decomposition. WOA layer optimizes LSTM parameters according to whale algorithm. The LSTM layer is used to model historical data. Based on the historical load data of a company, the artificial intelligence method is evaluated. Compared with RNN model, LSTM model, EEMD-ARMA model, and WOA-LSTM model, the proposed prediction method has higher accuracy.

The remainder of this article is summarized as follows. The second section introduces the basic principles of LSTM neural network, whale algorithm, and EEMD. The third section introduces the combined forecasting model and error evaluation index. The fourth section gives the relevant example analysis. The fifth section makes a summary.

2. Algorithm Preparation

2.1. LSTM. When ordinary recurrent neural network (RNN) processes complex data, improper parameter selection is easy to lead to gradient disappearance and gradient explosion. Compared with RNN, LSTM neural network adds logic gate control mechanism and state transfer unit, so that it not only retains the correlation with time but also increases the dependence between distant information. Figure 1 shows the cell unit of LSTM neural network. x_t in the figure is the input data at time t. h_{t-1} is the output of the hidden layer at time $t-1$. c_{t-1} is the state of cell unit at time $t-1$. c_t is the state of cell unit at time t. σ represents the sigmoid function. Output value h_t of LSTM neural network and unit status c_t at the current time are determined by the input value x_t at the current time and output value of hidden layer at last time h_{t-1} and unit status c_{t-1} shared decision.

The calculation formula is

$$f_t = \sigma\left(W_f \cdot [h_{t-1}, x_t] + b_f\right), \tag{1}$$

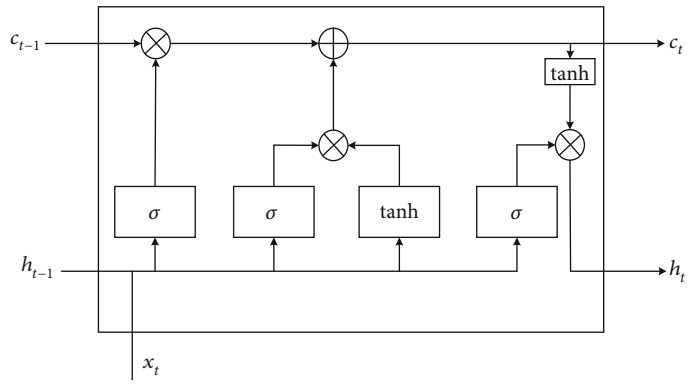

Figure 1: LSTM neural network unit.

$$i_t = \sigma(W_i \cdot [h_{t-1}, x_t] + b_i), \tag{2}$$

$$\tilde{c}_t = \tanh\,(W_c \cdot [h_{t-1}, x_t] + b_c), \tag{3}$$

$$c_t = f_t * c_{t-1} + i_t * \tilde{c}_t, \tag{4}$$

$$h_t = \sigma(W_o[h_{t-1}, x_t] + b_o) * \tanh\,(c_t). \tag{5}$$

In the formula, f_t, i_t, $\tilde{c}_t$, c_t, and $h_t$are forgetting gate, input gate, input node, cell state, and output layer, W_f, W_i, W_c, W_o and b_f, b_i, b_c, b_o is the weight matrix of forgetting gate, b_f is the weight matrix and offset term corresponding to forgetting gate, input gate, input node, and output gate, and σ is the sigmoid function.

2.2. Whale Optimization Algorithm. Bionic intelligent algorithms have developed rapidly, such as particle swarm optimization, leapfrog algorithm, and fish swarm algorithm. Mirjalili and Lewis creatively put forward whale optimization algorithm in the field of bionic intelligent algorithm [27]. Compared with other algorithms, whale algorithm is an intelligent optimization algorithm with simple operation, few parameters, and good optimization performance. By simulating the whale predation mechanism to represent the optimization process of the algorithm, the global and local search capabilities are better weighed and quantified. The flow chart is shown in Figure 2.

In WOA, search particles are initialized in space. When $|A| < 1$, WOA enters local search; when $|A| > 1$, WOA enters the global search. The formula is as follows:

$$a(t) = 2 - \frac{2t}{T}, \tag{6}$$

$$A(t) = 2a(t)r - a(t), \tag{7}$$

$$C(t) = 2r. \tag{8}$$

In the formula, t represents the current number of iterations and T represents the maximum number of iterations. r is any value between $[0, 1]$. In the whole iterative process, a gradually decreases from 2 to 0. A is a random number belonging to $[-a, a]$.

WOA enters the local search phase. One is the shrink surrounding method and the other is the spiral update method. The formula for the contraction phase is as follows:

$$\vec{X}(t+1) = \overrightarrow{X^*}(t) - A(t) \cdot \vec{D}(t), \tag{9}$$

$$\vec{D}(t) = \left| C(t) \cdot \overrightarrow{X^*}(t) - \vec{X}(t) \right|. \tag{10}$$

$\vec{D}$ stands for random distance, which is the distance between the target and the search particle. The spiral update method formula is as follows:

$$\vec{X}(t+1) = \overrightarrow{D'}(t) \cdot e^{bl} \cdot \cos\,(2\pi l) + \overrightarrow{X^*}(t), \tag{11}$$

$$\overrightarrow{D'}(t) = \left| \vec{X}^*(t) - \vec{X}(t) \right|. \tag{12}$$

X^* represents the optimal solution so far. $\vec{D}$ represents the random distance between the target prey and the search particle. $\overrightarrow{D'}$ represents the distance between the optimal solution and the search particle, b is a constant coefficient, and l is a random number in [-1,1]. p is a probability randomly generated from [0,1].

When $|A| > 1$, WOA enters the global search phase. The formula is as follows:

$$\vec{X}(t+1) = \overrightarrow{X_{\text{rand}}} - A(t) \cdot \vec{D}(t), \tag{13}$$

$$\vec{D}(t) = \left| C(t) \cdot \overrightarrow{X_{\text{rand}}} - \vec{X}(t) \right|. \tag{14}$$

$\overrightarrow{X_{\text{rand}}}$ represents the search particles randomly selected from the population.

The optimization process of whale optimization algorithm is as follows:

(1) Initialize the whale population

(2) In the process of evolution, whales update their position according to the optimum

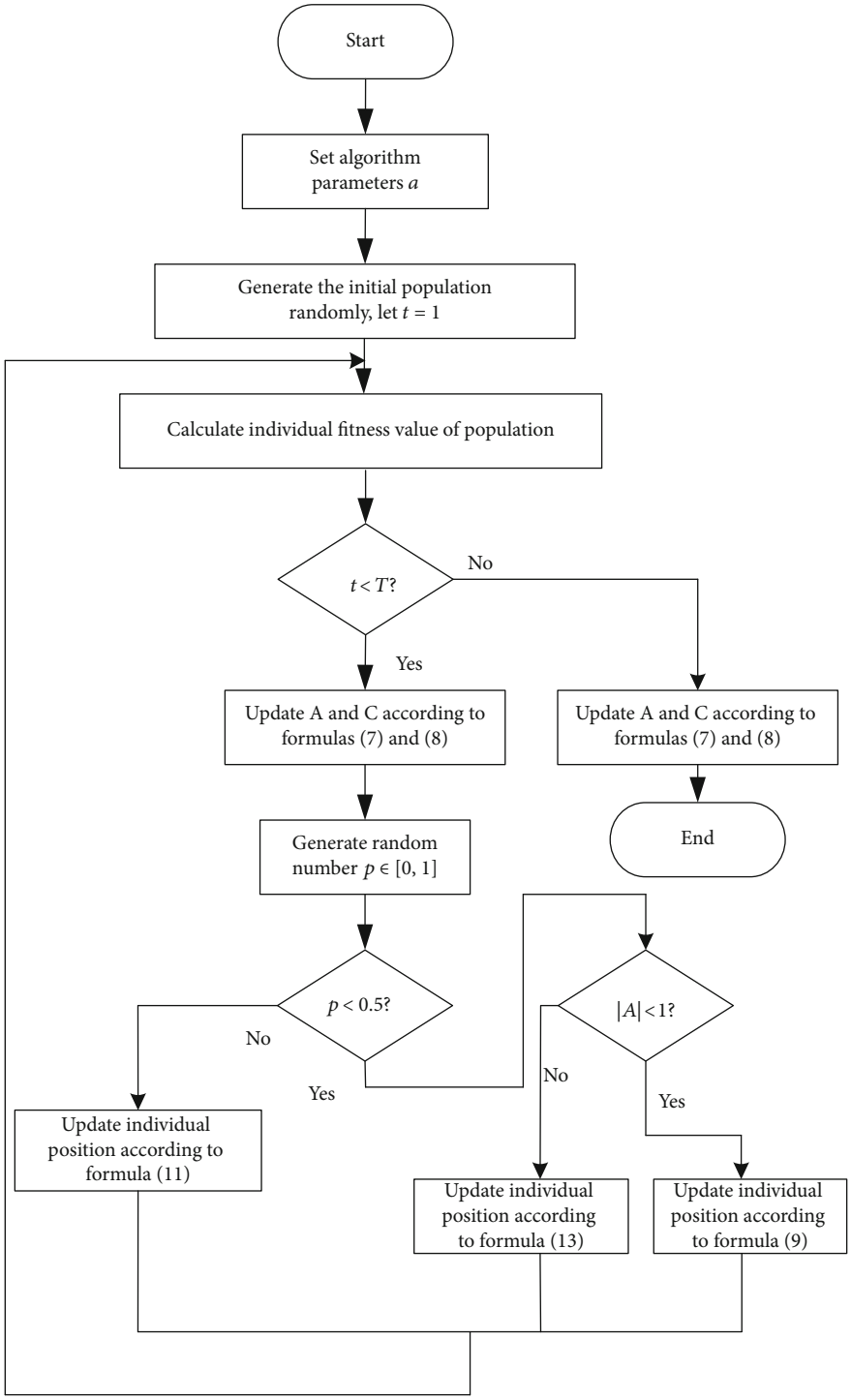

Figure 2: Flow chart of whale optimization algorithm.

(3) Determine the whale position update method according to p

(4) Iterate until the whale algorithm meets the termination requirements

The whale algorithm is used to optimize the parameters of LSTM model. In this paper, MAPE is used as the loss function of whale algorithm. When the loss value meets the requirements, the optimized parameter value is obtained. The definition formula of fitness function Training Loss is as follows:

$$\text{Training Loss} = \text{MAPE}(h, y) = \frac{1}{n}\sum_{i=1}^{n}\left|\frac{h(i) - y(i)}{y(i)}\right|. \quad (15)$$

$h(i)$ is the ith predicted value in the predicted results, $y(i)$ is the ith true value in the data samples, and n is the number of predicted samples. The more accurate the forecast value is, the smaller the loss value will be.

The detailed process is as follows:

(1) Initialization of LSTM model parameters

(2) Whale algorithm population initialization. A set of values composed of these three variables $(n, \varepsilon, \text{iter})$ are input into the whale algorithm as parameters to be optimized. The three parameters represent the number of hidden layer nodes, learning rate, and iteration times, respectively

(3) Take the initialized value as the historical optimal value to assign and train the parameters of LSTM

(4) Set the Training Loss obtained from the traditional LSTM training as the system requirement, and calculate the model loss value optimized by the whale algorithm

(5) If the loss value of the model optimized by whale algorithm is less than Training Loss, the requirements are met, and the final prediction model and parameter values are output

(6) If the loss value cannot be less than Training Loss or the number of iterations does not reach the maximum, update the parameters and retrain. Otherwise, stop training

2.3. Ensemble Empirical Mode Decomposition. When dealing with time series problems, EMD decomposition can stabilize the data. EMD can decompose the nonlinear and nonstationary signal into a series of IMF components, which are the local characteristic signals of different scales of the original signal.

Mode aliasing may occur in EEM mode decomposition. EEMD will add Gaussian white noise before decomposition and then EMD decomposition. In order to minimize the influence of white noise on the original sequence, repeat the experiment for many times, and finally, calculate the mean value of multiple groups of results. The decomposition steps of EEMD are as follows:

(1) Set the number of decomposition m

(2) The Gaussian white noise is added to the original sequence $x(T)$. The standard deviation of the added white noise is usually 0.2 times of the standard deviation of the original sequence, and the mean value is 0. The sequence formula after adding white noise is obtained as follows:

$$x'(t) = x(t) + \varepsilon^n(t). \tag{16}$$

In the formula $\varepsilon^n(t)(n = 1, 2, \cdots, m)$ is random Gaussian white noise, and m is the length of the original sequence

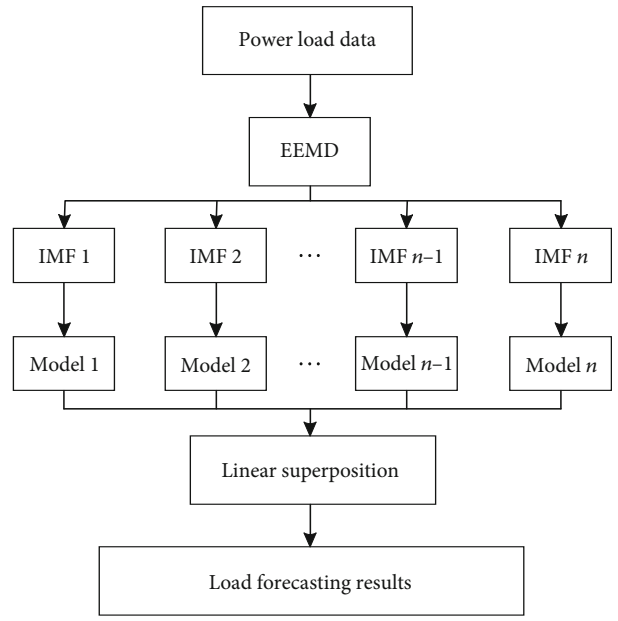

Figure 3: EEMD-WOA-LSTM model framework.

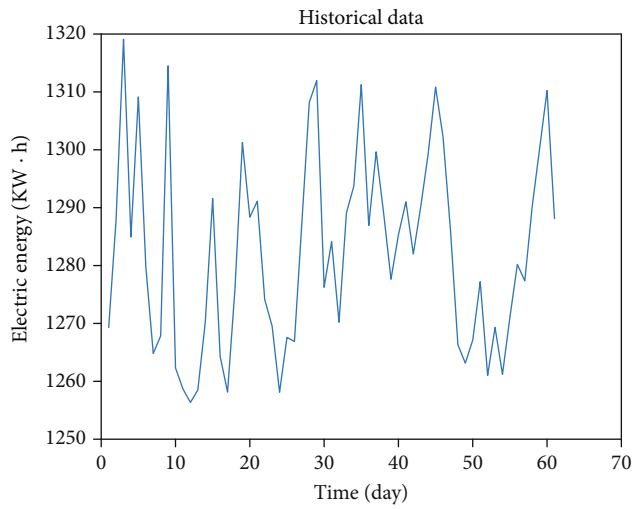

Figure 4: Raw data.

(3) After the previous step, we obtained all the $IMF_i^n(t)$ $(n = 1, 2, \cdots, m)$; i is the order of IMF

(4) Repeat steps 2 and 3 m times to get all IMF

(5) The noise interference can be eliminated by averaging the m times of IMF. The formula is as follows:

$$\overline{\text{IMF}}_i = \frac{1}{m}\sum_{n=1}^{m} \text{IMF}_i \tag{17}$$

Unlike EMD, EEMD results are not necessarily the same. It varies with the magnitude of white noise, so the EEMD decomposition cannot obtain a unique solution. Even if the same parameters are selected, the calculated results are still different due to the randomness of the noise. However, as

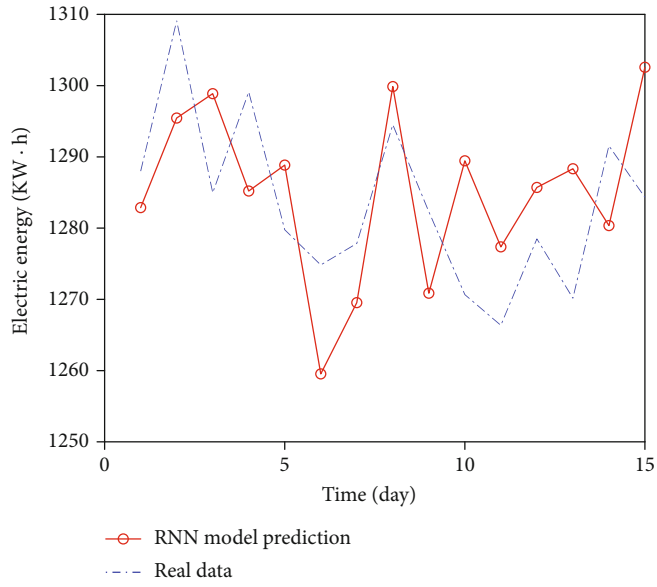

Figure 5: Comparison of RNN prediction results.

the number of tests increases, the influence can be offset when calculating the mean value. As long as the number of tests is enough, the results will tend to be consistent. In addition to the influence of the magnitude of Gaussian white noise on the decomposition results, the percentage also has a great influence on the results. If the percentage is too small, the effect is small or not. If the percentage is too large, it will cause interference and large error. At present, the more effective method to reduce interference is to have enough average times. Generally, when the average times is hundreds of times, the effect is good.

3. Main Result

3.1. EEMD-WOA-LSTM Combined Model. Figure 3 shows the framework of the model proposed in this paper. The EEMD-WOA-LSTM method proposed in this paper includes three stages: data decomposition, component prediction, and prediction result reconstruction.

EEMD-WOA-LSTM model makes full use of EEMD's ability to avoid component mode aliasing and WOA-LSTM's long-term memory of data. The three stages are as follows:

(1) EEMD performs data decomposition. Output multiple modal components with different characteristics

(2) Each IMF subsequence is predicted separately. For each component, an LSTM network is established to study its internal dynamic change law. Use WOA algorithm to update the LSTM network

(3) Normalize the prediction results of each IMF subsequence and superimpose the prediction values of each component

3.2. Prediction and Evaluation Index. In this paper, several commonly used error evaluation indexes in power load forecasting are adopted: mean absolute error (MAE), root mean square error (RMSE), and mean absolute percent error (MAPE).

(1) Mean absolute error (MAE):

$$\mathrm{MAE}(h, y) = \frac{1}{n}\sum_{i=1}^{n}|h(i) - y(i)| \tag{18}$$

(2) Root mean square error (RMSE):

$$\mathrm{RMSE}(h, y) = \sqrt{\frac{1}{n}\sum_{i=1}^{n}(h(i) - y(i))^2} \tag{19}$$

(3) Mean absolute percentage error (MAPE):

$$MAPE(h, y) = \frac{1}{n}\sum_{i=1}^{n}\left|\frac{h(i) - y(i)}{y(i)}\right| \tag{20}$$

In the formula, $h(i)$ is the ith predicted value in the prediction result, $y(i)$ is the ith true value in the data sample, and n is the number of prediction samples.

3.3. LSTM Prediction Accuracy Analysis. Select the load data of one equipment in the factory from April 1, 2018, to May 30, 2018, one sampling point at the same time every day, a total of 60 load data, as shown in Figure 4.

During this period, the production plan of this equipment is almost the same. The plant has constant temperature

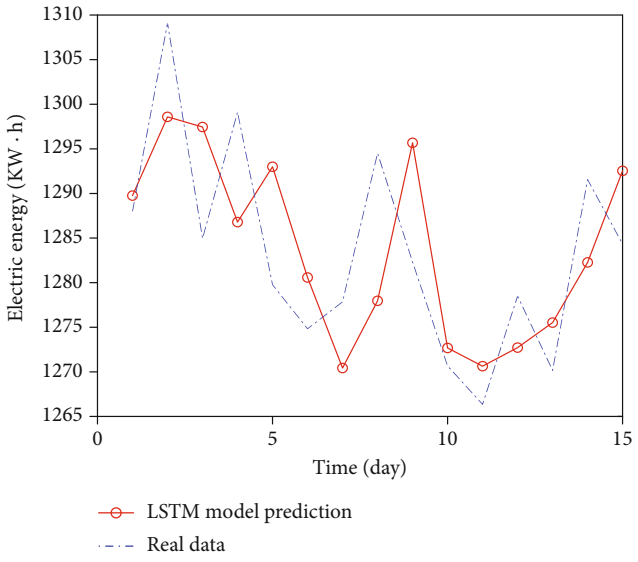

Figure 6: Comparison of LSTM prediction results.

Table 1: Calculation results of evaluation indicators of two algorithms.

Algorithm type	MAE	RMSE	MAPE
RNN	12.048	12.806	0.939
LSTM	8.556	9.576	0.665

and humidity throughout the year, so the power consumption is not affected by the external environment, and the data fluctuation is small. Take the raw data of the next 15 days as the test set. Through the simulation of RNN and LSTM prediction models, it is verified that LSTM has better prediction effect than RNN model. The number of hidden layer nodes of neural network is set as 18, the learning rate is 0.002, and the number of iterations is 200.

The 15-day power load forecasting results of RNN and LSTM models are shown in Figures 5 and 6, respectively.

Calculate the regression evaluation index according to equations (18)-(20), and get the MAE, RMSE, and MAPE of the two algorithms, as shown in Table 1.

As a whole, the prediction result of LSTM model is closer to the real curve, while the prediction result of RNN model deviates greatly. And the three evaluation indexes of LSTM model in Table 1 are smaller than those of RNN model.

At present, the method to determine the number of nodes in the hidden layer depends on experiments. Generally, some representative nodes are selected for simulation, and the interval of the optimal solution is determined through the simulation results, and the experiment is continued. Select the optimal number of hidden layer nodes as the final result. Fix other parameters unchanged, select some representative hidden layer nodes, and get the prediction result curve as shown in Figure 7. The error values of each prediction result are shown in Table 2.

The results in Table 2 show that the prediction results vary with the number of hidden layer nodes. When the

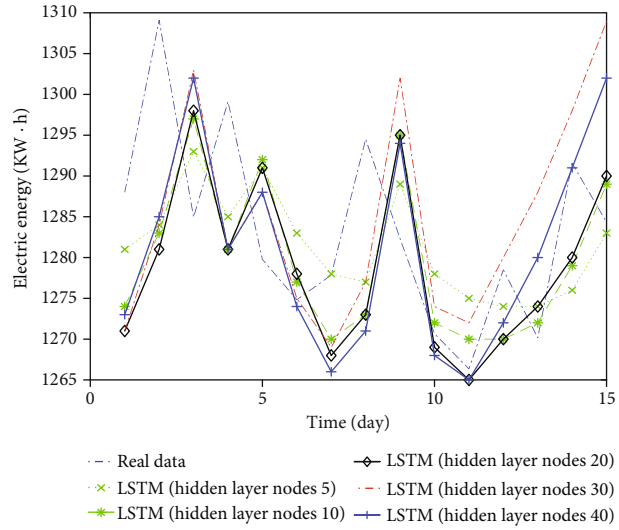

Figure 7: Prediction results of nodes in different hidden layers.

Table 2: Prediction error of nodes in different hidden layers.

Hidden layer nodes	MAE	RMSE	MAPE
5	9.280	11.238	0.720
10	9.117	11.107	0.703
20	11.155	13.395	0.865
30	12.809	15.116	0.995
40	11.265	13.623	0.874

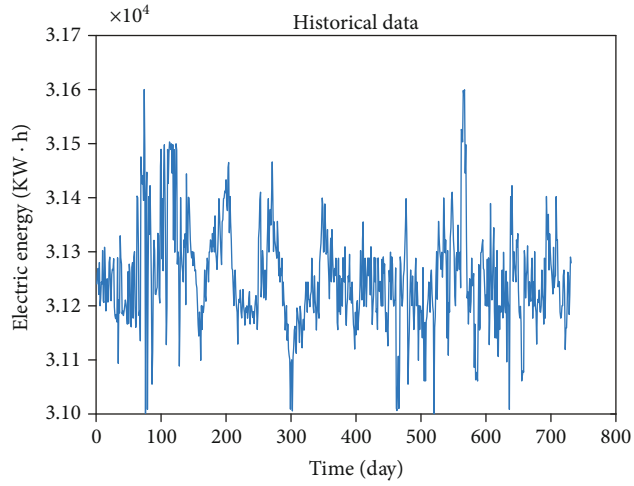

Figure 8: Raw data curve.

number of hidden layer nodes is less than 10, the three indicators are larger and the prediction accuracy is lower. When it is 10, the prediction accuracy increases significantly, and when the number of hidden layer nodes is more than 20, the accuracy decreases.

The advantages of the LSTM algorithm are as follows:

(1) LSTM has better fitting effect in processing complex data

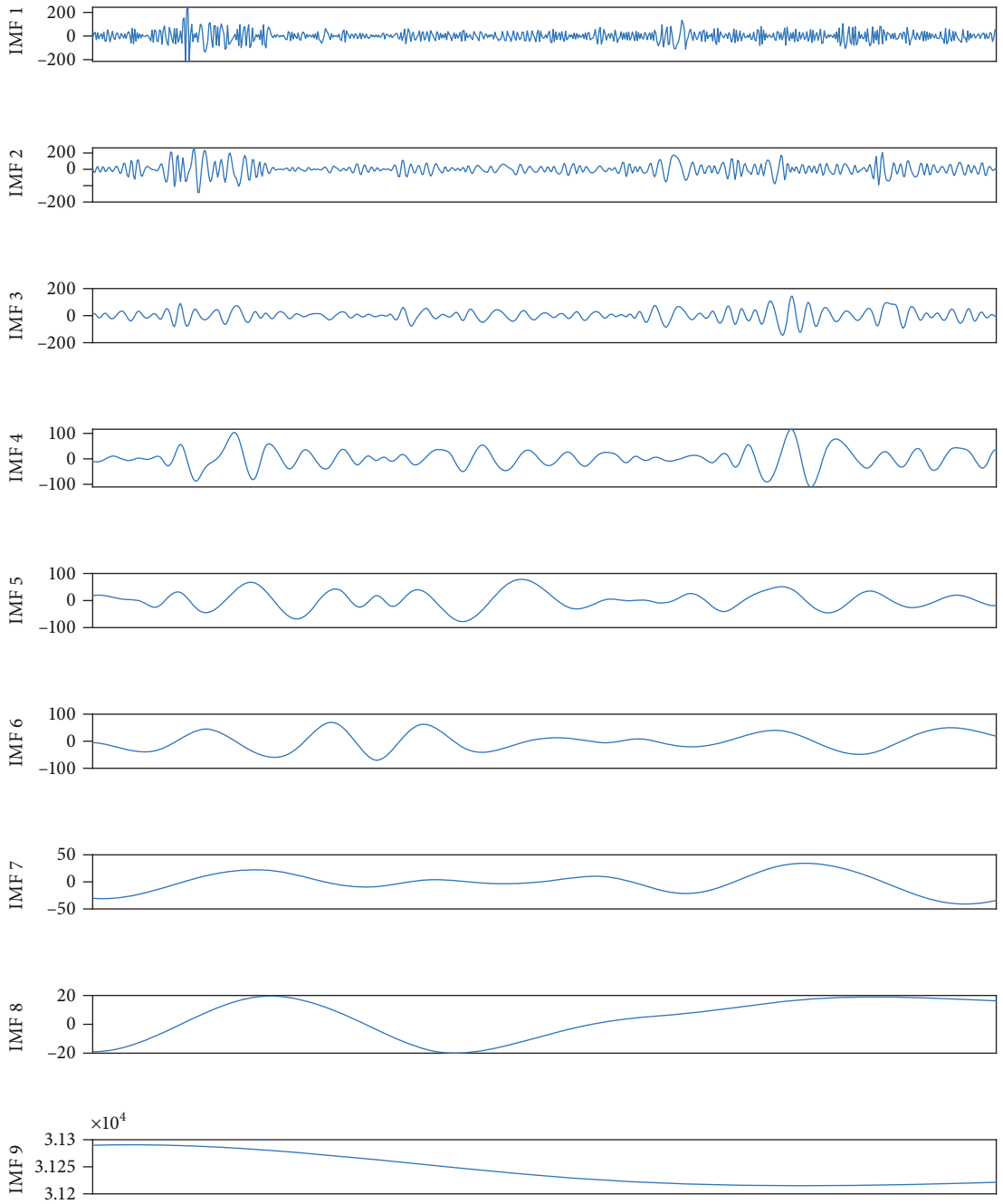

Figure 9: EMD decomposition data curve.

(2) LSTM solves the problem of dependence on memory or forgetting for such information that is far away from each other

(3) In the prediction comparison of the above two models, it is found that the MAE, RMSE, and MAPE of RNN are 12.048, 12.806, and 0.939, respectively, and the MAE, RMSE, and MAPE of LSTM neural network are 8.556, 9.576, and 0.665, respectively, which improves the accuracy by 29.0%, 25.2%, and 29.2%, respectively. Compared with various error evaluation indicators, LSTM model has better prediction results and can be used as a good model in the field of power load forecasting

3.4. Combined Forecast Model Data. In this paper, the real load data of a factory from January 1, 2019, to December 31, 2020, is taken as the original data. The sampling interval is 24 hours, that is, one sampling point per day. The original data curve is shown in Figure 8. Through the training of the data, predict the power consumption data in the next 30 days. In this paper, RNN model, LSTM model, EEMD-

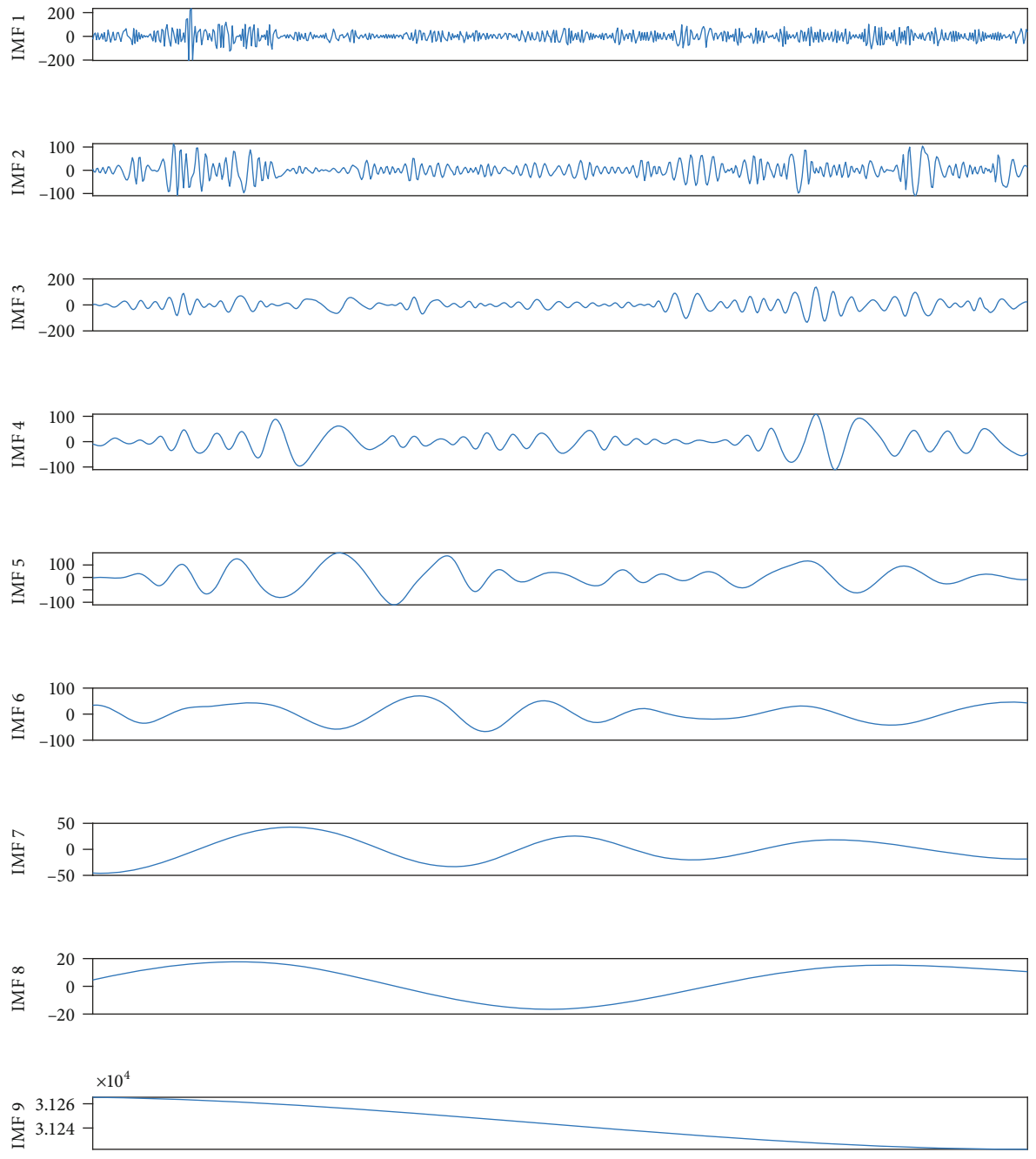

Figure 10: EEMD decomposition data curve.

ARMA model, WOA-LSTM model, and EEMD-WOA-LSTM model are used for prediction and data analysis.

3.5. Decomposition of Original Load Series. EMD and EEMD were used to decompose the time series of the plant. The comparison of EMD and EEMD decomposition data is shown in Figures 9 and 10.

IMF9 in Figure 9 and IMF9 in Figure 10 are respective trend items. In Figure 9, mode aliasing occurs. It can be seen from Figure 10 that EEMD overcomes the problem of modal aliasing and can decompose the power load signal into different frequencies with distinct characteristics. In order to achieve better prediction accuracy. We use EEMD for data decomposition. The decomposed feature components are input into the prediction model for learning.

3.6. Analysis of Experimental Results. In this paper, the rolling prediction method is used for model training, and RNN and LSTM prediction models are established for analysis. The number of hidden layer nodes of neural network is set as 80, the learning rate is 0.01, and the number of iterations is 500.

The prediction results of RNN model are shown in Figure 11. The results predicted by RNN are intuitively more

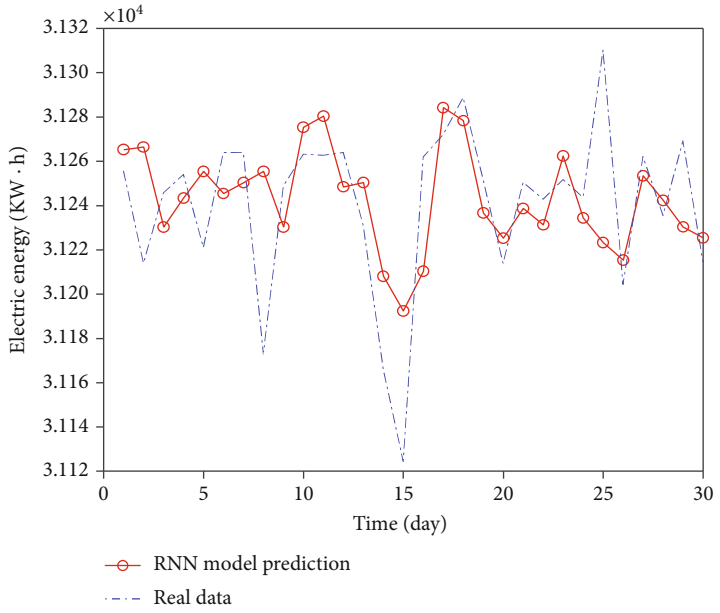

Figure 11: RNN data comparison chart.

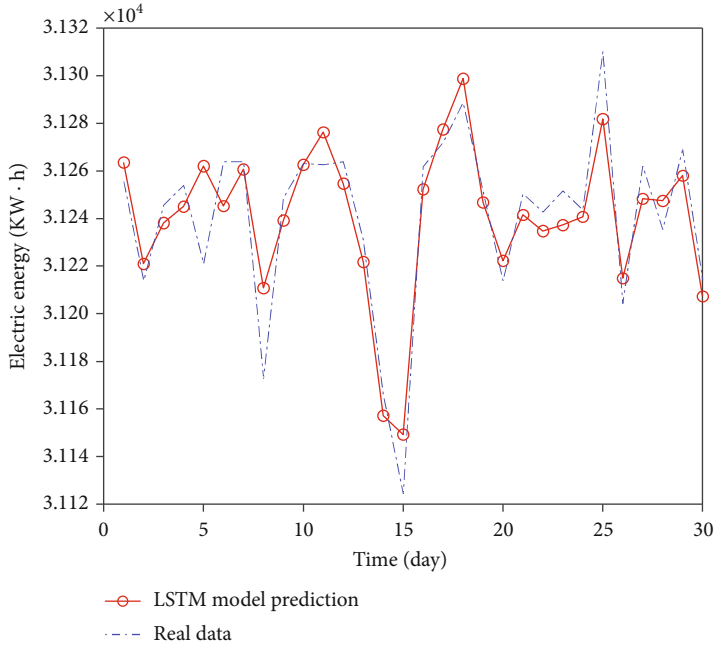

Figure 12: LSTM data comparison chart.

accurate than the traditional algorithm. However, for the extreme points, the RNN algorithm has poor fitting degree and the result deviation is large.

The LSTM model is used to predict the data. The prediction results are shown in Figure 12. From the visual point of view, the prediction results by LSTM neural network have improved the accuracy. The prediction for the data with small change range is relatively accurate. However, because the parameters are difficult to determine, the results have a certain offset for the data near the extreme points, and the overall prediction accuracy is not too high.

The number of components generated by EEMD decomposition depends on how many ARMA models need to be established, and each ARMA model is also different. In fact, the data samples decomposed by EEMD meet the requirements of ARMA modeling, that is to say, they are all stable sequences. Therefore, the process of stability determination is omitted. Generally, AIC and BIC are used to determine the order. However, when selecting the order, there is a large amount of calculation, so the well-known ergodic method is usually used. So fixed order modeling is a good method, and this paper adopts this method. The first step in the EEMD-

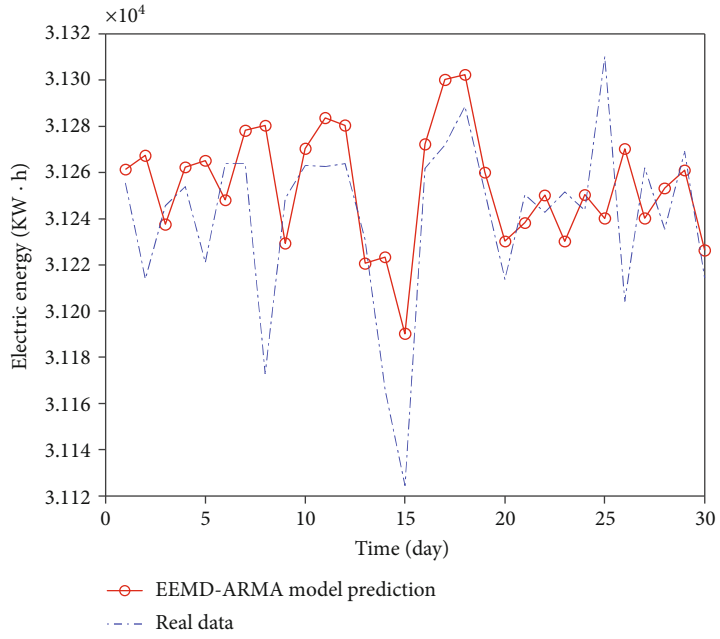

Figure 13: EEMD-ARMA data comparison chart.

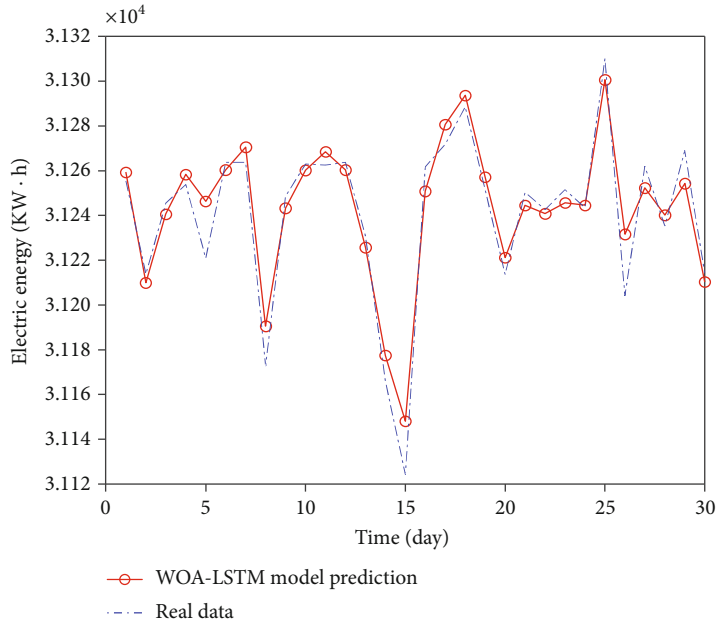

Figure 14: WOA-LSTM data comparison chart.

ARMA data prediction process is to use EEMD to decompose the data, then model each component separately for training, and finally superimpose the prediction results. The prediction curve is shown in Figure 13.

The WOA-LSTM model was used for analysis. Due to the large amount of data, the initial population size of whale algorithm is 50, the initial iteration times is 500, and the initialization parameters $(n, \varepsilon, \text{iter})$ are [10,100], [0.001,0.01], and [400,1000]. Through the optimization of LSTM neural network by WOA, the obtained combined model can better optimize the parameters of LSTM. It can better predict and fit the whole or at the peak, trough, and inflection point of extreme points than the previous algorithms, and the prediction accuracy is significantly improved. The prediction results are shown in Figure 14.

Finally, the EEMD-WOA-LSTM model is used to analyze and predict the load data. The prediction results are shown in Figure 15. Compared with WOA-LSTM model, this model has more accurate prediction results, higher fitting degree with real data, and higher prediction accuracy.

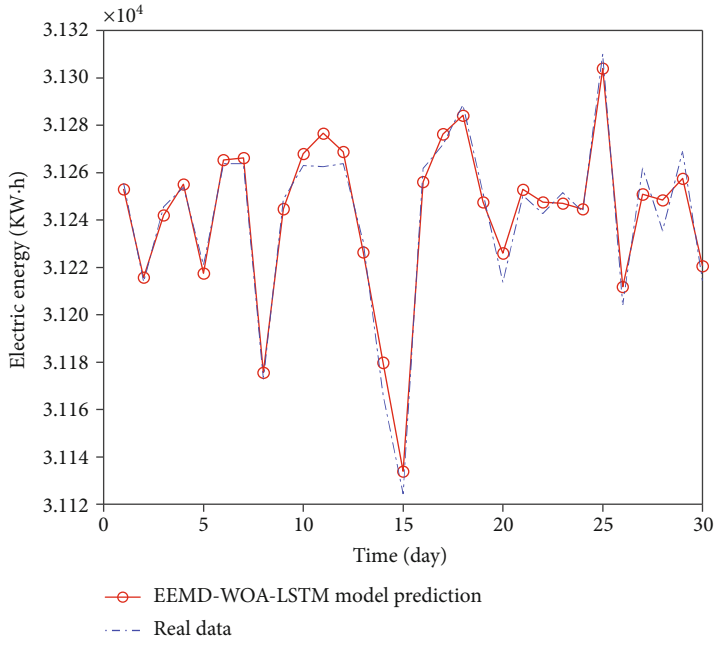

Figure 15: EEMD-WOA-LSTM data comparison chart.

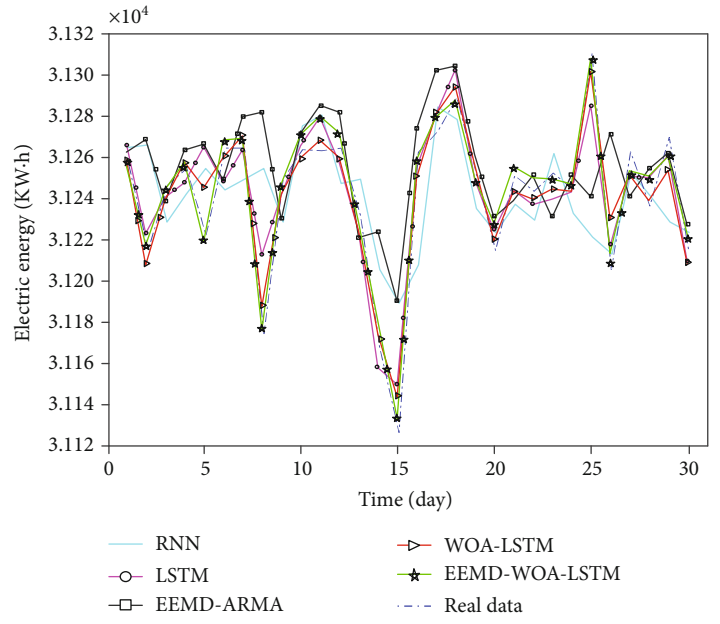

Figure 16: Comparison of prediction data of five models.

4. Results

The comparison of prediction results of the five models is shown in Figure 16. Calculate the regression evaluation indexes according to formula (18)-(20), and get three error evaluation indexes of the five models, as shown in Table 3. The prediction results of each model are shown in Table 4.

For RNN model, LSTM model, and WOA-LSTM model, the coincidence degree between the predicted value and the real value curve of the obtained results from high to low is WOA-LSTM model, LSTM model, and RNN model. WOA-LSTM model is the closest training model to real data

Table 3: Calculation results of regression evaluation indexes of prediction model.

Algorithm type	MAE	RMSE	MAPE
EEMD-ARMA	25.884	35.723	0.083
RNN	24.581	33.011	0.079
LSTM	12.113	15.254	0.039
WOA-LSTM	8.376	10.773	0.027
EEMD-WOA-LSTM	5.812	6.989	0.019

Table 4: Prediction results of each model.

Sample point	Real data	EEMD-ARMA	RNN	LSTM	WOA-LSTM	EEMD-WOA-LSTM
1	31255.53	31261.36	31265.21	31263.57	31259.36	31253.06
2	31213.88	31267.36	31266.36	31220.99	31210.03	31215.70
3	31245.61	31237.54	31230.25	31238.15	31240.52	31242.01
4	31253.90	31262.31	31243.36	31245.07	31258.33	31255.05
5	31220.98	31265.14	31255.51	31262.04	31246.29	31217.46
6	31263.84	31248.10	31245.36	31245.27	31260.36	31265.36
7	31263.86	31278.23	31250.31	31260.73	31270.58	31266.14
8	31172.79	31280.32	31255.36	31210.84	31190.64	31175.63
9	31248.67	31229.36	31230.31	31239.17	31243.35	31244.65
10	31263.06	31270.56	31275.31	31262.67	31260.25	31267.99
11	31262.59	31283.65	31280.36	31276.22	31268.47	31276.58
12	31263.84	31280.16	31248.36	31254.66	31260.36	31268.73
13	31230.94	31220.66	31250.32	31221.76	31225.74	31226.41
14	31166.04	31223.36	31208.04	31157.22	31177.51	31179.76
15	31124.32	31190.21	31192.34	31149.26	31148.15	31133.88
16	31261.80	31272.38	31210.24	31252.24	31250.85	31256.07
17	31271.93	31300.21	31284.14	31277.48	31280.69	31276.20
18	31288.68	31302.32	31278.34	31298.77	31293.64	31284.17
19	31251.52	31260.12	31236.65	31246.78	31257.12	31247.55
20	31213.71	31230.37	31225.21	31222.19	31221.25	31225.95
21	31250.40	31238.21	31238.64	31241.57	31244.55	31252.89
22	31242.72	31250.14	31231.21	31234.73	31240.89	31247.52
23	31251.60	31230.21	31262.35	31237.27	31245.64	31246.98
24	31243.60	31250.39	31234.36	31240.71	31244.62	31244.58
25	31310.12	31240.14	31223.42	31281.82	31300.66	31303.91
26	31204.21	31270.25	31215.32	31214.91	31231.64	31211.85
27	31262.06	31240.18	31253.36	31248.29	31252.36	31250.82
28	31235.40	31253.21	31242.31	31247.48	31240.25	31248.36
29	31269.14	31260.99	31230.32	31258.01	31254.36	31257.52
30	31214.37	31226.34	31225.36	31207.32	31210.31	31220.65

samples among the three, which shows that LSTM neural network optimized by whale optimization algorithm has good training effect for large and small-scale data training samples.

For all models, in the part where the real curve fluctuates little, the fitting degree of several algorithms is good, but at the extreme point, the fitting degree of EEMD-ARMA and LSTM models is poor. Although the original LSTM model is better than EEMD-ARMA model on the whole, there is a certain gap between the extreme point and the real value. The optimized WOA-LSTM model can fit the real curve well both in the whole and at the extreme points. EEMD-WOA-LSTM model has better prediction effect, and the fitting degree with the original data is the highest among these models. Compared with the WOA-LSTM model, the MAE of EEMD-WOA-LSTM model decreased by 30.6%, RMSE decreased by 35.1%, and MAPE decreased by 29.6%.

5. Discussion

This paper combines bionic algorithm and artificial intelligence algorithm and proposes an EEMD-WOA-LSTM combined model. EEMD is used to decompose the original load series into multiple characteristic components. The neural network is optimized by the whale algorithm and used to predict each component. The components obtained from the prediction are superimposed to form the final prediction result. The method is applied to the power load forecasting of a factory. The simulation results show that, compared with other methods listed in the paper, the EEMD-WOA-LSTM model has the lowest prediction error of 0.019 (MAPE) and high prediction accuracy. It is an ideal short-term load forecasting model. The artificial intelligence algorithm can be well applied to load forecasting to achieve efficient and accurate short-term load forecasting.

Data Availability

The load forecasting data used to support the results of this study has not been provided because it is private data of enterprises.

Conflicts of Interest

The authors declare that there is no conflict of interest regarding the publication of this paper.

Authors' Contributions

Lei Shao conceptualized the study. Chao Li performed data curation. Ji Li carried out formal analysis. Quanjie Guo and Huilong Yan investigated the study. Lei Shao was responsible for methodology. Chao Li supervised the study. Quanjie Guo validated the study. Quanjie Guo wrote the original draft. Quanjie Guo and Ji Li wrote, reviewed, and edited the manuscript.

References

[1] R. Zivanovic, "Local regression-based short-term load forecasting," *Journal Intell. Robot. Syst.,*, vol. 31, no. 1-3, pp. 115–127, 2001.

[2] R. C. Tsaur, "Forecasting by fuzzy double exponential smoothing model," *International Journal of Computer Mathematics*, vol. 80, no. 11, pp. 1351–1361, 2003.

[3] E. Paparoditis and T. Sapatinas, "Short-term load forecasting: the similar shape functional time-series predictor," *IEEE Transactions on Power Systems*, vol. 28, no. 4, pp. 3818–3825, 2013.

[4] M. Jin, X. Zhou, Z. M. Zhang, and M. M. Tentzeris, "Short-term power load forecasting using grey correlation contest modeling," *Expert Systems with Applications*, vol. 39, no. 1, pp. 773–779, 2012.

[5] H. H. Cevik and M. Cunkas, "Short-term load forecasting using fuzzy logic and ANFIS," *Neural Computing and Applications*, vol. 26, no. 6, pp. 1355–1367, 2015.

[6] M. Beccali, M. Cellura, V. Lo Brano, and A. Marvuglia, "Short-term prediction of household electricity consumption: assessing weather sensitivity in a Mediterranean area," *Renewable and Sustainable Energy Reviews*, vol. 12, no. 8, pp. 2040–2065, 2008.

[7] F. J. Marin, F. Garcia-Lagos, G. Joya, and F. Sandoval, "Global model for short-term load forecasting using artificial neural networks," *IEE Proc.-Gener. Transm. Distrib*, vol. 149, no. 2, pp. 121–125, 2002.

[8] H. Y. Yamin, S. M. Shahidehpour, and Z. Li, "Adaptive short-term electricity price forecasting using artificial neural networks in the restructured power markets," *International Journal of Electrical Power & Energy Systems*, vol. 26, no. 8, pp. 571–581, 2004.

[9] K. Kalaitzakis, G. S. Stavrakakis, and E. M. Anagnostakis, "Short-term load forecasting based on artificial neural networks parallel implementation," *Electric Power Systems Research*, vol. 63, no. 3, pp. 185–196.

[10] S. C. Bhattacharyya and L. T. Thanh, "Short-term electric load forecasting using an artificial neural network: case of northern Vietnam," *International Journal of Energy Research*, vol. 28, no. 5, pp. 463–472, 2004.

[11] L. Hernandez, "Artificial neural network for short-term load forecasting in distribution systems," *Energies*, vol. 7, no. 3, pp. 1576–1598, 2014.

[12] Q. Cai, B. Yan, B. Su et al., "Short-term load forecasting method based on deep neural network with sample weights," *International Transactions on Electrical Energy Systems*, vol. 30, no. 5, 2020.

[13] S. Mishra and S. K. Patra, "Short term load forecasting using a novel recurrent neural network," in *in TENCON 2008-2008 IEEE Region 10 Conference*, pp. 1–6, Hyderabad, India, 2008.

[14] A. Sherstinsky, "Fundamentals of recurrent neural network (RNN) and long short-term memory (LSTM) network," *Physica D: Nonlinear Phenomena*, vol. 404, p. 132306, 2020.

[15] S. Hochreiter, "The vanishing gradient problem during learning recurrent neural nets and problem solutions," *International Journal of Uncertainty, Fuzziness and Knowledge-Based Systems*, vol. 6, no. 2, pp. 107–116, 1998.

[16] F. Karim, S. Majumdar, H. Darabi, and S. Chen, "LSTM fully convolutional networks for time series classification," *IEEE Access*, vol. 6, pp. 1662–1669, 2018.

[17] K. Greff, R. K. Srivastava, J. Koutnik, B. R. Steunebrink, and J. Schmidhuber, "LSTM: a search space odyssey," *IEEE Transactions on Neural Networks and Learning Systems*, vol. 28, no. 10, pp. 2222–2232, 2017.

[18] A. Graves and J. Schmidhuber, "Framewise phoneme classification with bidirectional LSTM and other neural network architectures," *Neural Networks*, vol. 18, no. 5-6, pp. 602–610, 2005.

[19] Z. Zhao, W. H. Chen, X. M. Wu, P. C. Y. Chen, and J. M. Liu, "LSTM network: a deep learning approach for short-term traffic forecast," *IET Intelligent Transport Systems*, vol. 11, no. 2, pp. 68–75, 2017.

[20] L. L. Gao, Z. Guo, H. W. Zhang, X. Xu, and H. T. Shen, "Video captioning with attention-based LSTM and semantic consistency," *Multimedia*, vol. 19, no. 9, pp. 2045–2055, 2017.

[21] A. Ullah, J. Ahmad, K. Muhammad, M. Sajjad, and S. W. Baik, "Action recognition in video sequences using deep bi-directional LSTM with CNN features," *IEEE Access*, vol. 6, pp. 1155–1166, 2018.

[22] A. S. Santra and J.-L. Lin, "Integrating long short-term memory and genetic algorithm for short-term load forecasting," *Energies*, vol. 12, no. 11, p. 2040, 2019.

[23] Y. Hong, Y. J. Zhou, Q. B. Li, W. Z. Xu, and X. J. Zheng, "A deep learning method for short-term residential load forecasting in smart grid," *IEEE Access*, vol. 8, pp. 55785–55797, 2020.

[24] A. Moradzadeh, S. Zakeri, M. Shoaran, B. Mohammadi-Ivatloo, and F. Mohammadi, "Short-term load forecasting of microgrid via hybrid support vector regression and long short-term memory algorithms," *Sustainability*, vol. 12, no. 17, p. 7076, 2020.

[25] F. F. He, J. Z. Zhou, Z. K. Feng, G. B. Liu, and Y. Q. Yang, "A hybrid short-term load forecasting model based on variational mode decomposition and long short-term memory networks considering relevant factors with Bayesian optimization algorithm," *Applied Energy*, vol. 237, pp. 103–116, 2019.

[26] Z. R. Meng, Y. Q. Xie, and J. H. Sun, "Short-term load forecasting using neural attention model based on EMD," *Electrical Engineering*, vol. 104, no. 3, pp. 1857–1866, 2022.

[27] S. Mirjalili and A. Lewis, "The whale optimization algorithm," *Advances in Engineering Software*, vol. 95, pp. 51–67, 2016.

Hindawi
Applied Bionics and Biomechanics
Volume 2022, Article ID 2233417, 13 pages
https://doi.org/10.1155/2022/2233417

Research Article

A Magnetically Capsule Robot for Biomedical Application

Qiang Fu,[1,2] **Xi Zhang**,[2] **Songyuan Zhang**,[3] **Chunliu Fan**,[2] **Zhuocong Cai**,[2] **and Lili Wang**[4]

[1]*Tianjin Key Laboratory for Control Theory & Application in Complicated Systems, Tianjin, China*
[2]*School of Electrical Engineering and Automation, Tianjin University of Technology, Tianjin, China*
[3]*State Key Laboratory of Robotics and System, Harbin Institute of Technology, Harbin, China*
[4]*Tianjin Hospital of ITCWM Nankai Hospital, Tianjin, China*

Correspondence should be addressed to Songyuan Zhang; zhangsy@hit.edu.cn

Received 15 March 2022; Revised 10 June 2022; Accepted 25 June 2022; Published 21 July 2022

Academic Editor: Wen-Ming Chen

Magnetic-driven capsule robot has been widely studied due to its advantages of safety and reliability. However, when doctors carry out clinical examination, the capsule robot cannot achieve the ideal control effect due to the influence of the external magnetic field air gap. This paper is based on the kinetic energy theorem, combined with the principle of spiral mechanism in mechanical design foundation to construct a calculation method of energy utilization and to improve the control effect of capsule robot, suitable for the human gastrointestinal tract precise control of capsule robot to perform a variety of complex tasks. By calculating the energy utilization rate of the capsule robot under the control of external magnetic field, the method can improve the energy utilization rate by improving the equation parameters, so that the capsule robot can run according to the doctor's ideal performance in practical application. Based on the analysis of the magnetic driven screw capsule robot, the model of the utilization rate of the external magnetic field of the capsule robot is established, and the fluid simulation of the capsule robot is carried out by using the method of computational fluid dynamics. The simulation results and experimental results show that the control effect of capsule robot can be improved by calculating the energy utilization rate of the robot, which is of great significance to human clinical examination and treatment.

1. Introduction

Gastroscopy is an essential method for the diagnosis of internal gastrointestinal diseases. The traditional gastrointestinal endoscopy needs a manual operation, which can easily cause gastrointestinal tissue damage. It may even lead to infection or gastrointestinal bleeding, causing many people to give up the diagnosis and treatment of the gastrointestinal tract by traditional endoscopy [1–3]. The cure rate of gastrointestinal diseases is closely related to the time of discovery: the earlier the discovery, the more conducive to the treatment and recovery of the disease. Capsule robot has been widely studied because of their advantages, such as being safer, comfortable, and painless [4–6]. Compared with a traditional plug-in electronic endoscope, a capsule robot avoids the hidden dangers such as cross-infection and secondary trauma of traditional tubular endoscopes, reduces the pain in the inspection process, and widens the inspection field and detection breadth [7–9].

Capsule robot detection technology has developed rapidly; Israeli medical technologies pioneered the "M2A" capsule robot for gastrointestinal examinations [10–12]. Chongqing Jinshan Technology and Japan's Olympus have launched their capsule robots "OMOM" [13] and "Endo Capsule" [14]. However, these capsule robots can only rely on intestinal peristalsis to change the position in the body [15–17], and this passive motion mode cannot accurately detect the lesions, which is prone to missed diagnosis and misdiagnosis. Therefore, the capsule robot that can realize active movement has become the inevitable development trend of intestinal detection.

Fu et al. studied an external field-driven cable-free microrobot with bionic swimming characteristics. By changing the driving frequency of the time-varying oscillating

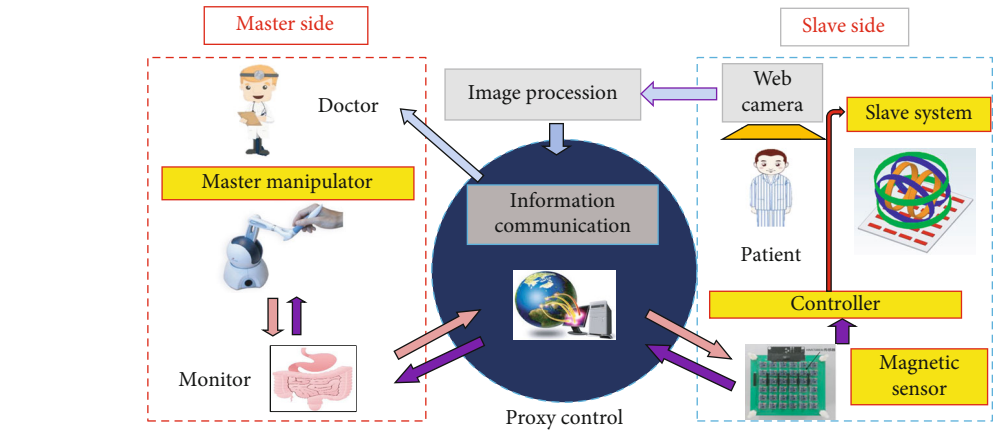

(a)

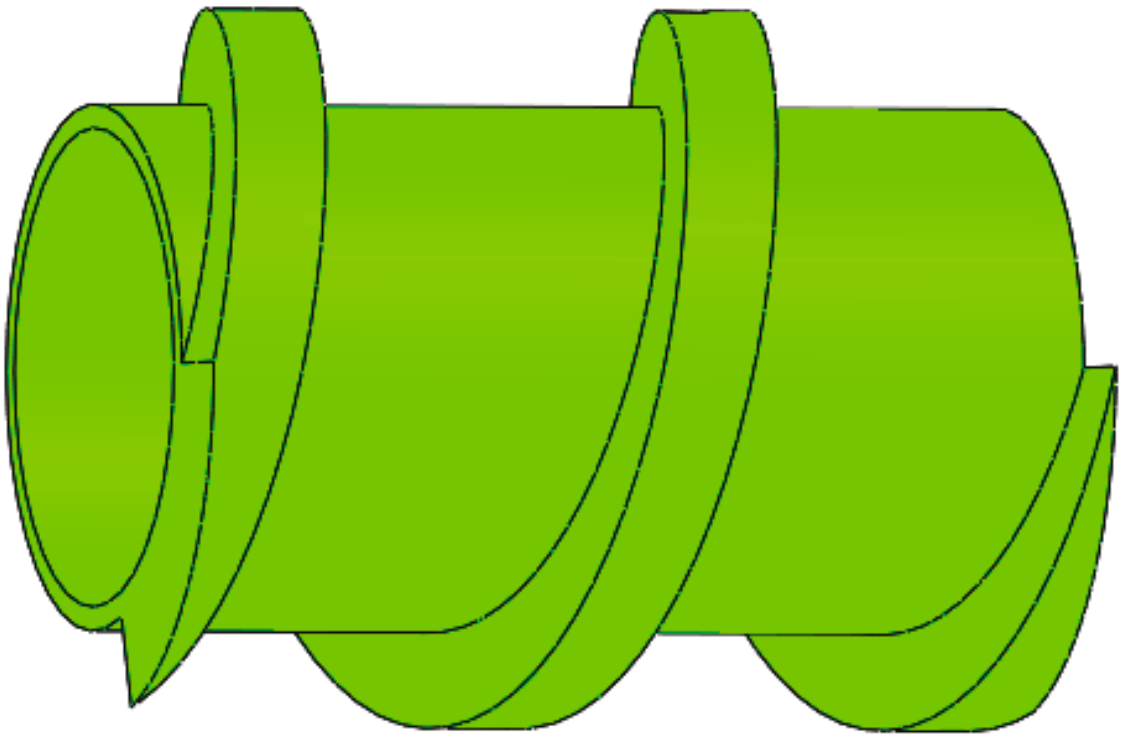

(b)

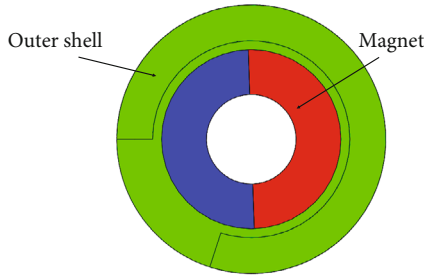

(c)

Figure 1: (a) Remote control of the system. (b) Overall structure of capsule robot. (c) Internal structure of capsule robot.

magnetic field, the film tail fin is driven to fluctuate to achieve more flexible movement in the intestines and stomach full of body fluids [18]. Fu et al. proposed a soft capsule robot for the continuous and stable control of the capsule robot in the body. Under the control of the external magnetic field, the motion is carried out in the rolling motion mode so that the motion is stable, continuous, and controlled in the gastrointestinal tract [19]. Fu et al. proposed a magnetically driven microrobot with a covered propeller structure, which improved the efficient propulsion performance of the capsule robot and reduced the harm to the stomach [20]. In addition, a new kind of rotating magnetic field hybrid microrobot is proposed, which combines the spiral structure with the biomimetic fin tail, so that the two motions can be controlled independently without interference, and the flexible motion with multiple degrees of freedom is realized [21]. However, the above literature does not consider whether the capsule robot can always maintain accurate and efficient control in a complex environment full of fluid.

To solve the above problems, this paper proposes a calculation method to improve the control of magnetic-driven spiral capsule robot, which is used in the visualization research of capsule robot control and improves the control effect of capsule robot. According to the kinetic energy theorem and the principle of spiral mechanism in mechanical design, the energy utilization equation is constructed to calculate the actual energy utilization percentage of the capsule robot. The results are used to reflect and analyse the motion control effect of capsule robot. This method can verify the control effect of capsule robot in actual medical process and adapt to complex gastrointestinal environment.

The structure of this paper is as follows: Firstly, the structure of the magnetically driven capsule robot is introduced. Then, the dynamic model of the robot is established, and the method of improving the robot's motion performance is analysed. Then, the feasibility of the method is verified by simulation and experiment. Finally, this paper summarizes and looks into the future.

2. System Configuration

Integrated console, display, three-axis Helmholtz coil, and $6 * 6$ magnetic sensor array constitute the remote-control system of the capsule robot (Figure 1(a)) [22]. The three-axis Helmholtz coil and sensor array actuate and locate the capsule robot. The integrated console and display are used for real-time image feedback of the capsule robot working in the human body.

2.1. Working Principle. When the patient swallowed the single module or multiple module capsule robot, the capsule robot arrived at the starting position through gastrointestinal peristalsis. At this point, the doctor can observe real-time images in the gastrointestinal tract on display and control the three-axis Helmholtz coil through the integrated console to generate an external rotating magnetic field to drive a single or multiple capsule robot forward or backwards in the patient [23–25]. The integrated console controls the three-axis Helmholtz coil to generate an external rotating magnetic field, driving the capsule robot forward or backwards.

Furthermore, use a $6 * 6$ magnetic sensor array as the positioning system, real-time positioning of the position and orientation of the capsule robot, to achieve accurate control of the capsule in the complex gastrointestinal environment, complete inspection, treatment, and other tasks.

Table 1: Capsule robot main parameters.

Symbol	Robot A	Robot B	Robot C
Length of capsule robot (mm)	20	20	20
Radius of capsule robot (mm)	5.5	5.5	5.5
Thread pitch (mm)	10	7	5
Thread height (mm)	2	2	2
Thread width (mm)	2	2	2
Material of body	Polythene	Polythene	Polythene
Weight of magnet (g)	5	5	5
Material of magnet (g)	1.5	1.5	1.5
Magnetization direction	Radial	Radial	Radial
Magnetization direction	NdFeB35	NdFeB35	NdFeB35

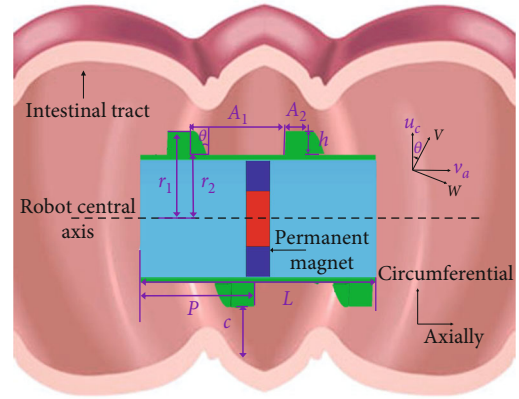

Figure 2: Capsule robot model.

2.2. Robot Structure. The capsule robot consists of modules with a polyethene shell and an O-ring magnet. When swallowing a multimodule capsule robot, based on the previous research on the motion characteristics of a multimodule capsule robot, the difference of starting and cut-off frequency of each module can be used to realize its separation or whole movement [26–28]. The parameters of capsule robots A, B, and C are used in this paper (Table 1). The overall structure of capsule robot A is shown in (Figure 1(b)), and its internal structure is shown in (Figure 1(c)). If the capsule robot rotates in the patient's body, it must obtain an axial positive magnetic moment generated by the three-axis Helmholtz coil. When the o-type permanent magnet inside the capsule robot rotates, the magnetic moment generated overcomes the resistance moment, resulting in a positive magnetic moment to start

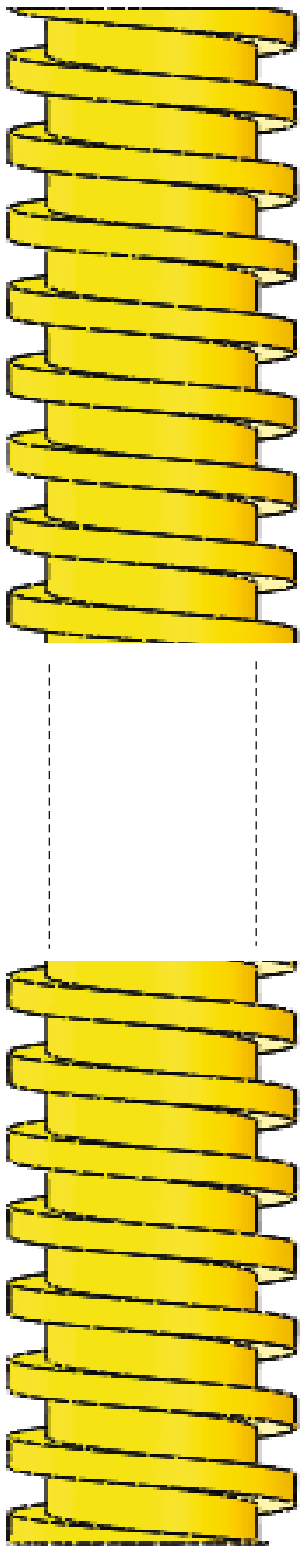

(a)

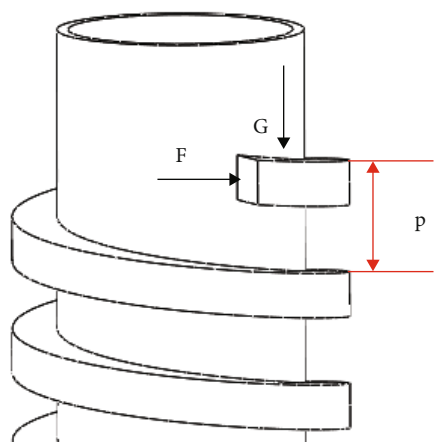

(b)

Figure 3: Continued.

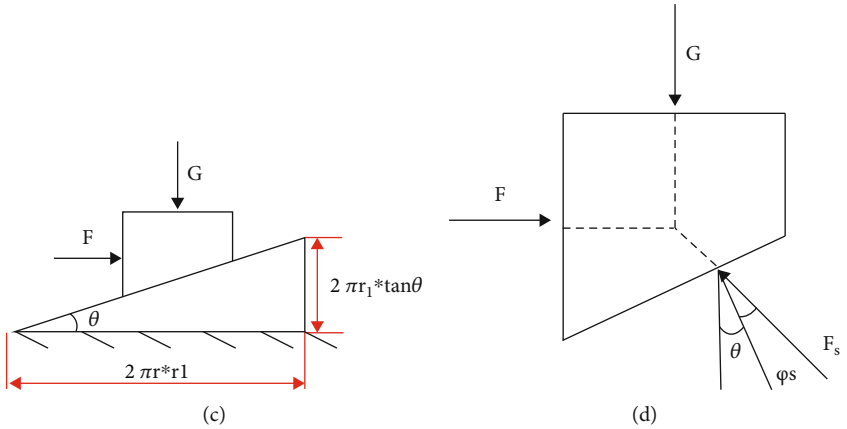

Figure 3: (a) Overall thread structure diagram. (b) Partial thread structure stress analysis diagram. (c, d) Thread section stress analysis diagram.

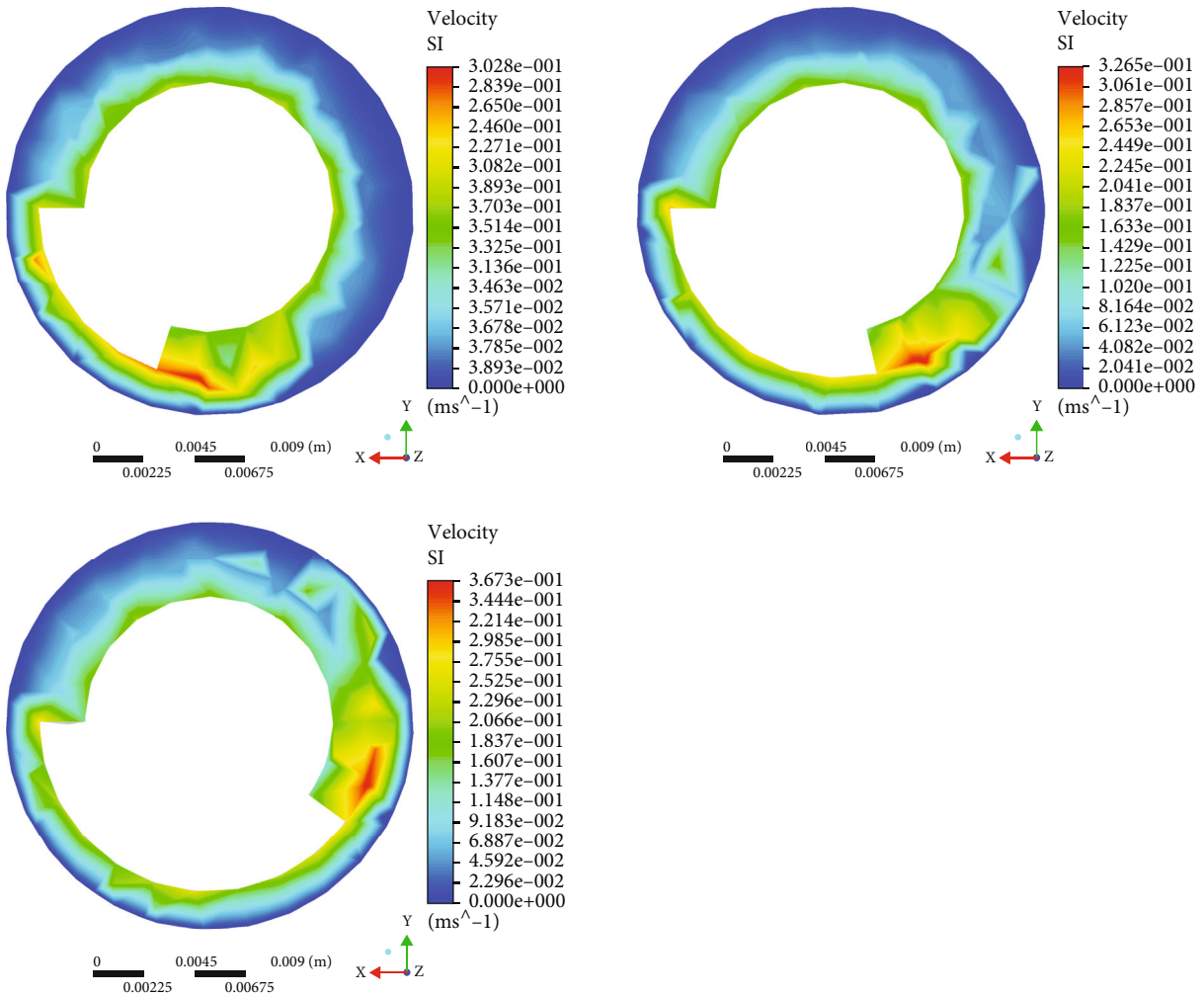

Figure 4: Simulation of inlet plane velocity profile of different capsule robots at the same rotational speed.

the robot. The motion state of capsule robot can be expressed by driving torque T in the following equation:

$$T = T_M - T_F, \tag{1}$$

where T_M is the magnetic moment generated by the capsule robot and T_F is the resistance moment generated.

When $T > 0$, it indicates that the capsule robot is in the state of start-up or acceleration. When $T = 0$, it means the capsule robot is in a static or uniform state. When $T < 0$, it

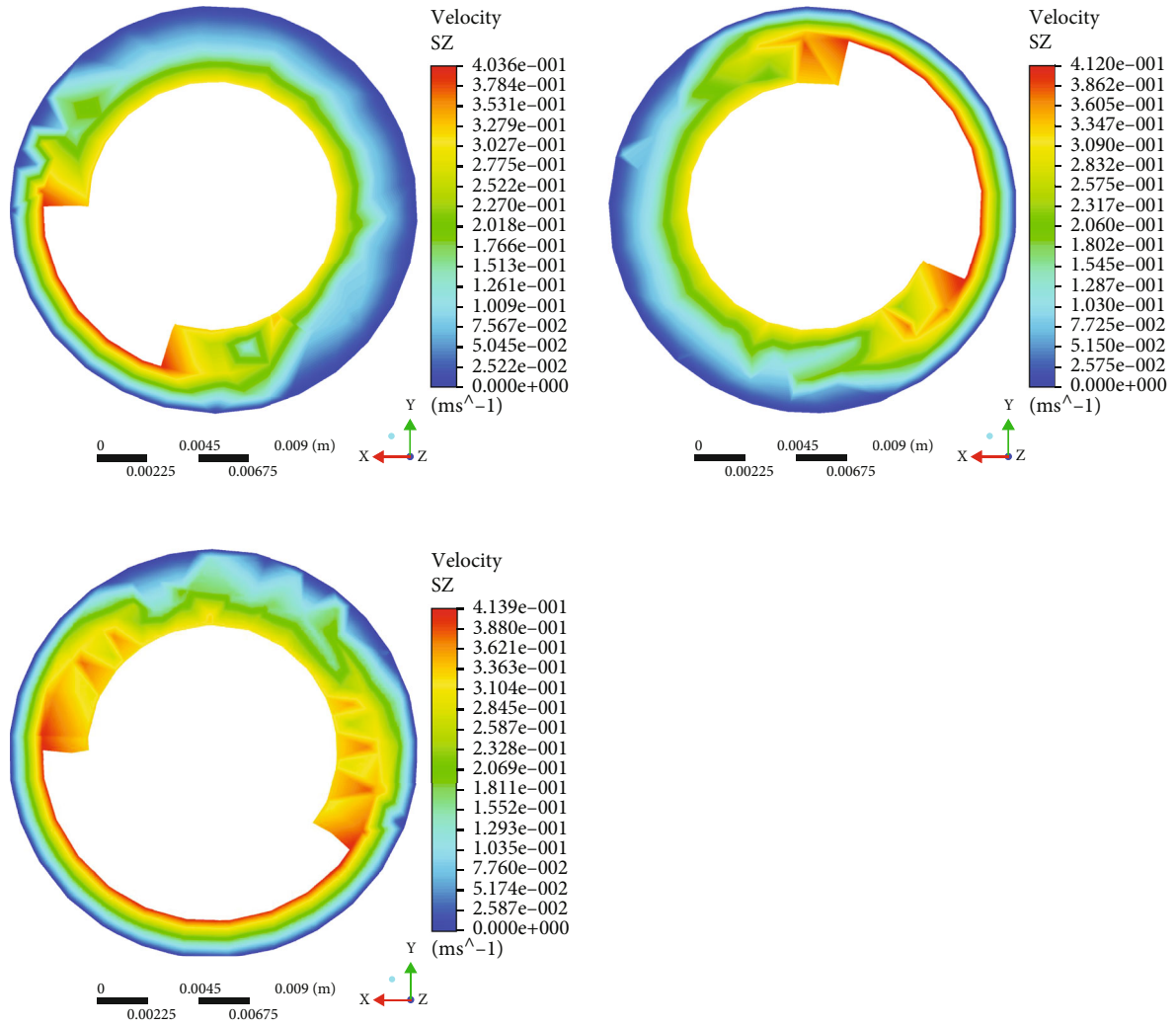

Figure 5: Simulation of intermediate plane velocity profile of capsule robot at the same rotational speed.

indicates that the capsule robot is in the deceleration or stop state [29].

3. Dynamic Model

3.1. The Analysis of the Force. The dynamics model of the capsule robot is established in the intestinal tract (Figure 2). Cartesian coordinate axes are established, and u_c is defined as circumferential velocity and v_a as axial velocity. A_1 and A_2 are, respectively, the thread spacing and thread width of the capsule robot, and r_1 and r_2 are the surface rotation radius of the capsule robot. L is the length of the capsule robot, and p is the pitch of the capsule robot [30]. The force analysis of the capsule robot is as follows:

The motion state of the capsule robot is by the following equation:

$$ma = F_P - F_D \pm G \mp \rho g V_D, \tag{2}$$

where F_P is propulsion force, F_D is resistance force, G is gravity acting on the microrobot, g is the acceleration of gravity, and V_D is drainage volume.

The resistance force F_D equation is expressed as follows:

$$F_D = C_D \frac{1}{2} \rho v^2 S + \mu_f N, \tag{3}$$

where C_D is the drag coefficient, v is the velocity of the capsule robot, S is the cross-sectional area of the simulated pipe, μ_f is the kinematic viscosity coefficient, and N is the normal force.

When the capsule robot rotates, the projection of circumferential velocity u_c and axial velocity v_a in X and Y directions is defined by the following equations:

$$W = u_c \sin\theta - v_a \cos\theta, \tag{4}$$

$$V = u_c \cos\theta + v_a \sin\theta, \tag{5}$$

where W and V represent the velocity component of the projection capsule robot relative to the fluid in X and Y directions, respectively, and θ represents the helix angle.

In order to facilitate calculation, based on previous research results on capsule robot kinematics [18–22],

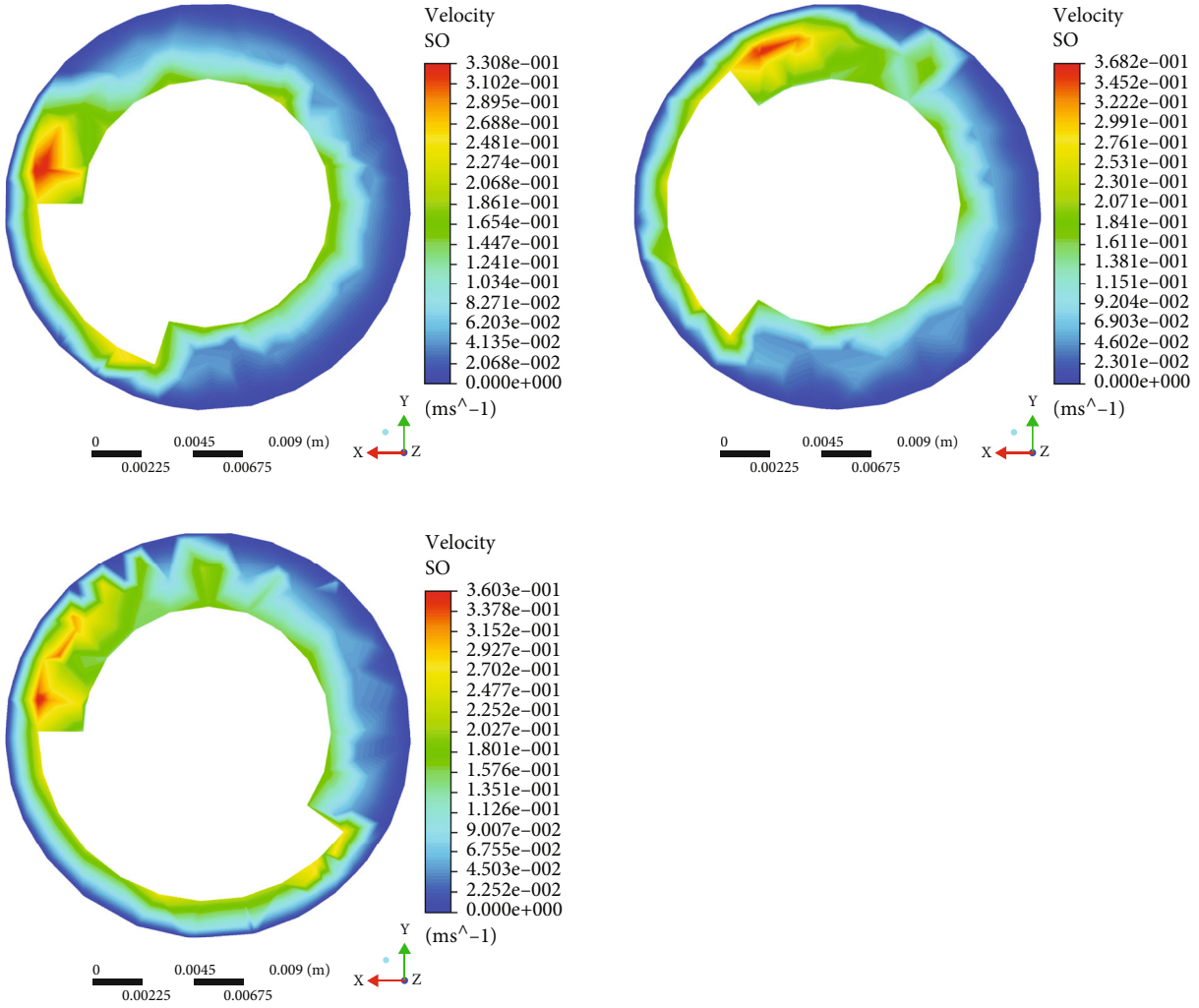

Figure 6: Simulation of exit plane velocity profile of different capsule robots at the same speed.

Equations (6) and (7) of axial propulsion force and resistance are derived from Equations (4) and (5):

$$F_{\text{pro}} = F_y \sin\theta - F_x \cos\theta, \tag{6}$$

$$F_{\text{res}} = F_y \cos\theta + F_x \sin\theta, \tag{7}$$

where F_{pro} represents the axial propulsion force in motion and F_{res} represents the axial resistance in motion.

In dynamic analysis, axial thrust F_{pro} decreases with increasing velocity. When the axial propulsion force is equal to the axial resistance, the acceleration of the capsule robot is 0, and the speed is the maximum, and it moves stably at this speed.

3.2. Energy Conversion Formula. According to the law of energy conservation, the motion performance of the capsule robot in various complex environments is considered. When the capsule robot moves from point A to point B, the total energy W is equal to the change of kinetic energy ΔK, where point A and point B are two uniform points, as follows:

$$W = \int_A^B \mathrm{d}W = \int_B^A \bar{F} \cdot d\bar{r} = \Delta K. \tag{8}$$

According to the energy conservation law, the equation of kinetic energy under ideal ΔKi and actual ΔKr conditions is defined by Equations (9) and (10). It follows that a change in velocity affects kinetic energy. Not all energy is converted into kinetic energy in the actual process, and part of the energy will be converted into heat energy due to resistance [31]:

$$\Delta K_i = \frac{1}{2} m v_{iB}^2 - \frac{1}{2} m v_{iA}^2, \tag{9}$$

$$\Delta K_r = \frac{1}{2} m v_{rB}^2 - \frac{1}{2} m v_{rA}^2. \tag{10}$$

The percentage of actual energy utilized η by the capsule robot in the process of movement is shown in the following equation:

$$\eta = \frac{\Delta K_r}{\Delta K_i} \times 100\%, \tag{11}$$

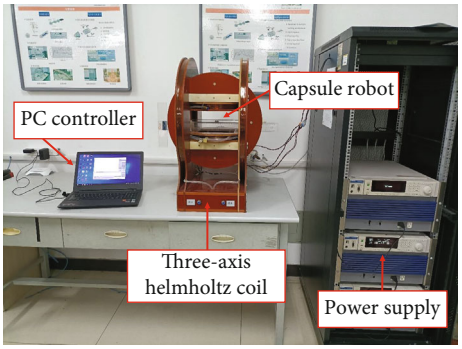

Figure 7: The electromagnetic actuation system.

The shell of capsule robot adopts screw structure (Figure 3(a)). So, the principle of screw mechanism in mechanical design foundation can be used to analyse the capsule robot [32]. Part of the screw structure (Figure 3(b)) and the force analysis is carried out on the inclined plane of the screw thread (Figures 3(c) and 3(d)). The work required by the capsule robot to move forward W_r is shown in the following equation:

$$W_r = G * S_r = G * 2\pi r_1 * \tan\theta, \tag{12}$$

where S_r is the actual horizontal movement distance of the capsule robot.

The work done to make the capsule robot move forward W_i is shown in the following equation:

$$W_i = G * S_i = G * 2\pi r_1 * \tan(\varphi_s + \theta), \tag{13}$$

where S_i is the ideal horizontal movement distance of the capsule robot and φ_s is the dynamic friction angle.

Therefore, the energy utilization rate η of the capsule robot can be deduced to the following equation:

$$\eta = \frac{W_r}{W_i} = \frac{S_r}{S_i} = \frac{\tan\theta}{\tan(\varphi_s + \theta)}. \tag{14}$$

According to Equation (14), the percentage of energy utilized by the capsule robot during the actual movement is equal to the percentage of the actual and ideal moving distance. The actual distance is the horizontal moving distance of the capsule robot, and the ideal moving distance is a multiple of the pitch, as shown in the following equation:

$$\eta = \frac{S_r}{S_i} = \frac{vt}{fpt} = \frac{v}{fp}, \tag{15}$$

where v is the speed of the capsule robot, f is the frequency, and p is the pitch of the capsule robot.

4. Dynamic Analysis

When the capsule robot moves in a fluid-filled pipe, because many variables are affecting the motion, in order to accurately simulate the motion of the capsule robot in the optimal state, a single variable control method is used to simulate the fluid of the capsule robot. The capsule robot model has dynamically meshed. Since the human intestine is similar to a cylinder, we built a cylinder with the same length as the actual experiment as the intestine in the simulation, about 500 mm. The inlet and outlet of the intestine and the direction of forwarding flow velocity are set. In the

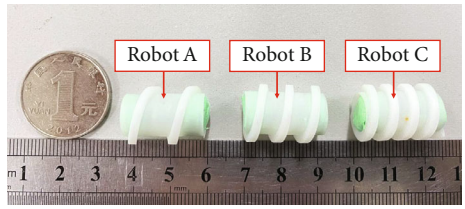

Figure 8: Capsule robots with different pitch.

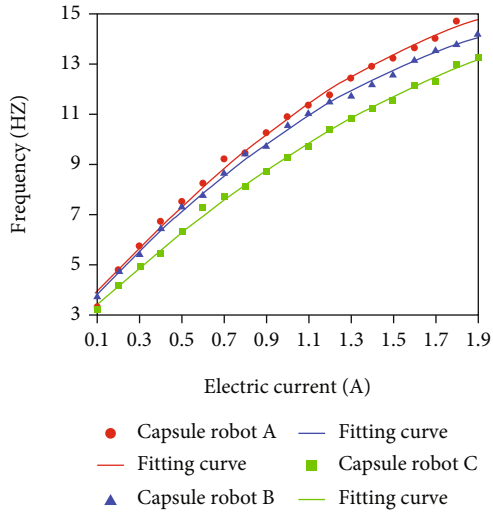

Figure 9: Start-up frequency at different current currents.

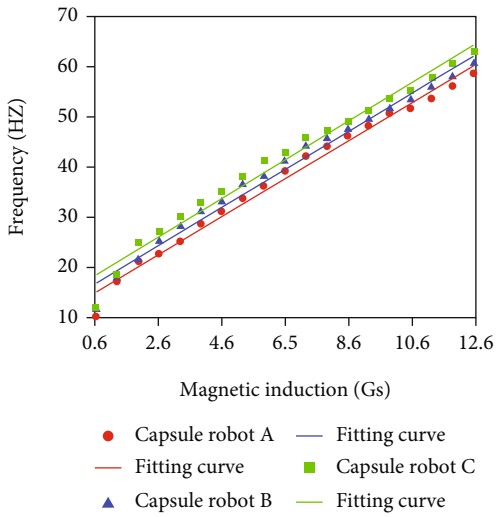

Figure 10: Cut-off frequency of different currents.

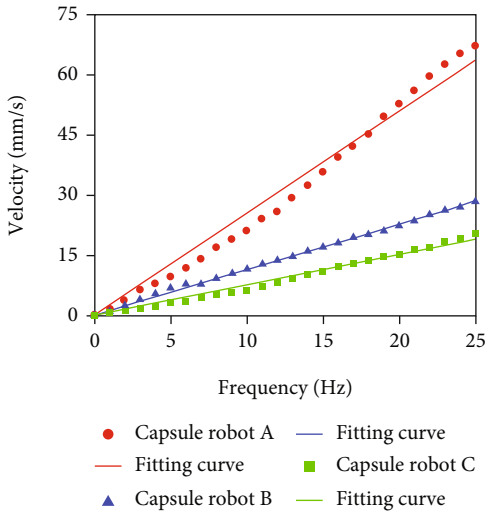

Figure 11: Relationship between frequency and velocity of capsule robot at different pitch.

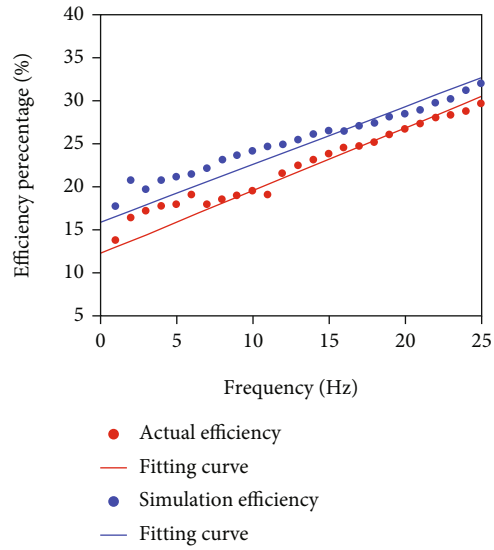

Figure 12: Efficiency of capsule robot at different frequencies.

fluid simulation, the horizontal movement of the capsule robot is studied. In order to reduce the influence of other factors, vertical forces such as gravity and buoyancy are ignored.

In the fluid simulation, a dynamic model with a rotating speed range of 0-150 rad/s and geometric parameters of 10 rad/s is established to carry out the whole fluid simulation at standard atmospheric pressure. Fluid simulation is carried out for capsule robots A, B, and C in Table 1, respectively, and the motion states of these three capsule robots in the pipeline are analysed from dynamics. Due to the different pitches of the three capsule robots, their cross-section shapes are different. Considering that the position of the capsule robot is unchanged in the simulation process, the influence of resistance can be ignored.

Set capsule robots A, B, and C at the same speed, observe their water inlet surface, and get the speed simulation diagram (Figure 4). When the three capsule robots rotate at the same speed, the shorter the pitch, the faster the fluid around the capsule robot. Observe the velocity simulation of capsule robots A, B, and C in the middle plane (Figure 5). It can be seen that at the same speed, the velocity of the three capsule robots is greater than the inlet surface, and the shorter the pitch, the greater the fluid velocity of the middle part of the capsule robot. By observing their outlet surfaces at the same speed, the velocity simulation diagram (Figure 6), it can be seen that the color distribution of the capsule robot at the outlet surface of the capsule robot is not uniform, indicating that the fluid growth rate of different parts of the capsule robot is not uniform at the same speed. By comparing the fluid cloud images of three different parts of the capsule robot, it can be seen that different parts of the capsule robot are affected by different fluid velocities and have different influences on its surroundings. This also lays a foundation for subsequent experiments, especially for selecting capsule robots, which can select the corresponding pitch according to different medical tasks [33].

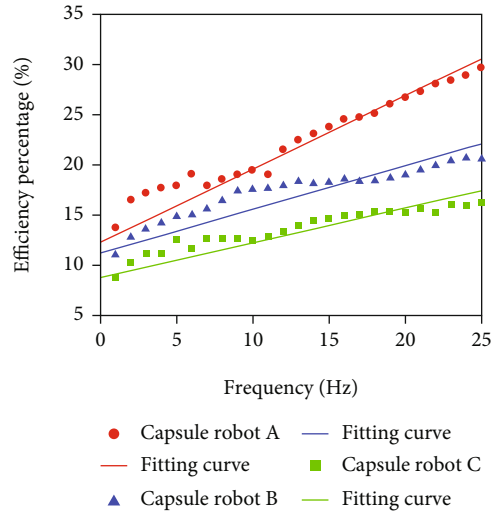

Figure 13: The actual working efficiency of three capsule robots at different frequencies.

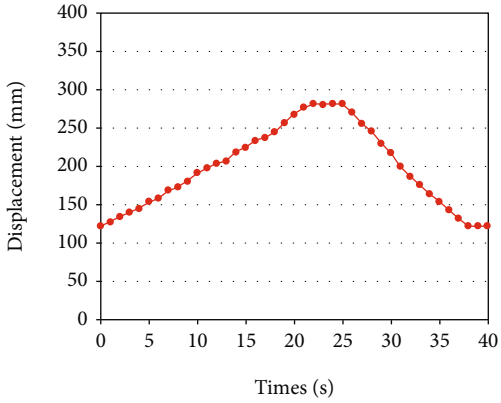

Figure 14: Multiple reciprocating motion.

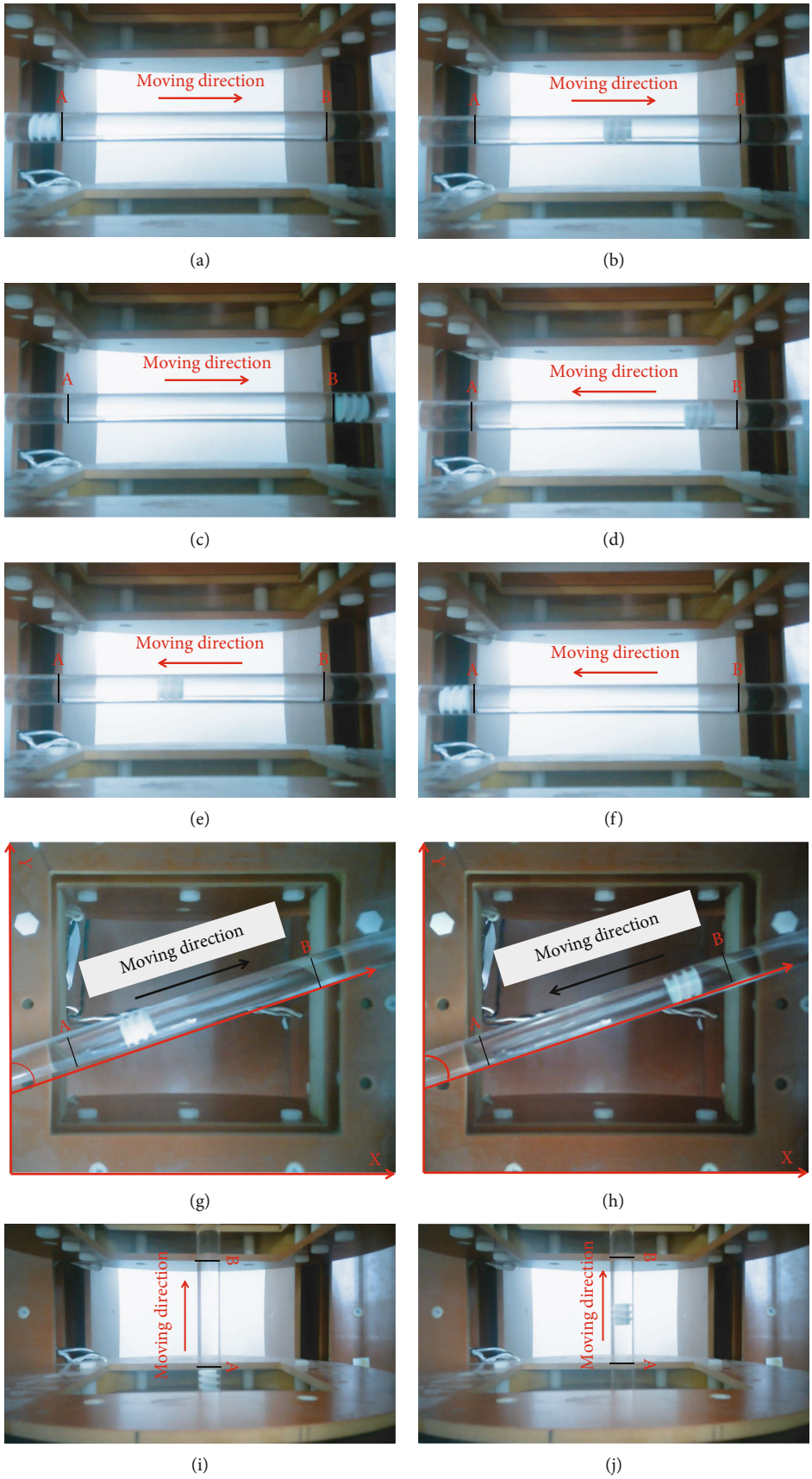

Figure 15: Continued.

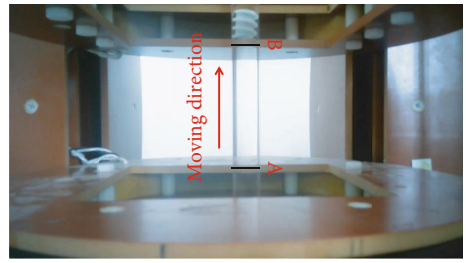

(k)

Figure 15: Hyperspatial motion. (a–c) The forward horizontal movement of the X-axis; (d, e) the reverse horizontal movement of the X -axis; (g, h) locomotion direction is 70° Y-axis; (i–k) the vertical movement of the Z-axis.

5. Experimental Results

The experimental platform was used to test the performance of capsule robot (Figure 7). The motion direction and rotation speed of the capsule robot in the liquid-filled pipe are controlled by adjusting the frequency and direction of the magnetic field. When the upper computer outputs the drive signal, the three-axis Helmholtz coil generates a uniform rotating magnetic field, and the capsule robot placed in the middle of the magnetic field gets the energy to drive the rotation.

5.1. Robot Kinematic Characteristic Experiment. By observing the capsule robots, A, B, and C (Figure 8), it can be seen that the three differences only lie in the pitch, which is 10 mm, 7 mm, and 5 mm, respectively. The capsule robots are put into the acrylic tube filled with water, respectively, to conduct the characteristic motion experiment, and the start-up and cut-off frequencies of capsule robots A, B, and C under different currents are measured (Figures 9 and *10*). The experimental results show that the start-up and cut-off frequencies of the capsule robot vary with the current. In the same current, the shorter the pitch of the capsule robot, the lower the start-up frequency, the higher the cut-off frequency. The difference between start-up and cut-off frequency simultaneously controls of multiple capsule robots or separate control in the same environment. This is to achieve the movement control of the multimodular capsule robot in the intestinal tract to better complete the task of medical treatment.

Adjust the input current to 0.5 A, and the velocities of capsule robots A, B, and C are measured at different frequencies. The external control signal adjusts the frequency from 0 Hz to 25 Hz (Figure 11). The experimental results show that the velocity increases with the increase of frequency. At the same frequency, the larger the pitch of the capsule robot, the faster the speed, the more energy is converted into kinetic energy, and the less energy is consumed to overcome resistance.

5.2. Energy Utilization Percentage Experiment of Capsule Robot. The established capsule robot model is placed in the simulation environment for experiments. Parameters are set at standard atmospheric pressure to simulate the movement of the capsule robot, and the velocity of movement at different frequencies is collected and put into Equation (15) to calculate the energy utilization rate of the capsule robot in the simulation environment. Compared with the energy utilization rate obtained in the actual motion characteristic experiment, the energy utilization rate curve of the capsule robot in the process of motion is obtained (Figure 12). The two curves of the simulation experiment and the actual experiment fluctuate around the starting frequency, but the overall trend is consistent. With the increase of frequency, the energy utilization rate increases, indicating that the control effect of the capsule robot is better. Then, the velocity of capsule robots B and C collected in the motion characteristic experiment is substituted into the following.

Equation (15) was used to obtain the energy utilization curve of capsule robots A, B, and C (Figure 13). When the frequency is constant, the smaller the capsule robot pitch is, the higher the energy utilization ratio is, which verifies the feasibility of the energy utilization ratio equation.

The energy efficiency equation reflects the accuracy of the motion control effect of the capsule robot and is also related to the flexibility of the motion control of the capsule robot. When the capsule robot controls the flexibility, the measured velocity is more accurate and the calculated energy utilization rate is more accurate. Therefore, round-trip movement experiment and multidimensional space movement experiment should be carried out to verify that the capsule robot can be flexibly controlled in human body.

In the round-trip movement experiment (Figure 14), the control magnetic field is rotated clockwise in the Y-Z plane until it stopped at 280 mm for 4 s. The counter clockwise rotation of the magnetic field returns the capsule robot 110 mm. The experimental results show that the capsule robot can start and stop flexibly according to different medical tasks. In the multidimensional space movement (Figure 15), the feasibility of the capsule robot moving in multidimensional space needs to be verified by horizontal movement, vertical movement, and 70° horizontal Y-axis movement, respectively, due to the complex actual intestinal environment of human body. The results show that the capsule robot can obtain the propulsion force by adjusting the rotating magnetic field, which verifies that the capsule robot can be flexibly controlled in multiple directions of the three-axis Helmholtz coil.

6. Conclusion

This paper presents a method to improve the control effect of magnetic driven spiral capsule robot. The capsule robot that tested the method is made of a shell made of polyethylene plastic and an O-ring magnet. By measuring the start-up and cut-off frequency of the capsule robot, determine the frequency control range of single or whole movement of the capsule robot. By comparing the simulation and actual experiment of capsule robot with the same pitch and the actual experiment of capsule robot with three different pitches, the curves obtained all show an upward trend, which verifies the different energy utilization results with different parameters in the equation, indicating the feasibility of this method. According to the experimental results, the energy efficiency of the capsule robot will be improved with the change of the size of the capsule robot's pitch. However, the increase of the pitch of the capsule robot will affect the stability of the motion, so in the future precise control of the capsule robot, the energy utilization equation can be considered to improve the control of the capsule robot, while considering the stability of the motion, in order to achieve the ideal control effect.

Data Availability

The data used to support the findings of this study are included within the article.

Conflicts of Interest

There are no conflicts of interest in this paper's publishing.

Acknowledgments

This work was supported in part by the Innovative Cooperation Project of Tianjin Scientific and Technological Support (18PTZWHZ00090), Natural Science Foundation of Tianjin City (18JCYBJC43200), and Tianjin Key Laboratory for Control Theory and Application in Complicated Systems (TJKL-CTACS-201903).

References

[1] S. T. Qi, "Surgical robot system and its clinical application," *Chinese Medical Equipment*, vol. ED-26, no. 6, pp. 56–59, 2011.

[2] Z. Liao, G. Wang, G. Chen, W. Zhou, and X. Jiang, "Expert consensus on clinical application of Magnetically controlled capsule gastroscopy in China," *Chinese Journal of Health Management*, vol. 37, no. 10, pp. 487–496, 2021.

[3] G. Iddan, G. Meron, A. Glukhovsky, and P. Swain, "Wireless capsule endoscopy," *Nature*, vol. 405, no. 6785, pp. 417-418, 2000.

[4] Z. Liao, G. Wang, G. Chen, W. Zou, and X. Jiang, "Clinical practice consensus for magnetically controlled capsule gastroscopy," *Chinese Journal of Practical Internal Medicine*, vol. 37, no. 10, pp. 885–894, 2021.

[5] G. Bao, K. Pahlavan, and L. Mi, "Hybrid localization of microrobotic endoscopic capsule inside small intestine by data fusion of vision and RF sensors," *IEEE Sensors Journal*, vol. 15, no. 5, pp. 2669–2678, 2015.

[6] J. W. Martin, B. Scaglioni, J. C. Norton et al., "Enabling the future of colonoscopy with intelligent and autonomous magnetic manipulation," *Nature Machine Intelligence*, vol. 2, no. 10, pp. 595–606, 2020.

[7] X. Hou, S. Guo, L. Shi et al., "Hydrodynamic analysis-based modeling and experimental verification of a new water-jet thruster for an amphibious spherical robot," *Sensors*, vol. 19, no. 2, 2019.

[8] J. Guo, Z. Bao, S. Guo, and Q. Fu, "Design and evaluation of a new push-type targeted drug delivery capsule robot," in *IEEE International Conference on Mechatronics and Automation*, pp. 1305–1310, Tianjin, China, 2019.

[9] Y. Zhang, D. Yang, and D. Wang, "Polarization criteria detection of a generalized spatial universal rotating magnetic vector," *IEEE Transactions on Magnetics*, vol. 54, no. 7, pp. 1–8, 2018.

[10] M. Yu, "M2A™capsule endoscopy: a breakthrough diagnostic tool for small intestine imaging," *Gastroenterology Nursing*, vol. 25, no. 1, pp. 24–27, 2002.

[11] S. Guo, Y. He, L. Shi et al., "Modeling and experimental evaluation of an improved amphibious robot with compact structure," *Robotics and Computer-Integrated Manufacturing*, vol. 51, pp. 37–52, 2018.

[12] D. S. Keller, A. Windsor, R. Cohen, and M. Chand, "Colorectal cancer in inflammatory bowel disease: review of the evidence," *Techniques in Coloproctology*, vol. 23, no. 1, pp. 3–13, 2019.

[13] M. Shi, M. Qi, C. Yi, J. Wang, and R. Chen, "Research on the rising motion and drag coefficient of bubbles in still water," *Computational Forces Academic Report*, vol. 36, no. 3, 2019.

[14] S. Zhang, Y. Zhang, W. Liu, Z. Jia, and H. Dai, "Bionic swimming characteristics of an outfield driven cable-free microrobot," *Chinese Journal of Mechanical Engineering*, vol. 41, no. 10, pp. 51–56, 2005.

[15] S. Zhang, Y. Zhang, K. Zhang, and L. Zhang, "Omnidirectional precession driving characteristics of an in-body micro-robot," *ROBOT*, vol. 28, no. 6, pp. 560–570, 2006.

[16] S. Zhang, Y. Zhang, S. Jiang et al., "Dynamic characteristics of variable diameter capsule robot in intestinal tract," *Science in China Press*, vol. 54, no. 16, pp. 2408–2415, 2009.

[17] S. Yim and M. Sitti, "Design and rolling locomotion of a magnetically actuated soft capsule endoscope," *IEEE Transactions on Robotics*, vol. 28, no. 1, pp. 183–194, 2012.

[18] Q. Fu, S. Guo, S. Zhang, H. Hirata, and H. Ishihara, "Characteristic evaluation of a shrouded propeller mechanism for a magnetic actuated microrobot," *Micromachines*, vol. 6, no. 9, pp. 1272–1288, 2015.

[19] Q. Fu, S. Guo, Y. Yamauchi, H. Hirata, and H. Ishihara, "A novel hybrid microrobot using rotational magnetic field for medical applications," *Biomedical Microdevices*, vol. 17, no. 2, pp. 31–42, 2015.

[20] Q. Fu, S. Guo, Q. Huang, H. Hirata, and H. Ishihara, "Development and evaluation of novel magnetic actuated microrobot with spiral motion using electromagnetic actuation system," *Journal of Medical and Biological Engineering*, vol. 36, no. 4, pp. 506–514, 2016.

[21] Q. Fu, S. Zhang, S. Guo, and J. Guo, "Performance evaluation of a magnetically actuated capsule microrobotic system for medical applications," *Micromachines*, vol. 9, no. 12, pp. 641–656, 2018.

[22] Q. Fu, C. Fan, X. Wang et al., "A compensation method for magnetic localization on capsule robot in medical application," *IEEE Sensors Journal*, vol. 21, no. 23, pp. 26690–26698, 2021.

[23] L. Zheng, S. Guo, Z. Wang, and T. Tamiya, "A multifunctional module-based capsule robot," *IEEE Sensors Journal*, vol. 21, no. 10, pp. 12057–12067, 2021.

[24] D. Pham and S. Aziz, "A real-time localization system for an endoscopic capsule using magnetic sensors," *Sensors*, vol. 14, no. 11, pp. 20910–20929, 2014.

[25] Y. Zhang et al., "Movement characteristics of a new type of intestinal capsule micro-robot," *Journal of Mechanical Engineering*, vol. 45, no. 8, 2009.

[26] M. Simi, P. Valdastri, C. Quaglia, A. Menciassi, and P. Dario, "Design, fabrication, and testing of a capsule with hybrid locomotion for gastrointestinal tract exploration," *IEEe/ASME Transactions on Mechatronics*, vol. 15, no. 2, pp. 170–180, 2010.

[27] Z. Cai, Q. Fu, S. Zhang et al., "Characteristic analysis of a magnetically actuated capsule microrobot in medical applications," *IEEE Transactions on Instrumentation and Measurement*, vol. 71, pp. 1–11, 2022.

[28] Q. Fu, X. Wang, J. Guo, S. Guo, and Z. Cai, "Magnetic localization technology of capsule robot based on magnetic sensor array," in *2020 IEEE International Conference on Mechatronics and Automation (ICMA)*, pp. 267–272, Beijing, China, 2020.

[29] Z. Cai, Q. Fu, S. Zhang et al., "Performance evaluation of a magnetically driven microrobot for targeted drug delivery," *Micromachines*, vol. 12, no. 10, p. 1210, 2021.

[30] S. Guo, F. Huang, J. Guo, and Q. Fu, "Study on the active movement capsule robot for biopsy," in *2020 IEEE International Conference on Mechatronics and Automation*, pp. 1780–1785, 2020.

[31] J. Guo, Z. Bao, Q. Fu, and S. Guo, "Design and implementation of a novel wireless modular capsule robotic system in pipe," *Medical & Biological Engineering & Computing*, vol. 58, no. 10, pp. 2305–2324, 2020.

[32] Z. Wang, S. Guo, J. Guo, Q. Fu, L. Zheng, and T. Tamiya, "Selective motion control of a novel magnetic-driven Minirobot with targeted drug sustained-release function," *IEEE/ASME Transactions on Mechatronics*, vol. 27, no. 1, pp. 336–347, 2022.

[33] X. Jin, S. Guo, J. Guo, P. Shi, T. Tamiya, and H. Hirata, "Development of a tactile sensing robot-assisted system for vascular interventional surgery," *IEEE Sensors Journal*, vol. 21, no. 10, pp. 12284–12294, 2021.

Hindawi
Applied Bionics and Biomechanics
Volume 2022, Article ID 4330518, 6 pages
https://doi.org/10.1155/2022/4330518

Research Article

Double-UV Photoionizaion Detector with Graphene Oxide-Coated Electrodes

Qi Zhou,[1,2] **Xu Zhang**,[3] **Xu Ma**,[4] **and Sixiang Zhang**[5]

[1]*School of Electrical Engineering and automation, Tianjin University of Technology and Education, Tianjin 300222, China*
[2]*Tianjin Key Laboratory of Information Sensing and Intelligent Control, Tianjin 300222, China*
[3]*School of Mechanical Engineering, Tianjin University of Technology and Education, Tianjin 300130, China*
[4]*School of Electrical and Electronic Engineering, Tianjin University of Technology, Tianjin 300130, China*
[5]*School of Mechanical Engineering, Hebei University of Technology, Tianjin 300130, China*

Correspondence should be addressed to Qi Zhou; 13820758091@163.com

Received 17 March 2022; Revised 12 June 2022; Accepted 16 June 2022; Published 19 July 2022

Academic Editor: Songyuan Zhang

The structure of a photoionization detector was optioned and researched. In order to solve the problem of the photoionization detector' lamp surface residue interference, a new structure of the self-cleaning double-UV detector was adopted. At the same time, the air flow field of the detector was simulated by the finite element method. Through analyzing the results of the simulation experiment, further optimization of the gas channel for the microdetector was carried out, and the ionization chamber with axial flow structure was finally chosen. The new nanomaterial, graphene oxide was used to modify the surface of the collector plate of detector to improve the gas sensitivity and sensitivity of the photoionization detector. Through the experimental analysis, the performance indexes of detector were described in detail. The minimum detection limit of the detector is 2.5×10^{-7}. The linearity response of the detector was analyzed, and the linear correlation coefficient reaches 0.993. The experimental results show that the double-UV detector can improve the overall gas sensing characteristics and provide an ideal detection unit for volatile organic compound (VOC) gas detection.

1. Introduction

Volatile organic compounds (VOCs) is an important part of air pollution and an important index of quantitative air pollution. The boiling point of VOCs gas is 50°C-260°C, and its saturated vapor pressure usually exceeds 133.32 Pa at room temperature. According to its chemical structure, VOCs gas can be roughly divided into alkanes, aromatics, esters, aldehydes, and so on [1, 2]. They exist widely in the atmosphere, water, and soil. On the one hand, they cause serious pollution to the environment [3]; on the other hand, they seriously endanger people's physical and mental health. Therefore, the detection of VOCs gas is particularly important in environmental protection. This paper mainly researches photoionization detector (PID) [4], which is the core component of VOCs gas detection, as the main object to carry out the theoretical and experimental research.

According to the requirements of VOC detection, a micro-PID was fabricated using MEMS technology. Different types of microchannel were designed. The effects of different physical and chemical parameters were experimentally investigated. The key parameters affecting the efficiency of microchannel such as carrier gas pressure [5], temperature, and flow rate, were experimentally investigated.

Graphene belongs to the category of two-dimensional materials, which has significant advantages in specific surface area and physical adsorption compared with activated carbon. In the laboratory, this material is generally obtained by chemical vapor deposition and other methods. Graphene oxide (GO) has a large specific surface area, but its structure is imperfect compared with intrinsic graphene, which is mainly reflected in unpaired electrons, so it is likely to combine with gas molecules [6]. Besides, there are many oxygen-containing functional groups in the microstructure of GO, which is the reason why it has a large specific surface area

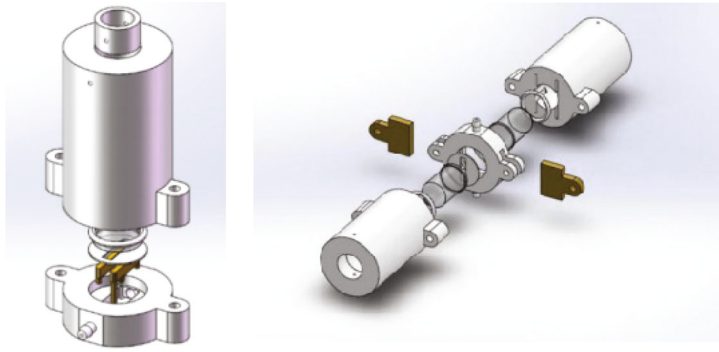

(a) Single UV (b) Double UV

Figure 1: The PID detector structure.

and strong adsorption capacity. Therefore, graphene has great room for development in the field of VOCs. It can greatly enhance the gas sensing properties of the plate surface by introducing graphene into the electrode of PID.

2. Materials and Methods

There is an ultraviolet light as the ionization source to ionize the gas molecules of the material in photo ionization detector. During the working process of PID, the inert gas in the UV lamp of PID is excited in the alternating high frequency electric field to form a plasma. Through releasing photons, the gas to be measured is ionized [7]. Therefore, the reaction in the ionization chamber has a great influence on the photocurrent produced by photoionization. Its ionization efficiency directly affects the determination of gas concentration by photoionization detector.

The traditional single-lamp PID detector is basically divided into one-dimensional structure and two-dimensional structure. Axial flow (Figure 1(a)) shows orthogonal relation between UV lamp path, gas path, and collecting plate, and the gas path diameter is determined to be 1.2 mm, and the electrode width is 1 mm [8, 9]. In order to improve ionization efficiency of photoionization detector for gas and to solve the problem of self-cleaning of the lamp surface, a new structure—dual-lamp PID detector—is presented. The comparison between the single-lamp and dual-lamp detector structures is shown in Figure 1.

The traditional PID sensor with single-lamp structure adopts three-dimensional orthogonal structure, and the gas is not in direct contact with the UV lamp, which improves the pollution of the lamp surface because of long-term use to a certain extent. However, when detecting sulfide and other easily adsorbable gases for a long time, the baseline will rise and the response will drop. When the ionization potential is close to the ionization energy of the UV lamp, the ionization efficiency decreases obviously. The dual-lamp structure adopts the structure of two UV lamps facing each other. On the one hand, the problem of cleaning the lamp surface can be improved. On the other hand, the luminous efficiency of the UV lamp can directly affect the performance of the sensor. But the effective spectral lines are few, therefore, the ionization efficiency can be increased when detecting gases with higher ionization potentials.

After determining the structure of the dual-lamp PID, the structure of the gas path in the ionization chamber is further optimized by simulation experiments [10]. The structure of the ionization chamber is shown in Figure 2(a)). Due to the larger volume of the rectangular ionization region of the sensor and the smaller size of the gas inlet, the convex structure will be formed when entering the ionization region. Therefore, the gas circuit structure has been improved. As shown in Figure 2(b)), the internal gas circuit structure of the sensor has been processed by the overimprovement of the cone to reduce the abrupt change in the cross-sectional area of the gas circuit structure inside the ionization chamber and ensure the interior of the ionization chamber, which ensures the internal volume of the ionization chamber and also ensures the performance of the sensor.

Through theoretical analysis and experiments, we know that when a rectangular plate is used to excite the UV lamp, the UV lamp emits a linear beam perpendicular to the two electrode plates. When a ring plate is used to excite the UV lamp, the lamp emits a cylindrical beam, and its diameter is approximately the same as the diameter of the lamp. The available area of the beam is large so that the gas to be measured in the chamber will be entirely exposed to ultraviolet light. Hence, a strong current signal is generated, the efficiency of the UV lamp is improved, and the difficulty of detecting the current signal is reduced. Therefore, gas circuit simulation results are used in the channel design, which is shown in Figure 3.

When the electrostatic field is an electric field, the calculation expression of the electric potential energy of neutral polarizable molecules is $-\alpha E(r)^2/2$ [11], where α represents the static molecular polarizability, r represents the position of the molecule, and L and K represent the radial and axial momentum between the molecule and the plate, respectively. From this, a dependency of the inverse square is determined. The effective electric potential energy obtained by its radial motion is [12]

$$U_r(r) = \frac{L}{2mr^2} - \frac{K^2}{2mr^2}. \quad (1)$$

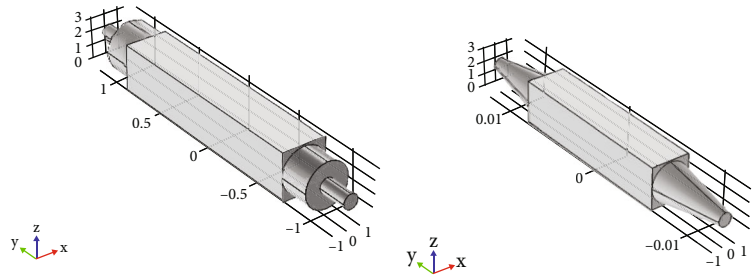

(a) Before optimizes (b) After optimizes

Figure 2: The whole gas path model.

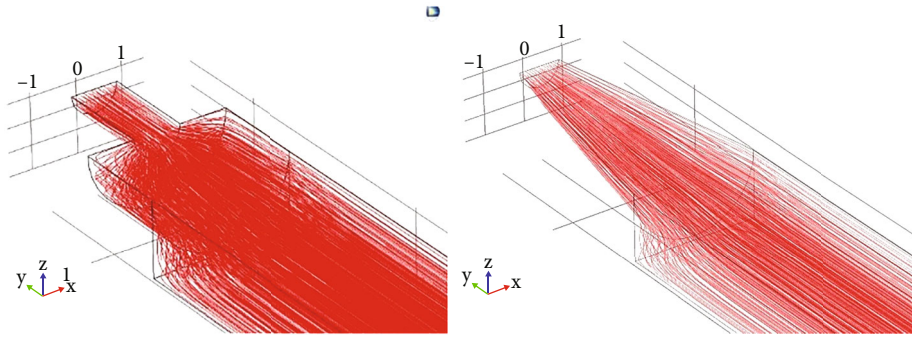

Figure 3: Gas circuit simulation results.

According to the above formula, two different ion motion models can be judged, which are closely related to the size of L and K. In the case of $L > K$, the molecule is finally captured by the graphene oxide layer because the polarization is greater than the radial potential energy. Otherwise, when $L < K$, the motion phenomenon of repulsive radial potential energy caused by the eccentric potential energy will occur, so we can draw a conclusion that whether molecules will be captured by the plates depends on the voltage between the plates, which indirectly determines the efficiency of plate ionization. Then, the probability formula of electron tunneling ionization in a strong field [13] is derived from the Ammosov-Delone-Krainov model, that is, the ionization efficiency formula of gas:

$$W_a(E) = \frac{4^n \xi_1}{n^* \Gamma(2n^*)} \left(\frac{2\xi_0}{E}\right)^{2n^m - 1} \exp\left(-\frac{2\xi_0}{3E}\right), \quad (2)$$

where W_a is the gas ionization efficiency, E is the electric field strength, and ξ_1 is the ionization energy required for gas ionization. Because the ionization energy is determined by the type of gas, the gas ionization efficiency is only related to the intensity of the electric field. The higher the voltage, the higher the ionization efficiency. The response mechanism of PID based on graphene oxide as the collector to gas is to use the electric field formed by the position of the nanotip. This tip effect combines with electric field, which can enhance microcurrent response obviously under equal voltage condition, thus improving gas sensing properties. Therefore, this method is beneficial to gas detection [14, 15].

3. Results and Discussion

A mass flow controller (MFC) was used to adjust pump suction flow, and volume flow is set to 50 mL/min [16], when the system is stable and the background gas is relatively stable. Low-concentration injection (toluene with a volume fraction of 500 ppb for single-lamp sensor and dual-lamp sensor) was carried out, respectively [17]. After processing response through microcurrent amplifier and then collecting after I/V conversion, the specific results are shown in Figure 4.

Voltage response value of dual-lamp sensor is $V_1 = 0.73$ V, and voltage response value of single-lamp sensor is $V_2 = 0.57$ V. Response margin is $\Delta V = 0.16$V. Through experiments, it was found that after low concentration gas detection, the baseline drift of a single-lamp sensor is significantly more serious than that of a dual-lamp sensor, and the required baseline stabilization time is longer than that of a dual-lamp sensor. After the baseline returns to zero and stabilizes, high-concentration injections (toluene with a volume fraction of 2 ppm) were performed for the single-lamp sensor and the dual-lamp sensor, respectively. Experimental results are shown in Figure 5.

The voltage response value of dual-lamp sensor is $V_1 = 2.41$ V and that of single-lamp sensor is $V_2 = 2.09$ V. The response difference is $\Delta V = 0.32$V. It can be seen that the

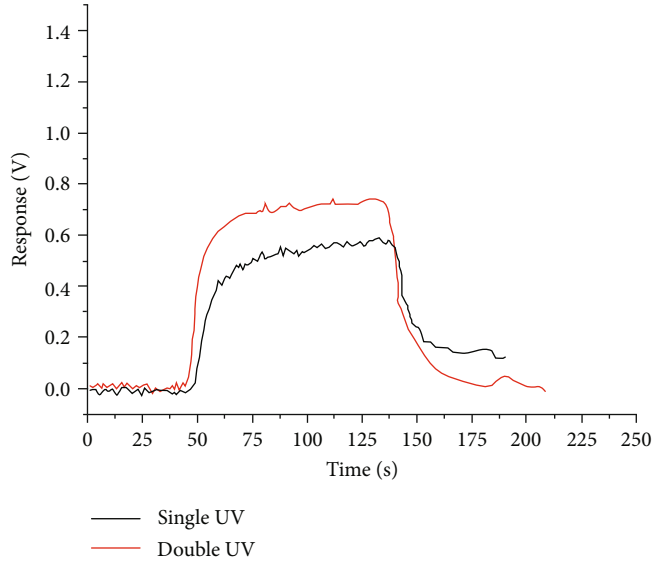

Figure 4: Single lamp-double light sensor response for 500 ppb.

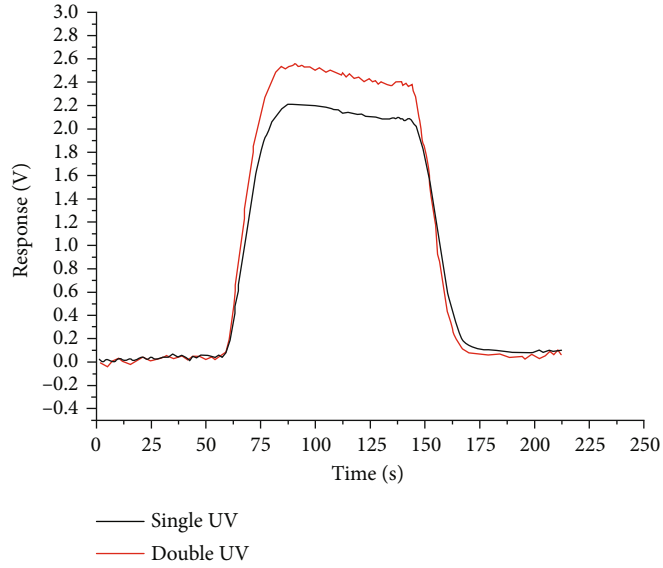

Figure 5: Single lamp-double light sensor response for 2 ppm.

performance of dual-lamp sensor is better than that of single-lamp sensor in a wide range (volume fraction is 500 ppb-2 ppm). And it can obviously improve the interference caused by the lamp pollution of the sensor.

The principle of chemical oxidation is to treat (intercalate and oxidize) graphite with a strong oxidant to obtain graphite oxide. The microstructure of this product has functional groups with good hydrophilicity, so that effect of the layers inside the graphite is reduced. Therefore, the strong oxidant can destroy the van der Waals force between each layer of graphite and then make each layer independent. The single-layer graphite oxide obtained in the above process is placed in an ultrasonic environment, separated by an organic solvent, and finally reduced to a single layer. The layered graphene [18] is dissolved in the solution and diluted to a 1 mg/mL graphene oxide solution, which is convenient for subsequent operation and treatment. Then, the Cu electrode was soaked in PEG solution of 5 mmol/L for 12 hours [19] and dried and soaked in graphene oxide solution for 5 hours. The amino group in the PEG solution [20] was combined with the carboxyl group in graphene oxide solution to make graphene oxide adhere to the surface of the plate. According to the different soaking times, the graphene oxide electrodes [21, 22] soaked for 1 time, 2 times, and 3 times were detected, respectively, with 500 ppb isobutene gas. It is concluded that the graphene oxide-covered

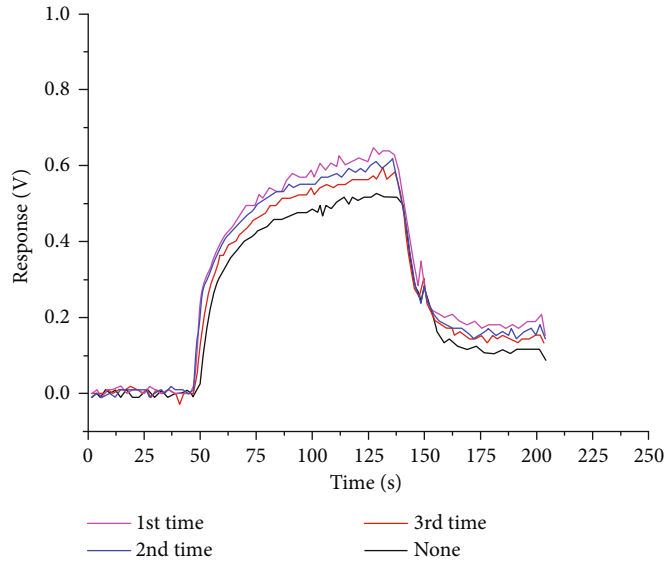

Figure 6: Voltage response contrast of the graphene oxide-coated electrode sensor with different soaked times.

electrode can effectively improve the gas sensing properties of the sensor, and the graphene oxide on the surface of the plate will combine more fully with the increase of soaking times. The voltage response value is shown in Figure 6.

4. Conclusions

In this article, the influence of single-lamp and dual-lamp on the signal of PID based on the principle of photoionization was mainly discussed, and the sensor plate was optimized by new nanomaterials. According to the principle model of the sensor, a complete dual-light ionization sensor structure model was established. Through the analysis of the comparative experimental results of high and low concentration toluene, the performance improvement of the new PID was verified. The graphene oxide electrodes with different immersion times were tested with 500 ppb isobutene, and the electrode parameters and properties were determined, which provides a reliable data basis and experience for the follow-up work. It is inferred from the experiment that there is a good linear relationship between the voltage response and the concentration of PID for toluene in the measurement range of 0 ppm-8 ppm, and the lowest detection limit is 250 ppb. It is concluded from the experiment that the voltage response and concentration of toluene PID have a good linear relationship in the measurement range of 0 ppm-8 ppm, and the minimum detection limit is 250 ppb.

Data Availability

No data were used to support this study.

Conflicts of Interest

The authors do not have any competing interest.

Acknowledgments

This work was supported (in part) by the Tianjin Natural Science Foundation under Grants 20JCZDJC00150 and 20JCZDJC00150. This work was supported (in part) by the Science Technology Research and Development Plan Foundation of Tianjin under Grant 2020KJ118.

References

[1] S. C. Terry, J. H. Jerman, and J. B. Angell, "A gas chromatographic air analyzer fabricated on a silicon wafer," *IEEE Transactions on Electron Devices*, vol. 26, no. 12, pp. 1880–1886, 1979.

[2] S. Ettre and K. I. Sakodynskii, "M. S. Tswett and the discovery of chromatography I: early work (1899–1903)," *Chromatographia*, vol. 35, no. 3-4, pp. 223–231, 1993.

[3] M. S. Tswett, "Physikalisch-chemische studien uber das chlorophyll," *Berichte der Deutschen Botanischen Gesellschaft*, vol. 24, no. 6, pp. 316–332, 1906.

[4] M. J. E. Golay, "Theory of chromatography in open and coated tubular columns with round and rectangular cross-sections," *Gas Chromatography*, vol. 2, pp. 36–55, 1958.

[5] M. Agah, J. A. Pltkay, and J. A. Driscoll, "Temperature-programmed micro fabricated gas chromatography columns," in *Technical Digest of the 12th International Conference on Solid-State Sensors, Actuators and Micro systems*, vol. 17, no. 3, pp. 1339–1342, Boston, Massachusetts, 2003.

[6] C. M. Yu, "High performance hand-held gas chromatography," in *Proceedings of the ASME 1998 International Mechanical Engineering Congress and Exposition. Micro-Electro-Mechanical Systems (MEMS)*, pp. 481–486, Anaheim, California, 1998.

[7] S. Zampolli, I. Elmi, J. Sturmann, S. Nicoletti, L. Dori, and G. C. Cardinali, "Selectivity enhancement of metal oxide gas sensors using a micromachined gas chromatographic column," *Sensors and Actuators B: Chemical*, vol. 105, no. 2, pp. 400–406, 2005.

[8] J. Workman, J. David, J. Veltkamp, and S. Doherty, "Process analytical chemistry," *Analytical Chemistry*, vol. 71, no. 12, pp. 121–180, 1999.

[9] X. Dai, F. Fan, Y. Ye et al., "An experimental study on investigating the postmortem interval in dichlorvos poisoned rats by GC/MS-based metabolomics," *Legal Medicine*, vol. 36, pp. 28–36, 2019.

[10] S. Barmaki, M.-A. Albert, and S. Laulan, "Probing electron dynamics in the double photoionization process of two-valence electron systems with extreme UV and soft X-ray free-electron laser pulses," *Chemical Physics*, vol. 517, pp. 24–29, 2019.

[11] Z. Zhou, X. Chen, H. Ma, C. Liu, C. Zhou, and F. Qi, "Real-time monitoring biomass pyrolysis via on-line photoionization ultrahigh-resolution mass spectrometry," *Fuel*, vol. 235, pp. 962–971, 2019.

[12] S. O. Agbroko and J. Covington, "A novel, low-cost, portable PID sensor for the detection of volatile organic compounds," *Sensors & Actuators: B. Chemical*, vol. 275, pp. 10–15, 2018.

[13] A. Heptner, T. Reinecke, N. Angerstein, and S. Zimmermann, "A novel ion selective gas sensor based on pulsed atmospheric pressure chemical ionization and ion-ion-recombination," *Sensors & Actuators: B. Chemical*, vol. 246, pp. 252–257, 2017.

[14] T. Laura, C. Rosaria, G. S. De, S. Ragusa, and L. Mondello, "Monodimensional (GC-FID and GC-MS) and comprehensive two-dimensional gas chromatography for the assessment of volatiles and fatty acids from Ruta chalepensis aerial parts," *Phytochemical Analysis*, vol. 25, no. 5, pp. 468–475, 2014.

[15] B. Ç. Özkan, M. Fırat, D. S. Chormey, and S. Bakırdere, "Accurate and sensitive determination of harmful aromatic amine products of azo dyes in wastewater and textile samples by GC–MS after multivariate optimization of binary solvent dispersive liquid-liquid microextraction," *Microchemical Journal*, vol. 145, pp. 84–89, 2019.

[16] R. Ligotski, U. Sager, U. Schneiderwind, C. Asbach, and F. Schmidt, "Prediction of VOC adsorption performance for estimation of service life of activated carbon based filter media for indoor air purification," *Building and Environment*, vol. 149, pp. 146–156, 2019.

[17] N. Vaze, Y. Jiang, L. Mena et al., "Erratum to "An integrated electrolysis – electrospray – ionization antimicrobial platform using engineered water nanostructures (EWNS) for food safety applications"," *Food Control*, vol. 85, pp. 151–160, 2018.

[18] E. Lazzari, A. dos Santos Polidoro, B. Onorevoli et al., "Production of rice husk bio-oil and comprehensive characterization (qualitative and quantitative) by HPLC/PDA and GC×GC/qMS," *Renewable Energy*, vol. 135, pp. 554–565, 2019.

[19] H. Akhavan, M. Ghadiri, and A. Zajkani, "A new model for the cantilever MEMS actuator in magnetorheological elastomer cored sandwich form considering the fringing field and Casimir effects," *Mechanical Systems and Signal Processing*, vol. 121, pp. 551–561, 2019.

[20] C. Kwan, A. P. Snyder, R. P. Erickson et al., "Chemical agent detection using GC-IMS: a comparative study," *IEEE Sensors Journal*, vol. 10, no. 3, pp. 451–460, 2010.

[21] K. Voronova, K. G. Torma, J. P. Kercher, A. Bodi, and B. Sztáray, "Dissociative photoionization of chromium hexacarbonyl: a round-trip ticket to non-statisticality and a detective story in thermochemistry," *International Journal of Mass Spectrometry*, vol. 438, pp. 63–71, 2019.

[22] M. Akbar, H. Shakeel, and M. Agah, "GC-on-chip: integrated column and photoionization detector," *Lab On Chip*, vol. 15, no. 7, pp. 1748–1758, 2015.

Hindawi
Applied Bionics and Biomechanics
Volume 2022, Article ID 3859307, 16 pages
https://doi.org/10.1155/2022/3859307

Research Article

Research on Energy Supply System Applied to Autonomous Underwater Observation Vehicles

Chunjie Wang,[1,2] Yugeng Chai,[1,2] and Lin Cui[3]

[1]*School of Electrical Engineering and Automation, Tianjin University of Technology, Tianjin 300382, China*
[2]*Tianjin Complex System Control Theory and Application Key Laboratory, Tianjin 300382, China*
[3]*National Ocean Technology Center, Tianjin 300112, China*

Correspondence should be addressed to Lin Cui; cuilin_oceanenergy@126.com

Received 16 March 2022; Accepted 6 June 2022; Published 29 June 2022

Academic Editor: Muye Pang

The discharge characteristics of seawater batteries can be used to prolong the working hours of autonomous underwater observation vehicles. However, the output voltage level of the seawater battery is low, so it cannot directly be used to power supply underwater observation vehicles. In this paper, a boost converter is proposed based on the seawater batteries to power supply autonomous underwater observation vehicles. The proposed converter greatly increases the voltage level of the seawater battery and directly supplies the underwater observation vehicles. Compared with the traditional boost converter, the voltage gain of the proposed converter is more than ten times higher than it under the same duty ratio condition. Its structure is asymmetric interleaved parallel, which can enable power devices to obtain lower voltage stress and ensure that the input current ripple is low. The operating principle and homeostasis property of the proposed converter are analyzed in detail. Finally, a prototype is built. Through simulation and experiment, the correctness of the theoretical design is verified and experimental results are analyzed.

1. Introduction

With the improvement of people's understanding of the ocean, the exploration and development of Marine environments covering 70% of the surface has received extensive attention. Autonomous underwater observation vehicle is an autonomous underwater equipment suitable for various environments, characterized by long working hours and wide range of activities [1–6]. Therefore, the energy supply requirements of this equipment are relatively high. Lithium battery has the characteristics of high specific energy and long cycle life [7], began to be applied to the power system of underwater vehicles in the early 21st century [8–11]. However, with the extension of the working hours of autonomous underwater observation vehicle, limited by the volume and weight of the vehicle itself [12–15], lithium battery cannot meet its requirements. Dissolved oxygen seawater battery, with seawater as the electrolyte, carbonized fibre or graphite are used to cathode, and active metal as anode, redox reactions with dissolved oxygen in seawater [16]. The reaction principle is as follows:

Anodes:

$$\mathrm{Mg} \longrightarrow \mathrm{Mg}^{2+} + 2\mathrm{e}^{-} \tag{1}$$

Cathode:

$$\mathrm{O}_2 + 2\mathrm{H}_2\mathrm{O} + 4\mathrm{e}^{-} \longrightarrow 4\mathrm{OH}^{-} \tag{2}$$

The output voltage is 1.2-1.4 V, and the battery has an open structure and does not need to design a water pressure shell, which is conducive to generate electricity in seawater at different depths. Compared with lithium batteries, seawater batteries do not need to carry electrolyte and cathode active substance, and the specific energy (318 W h/kg) is higher than lithium batteries (160 Wh/kg) [17–20], and they have the characteristics of long discharge time (3-5 years), safe, and reliable. Therefore, it is particularly suitable for powering equipment that has been working under the sea for a long time. However, due to the low concentration of dissolved oxygen in the ocean, the output power of dissolved oxygen seawater batteries is low [21, 22],

and it can only be applied to low-power underwater observation systems of vehicles. Based on the characteristics of the two types of batteries, the energy supply system of autonomous underwater observation vehicle can be designed as shown in Figure 1, lithium battery supplies power the power system of the vehicle, and dissolved oxygen seawater battery supplies power the observation system of the vehicles. Because the power supply technology of lithium battery is relatively mature, it will not be mentioned here.

The output voltage level of dissolved oxygen seawater battery is low, with a rated output of 1.3 V [23], and the voltage level required for observation system is high, so a high-gain DC-DC converter needs to be added to the output side of the seawater battery. The traditional boost converter voltage gain is lower; the higher voltage gain will make the duty cycle close to 1, while power device voltage stress is higher. So the researchers studied how to improve the voltage gain of the converter. Literature [24–26] introduces switched inductors in the boost converter, which increases the voltage gain, but the effect is insufficient. In literature [27, 28], interleaved parallel and switched capacitor are adopted to achieve high gain; due to absence of coupled inductors, the voltage gain of the converter is limited, and the voltage stress of the MOSFET and diode is high. In literature [29], multiset switched capacitors are proposed to obtain high-gain converter, but the increase in the number of switched capacitors undoubtedly increases the cost of circuits, and the efficiency and reliability of the converter cannot be satisfied. In literature [30, 31], coupled inductor was used to achieve high-gain conversion; due to the absence of interleaved parallel, the increase in voltage gain is still limited.

In this paper, a high-gain DC-DC converter with asymmetric interleaved parallel as a framework is proposed, combined with coupled inductor and switched capacitor structure. Firstly, while the converter obtains a higher voltage gain, the voltage stress obtained by the power device is less. On the other hand, the input current ripple of the converter can effectively be suppressed by asymmetric interleaved parallel structure, thus making the seawater battery power supply system more stable. Finally, a prototype is built to verify the feasibility of the proposed converter.

2. Principles of Operation and Analysis

The equivalent topology of the proposed converter is shown in Figure 2. The two MOSFET in the converter are controlled by the controller to realize 180° interleaved conduction; the diodes D_2 and D_3 and capacitors C_2 and C_3 constitute the switch capacitor structure and the output diode D_4 as the output of the converter. The input of the converter is a dual coupled inductor structure, including leakage inductance L_{k1} and L_{k2}, magnetizing inductance L_{m1} and L_{m2}, and two ideal transformers; the diode D_1 and the capacitor C_1 form the clamping circuit. The turn ratio of the two coupled inductors can be expressed as $N_{S1}/N_{p1} = N_1$ and $N_{S2}/N_{p2} = N_2$.

In order to facilitate analysis, it is assumed that the effects of all parasitic elements are ignored. During a cycle, there are 8 working modes and the driving signals of S_1 and S_2 are interleaved 180°. Figure 3 shows the key waveforms of the proposed converter, and the transient modes I, II, V, and VI due to leakage should be ignored. After ignoring, the modes in a cycle are III, VI, VII, and VIII. The topological stages of the circuit are shown in Figure 4.

In mode III $[t_2 - t_3]$, at t_2, MOSFET S_2 is off, S_1 is still open, diodes D_1 and D_3 are on, and diodes D_2 and D_4 are off, as shown in Figure 4(a). The current on the diode D_3 is expressed as

$$i_{D3}(t) = i_{D3}(t_2) + \frac{V_{C3}}{n^2(L_{k1} + L_{k2})}(t - t_2). \tag{3}$$

In mode VI $[t_5 - t_6]$, at t_5, MOSFETs S_1 and S_2 are in conduction state, and diodes D_1, D_2, D_3, and D_4 are cut off, as shown in Figure 4(b). The magnetizing inductance L_{m1} current is expressed as

$$i_{Lm1}(t) = i_{Lm1}(t_5) + \frac{V_{in}}{L_{m1} + L_{k1}}(t - t_5). \tag{4}$$

In mode VII $[t_6 - t_7]$, at time t_6, MOSFET S_1 is off, S_2 is on, diodes D_2 and D_4 are on, and diodes D_1 and D_3 are off, as shown in Figure 4(c). Input current is expressed as

$$i_{in}(t) = i_{in}(t_6) + \left[\frac{(V_{C1} + V_{C2} + V_{C3} + V_o) - V_{in}}{L_{k1} + L_{m1}} + \frac{V_{in}}{L_{k2} + L_{m2}}\right](t - t_6). \tag{5}$$

In mode VIII $[t_7 - t_8]$, at t_7, the switch S_1 is kept off, S_2 remains on, diode D_2 is on, and diodes D_1, D_3, and D_4 are cut off, as shown in Figure 4(d). The energy of leakage inductance L_{k1} is completely transferred to capacitor C_2, and the current i_{S2} is expressed as

$$i_{S2}(t) = i_{Lm1}(t) + i_{Lm2}(t). \tag{6}$$

3. Performance Analysis

3.1. Steady-State and Performance Analysis. According to magnetism chain conservation, the relationship between magnetizing inductance L_{m1} and L_{m2} is expressed as

$$\begin{cases} Du_{Lm1-on} + (1 - D)u_{Lm1-off} = 0, \\ Du_{Lm2-on} + (1 - D)u_{Lm2-off} = 0. \end{cases} \tag{7}$$

In the formula, D is the duty ratio of the S_1 and S_2. Available in formula (7),

$$\begin{aligned} V_{C1} &= \frac{V_{in}}{1 - D}, \\ V_{C2} &= N_2 k_2 V_{in} + N_1 k_1 V_{in} \frac{D}{1 - D}, \\ V_{C3} &= N_1 k_1 V_{in} + N_2 k_2 V_{in} \frac{D}{1 - D}. \end{aligned} \tag{8}$$

According to mode VII, the output voltage is expressed as

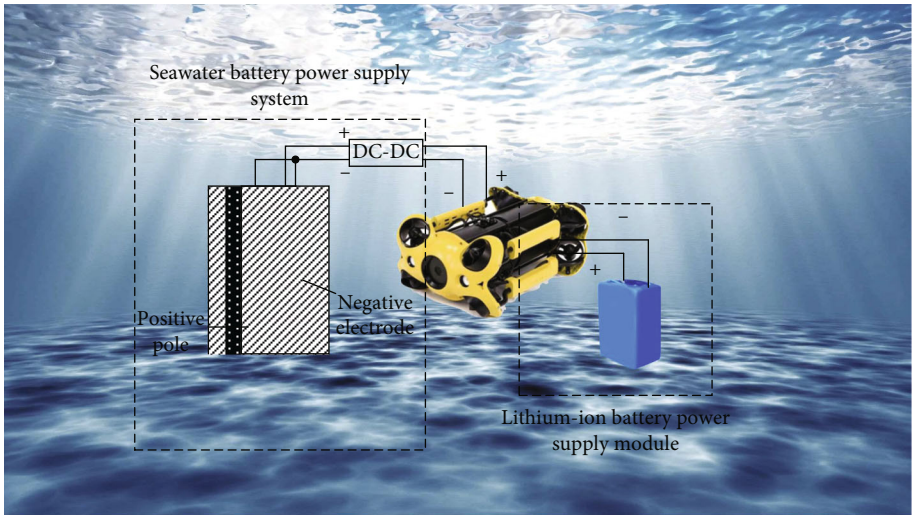

Figure 1: Energy supply system for autonomous underwater observation vehicles.

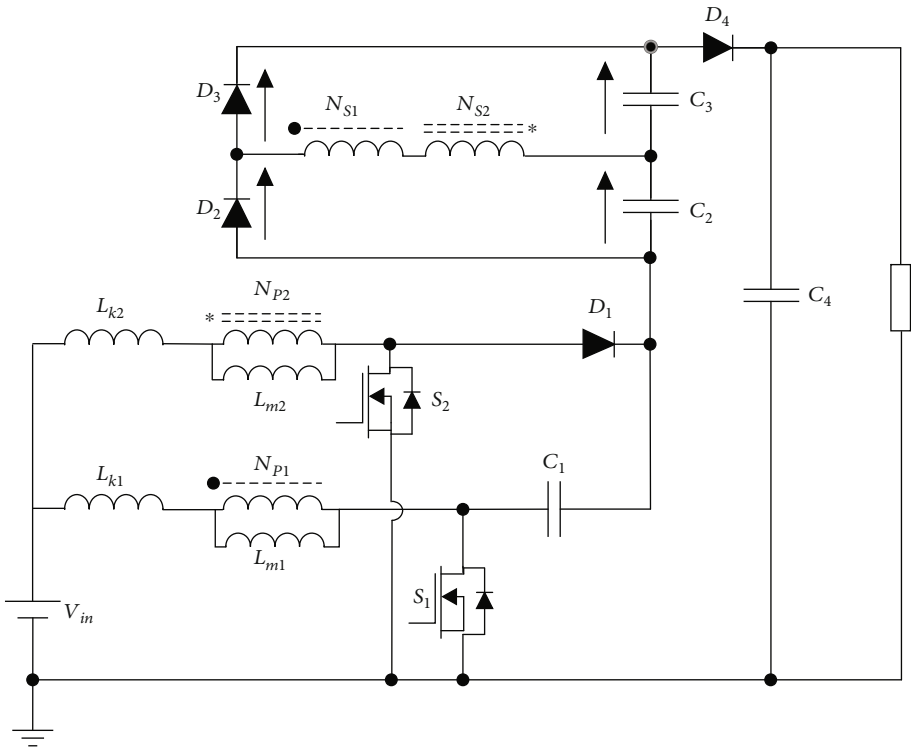

Figure 2: Equivalent topology of the proposed converter.

$$V_o = V_{C1} + V_{C2} + V_{C3} + \frac{V_{in}}{1-D}. \tag{9}$$

The voltage gain is expressed as

$$M_{CCM} = \frac{2 + k_1 N_1 + k_2 N_2}{1-D}. \tag{10}$$

In the actual coupling inductance design, because the coefficient of coupling is close to 1, it has little effect on the voltage gain. In order to facilitate the analysis, the leakage inductance is not considered in the following case, that is, $k_1 = k_2 = 1$. The ideal voltage gain is expressed as

$$M_{CCM} = \frac{2 + N_1 + N_2}{1-D}. \tag{11}$$

According to formula (11), the ideal voltage gain of the converter is related to turn ratio n and the duty ratio D. As shown in Figure 5, when D remains unchanged, the higher n , the higher the voltage gain of the converter.

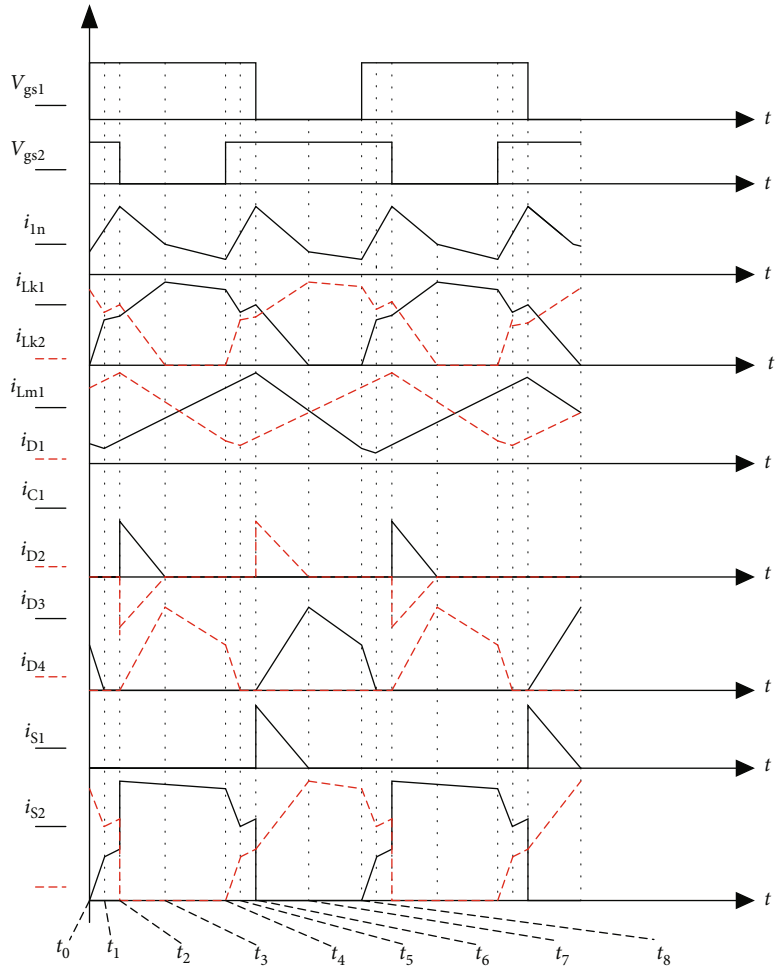

Figure 3: Key waveforms of the proposed converter.

The voltage stress pushed to S_1 and S_2 is expressed as

$$V_{S2} = V_{C1} = \frac{V_{in}}{1-D} = \frac{V_o}{2+N_1+N_2},$$
$$V_{S1} = \frac{V_{in}}{1-D} = \frac{V_o}{2+N_1+N_2}. \quad (12)$$

The voltage stress of the diode D_1 is expressed as

$$V_{D1} = V_o - V_{C2} - V_{C3} = \frac{2V_{in}}{1-D}. \quad (13)$$

The voltage stress of the diode D_4 is expressed as

$$V_{D4} = V_o - V_{C2} - V_{C3} - V_{C1} = \frac{V_{in}}{1-D}. \quad (14)$$

The voltage stress of the diodes D_2 and D_3 is expressed as

$$V_{D2} = V_{D3} = V_{C2} + V_{C3} = \frac{N_1+N_2}{1-D}V_{in}. \quad (15)$$

The ratio curve in Figure 6 is obtained using the ratio V_{stress}/V_o. It is not difficult to see that the voltage stress of all power devices is lower than output voltage. MOSFETs S_1 and S_2 and diodes D_1 and D_4 decrease with the increase of turn ratio n, and diodes D_2 and D_3 increase with it.

3.2. Comparison. The high-gain converter is proposed in this paper, fewer power devices are required, and their voltage stress is lower. To further reflect its advantage, the proposed converter is compared with many typical topologies in recent years. The performance parameters are shown in Table 1.

In order to compare the performance of converter, set the coupled inductor turn ratio $n = 3$. The voltage gain comparison curve between the proposed converter and the other four converters is shown in Figure 7, and the proposed converter has a highest voltage gain compared with other typical of boost converters.

The voltage stress comparison curve of the MOSFET is shown in Figure 8. The ratio curve is obtained using the ratio V_{stress}/V_o. Compared with other typical converters, the proposed converter has the lowest voltage stress, so MOSFET

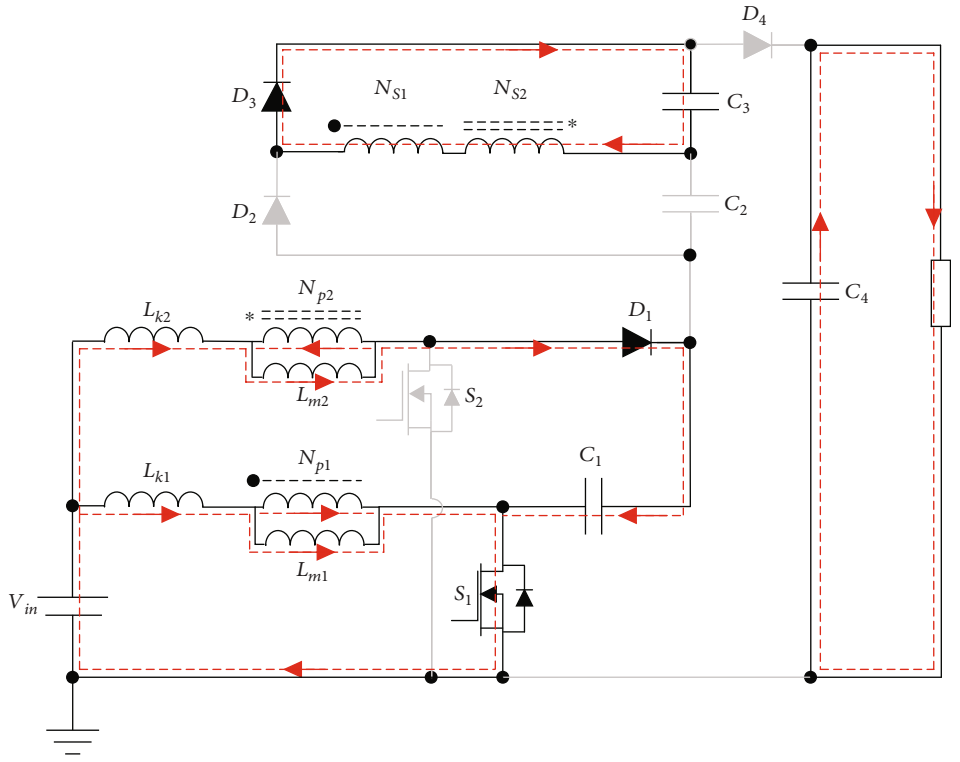

(a)

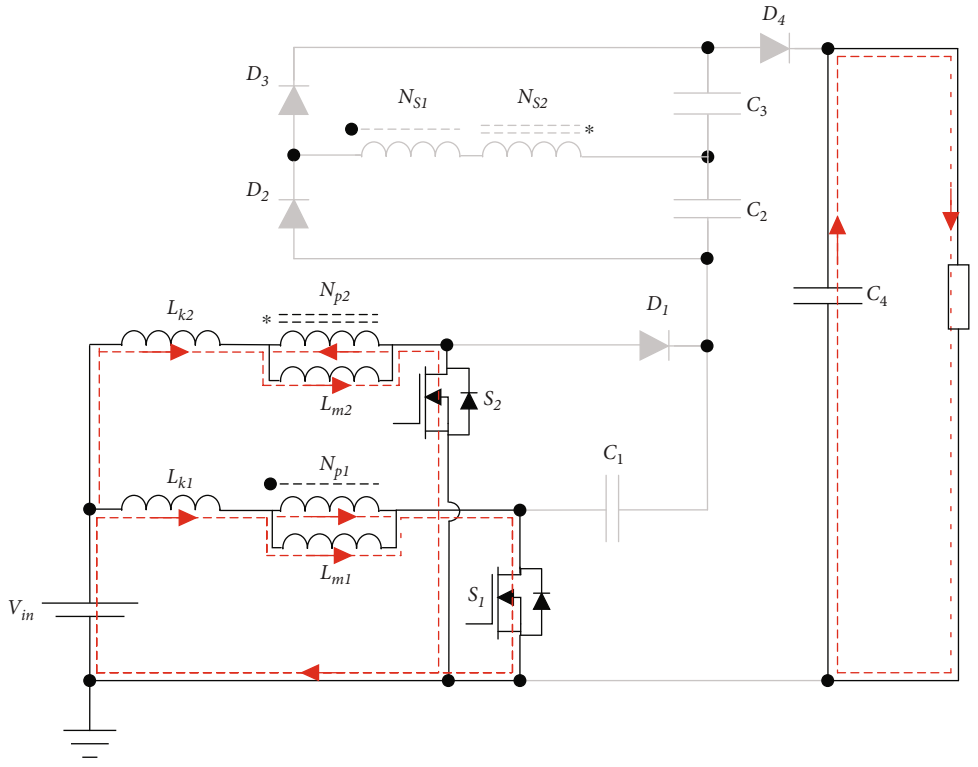

(b)

Figure 4: Continued.

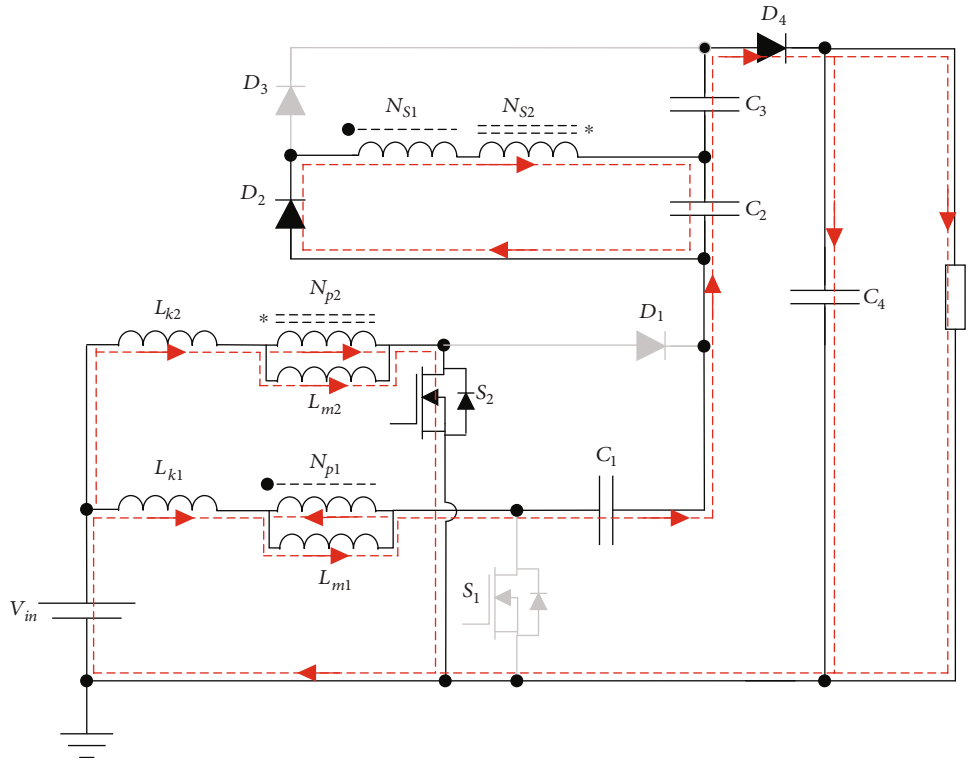

(c)

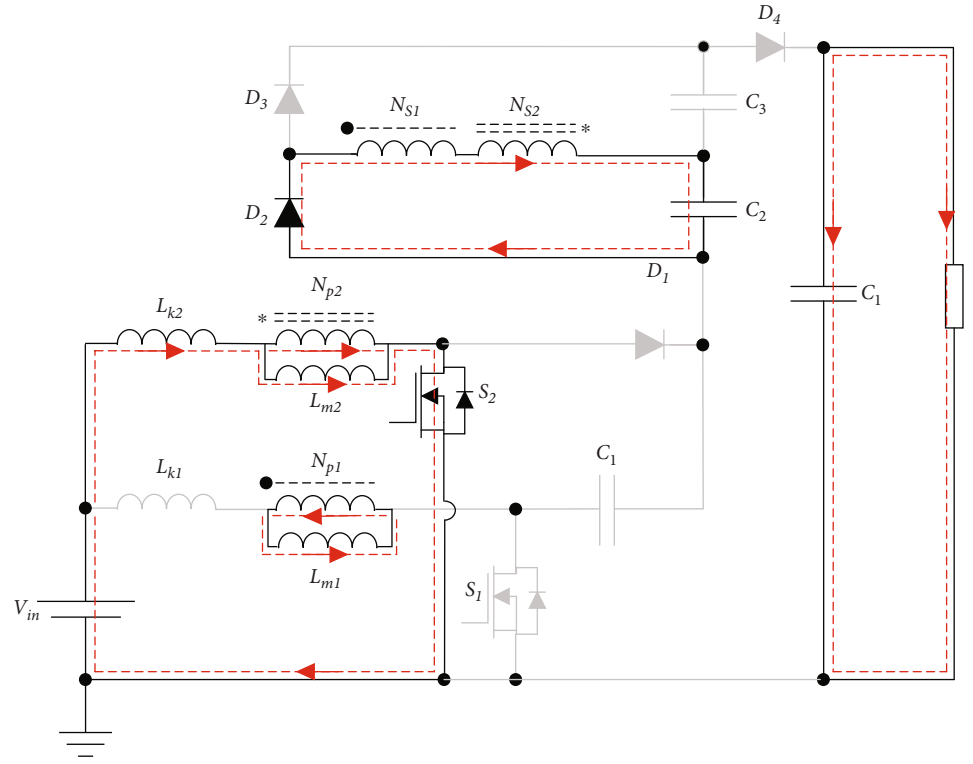

(d)

Figure 4: Operation modes of the proposed converter.

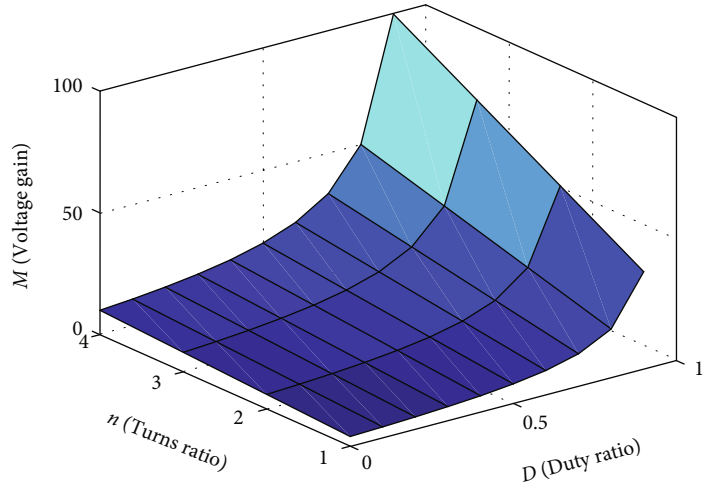

Figure 5: Voltage gain curve ($N_1 = N_2 = n$).

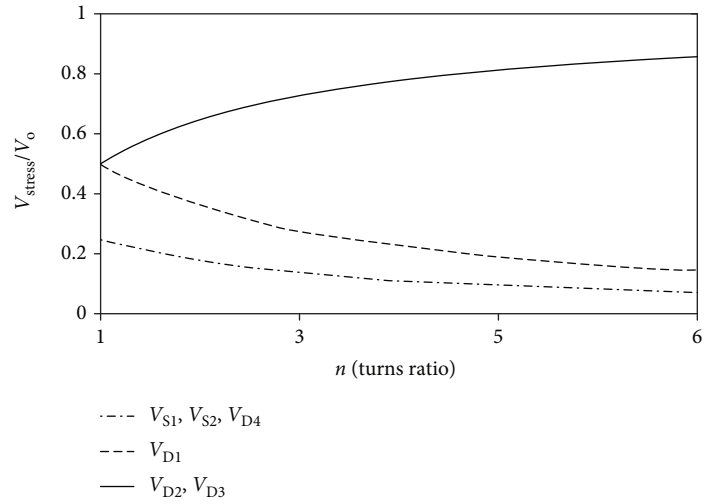

Figure 6: Normalized semiconductor voltage stress versus turn ratios.

Table 1: Comparison of the proposed converter to typical converters.

Topologies	No. of switches/diode/capacitors/inductance	Voltage gain	Switch voltage stress
Ref. [24]	1/5/4/2	$4/1 - D$	$V_o/2$
Ref. [27]	2/4/4/2	$4/1 - D$	$V_o/4$
Ref. [29]	4/6/6/1	$2n/1 - D$	$V_o/2n$
Ref. [30]	1/3/4/2	$n + 2/1 - D$	$V_o/n + 2$
Proposed	2/4/4/2	$2n + 2/1 - D$	$V_o/2n + 2$

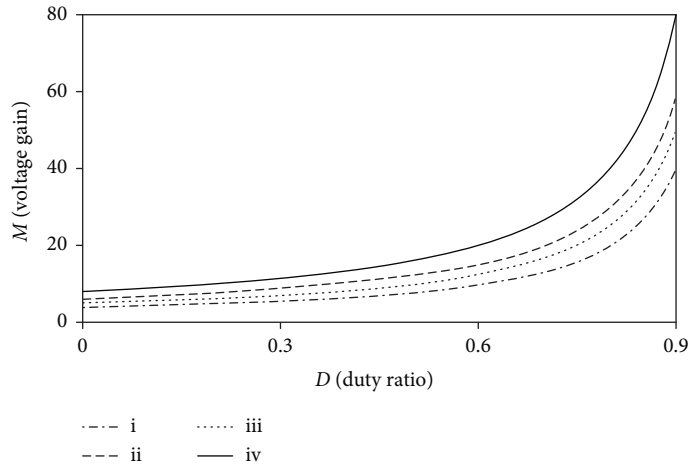

Figure 7: Comparison of the voltage gain when $n = 3$. (i) Converter in [24, 27]. (ii) Converter in [29]. (iii) Converter in [30]. (iv) Proposed converter.

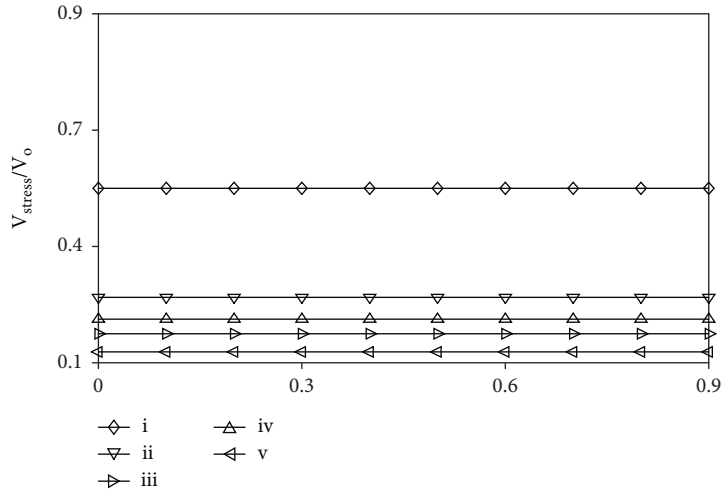

Figure 8: Voltage stress comparison of MOSFET. (i) Converter in [24]. (ii) Converter in [27]. (iii) Converter in [29]. (iv) Converter in [30]. (v) Proposed converter.

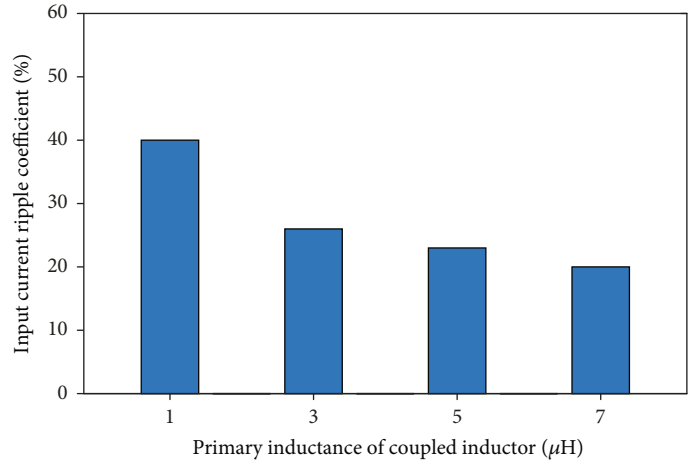

Figure 9: The relationship between the original inductor and current ripple.

Table 2: Comparison of capacitance theory and actual values.

Capacitor	C_1	C_2	C_3	C_4
Theoretical value (μF)	20	60	60	50
Experiment value (μF)	100	100	100	100
Theoretical pressure resistance (V)	6	17.6	17.6	24
Experimental pressure resistance (V)	50	50	50	50

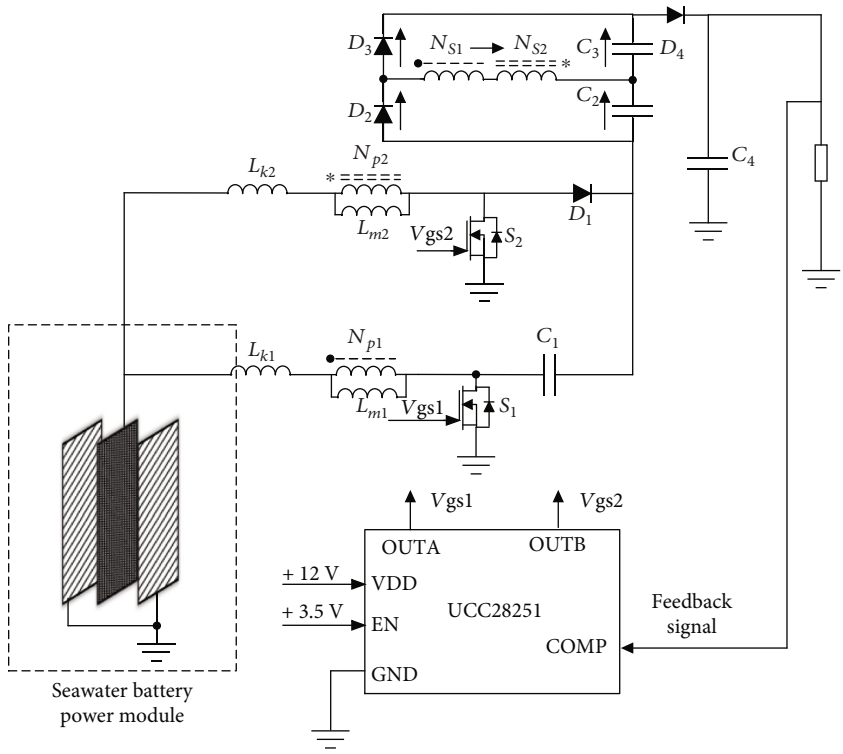

Figure 10: Control strategy for the seawater battery.

devices with lower voltage stress can be selected at work. Devices with low voltage stress will get smaller loss.

4. Design Considerations

4.1. Coupled Inductor Design. The turn ratio of the coupled inductor is determined by the voltage gain and the duty ratio, expressed as follows:

$$n = \frac{V_o(1-D)}{2V_{in}} - 1. \tag{16}$$

The value of magnetizing inductance depends on the acceptability of current ripple on the inductance. At the same time, due to the limitations of the characteristics of the seawater cell, the input current ripple large will lead to the unstable output voltage of the seawater cell. Therefore, the coupled inductor current ripple of the converter is set as $\alpha\%$. The value of magnetizing inductance is expressed as

$$L_m = L_{m1} = L_{m2} = \frac{V_{in}D}{\alpha\% I_{in} f_s} = \frac{D(1-D)V_o}{2\alpha\% I_{in} f_s}. \tag{17}$$

Magnetizing inductance has a great effect on suppressing current ripple, and the input current ripple coefficient under different magnetizing inductance can be obtained, as shown in Figure 9:

The current ripple of the coupled inductor will directly affect the stability of the system. Therefore, according to Figure 9, magnetizing inductance value of 7 μH can be selected to suppress the current ripple and improve the stability of the system.

4.2. Capacitor Design. The capacitance is designed based on the voltage ripple and the output power, and the voltage ripple coefficient is $\mu\%$. The value of C_1 to C_4 is expressed as follows:

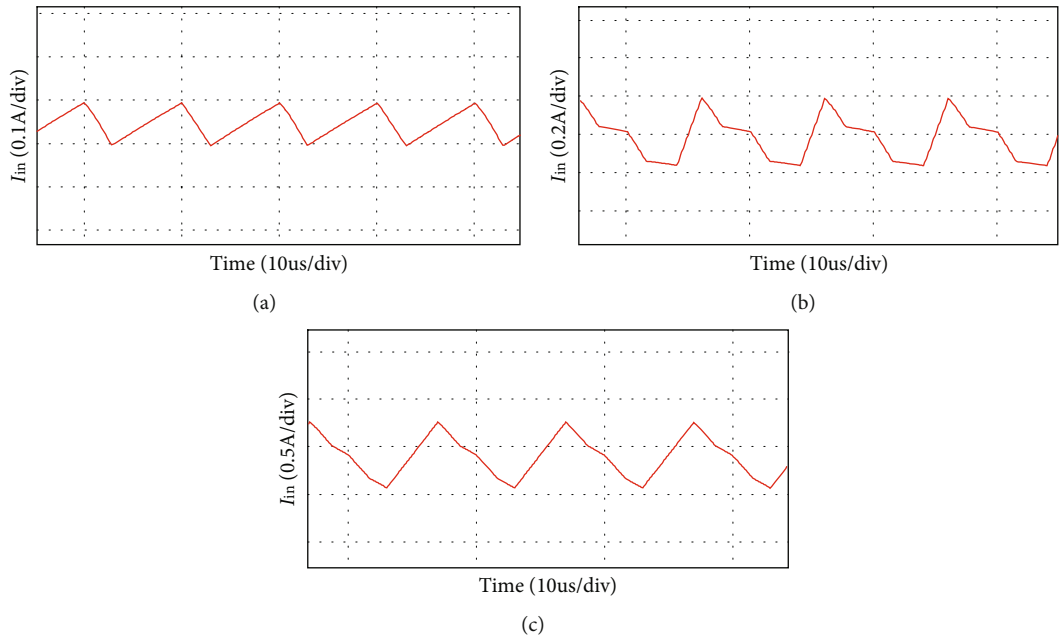

Figure 11: Input current ripple under different duty ratio and turn number ratio.

$$
\begin{aligned}
C_1 &\geq \frac{2P_o}{\mu\%V_{C1}V_o f_s} = \frac{2P_o(1-D)}{\mu\%V_{C1}f_s V_{in}(2n+2)},\\
C_2 &\geq \frac{P_o}{\mu\%V_{C2}V_o f_s} = \frac{P_o(1-D)}{\mu\%V_{C2}f_s V_{in}(2n+2)},\\
C_3 &\geq \frac{P_o}{\mu\%V_{C3}V_o f_s} = \frac{P_o(1-D)}{\mu\%V_{C3}f_s V_{in}(2n+2)},\\
C_4 &\geq \frac{P_o}{\mu\%V_{C4}V_o f_s} = \frac{P_o(1-D)}{\mu\%V_{C4}f_s V_{in}(2n+2)}.
\end{aligned}
\tag{18}
$$

According to the above calculation, based on the actual, the capacitance values of C_1 to C_4 can be the same; in order to make the supply system operate stably, considering the actual circuit parasitic elements, it is necessary to add a certain margin on the basis of theoretical calculation.

The theoretical values and the experiment values of each capacitance can be expressed in Table 2:

5. Simulation and Experimental Validation

The designed high-gain converter has a rated power of 10 W and a rated output voltage of 24 V. Seawater battery rated output voltage is 1.3 V. In order to verify the correctness of the above theoretical analysis, the system can be built as shown in Figure 10:

5.1. Effect of Simulation Parameters on Current Ripple. In order to further study the working characteristics of the converter, the optimal duty ratio and turn ratio are obtained by simulation. The input current ripple is related to duty ratio and turn ratio. When other device parameters are kept unchanged, the duty ratio of the converter and the turn ratio of the coupled inductor are changed, and the simulation results are shown in Figure 11.

Table 3: Input current ripple coefficient under different turn number ratio and duty cycle.

n (turn ratio)	D (duty ratio)	Current ripple coefficient
2	60%	5.3%
3	50%	1.8%
4	40%	12.3%

Table 4: Simulation parameters.

The proposed converter parameters	Value
V_{in} (V)	1.3
n (turn ratio)	$N_s/N_p = 1:3$
L_{m1}, L_{m2} (μH)	7
C_1, C_2, C_3, C_4 (μF)	100
f_s (KHz)	100
D (duty ratio cycle)	50%

(a) The current ripple is when $n = 3$, $D = 50\%$, the input current

(b) The current ripple is when $n = 2$, $D = 60\%$, the input current

(c) The current ripple is when $n = 4$, $D = 40\%$, the input current

According to formula (17), when the duty ratio increases, the output voltage is kept unchanged, and the current ripple will change with the duty ratio. Therefore, through simulation, the optimal combination of turn ratio and duty ratio in Table 3

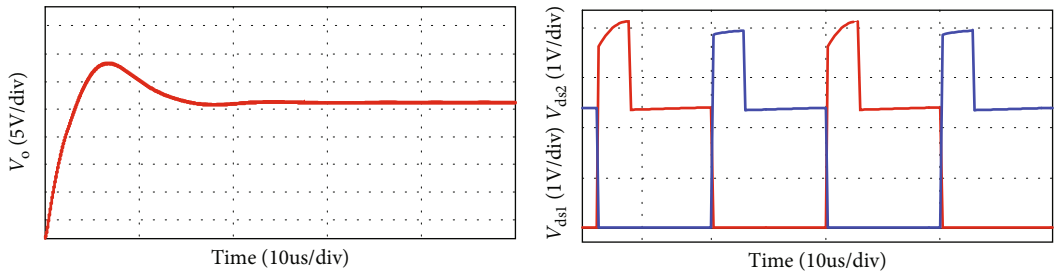

Figure 12: Voltage simulation waveform.

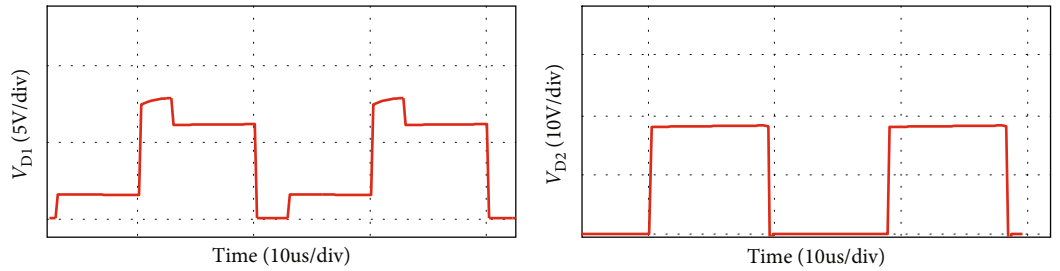

Figure 13: Diode D_1 (a) and D_2 (b) voltage waveform.

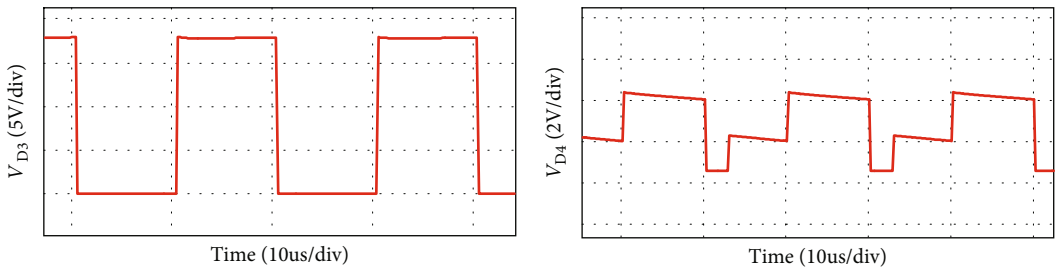

Figure 14: Diode D_3 (a) and D_4 (b) voltage waveform.

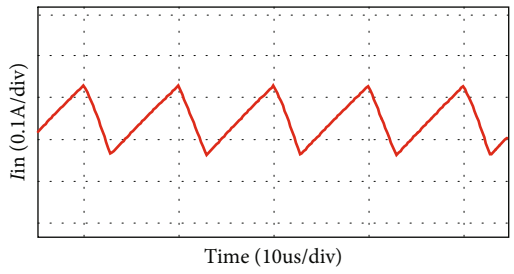

Figure 15: Input current ripple waveform.

Table 5: Simulation results under seawater battery output conditions.

V_{in} (V)	I_{in} (A)	Current ripple (A)	S_1, S_2 voltage stress (V)	Duty ratio (%)	V_{out} (V)
1.2	8.33	0.31	3.62	55	24
1.25	8.00	0.22	3.54	52	24
1.3	7.69	0.15	3.80	50	24
1.35	7.41	0.18	3.71	45	24
1.4	7.14	0.29	3.76	41	24

can be obtained. When the duty ratio is 50%, the current ripple is the lowest.

After simulation analysis and theoretical analysis, in order to minimize the input current ripple of the system, the coupled inductor turn ratio can be set at 1 : 3. The duty ratio is $D = 50\%$.

5.2. Simulation Verification. According to the theoretical calculation and the above simulation conclusions, the simulation parameters of Table 4 are set, and the model can be built. The simulation results are as follows.

The simulation waveform of output voltage and S_1, S_2 voltage is shown in Figure 12. The output voltage is 24 V,

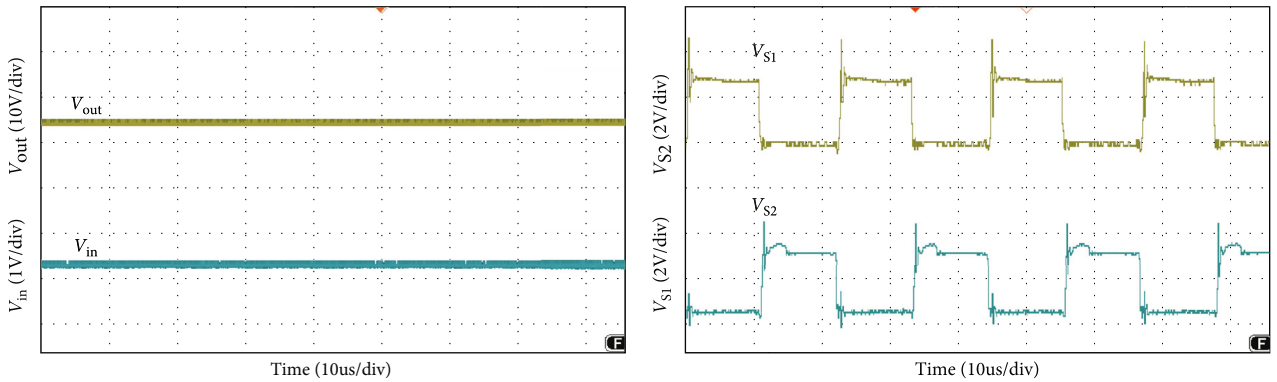

Figure 16: Stress wave form of input/output voltage and switches voltage.

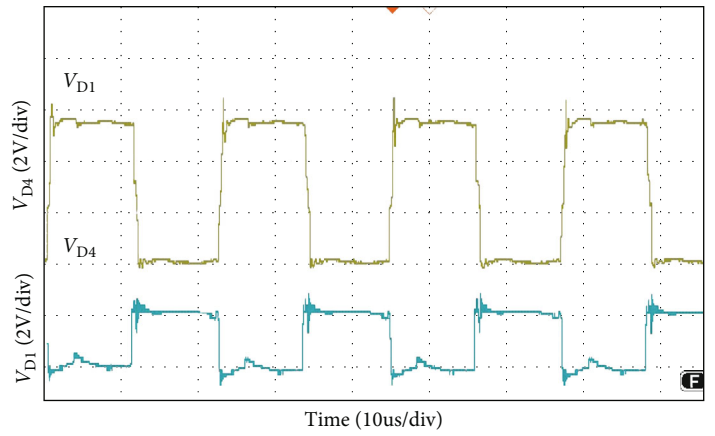

Figure 17: Diode voltage stress waveform.

as shown in Figure 12(a) and the voltage stress of switches S_1, S_2 is 3.8 V, as shown in Figure 12(b). Figures 13 and 14 show the diode voltage simulation waveform, diode D_1 voltage stress is 5.7 V, as shown in Figure 13(a). The voltage stress of diodes D_2 and D_3 is 17.8 V, and diode $D4$ voltage stress is 3.4 V. Current simulation waveform is shown in Figure 15 and the input current ripple value is 0.15 A.

In order to fully verify the performance of the power supply system of the seawater battery under the condition of the proposed converter, the output voltage range (1.2-1.4 V) of

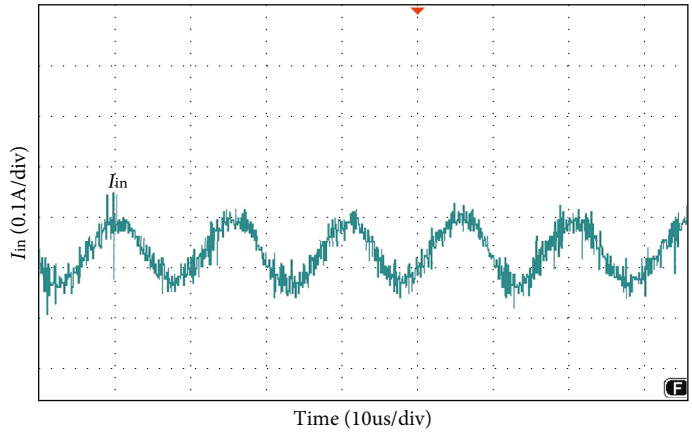

Figure 18: Input current ripple.

Table 6: Experimental results under seawater battery output conditions.

V_{in} (V)	I_{in} (A)	Current ripple (A)	S_1, S_2 voltage stress (V)	Duty ratio (%)	V_{out} (V)	Efficiency (%)
1.2	10.7	0.38	3.84	57	23.6	78.2
1.25	10.1	0.27	3.67	53	23.8	79.1
1.3	9.4	0.2	4.00	50	24.0	81.9
1.35	8.9	0.22	3.92	46	24.0	82.5
1.4	8.5	0.34	3.86	43	24.2	84.2

Table 7: Theoretical loss value.

Element	Coupled inductance	D_1	D_2	D_3	D_4	S_1, S_2
P_{loss} (W)	1.57	0.15	0.21	0.21	0.21	0.24

the seawater battery is simulated. The simulation results are shown in Table 5:

After simulation, it can be obtained that under the condition that the output voltage range (1.2-1.4 V) of the seawater battery, the input current ripple of the proposed converter is maintained at 0.15-0.29 A, the current ripple is generally low, the voltage stress of the switching device is maintained at 3.54-3.76 V, and the voltage stress is low and the fluctuation is small.

5.3. Experiment and Results Analysis. In order to further verify the correctness of theoretical analysis and simulation parameters, a prototype is built in the laboratory, and the experimental waveform is obtained and analyzed.

As shown in Figure 16(a), the load voltage of the converter is about 24 V, which achieves the high gain effect of theoretical analysis. The voltage stress of the MOSFETs S_1 and S_2 is about 4 V. Due to the influence of the parasitic capacitance in the MOSFET, the parasitic capacitance discharge generates the spike voltage shown in Figure 16(b). Because the diode retains a safety margin for the voltage during the selection process, it has little impact on the system. The voltage stress of each diode

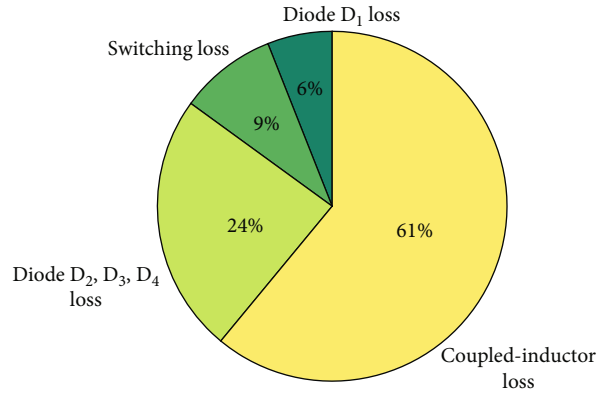

Figure 19: Loss distribution of the converter.

is shown in Figure 17, the voltage stress of the diode D_1 is about 6 V, D_4 is about 4 V, and D_3 is about 18 V compared to the actual voltage of the diode which is low compared to the theoretical analysis, but the voltage waveform meets the theoretical analysis and has good performance. Figure 18 is the input current ripple waveform of the converter. Due to the existence of parasitic inductance and parasitic resistance in the actual circuit, the current ripple is somewhat disturbed. It can be seen from the waveform that the current ripple is about 0.2 A, so the structure effectively reduces the input current ripple.

Other output voltage of seawater batteries is tested. Within the output voltage range of seawater batteries, the performance of the 1.2-1.4 V seawater battery power supply system is shown in Table 6.

Through the experimental results, it can be obtained that under the condition of the output voltage of the seawater battery, the current ripple range of the converter is 0.2-0.38 A, and the actual current ripple is close to the simulated current ripple. The influence of parasitic elements in the actual circuit is considered, and the range of current ripples is acceptable. The voltage stress of the switches is 3.67-4 V, compared with the simulation results, and the results are acceptable. The efficiency of the seawater battery power supply system has reached 78.2-84.2%.

5.4. Loss Analysis. The main loss in the converter comes from the heating of the power device, where the power device is the coupled inductor, diode, and MOSFET.

5.4.1. MOSFET Loss. The on-state loss of the MOSFET mainly comes from the on resistance $R_{d(on)}$ of the switches. The on-state loss is expressed as follows:

$$P_{loss(on)} = R_{d(on)} \times i_{ds}^2. \tag{19}$$

In formula (19), i_{ds} is the effective value of the current flowing through the DS of the MOSFET.

The shutdown loss of the MOSFETs is not only related to the frequency f_s but also related to the parasitic output capacitance C_{oss1}; the shutdown loss is expressed as follows:

$$P_{loss(off)} = \frac{i_{ds}^2 \times t_f^2 \times f_s}{48 \times C_{oss1}}. \tag{20}$$

The t_f is the fall time of the switches.

The switching status of the MOSFETs S_1 and S_2 is the same, and the total loss of the switches can be expressed as

$$P_S = 2(P_{loss-on} + P_{loss-off}). \tag{21}$$

5.4.2. Diode Loss. The loss on diode is the product of current i_F and the forward voltage drop V_F of diode. The loss of diode can be expressed as

$$P_D = f_s \times \int_0^{T_S/2} V_F \times i_F(t)dt. \tag{22}$$

5.4.3. Transformer Loss. Transformer loss is the main part of the magnetic component loss. It mainly includes core loss and winding loss, among which core loss includes hysteresis loss and eddy current loss.

The hysteresis loss is proportional to B and is expressed as follows:

$$P_h = K_h \times f_s \times B^{1.6} \times V. \tag{23}$$

K_h is the proportional coefficient related to the material.

The eddy current loss in dynamic alternating magnetic field is

$$P_c = \frac{\pi^2 f_s^2 B^2 d^2}{6\rho}. \tag{24}$$

In formula (24), d is the material density, measured in unit g/cm^3, and ρ is resistivity.

Core loss of the transformer may be expressed as

$$P_{core} = P_h + P_c. \tag{25}$$

Winding loss mainly comes from the copper loss of the primary winding and the secondary winding, which is expressed as P_{cu_p} and P_{cu_s}, including the alternating current winding R_{ac_p} and R_{ac_s}. The i_p, i_s is the current flowing through, and the losses of the primary side and secondary side winding are expressed as

$$\begin{aligned} P_{cu\_p} &= i_p^2 \times R_{ac\_p}, \\ P_{cu\_s} &= i_s^2 \times R_{ac\_s}. \end{aligned} \tag{26}$$

The winding loss of a transformer is the sum of the copper loss of the primary and secondary side transformers, which is expressed as follows:

$$P_{cu} = P_{cu\_p} + P_{cu_s}. \tag{27}$$

The total transformer loss can therefore be expressed as

$$P_T = 2(P_{cu} + P_{core}) \tag{28}$$

5.4.4. Converter Loss Distribution. In fact, there are some other losses in the converter, such as wire loss and delay loss, but these losses are often very small and negligible. After calculation, the loss of each power device is shown in Table 7.

The total power loss of the proposed converter can be expressed as

$$P_{loss} = P_S + P_D + P_T. \tag{29}$$

The loss of each power device is calculated according to the theory, and percentages are reflected in Figure 19. The proportion of transformer loss is the largest. According to the loss analysis, winding loss (P_{cu}) is considered to be the main loss of the transformer, which is caused by the low rated power of the converter and the high carry currents of the transformer.

Under the rated state of the converter, the ideal conversion efficiency of the proposed converter can be calculated from (29), with a result of 83.1%, and the difference is 1.9% compared with the actual conversion efficiency. Due to the existence of parasitic resistance in the line and the existence of the parasitic capacitance and the parasitic diode in the switching, it has a certain impact on the efficiency of the converter, but the impact is small, and the actual value is close to the theoretical value.

6. Conclusions

In this paper, the DC/DC converter in the energy supply system of the autonomous underwater observation vehicles is taken as the research object, exploring the improvement of output voltage level of seawater batteries, through DC/DC converters, to supply power in the underwater observation vehicle. The topology of the proposed converter is studied and verified by simulation and experiment. The main conclusions are as follows:

(1) Under the range of output voltage 1.2-1.4 V of dissolved oxygen seawater battery, DC/DC converters can improve the voltage level. Under the premise of maintaining the output voltage of 24 V, the efficiency reaches 78-84%

(2) Under the asymmetric interleaved parallel structure, combined with the coupled inductor and clamping circuit, not only the input current ripple is suppressed, but also the voltage stress of the MOSFETs is controlled by about 4 V

(3) In the study of improving the voltage level, the combination of coupled inductors and switched capacitance in the topology can enable the converter to obtain higher voltage gain under low duty cycle

7. Future Work

Based on the current theoretical calculation and experimental results, an experimental platform for mixed power supply of seawater batteries and lithium batteries will be built. Due to the large loss of transformers in the proposed converter, it will be further optimized to improve the efficiency of the seawater battery power supply system. Further verify the correctness of the proposed system.

Data Availability

The data underlying the results presented in the study are available within the manuscript.

Conflicts of Interest

The authors declare that they have no conflicts of interest.

References

[1] T. Matsuda, "Low-cost high-performance seafloor surveying by multiple autonomous underwater vehicles," *Applied Ocean Research*, vol. 11, no. 7, p. 102762, 2021.

[2] J. A. Howe, K. Husum, M. E. Inall et al., "Autonomous underwater vehicle (AUV) observations of recent tidewater glacier retreat, western Svalbard," *Marine Geology*, vol. 417, p. 106009, 2019.

[3] K. Duan, S. Fong, and C. L. P. Chen, "Reinforcement learning based model-free optimized trajectory tracking strategy design for an AUV," *Neurocomputing*, vol. 469, pp. 289–297, 2022.

[4] B. Chen, J. Hu, Y. Zhao, and B. K. Ghosh, "Finite-time observer based tracking control of uncertain heterogeneous underwater vehicles using adaptive sliding mode approach," *Neuro computing*, vol. 481, pp. 322–332, 2022.

[5] Y. Sun, Y. Du, and H. Qin, "Distributed adaptive neural network constraint containment control for the benthic autonomous underwater vehicles," *Neuro computing*, vol. 484, pp. 89–98, 2022.

[6] A. Chiche, G. Lindbergh, I. Stenius, and C. Lagergren, "A strategy for sizing and optimizing the energy system on long-range AUVs," *IEEE Journal of Oceanic Engineering*, vol. 46, no. 4, pp. 1132–1143, 2021.

[7] Y. Wang, X. Zhang, and Z. Chen, "Low temperature preheating techniques for Lithium-ion batteries: recent advances and future challenges," *Applied Energy*, vol. 313, p. 118832, 2022.

[8] Y.-F. Wang and J.-T. Wu, "Performance improvement of thermal management system of lithium-ion battery module on purely electric AUVs," *Applied Thermal Engineering*, vol. 146, pp. 74–84, 2019.

[9] Z. Mao and S. Yan, "Design and analysis of the thermal-stress coupled topology optimization of the battery rack in an AUV," *Ocean Engineering*, vol. 148, pp. 401–411, 2018.

[10] C. Deutsch, A. Chiche, S. Bhat, C. Lagergren, G. Lindbergh, and J. Kuttenkeuler, "Evaluation of energy management strategies for fuel cell/battery-powered underwater vehicles against field trial data," *Energy Conversion and Management: X*, vol. 14, p. 100193, 2022.

[11] W. D. Toh, B. Xu, J. Jia, C. S. Chin, J. Chiew, and Z. Gao, "Lithium iron phosphate (LiFePO4) battery power system for deep-water emergency operation," *Energy Procedia*, vol. 143, pp. 348–353, 2017.

[12] H. Weydahl, M. Gilljam, T. Lian, T. C. Johannessen, S. I. Holm, and J. Ø. Hasvold, "Fuel cell systems for long-endurance autonomous underwater vehicles - challenges and benefits," *International Journal of Hydrogen Energy*, vol. 45, no. 8, pp. 5543–5553, 2020.

[13] M. Yuan, Y. Li, Y. Li, S. Pang, and J. Zhang, "A fast way of single-beacon localization for AUVs," *Applied Ocean research*, vol. 119, p. 103037, 2022.

[14] F. Hu, Y. Huang, Z. Xie, J. Yu, Z. Wang, and J. Qiao, "Conceptual design of a long-range autonomous underwater vehicle based on multidisciplinary optimization framework," *Ocean Engineering*, vol. 248, p. 110684, 2022.

[15] S. McPhail, "Autosub6000: a deep diving long range AUV," *Journal of Bionic Engineering*, vol. 6, no. 1, pp. 55–62, 2009.

[16] J. Yu, B.-Q. Li, C.-X. Zhao, and Q. Zhang, "Seawater electrolyte-based metal–air batteries: from strategies to applications," *Energy & Environmental Science*, vol. 13, no. 10, p. 3253, 2020.

[17] R. Schmuch, R. Wagner, G. Hörpel, T. Placke, and M. Winter, "Performance and cost of materials for lithium-based rechargeable automotive batteries," *Nature Energy*, vol. 3, no. 4, p. 267, 2018.

[18] Ø. Hasvold, T. Lian, E. Haakaas, N. Størkersen, O. Perelman, and S. Cordier, "CLIPPER: a long-range, autonomous underwater vehicle using magnesium fuel and oxygen from the sea," *Journal of Power Sources*, vol. 136, no. 2, pp. 232–239, 2004.

[19] T. Zheng, Y. Hu, Y. Zhang, S. Yang, and F. Pan, "Composition optimization and electrochemical properties of Mg-Al-Sn-Mn alloy anode for Mg-air batteries," *Materials & Design*, vol. 137, pp. 245–255, 2018.

[20] J. Yu, C.-X. Zhao, J.-N. Liu, B. Q. Li, C. Tang, and Q. Zhang, "Seawater-based electrolyte for zinc-air batteries," *Green Chemical Engineering*, vol. 1, no. 2, p. 117, 2020.

[21] Ø. Hasvold, H. Henriksen, E. Melv et al., "Sea-water battery for subsea control systems," *Journal of Power Sources*, vol. 65, no. 1–2, pp. 253–261, 1997.

[22] M. Shinohara, E. Araki, M. Mochizuki, T. K. Zawa, and K. Suyehiro, "Practical application of a sea-water battery in deep-sea basin and its performance," *Journal of Power Sources*, vol. 187, no. 1, pp. 253–260, 2009.

[23] P. K. Shen, A. C. C. Tseung, and C. Kuo, "Development of an aluminium/sea water battery for sub-sea applications," *Journal of Power Sources*, vol. 47, no. 1–2, pp. 119–127, 1994.

[24] N. Tewari and V. T. Sreedevi, "A novel single switch dc-dc converter with high voltage gain capability for solar PV based power generation systems," *Solar Energy*, vol. 171, pp. 466–477, 2018.

[25] T. Yao, C. Nan, and R. Ayyanar, "A new soft-switching topology for switched inductor high gain boost," *IEEE Transactions on Industry Applications*, vol. 54, no. 3, pp. 2449–2458, 2018.

[26] T. Jalilzadeh, N. Rostami, E. Babaei, and M. Maalandish, "Ultra-step-up dc–dc converter with low-voltage stress on devices," *IET Power Electronics*, vol. 12, no. 3, pp. 345–357, 2019.

[27] C. Pan, C. Chuang, and C. Chu, "A novel transformer-less adaptable voltage quadrupler DC converter with low switch voltage stress," *IEEE Transactions on Power Electronics*, vol. 29, no. 9, pp. 4787–4796, 2014.

[28] L. Zhou, S. Chen, Q. Luo, and B. Zhu, "Interleaved non-isolated high step-up DC/DC converter based on the diode-capacitor multiplier," *IET Power Electronics*, vol. 7, no. 2, pp. 390–397, 2014.

[29] C.-M. Young, M.-H. Chen, T. A. Chang, C. C. Ko, and K. K. Jen, "Cascade Cockcroft–Walton voltage multiplier applied to transformerless high step-up DC–DC converter," *IEEE Transactions on Industrial Electronics*, vol. 60, no. 2, pp. 523–537, 2013.

[30] H. Ardi, A. Ajami, and M. Sabahi, "A novel high step-up DC–DC converter with continuous input current integrating coupled inductor for renewable energy applications," *IEEE Transactions on Industrial Electronics*, vol. 65, no. 2, pp. 1306–1315, 2018.

[31] M. Forouzesh, K. Yari, A. Baghramian, and S. Hasanpour, "Single-switch high step-up converter based on coupled inductor and switched capacitor techniques with quasi-resonant operation," *IET Power Electronics*, vol. 10, no. 2, pp. 240–250, 2017.

Hindawi
Applied Bionics and Biomechanics
Volume 2022, Article ID 2073067, 17 pages
https://doi.org/10.1155/2022/2073067

Research Article

Classical and Bayesian Inference Using Type-II Unified Progressive Hybrid Censored Samples for Pareto Model

M. Nagy and Adel Fahad Alrasheedi

Department of Statistics and Operations Research, College of Science, King Saud University, P.O. Box 2455, Riyadh 11451, Saudi Arabia

Correspondence should be addressed to M. Nagy; mnaji@ksu.edu.sa

Received 15 January 2022; Revised 17 February 2022; Accepted 8 March 2022; Published 29 April 2022

Academic Editor: Muye Pang

In the lifetime and reliability experiments, the censored samples play a fundamental and important role in order to control time and cost. The researchers developed the censored sample schemes to solve the problems that arise by applying the previous methods. Recently, Górny and Cramer (2018) proposed a new general type of censored sample called Type-II unified progressive hybrid censored sample. In this paper, we present an overview of the Type-II unified progressive hybrid censored sample. We used this censored sample to compute the maximum likelihood estimates of unknown parameters from the Pareto distribution, as well as Bayesian estimates for unknown parameters under three different error loss functions. The point and interval Bayesian predictions one- and two-sample Bayesian predictions from the Pareto distribution are shown. Simulation studies are carried out to compare the efficacy of the various inference approaches. Finally, real data sets are examined to determine the applicability of the proposed model and various estimating approaches.

1. Introduction

In order to time and expense constraints, experiments in reliability analysis frequently end before all units in the test have failed. In such circumstances, failure information is only accessible for a portion of the sample, and only limited information is given on all units that have not failed. Data that has been censored is referred to as censored data. There are several different censoring schemes such as Type-I and Type-II. Since Epstein [1] presented Type-I hybrid censoring, various hybrid censoring modifications have been developed to address the model's flaws. Due to the fact that Type-I hybrid censoring does not guarantee the observation of at least one of the failures, Childs et al. [2] developed Type-II hybrid censoring, which ensures the observation of at least m failures from the n units put on the life test. However, the main disadvantage of this censoring system is that the experimenter has not controlled the test time. The disadvantages of both Type-I and Type-II hybrid censoring are mitigated by Chandrasekar et al. [3]. In addition, the unified hybrid censoring methods are even more flexible than hybrid censoring techniques (see, e.g., Balakrishnan et al. [4]; Huang and Yang [5]; Park and Balakrishnan [6]). In unified hybrid censoring method, consider, n identical units are placed on a life-testing device. Fix the integers k, $m \in \{1, 2, \cdots, n\}$, and T_1 and $T_2 \in (0, \infty)$ such that $k < m$ and $T_1 < T_2$. The experiment is stopped at min $(\max(T_1, Y_{m:n}), T_2)$ if the k^{th} failure occurs before time T_1. Otherwise, the experiment is stopped at min $(\max(Y_{k:n}, T_2), Y_{m:n})$%. We can guarantee that the experiment will be completed at most in time T_2 with at least k failures, and if not, we can guarantee exactly k failures under this censoring strategy.

If one of these units is inadvertently broken but the experiment has not yet been terminated, this unit must be removed from the life test, and the progressive censoring methodology is the best method for this case. Complete failures of m units will be observed in Type-II progressive censoring methods. When the first failure occurs, R_1 of the $n - 1$ remaining units is chosen at random and removed from the lifetime test. R_2 of the $n - R_1 - 2$ surviving units is randomly

selected and eliminated at the second observed failure. Finally, R_m surviving units are removed after the m^{th} failure, and the experiment comes to an end. We will denote the m ordered failure times thus observed by $Y_{1:m:n}, \cdots, Y_{m:m:n}$. It is evident that $n = m + \sum_{k=1}^{m} R_k$.

The downsides of the Type-II progressive censoring system are that if the units are highly reliable, the experiment can take a long time. Therefore, Kundu and Joarder [7] and Childs et al. [8] proposed a progressive hybrid censoring scheme (PHCS) in which the life-testing experiment is ended at time $\min\{Y_{m:m:n}, T\}$, with $T \in (0,\infty)$. For more details, we refer our readers to Tomer and Panwar [9], Panahi [10], Almarashi et al. [11], and Moihe El-Din et al. [12, 13]. On the other hand, the disadvantage of the PHCS is that it cannot be applied when only a few failures are likely to occur before time T. For this reason, Cho et al. [14] proposed a Type-I generalized PHCS in which the life-testing experiment is terminated at the time $\min\{\max(T, Y_{k:m:n}), Y_{m:m:n}\}$ for prefixed $k < m\{1, 2, \cdots, n\}$. Moreover, Lee et al. [15] proposed Type-II generalized PHCS, in which the life-testing experiment is terminated at time $\min\{\max(T_1, Y_{m:m:n}), T_2\}$ for prefixed $T_1 < T_2(0, \infty)$. For recent work on this topic, see, for example, Moihe El-Din and Nagy [16], Nagy et al. [17, 18], and Nagy and Alrasheedi [19].

While generalized PHCS are superior to Type-I and Type-II PHSC, they do have significant disadvantages. Therefore, Górny and Cramer [20] developed a general type of generalized PHCS, called Type-II unified PHCS to address some of the shortcomings of these schemes. Under Type-II unified PHCS, we can guarantee that the lifetime experiment will be completed at no later than T_2 with at least k number of unit failures; this ensures that the statistical inference is carried out with more efficiency. For recent work on the Type-II unified PHCS, see, for example, Górny and Cramer in [21] and Kim and Lee in [22].

The following is how the rest of the article is structured: Section 2 provides an overview of the Type-II unified PHCS. Section 3 determines the maximum likelihood estimates (ML) of unknown parameters, while Section 4 derives the Bayesian estimates for the unknown parameters with three loss functions. Sections 5 and 6 calculate the point and interval Bayesian predictions for one- and two-sample Bayesian predictions, respectively. Simulation studies are carried out in Section 7 to compare the efficacy of the offered inference methodologies. A real data is utilized to demonstrate the theoretical findings in Section 8. Finally, the paper is concluded in Section 9.

2. The Type-II Unified PHCS and Likelihood Function

Consider a life test in which n identical items are put on test. Then, the Type-II unified PHCS may be described as follows. Let $T_1, T_2 \in (0,\infty)$ and integer $k, m \in \{1, 2, \cdots, n\}$ are prefixed such that $T_1 < T_2$ and $k < m$ with $R = (R_1, R_2, \cdots, R_m)$ is also prefixed integers satisfying $n = m + R_1 + \cdots + R_m$. At the time of first failure, R_1 of the remaining units are randomly removed. Similarly, at the time of the second failure R_2, of the remaining units are removed and so on. If the k^{th} failure occurs before time T_1, the experiment is terminated at $\min\{\max(Y_{m:m:n}, T_1), T_2\}$. If the k^{th} failure occurs between T_1 and T_2, the experiment is terminated at $\min(Y_{rm:m:n}, T_2)$ and if the k^{th} failure occurs after time T_2, the experiment is terminated at $Y_{k:n}$. Under this censoring scheme, we can guarantee that the experiment would be completed at most in time T_2 with at least k failure and if not, we can guarantee exactly k failures. Let D_1 and D_2 denote the numbers of observed failures up to time T_1 and T_2, respectively. In addition, d_1 and d_2 are the observed values of D_1 and D_2, respectively.

Under the UPHCS described above, we have one of the following types of observations:

(1) If the k^{th} failure occurs before time T_1, the experiment is terminated at $\min\{\max(Y_{m:m:n}, T_1), T_2\}$ and then we have the following three subcases:

(a) If the m^{th} failure occurs before T_1, i.e., $0 < Y_{k:m:n} < Y_{m:m:n} < T_1 < T_2$, then instead of terminating the test by withdrawing the remaining R_m items after the m^{th} failure, we continue to observe failures (without any further withdrawals) up to the experiment end at time $T^* = T_1$. Therefore, the observed failure times are $\{Y_{1:m:n} < \cdots < Y_{k:m:n} < \cdots < Y_{m:m:n} < \cdots < Y_{d_1:n}\}$

(b) If the m^{th} failure occurs between T_1 and T_2, i.e., $0 < Y_{k:m:n} < T_1 < Y_{m:m:n} < T_2$, then the experiment will end at $T^* = Y_{m:m:n}$ and the observed failure times are $\{Y_{1:m:n} < \cdots < Y_{k:m:n} < \cdots < Y_{d_1:m:n} < \cdots < Y_{m:m:n}\}$

(c) If the m^{th} failure occurs after T_2, i.e., $0 < Y_{k:m:n} < T_1 < T_2 < Y_{m:m:n}$, then the experiment will end at $T^* = T_2$ and the observed failure times are $\{Y_{1:m:n} < \cdots < Y_{k:m:n} < \cdots < Y_{d_1:m:n} < \cdots < Y_{d_2:m:n}\}$

(2) If the time T_1 pass before the k^{th}, then the experiment will end at $\min\{\max(Y_{k:m:n}, T_2), Y_{m:m:n}\}$ and then we have the following three subcases:

(a) If T_2 passes before the k^{th} failure occurs, i.e., $0 < T_1 < T_2 < Y_{k:m:n} < Y_{m:m:n}$, then the experiment will end at $T^* = Y_{k:m:n}$ and we will observe $\{Y_{1:m:n} < \cdots < Y_{d_1:m:n} < \cdots < Y_{d_2:m:n} < \cdots < Y_{k:m:n}\}$

(b) If the m^{th} failure occurs before T_2, i.e., $0 < T_1 < Y_{k:m:n} < Y_{m:m:n} < T_2$, then the experiment will end at $T^* = Y_{m:m:n}$ and we will observe $\{Y_{1:m:n} < \cdots < Y_{d_1:m:n} < \cdots < Y_{k:m:n} < \cdots < Y_{m:m:n}\}$

(c) If the time T_2 between $Y_{k:m:n}$ and $Y_{m:m:n}$, i.e., $0 < T_1 < Y_{k:m:n} < T_2 < Y_{m:m:n}$, then the experiment will end at $T^* = T_2$ and the observed failure times are $\{Y_{1:m:n} < \cdots < Y_{d_1:m:n} < \cdots < Y_{k:m:n} < \cdots < Y_{d_2:m:n}\}$

Let $\underline{\mathbf{Y}}$ be the Type-II unified progressive hybrid censored sample from distribution with the probability density function (PDF) $g(y)$, and the cumulative distribution function (CDF) $G(y)$, then, based on the Type-II unified PHCS, the likelihood function is given by

$$L_{\underline{\mathbf{Y}}}(\underline{\mathbf{Y}}) = \begin{cases} \left[\prod_{i=1}^{d_1}\sum_{j=1}^{m}(\tilde{R}_j+1)\right]\prod_{i=1}^{d_1} g(y_{i:m:n})\left[\bar{G}(y_{i:m:n})\right]^{\tilde{R}_i}\left[\bar{G}(T_1)\right]^{\tilde{R}_{t_1}} & \text{in Case } 1_a, \\ \left[\prod_{i=1}^{m}\sum_{j=1}^{m}(\tilde{R}_j+1)\right]\prod_{i=1}^{m} g(y_{i:m:n})\left[\bar{G}(y_{i:m:n})\right]^{\tilde{R}_i} & \text{in Case } 1_b, \\ \left[\prod_{i=1}^{d_2}\sum_{j=1}^{m}(\tilde{R}_j+1)\right]\prod_{i=1}^{d_2} g(y_{i:m:n})\left[\bar{G}(y_{i:m:n})\right]^{\tilde{R}_i}\left[\bar{G}(T_2)\right]^{\tilde{R}_{t_2}} & \text{in Case } 1_c, \\ \left[\prod_{i=1}^{k}\sum_{j=1}^{m}(\tilde{R}_j+1)\right]\prod_{i=1}^{k} g(y_{i:m:n})\left[\bar{G}(y_{i:m:n})\right]^{\tilde{R}_i} & \text{in Case } 2_a, \\ \left[\prod_{i=1}^{m}\sum_{j=1}^{m}(\tilde{R}_j+1)\right]\prod_{i=1}^{m} g(y_{i:m:n})\left[\bar{G}(y_{i:m:n})\right]^{\tilde{R}_i} & \text{in Case } 2_b, \\ \left[\prod_{i=1}^{d_2}\sum_{j=1}^{m}(\tilde{R}_j+1)\right]\prod_{i=1}^{d_2} g(y_{i:m:n})\left[\bar{G}(y_{i:m:n})\right]^{\tilde{R}_i}\left[\bar{G}(T_2)\right]^{\tilde{R}_{t_2}} & \text{in Case } 2_c, \end{cases} \tag{1}$$

Therefore, these cases can be combined and obtained as

$$L(\theta \mid \underline{\mathbf{Y}})\left[\prod_{i=1}^{d^*}\sum_{j=1}^{m}(\tilde{R}_j+1)\right]\prod_{i=1}^{d^*} g(y_{i:m:n})\left[\bar{G}(y_{i:m:n})\right]^{\tilde{R}_i}\left[\bar{G}(T_1)\right]^{\tilde{R}_{t_1}}\left[\bar{G}(T_2)\right]^{\tilde{R}_{t_2}}, \tag{2}$$

where $\bar{G} = 1 - G$ and

$$\underline{\mathbf{Y}} = \begin{cases} (y_{1:m:n}, \cdots, y_{k:m:n}, \cdots, y_{m-1:m:n}, y_{m:m:n}, \cdots, y_{d1:n}) & \text{in Case } 1_a, \\ (y_{1:m:n}, \cdots, y_{k:m:n}, \cdots, y_{d1:m:n}, \cdots, y_{m:m:n}) & \text{in Case } 1_b, \\ (y_{1:m:n}, \cdots, y_{k:m:n}, \cdots, y_{d1:m:n}, \cdots, y_{d2:m:n}) & \text{in Cases } 1_c, \\ (y_{1:m:n}, \cdots, y_{d1:m:n}, \cdots, y_{d2:m:n}, \cdots, y_{k:m:n}) & \text{in Case } 2_a, \\ \left(y_{1:m:n}, \cdots, y_{d_1}, \cdots, y_{k:m:n}, \cdots, y_{m:m:n}\right) & \text{in Case } 2_b, \\ (y_{1:m:n}, \cdots, y_{d1:m:n}, \cdots, y_{k:m:n}, \cdots, y_{d2:m:n}) & \text{in Cases } 2_c, \end{cases}$$

$$d^* = \begin{cases} d_1 & \text{in Case } 1_a, \\ m & \text{in Cases } 1_b \text{ and } 2_b, \\ d_2 & \text{in Cases } 1_c \text{ and } 2_c, \\ k & \text{in Case } 2_a, \end{cases}$$

$$\tilde{R} = \begin{cases} \left(R_1, \cdots, R_k, \cdots, R_{m-1}, 0, \cdots, 0, R_{t_1}\right) & \text{in Case } 1_a, \\ \left(R_1, \cdots, R_k, \cdots, R_{d_1}, \cdots, R_m\right) & \text{in Case } 1_b, \\ \left(R_1, \cdots, R_k, \cdots, R_{d_1}, \cdots, R_{t_2}\right) & \text{in Cases } 1_c, \\ \left(R_1, \cdots, R_{d_1}, \cdots, R_{d_2}, \cdots, R_{k^*}\right) & \text{in Case } 2_a, \\ \left(R_1, \cdots, R_{d_1}, \cdots, R_k, \cdots, R_m\right) & \text{in Case } 2_b, \\ \left(R_1, \cdots, R_{d_1}, \cdots, R_k, \cdots, R_{t_2}\right) & \text{in Cases } 2_c, \end{cases} \tag{3}$$

with $\tilde{R}_{k^*} = n - k - \sum_{j=1}^{k-1}\tilde{R}_j, \tilde{R}_{t_1}$ is the number of surviving units that are eliminated at T_1, given by

$$\tilde{R}_{t_1} = \begin{cases} n - d_1 - \sum_{j=1}^{m-1}\tilde{R}_j & \text{in Case } 1_a, \\ 0 & \text{in all other cases,} \end{cases} \tag{4}$$

and $\tilde{R}_{t_2}$ is the number of surviving units that are eliminated at T_2, given by

$$\tilde{R}_{t_2} = \begin{cases} n - d_2 - \sum_{j=1}^{d_2}\tilde{R}_j & \text{in Cases } 1_c \text{ and } 2_c, \\ 0 & \text{in all other cases.} \end{cases} \tag{5}$$

Special cases: The Type-II unified PHCS is a generalization of many censoring schemes, for example:

(1) If $R_i = 0$ for all $i < m$ and $R_m = n - m$, the Type-II unified PHCS becomes unified HCS

(2) If $T_2 = \infty$, the Type-II unified PHCS becomes generalized Type-I PHCS

(3) If $k = m$, the Type-II unified PHCS becomes generalized Type-II PHCS

(4) If $T_1 = 0$ and $k = m$, the Type-II unified PHCS becomes Type-I PHCS

(5) If $T_2 = \infty$ and $k = 0$, the Type-II unified PHCS becomes Type-II PHCS

Note: In order for the experiment to be terminated at time T_1, R_m must be not equal to zero; if R_m is equal to zero and the m^{th} failure occurs before T_1, then the experiment is terminated at $Y_{m:m:n}$.

3. The ML Estimation

In this section, we derive the ML inference of the unknown parameters λ and θ for the Pareto distribution which was introduced by Pareto [23] as a model for the distribution of income, based on the Type-II unified PHCS. Using the exponential form, Pareto distribution has the following density function (PDF) and distribution function (CDF), respectively, given by

$$g(y \mid \lambda, \theta) = \frac{\lambda}{y}\exp\left[-\lambda \ln\left(\frac{y}{\theta}\right)\right], \lambda, \theta > 0, y \geq \theta, \tag{6}$$

$$G(y \mid \lambda, \theta) = 1 - \exp\left[-\lambda \ln\left(\frac{y\%}{\theta}\right)\right], \lambda, \theta > 0, y \geq \theta.\%. \tag{7}$$

From (7), (6), and (2), the likelihood function of λ, θ under the Type-II unified PHCS can be derived as

$$L(\lambda,\theta \mid \underline{\mathbf{Y}}) = \left[\prod_{i=1}^{d^*}\sum_{j=i}^{m}\left(\tilde{R}_j+1\right)\right]\lambda^{d^*} \cdot \left(\prod_{i=1}^{d^*}\frac{1}{y_i}\right)\exp\left\{-\lambda\left[\eta\left(\underline{\mathbf{y}}\right)+\tilde{R}_{t_1}\ln T_1+\tilde{R}_{t_2}\ln T_2-n\ln\theta\right]\right\}, \tag{8}$$

where $\eta(\underline{\mathbf{y}}) = \sum_{i=1}^{d^*}(\tilde{R}_i+1)\ln y_i$, and $y_i = y_{i:d^*:n}$ for simplicity of notation.

Since the likelihood function (8) is an increasing function in θ, but θ is the lower bound of y_i for all $y_i \in \underline{\mathbf{Y}}$, so its maximum value will be attained at the maximum value y_1 of θ. From (8), the log-likelihood function of (λ, θ) is given by

$$\ln\left[L(\lambda,\theta \mid \underline{\mathbf{Y}})\right] \propto d^*\ln(\lambda) - \lambda\left[\eta\%\left(\underline{\mathbf{y}}\right)+\tilde{R}_{t_1}\ln T_1+\tilde{R}_{t_2}\ln T_2-n\ln(\theta)\right]. \tag{9}$$

To maximize relative to λ, differentiate (9) with respect to λ and solve the equation

$$\frac{\partial\ln\left[L(\lambda,\theta \mid \underline{\mathbf{Y}})\right]}{\partial\lambda} = 0, \tag{10}$$

so the ML estimator $\widehat{\lambda}_{ML}$ of λ is obtained as

$$\widehat{\lambda}_{ML} = \frac{d^*}{\eta\left(\underline{\mathbf{y}}\right)+\tilde{R}_{t_1}\ln T_1+\tilde{R}_{t_2}\ln T_2-n\ln(y_{1:n})}. \tag{11}$$

3.1. Approximate Confidence Intervals for λ and θ. For large d^*, the observed Fisher information matrix of the parameters λ and θ is given by

$$I\left(\widehat{\lambda},\widehat{\theta}\right) = \begin{bmatrix} -\dfrac{\partial^2\ln L(\lambda,\theta \mid \underline{\mathbf{Y}})}{\partial\lambda^2} & -\dfrac{\partial^2\ln L(\lambda,\theta \mid \underline{\mathbf{Y}})}{\partial\lambda\partial\theta} \\ -\dfrac{\partial^2\ln L(\lambda,\theta \mid \underline{\mathbf{Y}})}{\partial\theta\partial\lambda} & -\dfrac{\partial^2\ln L(\lambda,\theta \mid \underline{\mathbf{Y}})}{\partial\theta^2} \end{bmatrix}_{\left(\widehat{\lambda}_{ML},\widehat{\theta}_{ML}\right)}, \tag{12}$$

where

$$\begin{aligned} \frac{\partial^2\ln L(\lambda,\theta \mid \underline{\mathbf{Y}})}{\partial\lambda^2} &= -\frac{d^*}{\lambda^2}, \\ \frac{\partial^2\ln L(\lambda,\theta \mid \underline{\mathbf{Y}})}{\partial\theta^2} &= -\frac{n\lambda}{\theta^2}, \\ \frac{\partial^2\ln L(\lambda,\theta \mid \underline{\mathbf{Y}})}{\partial\lambda\partial\theta} &= -\frac{n}{\theta}, \end{aligned} \tag{13}$$

and a $100(1-\alpha)\%$ two-sided approximate confidence intervals for the parameters λ and θ are then

$$\begin{aligned} &\left(\widehat{\lambda}-z_{\alpha/2}\sqrt{V\left(\widehat{\lambda}\right)},\ \widehat{\lambda}+z_{\alpha/2}\sqrt{V\left(\widehat{\lambda}\right)}\right), \\ &\left(\widehat{\theta}-z_{\alpha/2}\sqrt{V\left(\widehat{\theta}\right)},\ \widehat{\theta}+z_{\alpha/2}\sqrt{V\left(\widehat{\theta}\right)}\right), \end{aligned} \tag{14}$$

respectively, where $V(\widehat{\lambda})$ and $V(\widehat{\theta})$ are the estimated variances of $\widehat{\lambda}_{ML}$ and $\widehat{\theta}_{ML}$, which are given by the first and the second diagonal element of $I^{-1}(\widehat{\lambda},\widehat{\theta})$, and $z_{\alpha/2}$ is the upper $(\alpha/2)$ percentile of the standard normal distribution.

4. Bayesian Estimation

In this study, we investigate three forms of loss functions for Bayesian estimation. The first is the squared error loss function (SELF), which is a symmetric function that values overestimation and underestimation equally when estimating parameters. The LINEX loss function (LLF), which is asymmetric and offers different weights due to overestimation and underestimation, is the second option. The generalization of the entropy loss function is the third loss function (GELF).

Under the assumption that both parameters λ and θ are unknown, we can use the joint prior density function of λ and θ proposed by Lwin [24] and generalized by Arnold and Press [25] for Bayesian Estimations. The generalized Lwin prior is given by

$$\pi(\lambda,\theta) \propto \frac{\lambda^{a_1}}{\theta}\exp\left[-\lambda(\ln a_2 - b_1\ln\theta)\right], \lambda>0, 0<\theta<d, \tag{15}$$

where a_1, b_1, a_2, b_2 are positive constants and $b_2^{b_1} < a_2$.

Upon combining (8) and (15), given UPHCS, the posterior density function of λ, θ is obtained as

$$\begin{aligned} \pi^*(\lambda,\theta \mid \underline{\mathbf{Y}}) &= \frac{L(\lambda,\theta \mid \underline{\mathbf{Y}})\pi(\lambda,\theta)}{\int_0^\infty L(\lambda,\theta \mid \underline{\mathbf{Y}})\pi(\lambda,\theta)d\lambda d\theta} \\ &= I^{-1}\lambda^{d^*+a_1}\theta^{-1}\exp\left\{\left[-\lambda\eta\left(\underline{\mathbf{y}}\right)+\tilde{R}_{t_1}\ln T_1 + \tilde{R}_{t_2}\ln T_2-(n+b_1)\ln\theta+\ln a_2\right]\right\}, \end{aligned} \tag{16}$$

where

$$I = \int_0^{\delta}\int_0^{\infty} \lambda^{d^*+a_1}\theta^{-1} \exp\left\{-\lambda\left[\eta\left(\underline{\mathbf{y}}\right) + \tilde{R}_{t_1} \ln T_1 + \tilde{R}_{t_2} \ln T_2 - (n+b_1)\ln\theta + \ln a_2\right]\right\} d\lambda d\theta = \frac{\Gamma(d^*+a_1)}{n+b_1}\left[\eta\left(\underline{\mathbf{y}}\right) + \tilde{R}_{t_1} \ln T_1 + \tilde{R}_{t_2} \ln T_2 - (n+b_1)\ln\delta + \ln a_2\right]^{-(d^*+a_1)}, \tag{17}$$

with $\delta = \min(y_{1:n}, b_2)$.

4.1. The Bayesian Estimation under SELF. A commonly used loss function is the squared error loss function (SELF) defined as follows:

$$L_{BS}\left(\widehat{\beta}, \beta\right) \propto \left(\widehat{\beta} - \beta\right)^2 \tag{18}$$

The Bayesian estimate $\widehat{\beta}_{BS}$ for the unknown parameter β, relative to the squared error loss function, is given by

$$\widehat{\beta}_{BS} = E_{\pi^*}[\beta] \tag{19}$$

By using (16), the Bayesian estimator of λ under the squared error loss function is the mean of the posterior density function, given by

$$\widehat{\lambda}_{BS} = \int_0^{\delta}\int_0^{\infty} \lambda\pi^*(\lambda, \theta \mid \underline{\mathbf{Y}}) d\lambda d\theta. \tag{20}$$

Hence, the Bayesian estimator of λ under the squared error loss function is obtained as

$$\widehat{\lambda}_{BS} = \frac{d^* + a_1}{\eta\left(\underline{\mathbf{y}}\right) + \tilde{R}_{t_1} \ln T_1 + \tilde{R}_{t_2} \ln T_2 - (n+b_1)\ln\delta + \ln a_2}, \tag{21}$$

and the Bayesian estimator of θ under the squared error loss function is obtained as

$$\begin{aligned}\widehat{\theta}_{BS} &= \int_0^{\delta}\int_0^{\infty} \theta\pi^*(\lambda, \theta \mid \underline{\mathbf{Y}}) d\lambda d\theta = I^{-1}\delta \int_0^{\infty} \frac{\lambda^{d^*+a_1}}{\lambda(n+b_1)+1} \exp\left\{-\lambda\left[\eta\left(\underline{\mathbf{y}}\right) + \tilde{R}_{t_1} \ln T_1 + \tilde{R}_{t_2} \ln T_2 - (n+b_1)\ln\delta + \ln a_2\right]\right\} d\lambda \\ &= \frac{I^{-1}\delta}{(n+b_1)}\left[\eta\left(\underline{\mathbf{y}}\right) + \tilde{R}_{t_1} \ln T_1 + \tilde{R}_{t_2} \ln T_2 - (n+b_1)\ln\delta + \ln a_2\right]^{-(d^*+a_1)} \\ &\quad \times \int_0^{\infty} \frac{t^{d^*+a_1} e^{-t}}{t + \left[\eta\left(\underline{\mathbf{y}}\right) + \tilde{R}_{t_1} \ln T_1 + \tilde{R}_{t_2} \ln T_2 - (n+b_1)\ln\delta + \ln a_2\right]/(n+b_1)} dt \\ &= \frac{\delta}{\Gamma(d^*+a_1)} \Phi\left(d^* + a_1, \frac{\left[\eta\left(\underline{\mathbf{y}}\right) + \tilde{R}_{t_1} \ln T_1 + \tilde{R}_{t_2} \ln T_2 - (n+b_1)\ln\delta + \ln a_2\right]}{(n+b_1)}\right),\end{aligned} \tag{22}$$

where

$$\Phi(y, y) = \int_0^{\infty} \frac{t^y e^{-t}}{t+y} dt. \tag{23}$$

A partial tabulation of $\psi(y, y) = (y/\Gamma(y))\Phi(y-1, y)$ has been provided by Arnold and Press in [25].

4.2. The Bayesian Estimation under GELF. Another commonly used asymmetric loss function is the general entropy (GE) loss function given by

$$L_{BE}\left(\widehat{\beta}, \beta\right) \propto \left(\frac{\widehat{\beta}}{\beta}\right)^{\omega} - \omega \ln\left(\frac{\widehat{\beta}}{\beta}\right) - 1. \tag{24}$$

For $\omega > 0$, a positive error has a more serious effect than a negative error, and for $\omega < 0$, a negative error has a more serious effect than a positive error. In this case, the Bayesian estimate $\widehat{\beta}_{BE}$ relative to the GE loss function is given by

$$\widehat{\theta}_{BE} = \{E_{\pi^*}[\beta]^{-\omega}\}^{\frac{-1}{\omega}}, \tag{25}$$

provided that the involved expectation $E_{\pi^*}[\beta]^{-\omega}$ is finite. It can be shown that, when $\omega = 1$, the Bayesian estimate in Eq. (25) coincides with the Bayesian estimate under the weighted squared error loss function. Similarly, when $\omega = -1$, the Bayesian estimate in Eq. (25) coincides with the Bayesian estimate under the SE loss function.

By using (16), the Bayesian estimator of λ under GELF is given by

$$\begin{aligned}\widehat{\lambda}_{BE} &= \left\{\int_0^{\delta}\int_0^{\infty}\lambda^{-\omega}\pi^*(\lambda,\theta\mid\underline{\mathbf{Y}})d\lambda d\theta\right\}^{\frac{-1}{\omega}} \\ &= \left\{\frac{\Gamma(d^*+a_1-\omega)\left[\eta\left(\underline{\mathbf{y}}\right)+\tilde{R}_{t_1}\ln T_1+\tilde{R}_{t_2}\ln T_2-(n+b_1)\ln(\delta)+\ln(a_2)\right]^{(d^*+a_1)}}{\Gamma(d^*+a_1)\left[\eta\left(\underline{\mathbf{y}}\right)+\tilde{R}_{t_1}\ln T_1+\tilde{R}_{t_2}\ln T_2-(n+b_1)\ln(\delta)+\ln(a_2)+\varepsilon\right]^{(d^*+a_1-\omega)}}\right\}^{\frac{-1}{\omega}}\end{aligned} \tag{26}$$

and the Bayesian estimator of θ under GEF is obtained as

$$\widehat{\theta}_{BE} = \left\{\int_0^{\delta}\int_0^{\infty}\theta^{-\omega}\pi^*(\lambda,\theta\mid\underline{\mathbf{Y}})d\lambda d\theta\right\}^{\frac{-1}{\omega}} = \left\{I^{-1}\int_0^{\delta}\frac{\Gamma(d^*+a_1+1)}{\theta^{1-\omega}}\left[\eta\left(\underline{\mathbf{y}}\right)+\tilde{R}_{t_1}\ln T_1+\tilde{R}_{t_2}\ln T_2-(n+b_1)\ln(\theta)+\ln(a_2)\right]^{(d^*+a_1+1)}d\theta\right\}. \tag{27}$$

4.3. The Bayesian Estimation under LLF. Under the assumption that the minimal loss occurs at $\widehat{\beta}=\beta$, the LINEX loss function can be expressed as

$$L_{BL}\left(\widehat{\beta},\beta\right) = \exp\left[\varepsilon\left(\widehat{\beta}-\beta\right)\right]-\varepsilon\left(\widehat{\beta}-\beta\right)-1 \tag{28}$$

where $\varepsilon\neq 0$. The sign and magnitude of the shape parameter υ represent the direction and degree of asymmetry, respectively. It is easily seen the (unique) Bayesian estimator of θ, denoted by $\widehat{\theta}_L$ under the LINEX loss function, and the value $\widehat{\beta}_L$ which minimizes $E_{\pi^*}[L_L(\widehat{\beta},\beta)]$ is given by

$$\widehat{\beta}_{BL} = \frac{-1}{\varepsilon}\ln\{E_{\pi^*}[\exp(-\upsilon\beta)]\}, \tag{29}$$

provided that the involved expectation $E_{\pi^*}[\exp(-\upsilon\beta)]$ is finite.

By using (16), the Bayesian estimator of λ under LLF is given by

$$\begin{aligned}\widehat{\lambda}_{BL} &= \frac{-1}{\varepsilon}\ln\left\{\int_0^{\delta}\int_0^{\infty}\exp(-\upsilon\lambda)\pi^*(\lambda,\theta\mid\underline{\mathbf{Y}})d\lambda d\theta\right\} \\ &= \frac{-1}{\varepsilon}\ln\left\{\frac{\left[\eta\left(\underline{\mathbf{y}}\right)+\tilde{R}_{t_1}\ln T_1+\tilde{R}_{t_2}\ln T_2-(n+b_1)\ln(\delta)+\ln(a_2)\right]^{(d^*+a_1)}}{\left[\eta\left(\underline{\mathbf{y}}\right)+\tilde{R}_{t_1}\ln T_1+\tilde{R}_{t_2}\ln T_2-(n+b_1)\ln(\delta)+\ln(a_2)+\varepsilon\right]^{(d^*+a_1)}}\right\},\end{aligned} \tag{30}$$

and the Bayesian estimator of θ under LLF is obtained as

$$\begin{aligned}\widehat{\theta}_{BL} &= \frac{-1}{\varepsilon}\ln\left\{\int_0^{\delta}\int_0^{\infty}\exp(-\upsilon\theta)\pi^*(\lambda,\theta\mid\underline{\mathbf{Y}})d\lambda d\theta\right\} \\ &= \frac{-1}{\varepsilon}\ln\left\{I^{-1}\int_0^{\delta}\frac{\Gamma(d^*+a_1+1)}{\theta}\exp(-\upsilon\theta)\times\left[\eta\left(\underline{\mathbf{y}}\right)+\tilde{R}_{t_1}\ln T_1+\tilde{R}_{t_2}\ln T_2-(n+b_1)\ln(\theta)+\ln(a_2)\right]^{(d^*+a_1+1)}d\theta\right\}.\end{aligned} \tag{31}$$

5. One-Sample Bayesian Prediction

For $q = 1, 2, \cdots, \tilde{R}_j$, let $Y_{q:\tilde{R}_j}$ denote the q^{th} order statistic out of $\tilde{R}_j$ removed units at stage j. Then, the conditional density function of $Y_{q:\tilde{R}_j}$, given the observed Type-II unified PHCS, is given, see Basak et al. [26], by

$$g\left(Y_{q:\tilde{R}_j} \mid \underline{\mathbf{Y}}\right) = g(y \mid \underline{\mathbf{Y}}) = \frac{\tilde{R}_j!}{(q-1)!(\tilde{R}_j - q)!} \frac{\left[G(y) - G\left(y_j\right)\right]^{q-1} [1 - G(y)]^{\tilde{R}_j - q} g(y)}{\left[1 - G\left(y_j\right)\right]^{\tilde{R}_j}}, \quad y > y_j, \tag{32}$$

where

$$j = \begin{cases} 1, \cdots, k, \cdots, m-1, t_1 & \text{in Case } 1_a, \\ 1, \cdots, k, \cdots, d_1, \cdots, m & \text{in Case } 1_b, \\ 1, \cdots, k, \cdots, d_1, \cdots, t_2 & \text{in Cases } 1_c, \\ 1, \cdots, d_1, \cdots, d_1, \cdots, k^* & \text{in Case } 2_a, \\ 1, \cdots, d_1, \cdots, k, \cdots, m & \text{in Case } 2_b, \\ 1, \cdots, d_1, \cdots, k, \cdots, t_2 & \text{in Cases } 2_c, \end{cases} \tag{33}$$

with $y_{t_1} = T_1$ and $y_{t_2} = T_2$.

By using (6) and (7) in (32), given Type-II unified PHCS, the conditional density function of $Y_{q:\tilde{R}_j}$ is then given as follows:

$$g(y \mid \underline{\mathbf{Y}}) = \sum_{h=0}^{q-1} C_h \frac{\lambda}{y} \exp\left\{-\lambda\left[\varpi_h\left(\ln y - \ln y_j\right)\right]\right\}, y > y_j, \tag{34}$$

where $C_h = (-1)^h \binom{q-1}{h} \tilde{R}_j!/(q-1)!(\tilde{R}_j - q)!$ and $\varpi_h = h + \tilde{R}_j - q + 1$ for $h = 0, \cdots, q-1$..

Upon combining (16) and (34), the Bayesian predictive density function of $Y_{q:\tilde{R}_j}$, given UPHCS, is obtained as

$$\begin{aligned} (y \mid \underline{\mathbf{Y}}) &= I^{-1} \sum_{h=0}^{q-1} C_h \int_0^{\delta} \int_0^{\infty} \frac{\lambda^{d^* + a_1 + 1}}{\theta y} \exp \\ &\quad \cdot \left\{-\lambda\left[\eta\left(\underline{\mathbf{y}}\right) + \tilde{R}_{t_1} \ln T_1 + \tilde{R}_{t_2} \ln T_2 - (n + b_1) \ln \theta + \ln a_2\right]\right\} \\ &\quad \times \exp\left\{-\lambda\left[\varpi_h\left(\ln y - \ln y_j\right)\right]\right\} d\lambda d\theta \\ &= \frac{I^{-1}\Gamma(d^* + a_1 + 1)}{(n + b_1)} \sum_{h=0}^{q-1} \frac{C_h}{y} \left[\eta\left(\underline{\mathbf{y}}\right) + \tilde{R}_{t_1} \ln T_1 + \tilde{R}_{t_2} \ln T_2 \right. \\ &\quad \left. - (n + b_1) \ln \delta + \ln a_2 + \varpi_h\left(\ln y - \ln y_j\right)\right]^{-(d^* + a_1 + 1)}. \end{aligned} \tag{35}$$

The Bayesian predictive survival function of $Y_{q:\tilde{R}_j}$, given Type-II unified PHCS, is given as

$$\begin{aligned} \bar{G}^*(t \mid \underline{\mathbf{Y}}) &= \int_t^{\infty} g^*(y \mid \underline{\mathbf{Y}}) dy = \frac{I^{-1}\Gamma(d^* + a_1)}{(n + b_1)} \sum_{h=0}^{q-1} \frac{C_h}{\varpi_h} \\ &\quad \cdot \left[\eta\left(\underline{\mathbf{y}}\right) + \tilde{R}_{t_1} \ln T_1 + \tilde{R}_{t_2} \ln T_2 \right. \\ &\quad \left. - (n + b_1) \ln \delta + \ln a_2 + \varpi_h\left(\ln t - \ln y_j\right)\right]^{-(d^* + a_1)}. \end{aligned} \tag{36}$$

The Bayesian point predictor of Y under the squared error loss function is the mean of the predictive density, given by

$$\hat{Y}_{q:\tilde{R}_j} = \int_0^{\infty} y f^*(y \mid \underline{\mathbf{Y}}) dy, \tag{37}$$

where $g^*(y \mid \underline{\mathbf{Y}})$ is given as in (35). The Bayesian predictive bounds of $100(1-\alpha)\%$ two-sided equi-tailed (ET) interval for $Y_{s:n}$ can be obtained by solving the following two equations:

$$\bar{G}^*(L_{ET} \mid \underline{\mathbf{Y}}) = \frac{\alpha}{2} \quad \text{and} \quad \bar{G}^*(U_{ET} \mid \underline{\mathbf{Y}}) = 1 - \frac{\alpha}{2}, \tag{38}$$

where $\bar{G}^*(t \mid \underline{\mathbf{Y}})$ is given as in (36), and L_{ET} and U_{ET} denote the lower and upper bounds, respectively.

6. Two-Sample Bayesian Prediction

Let $Y_{1:\ell:m} \le Y_{2:\ell:N} \le \cdots \le Y_{\ell:\ell:N}$ be a future independent progressive Type-II censored sample from the same population with censoring scheme $\underline{\mathbf{S}} = (S_1, \cdots, S_\ell)$. In this section, we develop a general procedure for deriving the point and interval predictions for $Y_{s:\ell:N}$, $1 \le s \le \ell$, based on the observed UPHCS. The marginal density function of $Y_{s:\ell:N}$ is given by Balakrishnan et al. [27] as

$$g_{Y_{s:\ell:N}}(y_s \mid \theta) = C_{N,s} \sum_{h=0}^{s-1} c_{h,s-1} [1 - G(y_s)]^{W_{h,s}-1} g(y_s), \tag{39}$$

where $1 \le s \le q$,

$C_{N,s} = N(N - S_1 - 1) \cdots (N - S_1 \cdots - S_{s-1} + 1)$, $W_{h,s} = N - S_1 - \cdots - S_{s-h-1} - s + h + 1$,and $c_{h,s-1} = (-1)^h \{[\prod_{u=1}^{h} \sum_{\%\varepsilon = s-h}^{s-h+u-1} (S_\varepsilon + 1)][\prod_{u=1}^{s-h-1} \sum_{\varepsilon=u}^{s-h-1} (S_\varepsilon + 1)]\}^{-1}$..

Upon substituting (7) and (6) in (39), the marginal density function of $Y_{s:\ell:N}$ is then obtained as

$$g_{Y_{s:\ell:N}}(y_s \mid \theta) = C_{N,s} \sum_{h=0}^{s-1} c_{h,s-1} \frac{\lambda}{y_s} \exp\left\{-\lambda\left[W_{h,s} \ln\left(\frac{y_s}{\%\theta}\right)\right]\right\}, \quad y_s > 0. \tag{40}$$

Table 1: The values of MSE and EB of ML and Bayesian estimates for λ based on the different Type-II unified PHCSs.

(n,m,k)	Sch.	(T_1,T_2)	$\widehat{\lambda}_{ML}$	$\widehat{\lambda}_{BS}$		$\widehat{\lambda}_B$ $\widehat{\lambda}_{BE}$		$\widehat{\lambda}_{BL}$	
				IP	NIP	IP	NIP	IP	NIP
						MSE			
(50,20,10)	1	(5,10)	0.2637	0.2075	0.2341	0.1954	0.2191	0.1999	0.2247
	2		0.2823	0.2215	0.2516	0.2083	0.2353	0.2133	0.2414
(50,30,15)	1		0.2192	0.1891	0.2053	0.1837	0.1989	0.1851	0.2006
	2		0.2193	0.1899	0.2064	0.1854	0.2010	0.1861	0.2020
(50,40,20)	1		0.2009	0.1794	0.1920	0.1768	0.1889	0.1768	0.1890
	2		0.1996	0.1782	0.1904	0.1751	0.1869	0.1755	0.1873
(50,20,10)	1	(10,20)	0.2382	0.1868	0.2107	0.1759	0.1972	0.1799	0.2022
	2		0.1949	0.2158	0.2333	0.1875	0.2118	0.1920	0.2406
(50,30,15)	1		0.1503	0.1331	0.1420	0.1326	0.1412	0.1314	0.1400
	2		0.1672	0.1452	0.1555	0.1419	0.1516	0.1425	0.1523
(50,40,20)	1		0.1672	0.1452	0.1555	0.1419	0.1516	0.1425	0.1523
	2		0.1877	0.1676	0.1779	0.1633	0.1732	0.1647	0.1747
(50,20,10)	1	(15,30)	0.2144	0.2300	0.2474	0.2531	0.2724	0.2356	0.2534
	2		0.1754	0.1942	0.2100	0.2186	0.2363	0.2005	0.2165
(50,30,15)	1		0.1208	0.1320	0.1396	0.1193	0.1271	0.1183	0.1260
	2		0.1098	0.1173	0.1241	0.1311	0.1387	0.1208	0.1278
(50,40,20)	1		0.1505	0.1307	0.1400	0.1277	0.1364	0.1283	0.1371
	2		0.1770	0.1581	0.1674	0.1539	0.1627	0.1554	0.1643
						EB			
(50,20,10)	1	(5,10)	0.1102	0.0459	0.0547	0.0086	0.0131	0.0326	0.0397
	2		0.1178	0.0516	0.0618	0.0141	0.0199	0.0382	0.0465
(50,30,15)	1		0.0669	0.0265	0.0299	0.0006	0.0021	0.0175	0.0202
	2		0.0642	0.0232	0.0261	0.0033	0.0024	0.0140	0.0162
(50,40,20)	1		0.0515	0.0167	0.0184	0.0065	0.0064	0.0088	0.0099
	2		0.0527	0.0187	0.0205	0.0039	0.0036	0.0110	0.0122
(50,20,10)	1	(10,20)	0.0992	0.0413	0.0492	0.0077	0.0118	0.0293	0.0357
	2		0.1060	0.0464	0.0556	0.0127	0.0179	0.0344	0.0419
(50,30,15)	1		0.0319	0.0030	0.0025	0.0005	0.0019	0.0111	0.0111
	2		0.0480	0.0113	0.0130	0.0030	0.0022	0.0030	0.0041
(50,40,20)	1		0.0464	0.0150	0.0166	0.0051	0.0061	0.0079	0.0089
	2		0.0474	0.0168	0.0185	0.0035	0.0032	0.0099	0.0110
(50,20,10)	1	(15,30)	0.2071	0.2243	0.2417	0.2484	0.2677	0.2303	0.2480
	2		0.1674	0.1884	0.2040	0.2138	0.2314	0.1950	0.2111
(50,30,15)	1		0.0287	0.0027	0.0023	0.0244	0.0254	0.0100	0.0100
	2		0.0470	0.0102	0.0117	0.0119	0.0119	0.0027	0.0037
(50,40,20)	1		0.0520	0.0233	0.0254	0.0044	0.0054	0.0168	0.0184
	2		0.0510	0.0225	0.0245	0.0036	0.0046	0.0160	0.0176

Table 2: The values of MSE and EB of ML and Bayesian estimates for θ based on the different Type-II unified UHCSs.

(n,m,k)	Sch.	(T_1,T_2)	$\widehat{\theta}_{ML}$	$\widehat{\theta}_{BS}$		$\widehat{\theta}_B$ $\widehat{\theta}_{BE}$		$\widehat{\theta}_{BL}$	
				IP	NIP	IP	NIP	IP	NIP
						MSE			
(50,20,10)	1	(5,10)	0.0820	0.0604	0.0673	0.0671	0.0674	0.0544	0.0598
	2		0.0911	0.0671	0.0674	0.0672	0.0675	0.0604	0.0664
(50,30,15)	1		0.0771	0.0569	0.0634	0.0570	0.0572	0.0512	0.0563
	2		0.0857	0.0632	0.0635	0.0633	0.0636	0.0569	0.0626
(50,40,20)	1		0.0758	0.0602	0.0604	0.0603	0.0605	0.0542	0.0596
	2		0.0842	0.0601	0.0603	0.0602	0.0604	0.0541	0.0595
(50,20,10)	1	(10,20)	0.0738	0.0544	0.0606	0.0604	0.0607	0.0489	0.0538
	2		0.0820	0.0604	0.0607	0.0605	0.0608	0.0544	0.0598
(50,30,15)	1		0.0694	0.0512	0.0631	0.0513	0.0515	0.0461	0.0507
	2		0.0771	0.0630	0.0631	0.0631	0.0633	0.0567	0.0623
(50,40,20)	1		0.0682	0.0600	0.0601	0.0601	0.0602	0.0540	0.0594
	2		0.0758	0.0600	0.0601	0.0600	0.0602	0.0540	0.0594
(50,20,10)	1	(15,30)	0.0664	0.0489	0.0545	0.0544	0.0546	0.0440	0.0484
	2		0.0738	0.0544	0.0546	0.0544	0.0547	0.0489	0.0538
(50,30,15)	1		0.0625	0.0461	0.0568	0.0461	0.0464	0.0415	0.0456
	2		0.0694	0.0567	0.0568	0.0568	0.0570	0.0510	0.0561
(50,40,20)	1		0.0614	0.0540	0.0541	0.0600	0.0542	0.0486	0.0535
	2		0.0682	0.0599	0.0600	0.0540	0.0601	0.0486	0.0593
						EB			
(50,20,10)	1	(5,10)	0.0555	0.0005	0.0010	0.0006	0.0021	0.0004	0.0005
	2		0.0617	0.0006	0.0009	0.0005	0.0020	0.0005	0.0006
(50,30,15)	1		0.0519	0.0034	0.0048	0.0045	0.0059	0.0031	0.0034
	2		0.0577	0.0037	0.0052	0.0048	0.0063	0.0034	0.0037
(50,40,20)	1		0.0526	0.0031	0.0045	0.0041	0.0056	0.0028	0.0030
	2		0.0584	0.0029	0.0043	0.0039	0.0053	0.0026	0.0028
(50,20,10)	1	(10,20)	0.0500	0.0005	0.0009	0.0005	0.0019	0.0004	0.0005
	2		0.0555	0.0005	0.0008	0.0005	0.0018	0.0005	0.0005
(50,30,15)	1		0.0467	0.0031	0.0043	0.0041	0.0053	0.0028	0.0031
	2		0.0519	0.0036	0.0049	0.0046	0.0060	0.0032	0.0035
(50,40,20)	1		0.0473	0.0020	0.0033	0.0030	0.0043	0.0018	0.0020
	2		0.0526	0.0019	0.0032	0.0029	0.0042	0.0017	0.0019
(50,20,10)	1	(15,30)	0.0450	0.0004	0.0008	0.0005	0.0017	0.0003	0.0004
	2		0.0500	0.0005	0.0007	0.0004	0.0016	0.0004	0.0005
(50,30,15)	1		0.0421	0.0028	0.0039	0.0036	0.0048	0.0025	0.0028
	2		0.0467	0.0032	0.0044	0.0041	0.0054	0.0029	0.0032
(50,40,20)	1		0.0426	0.0019	0.0031	0.0029	0.0041	0.0017	0.0019
	2		0.0473	0.0017	0.0031	0.0026	0.0038	0.0015	0.0017

Table 3: The ACL of 95% and 99% confidence intervals and corresponding CP for $\widehat{\lambda}_{ML}$ and $\widehat{\lambda}_B$ at the different priors and Type-II unified PHCSs.

(n,m,k)	Sch.		95%						99%					
		$\widehat{\lambda}_{ML}$		$\widehat{\lambda}_B$ IP		$\widehat{\lambda}_B$ NIP		$\widehat{\lambda}_{ML}$		$\widehat{\lambda}_B$ IP		$\widehat{\lambda}_B$ NIP	
		(T_1,T_2)	ACL	CP	ACL	CP	ACL	CP	ACL	CP	ACL	CP	ACL	CP
(50,20,10)	1	(5,10)	0.988	0.985	0.940	0.979	0.968	0.996	1.391	0.990	1.240	0.979	1.257	1.000
	2		0.988	0.977	0.940	0.971	0.968	0.993	1.391	0.986	1.240	0.977	1.253	0.989
(50,30,15)	1		0.800	0.981	0.761	0.973	0.786	0.981	1.134	0.991	1.003	0.988	1.089	0.983
	2		0.682	0.985	0.650	0.981	0.654	0.997	0.924	0.986	0.820	0.982	0.869	0.975
(50,40,20)	1		0.532	1.000	0.506	0.979	0.513	0.978	0.758	0.995	0.672	1.000	0.716	0.989
	2		0.410	0.986	0.384	0.977	0.509	1.000	0.752	1.000	0.667	1.000	0.711	1.000
(50,20,10)	1	(10,20)	0.677	0.991	0.643	0.988	0.675	0.995	0.954	0.976	0.849	0.980	0.875	0.985
	2		0.711	0.986	0.675	0.982	0.707	0.989	1.001	0.977	0.891	1.000	0.917	0.978
(50,30,15)	1		0.789	0.995	0.750	1.000	0.775	0.983	1.109	0.984	0.989	0.974	1.004	0.989
	2		0.800	1.000	0.761	1.000	0.786	0.975	1.125	0.986	1.003	0.982	1.018	0.984
(50,40,20)	1		0.601	0.976	0.572	0.980	0.583	0.989	0.813	0.984	0.726	0.979	0.727	0.990
	2		0.793	0.977	0.754	0.997	0.777	0.972	1.114	1.000	0.993	0.974	1.006	1.000
(50,20,10)	1	(15,30)	0.541	0.984	0.514	0.974	0.544	0.985	0.764	0.983	0.678	0.974	0.710	0.971
	2		0.563	0.986	0.534	0.982	0.564	0.978	0.794	0.991	0.705	0.987	0.737	0.994
(50,30,15)	1		0.681	0.984	0.648	0.979	0.673	0.989	0.938	1.000	0.854	0.988	0.703	1.000
	2		0.702	1.000	0.667	0.974	0.692	0.984	0.969	0.978	0.879	0.986	0.751	0.995
(50,40,20)	1		0.793	0.983	0.754	0.974	0.777	0.990	1.114	0.992	0.993	0.992	1.003	0.984
	2		0.793	0.991	0.754	0.987	0.777	1.000	1.117	0.975	0.993	1.000	1.032	0.986

Table 4: The ACL of 95% and 99% confidence intervals and corresponding CP for $\widehat{\theta}_{ML}$ and $\widehat{\theta}_B$ at the different priors and Type-II unified PHCSs.

(n,m,k)	Sch.		95%						99%					
		$\widehat{\theta}_{ML}$		$\widehat{\theta}_B$ IP		$\widehat{\theta}_B$ NIP		$\widehat{\theta}_{ML}$		$\widehat{\theta}_B$ IP		$\widehat{\theta}_B$ NIP	
		(T_1,T_2)	ACL	CP	ACL	CP	ACL	CP	ACL	CP	ACL	CP	ACL	CP
(50,20,10)	1	(5,10)	0.269	0.963	0.249	0.943	0.263	0.945	0.405	0.992	0.354	0.990	0.375	0.990
	2		0.370	0.963	0.351	0.944	0.354	0.945	0.512	0.991	0.456	0.990	0.466	0.989
(50,30,15)	1		2.447	0.969	2.379	0.950	2.282	0.950	2.699	0.983	2.478	0.983	2.385	0.980
	2		2.757	0.953	2.749	0.945	2.503	0.923	3.019	0.965	2.845	0.976	2.595	0.951
(50,40,20)	1		4.188	0.973	4.073	0.955	3.904	0.953	4.536	0.982	4.170	0.982	4.004	0.978
	2		4.276	0.978	4.151	0.957	3.994	0.960	4.629	0.984	4.246	0.984	4.093	0.980
(50,20,10)	1	(10,20)	0.326	0.986	0.298	0.965	0.322	0.968	0.505	0.995	0.437	0.993	0.473	0.993
	2		0.309	0.982	0.283	0.962	0.305	0.964	0.480	0.995	0.416	0.994	0.449	0.993
(50,30,15)	1		0.294	0.964	0.276	0.942	0.285	0.948	0.428	0.988	0.378	0.986	0.392	0.987
	2		0.437	0.962	0.414	0.942	0.418	0.945	0.577	0.988	0.515	0.986	0.525	0.987
(50,40,20)	1		4.574	0.984	4.469	0.963	4.244	0.966	4.944	0.993	4.565	0.991	4.344	0.991
	2		4.564	0.987	4.523	0.966	4.169	0.969	4.933	0.996	4.619	0.994	4.269	0.994
(50,20,10)	1	(15,30)	0.395	0.983	0.361	0.965	0.392	0.963	0.609	0.995	0.526	0.994	0.572	0.993
	2		0.378	0.985	0.346	0.967	0.375	0.965	0.584	0.995	0.504	0.993	0.548	0.994
(50,30,15)	1		0.280	0.968	0.261	0.948	0.273	0.950	0.423	0.990	0.372	0.988	0.390	0.988
	2		0.287	0.967	0.268	0.949	0.279	0.948	0.427	0.990	0.377	0.989	0.393	0.988
(50,40,20)	1		2.774	0.976	2.940	0.956	2.343	0.957	3.041	0.991	3.037	0.989	2.443	0.990
	2		2.402	0.973	2.644	0.953	1.931	0.955	2.648	0.991	2.741	0.989	2.031	0.990

Table 5: The real data.

1.2	2.1	2.6	2.7	2.9	2.9	4.8	5.7	5.9	7.0	7.4	15.3	32.6	38.6	50.2

Upon combining (16) and (39), given UPHCS, the Bayesian predictive density function of $Y_{s:\ell:N}$ is obtained as

$$g^*_{Y_{s:\ell:N}}(y_s \mid \underline{\mathbf{Y}}) = \begin{cases} g^*_{1Y_{s:\ell:N}}(y_s \mid \underline{\mathbf{Y}}), & 0 < y_s \le \delta, \\ g^*_{2Y_{s:\ell:N}}(y_s \mid \underline{\mathbf{Y}}), & y_s > \delta, \end{cases} \tag{41}$$

where

$$\begin{aligned} g^*_{1Y_{s:\ell:N}}(y_s \mid \underline{\mathbf{Y}}) &= \int_0^{y_s}\int_0^{\infty} g_{Y_{s:\ell:N}}(y_s \mid \underline{\mathbf{Y}})\pi^*(\lambda,\theta \mid \underline{\mathbf{Y}})d\lambda d\theta \\ &= I^{-1}\Gamma(d^* + a_1 + 1)C_{N,s}\sum_{h=0}^{s-1}\frac{c_{h,s-1}}{\%(n + b_1 + W_{h,s})y_s} \\ &\quad \times \left[\eta\left(\underline{\mathbf{y}}\right) + \tilde{R}_{t_1}\ln T_1 + \tilde{R}_{t_2}\ln T_2 \right. \\ &\quad \left. - (n + b_1)\ln y_s + \ln a_2\right]^{-(d^*+a_1+1)}, \end{aligned}$$

$$\begin{aligned} g^*_{2Y_{s:\ell:N}}(y_s \mid \underline{\mathbf{Y}}) &= \int_0^{\delta}\int_0^{\infty} g_{Y_{s:\ell:N}}(y_s \mid \underline{\mathbf{Y}})\pi^*(\lambda,\theta \mid \underline{\mathbf{Y}})d\lambda d\theta \\ &= I^{-1}\Gamma(d^* + a_1 + 1)C_{N,s}\sum_{h=0}^{q-1}\frac{c_{h,s-1}}{(n + b_1 + W_{h,s})y_s} \\ &\quad \times \left[\eta\left(\underline{\mathbf{y}}\right) + \tilde{R}_{t_1}\ln T_1 + \tilde{R}_{t_2}\ln T_2 \right. \\ &\quad \left. - (n + b_1 + W_{h,s})\ln \delta + W_{h,s}\ln y_s + \ln a_2\right]^{-(d^*+a_1+1)}. \end{aligned} \tag{42}$$

From (41), we simply obtain the predictive survival function of $Y_{s:\ell:N}$, given UPHCS, as

$$\bar{G}^*_{Y_{s:\ell:N}}(t \mid \underline{\mathbf{Y}}) = \int_t^{\infty} g^*(y_s \mid \underline{\mathbf{Y}})dy_s = \begin{cases} \bar{G}^*_{1Y_{s:\ell:N}}(t \mid \underline{\mathbf{Y}}), & 0 < t \le \delta, \\ \bar{G}^*_{2Y_{s:\ell:N}}(t \mid \underline{\mathbf{Y}}), & t > \delta, \end{cases} \tag{43}$$

where

$$\begin{aligned} \bar{G}^*_{1Y_{s:\ell:N}}(t \mid \underline{\mathbf{Y}}) &= \int_{0_t}^{\delta_\infty} g^*_{1Y_{s:\ell:N}}(y_s \mid \underline{\mathbf{Y}})dy_s + \int_{0_\delta}^{\infty_\infty} g^*_{2Y_{s:\ell:N}}(y_s \mid \underline{\mathbf{Y}})dy_s \\ &= I^{-1}\Gamma(d^* + a_1)C_{N,s}\sum_{h=0}^{s-1}\frac{c_{h,s-1}}{(n + b_1)(n + b_1 + W_{h,s})W_{h,s}} \\ &\quad \times \left\{(n + b_1 + W_{h,s})\left[\eta\left(\underline{\mathbf{y}}\right) + \tilde{R}_{t_1}\ln T_1 + \tilde{R}_{t_2}\ln T_2 \right.\right. \\ &\quad \left. - (n + b_1)\ln \delta + \ln a_2\right]^{-(d^*+a_1)} \\ &\quad - W_{h,s}\left[\eta\left(\underline{\mathbf{y}}\right) + \tilde{R}_{t_1}\ln T_1 + \tilde{R}_{t_2}\ln T_2 \right. \\ &\quad \left.\left. - (n + b_1)\ln t + \ln a_2\right]^{-(d^*+a_1)}\right\} \end{aligned}$$

$$\begin{aligned} \bar{G}^*_{2Y_{s:\ell:N}}(t \mid \underline{\mathbf{Y}}) &= \int_{0_t}^{\infty_\infty} g^*_{2Y_{s:\ell:N}}(y_s \mid \underline{\mathbf{Y}})dy_s \\ &= I^{-1}\Gamma(d^* + a_1)C_{N,s}\sum_{h=0}^{s-1}\frac{c_{h,s-1}}{W_{h,s}(n + b_1 + W_{h,s})} \\ &\quad \times \left[\eta\left(\underline{\mathbf{y}}\right) + \tilde{R}_{t_1}\ln T_1 + \tilde{R}_{t_2}\ln T_2 \right. \\ &\quad \left. - (n + b_1 + W_{h,s})\ln \delta + W_{h,s}\ln t + \ln a_2\right]^{-(d^*+a_1)}. \end{aligned} \tag{44}$$

The Bayesian point predictor of $Y_{s:\ell:N}$, $1 \le s \le m$, under the squared error loss function is the mean of the predictive density, given by

$$\widehat{Y}_{s:\ell:N} = \int_0^{\infty} y_s g^*_{Y_{s:\ell:N}}(y_s \mid \underline{\mathbf{Y}})dy_s, \tag{45}$$

where $g^*_{Y_{s:\ell:N}}(y_s \mid \underline{\mathbf{Y}})$ is given as in (41).

The Bayesian predictive bounds of $100(1-\alpha)\%$ ET interval for $Y_{s:\ell:N}$, $1 \le s \le m$, can be obtained by solving the following two equations:

$$\bar{G}^*_{Y_{s:\ell:N}}(L_{ET} \mid \underline{\mathbf{Y}}) = \frac{\alpha}{2} \text{ and } \bar{G}^*_{Y_{s:\ell:N}}(U_{ET} \mid \underline{\mathbf{Y}}) = 1 - \frac{\alpha}{2}, \tag{46}$$

where $\bar{G}^*_{Y_{s:\ell:N}}(t \mid \underline{\mathbf{Y}})$ is given as in (43), and L_{ET} and U_{ET} denote the lower and upper bounds, respectively.

7. Simulation Study

In this section, we present a simulation study to compare the performance of the classical ML and Bayesian estimation procedures under different Type-II unified PHCS. Extensive computations were performed using the statistical software maple.

Firstly, we show how we generate Type-II unified PHC data from Pareto distribution. For given values of n, m, T_1, T_2, and $R = (R_1, \cdots, R_m)$. We will use the transformation which was suggested by Balakrishnan and Aggarwala in [28] to generate Type-II progressive censored data from Pareto distribution. Let the generated Type-II PC data is $(y_{1,m,n}, y_{2,m,n}, \cdots, y_{m,m,n})$, if $y_{m,mn} < T_1$, we set $R_m = 0$ and use the transformation which was suggested by Ng et al. in [29] to generate R_m order statistics from left truncated Pareto distribution with truncated value $y_{m,m,n}$. Now, we m Type-II progressive censored data and R_m order statistics as the following $(y_{1,m,n}, y_{2,m,n}, \cdots, y_{m,m,n}, y_{m+1,n}, y_{m+R_m,n})$. Then, we determined the termination time of the experiment and the corresponding observed Type-II unified PHC data as shown in Section 2.

Table 6: The different Type-II unified HPCS with $(m, k) = (9, 6)$ and different choices of T_1 and T_2.

*Scheme*1	$(t_1, t_2) = (2, 4)$
	$T^* = X_{k:m:n}$
	$d^* = 6$
	$\underline{\mathbf{Y}} = (1.2,2.1,2.6,2.7,2.9,4.8)$
	$\tilde{R} = (0,0,2,0,0,7)$
	$(\tilde{R}_{t_1}, \tilde{R}_{t_2}) = (0, 0)$
*Scheme*2	$(t_1, t_2) = (3, 6)$
	$T^* = t_2$
	$d^* = 7$
	$\underline{\mathbf{Y}} = (1.2,2.1,2.6,2.7,2.9,4.8,5.7)$
	$\tilde{R} = (0,0,2,0,0,2,0)$
	$(\tilde{R}_{t_1}, \tilde{R}_{t_2}) = (0, 4)$
*Scheme*3	$(t_1, t_2) = (6, 12)$
	$T^* = X_{m:m:n}$
	$d^* = 9$
	$\underline{\mathbf{Y}} = (1.2,2.1,2.6,2.7,2.9,4.8,5.7,7.0,7.4)$
	$\tilde{R} = (0,0,2,0,0,2,0,0,2)$
	$(\tilde{R}_{t_1}, \tilde{R}_{t_2}) = (0, 0)$
*Scheme*4	$(t_1, t_2) = (10, 20)$
	$T^* = t_1$
	$d^* = 9$
	$\underline{\mathbf{Y}} = (1.2,2.1,2.6,2.7,2.9,4.8,5.7,7.0,7.4)$
	$\tilde{R} = (0,0,2,0,0,2,0,0,0)$
	$(\tilde{R}_{t_1}, \tilde{R}_{t_2}) = (2, 0)$

Table 7: The ML and Bayesian estimates of λ based on the different Type-II unified PHCSs from real data.

Sch.	$\widehat{\lambda}_{ML}$	$\widehat{\lambda}_{BS}$		$\widehat{\lambda}_B$ $\widehat{\lambda}_{BE}$		$\widehat{\lambda}_{BL}$	
		IP	NIP	IP	NIP	IP	NIP
1	0.3831	0.3504	0.3192	0.3108	0.2718	0.3458	0.3142
2	0.4320	0.3964	0.3780	0.3620	0.3378	0.3919	0.3730
3	0.5140	0.4641	0.4569	0.4280	0.4143	0.4586	0.4505
4	0.4898	0.4493	0.4408	0.4177	0.4043	0.4446	0.4355

We simulate Type-II unified PHCS for different combinations for a sample of size $n = 50$, with different values of $m = 2k$, and $T_2 = 2T_1$ from the Pareto distribution. For convenience, we consider the true values of the unknown parameters as $\lambda = 1$ and $\theta = 3$.

For the point estimate, we computed the ML estimate and Bayesian estimates of λ and θ, under SELF, LLF (with $\varepsilon = 0.5$), and GELF (with $\omega = 0.5$) using informative prior (IP) and non-informative priors (NIP) values for the mean square error (MSE) and the estimated bias

Table 8: The 95% and 99% confidence intervals estimates of λ based on the different Type-II unified PHCSs from real data.

Sch.	95%						99%					
	$\widehat{\lambda}_{ML}$		$\widehat{\lambda}_B$ IP		$\widehat{\lambda}_B$ NIP		$\widehat{\lambda}_{ML}$		$\widehat{\lambda}_B$ IP		$\widehat{\lambda}_B$ NIP	
	LB	UB	LB	UB	LB	UB	LB	UB	LB	UB		UB
1	0.2494	0.7597	0.1362	0.6639	0.1037	0.6539	0.1474	0.8618	0.0973	0.7995	0.0688	0.8041
2	0.3453	0.9182	0.1774	0.7020	0.1520	0.7052	0.2308	1.0328	0.1339	0.8299	0.1100	0.8456
3	0.3453	0.9182	0.2186	0.8005	0.1972	0.8237	0.2308	1.0328	0.1683	0.9395	0.1468	0.9785
4	0.3113	0.7802	0.2209	0.7575	0.2016	0.7721	0.2175	0.8740	0.1728	0.8834	0.1534	0.9100

Table 9: The ML and Bayesian estimates of θ based on the different Type-II unified PHCSs from real data.

Sch.	$\widehat{\theta}_{ML}$	$\widehat{\theta}_{BS}$		$\widehat{\theta}_B$ $\widehat{\theta}_{BE}$		$\widehat{\theta}_{BL}$	
		IP	NIP	IP	NIP	IP	NIP
1	1.2000	1.0093	0.9623	0.9092	0.8674	1.0009	0.9499
2	1.2000	1.0093	0.9623	0.9092	0.8674	1.0009	0.9499
3	1.2000	1.0551	1.0317	0.9501	0.9292	1.0501	1.0251
4	1.2000	1.0522	1.0284	0.9475	0.9262	1.0471	1.0217

Table 10: The 95% and 99% confidence intervals estimates of θ based on the different Type-II unified PHCSs from real data.

Sch.	95%						99%					
	$\widehat{\theta}_{ML}$		$\widehat{\theta}_B$ IP		$\widehat{\theta}_B$ NIP		$\widehat{\theta}_{ML}$		$\widehat{\theta}_B$ IP		$\widehat{\theta}_B$ NIP	
	LB	UB	LB	UB	LB	UB	LB	UB	LB	UB	LB	UB
1	0.4985	1.3143	0.5297	1.1950	0.3840	1.1937	0.3126	1.3189	0.3126	1.1990	0.1676	1.1987
2	0.4985	1.3143	0.5297	1.1950	0.3840	1.1937	0.3126	1.3189	0.3126	1.1990	0.1676	1.1987
3	0.6346	1.3158	0.6842	1.1962	0.6056	1.1956	0.4961	1.3192	0.4961	1.1992	0.4009	1.1991
4	0.6297	1.3156	0.6792	1.1961	0.6022	1.1954	0.4944	1.3191	0.4944	1.1992	0.4030	1.1991

(EB) for each estimate. We construct also the average confidence length (ACL) and the coverage probabilities (CP) of the 90% and 95% asymptotic confidence intervals and Bayesian credible intervals for λ_b and θ_b, using 1,000 simulations.

We take the different censoring schemes as follows:

(1) Scheme 1 $R_m = R_k = n - m/2, R_i = 0$ for all $i \neq k, m$.

(2) Scheme 2 $R_1 = R_m = n - m/2, R_i = 0$ for all $i \neq 1, m$..

The average estimates, MSE and EB for ML and Bayesian estimates of λ and θ, have been reported in Tables 1 and 2, respectively, also, Tables 3 and 4 are present the ACL of 90 % and 95% confidence intervals with corresponding CP for $\widehat{\lambda}$ and $\widehat{\theta}$, respectively.

8. Numerical Example

In this section, we use the real data set to show the performance of the inferential results established for the Pareto distribution based on the Type-II unified PHSC, in addition to comparing ML and Bayesian estimates through Monte Carlo simulations. This real data set contains the failure times (in hours) of one plane's ac system from a pair of real data sets collected by Bain and Engelhardt [30]. Moreover, Guo and Gui [31] demonstrated that these data sets closely matched the inverse Pareto distribution. For further proceeding, before using these data, we ran Kolmogorov-Smirnov (KS) goodness of fit tests to see if they followed the Pareto distribution or not. For these data sets, the KS test statistics with their related p-values are

Table 11: Bayesian point predictor with 95% and 99% ET prediction intervals for $Y_{q:\tilde{R}_j}$ for $q = 1, \cdots, \tilde{R}_j$, with $j = 1, \cdots, d^*, \tilde{R}_{t_1}$, and $\tilde{R}_{t_2}$.

Sch.	j	q	95%					99%				
				IP		NIP			IP		NIP	
			$\widehat{X}_{q:R_j^*}$	LB	UB	LB	UB	$\widehat{X}_{q:R_j^*}$	LB	UB	LB	UB
1	3	1	5.22	1.883	8.561	1.695	9.417	7.830	3.305	12.354	2.975	13.590
		2	7.61	4.271	10.948	3.843	12.043	10.217	5.692	14.741	5.123	16.215
	6	1	8.33	4.993	11.671	4.494	12.838	10.939	6.415	15.464	5.773	17.010
		2	12.19	8.851	15.529	7.966	17.082	14.798	10.273	19.322	9.246	21.255
		3	18.09	14.750	21.427	13.275	23.570	20.696	16.172	25.221	14.555	27.743
		4	22.24	18.903	25.581	17.013	28.139	24.849	20.325	29.374	18.292	32.311
		5	26.79	23.449	30.127	21.104	33.139	29.396	24.871	33.920	22.384	37.312
		6	33.63	30.295	36.972	27.265	40.669	36.241	31.716	40.765	28.545	44.842
		7	62.51	59.169	65.847	53.252	72.431	65.116	60.591	69.640	54.532	76.604
2	3	1	7.39	4.046	10.724	3.642	11.796	9.993	5.468	14.517	4.921	15.969
		2	10.90	7.557	14.234	6.801	15.658	13.503	8.979	18.028	8.081	19.830
	6	1	12.58	9.242	15.920	8.318	17.512	15.189	10.664	19.713	9.598	21.684
		2	18.88	15.546	22.224	13.992	24.446	21.493	16.968	26.017	15.271	28.619
	t_2	1	11.78	8.444	15.122	7.600	16.634	14.391	9.866	18.915	8.880	20.807
		2	17.16	13.822	20.499	12.440	22.549	19.768	15.244	24.293	13.719	26.722
		3	23.07	19.726	26.404	17.754	29.044	25.673	21.148	30.197	19.033	33.217
		4	30.68	27.337	34.014	24.603	37.416	33.283	28.759	37.808	25.883	41.589
3	3	1	9.04	5.706	12.384	5.136	13.622	11.653	7.128	16.177	6.415	17.795
		2	14.43	11.093	17.770	9.983	19.547	17.039	12.514	21.563	11.263	23.720
	6	1	10.44	7.105	13.783	6.395	15.161	13.052	8.527	17.576	7.675	19.334
		2	15.41	12.070	18.747	10.863	20.622	18.016	13.492	22.541	12.142	24.795
	9	1	16.66	13.325	20.002	11.993	22.003	19.271	14.747	23.796	13.272	26.175
		2	26.15	22.815	29.492	20.533	32.441	28.761	24.236	33.286	21.813	36.614
4	3	1	23.13	19.791	26.468	17.811	29.115	25.737	21.212	30.261	19.091	33.287
		2	38.14	34.798	41.475	31.318	45.623	40.744	36.220	45.269	32.598	49.796
	6	1	17.79	14.453	21.131	13.008	23.244	20.400	15.875	24.924	14.288	27.417
		2	26.71	23.369	30.046	21.032	33.051	29.315	24.790	33.839	22.311	37.223
	t_1	1	31.14	27.800	34.477	25.020	37.925	33.746	29.222	38.271	26.299	42.098
		2	36.99	33.648	40.325	30.283	44.358	39.594	35.070	44.119	31.563	48.530

more than 0.05, so we can assume that these data sets follow Pareto distribution at a 0.05% level of significance. This real data are ordered in Table 5.

We will use these data to generate the Type-II unified PHCS, suppose $m = 9$, $k = 6$, $R_i = 2$ for $i = 3,6,9$, and $R_i = 0$ otherwise with different values of T_1 and T_2 with $T_2 = 2\,T_1$. Table 6 shows different Type-II unified PHCSs.

After generating the Type-II unified PHC data with the different unified PHCS, we ran KS goodness of fit tests for all Type-II unified PHC data to see if they followed the Pareto distribution or not. For all these Type-II unified PHC data sets, the KS test statistics with their related p-values are more than 0.05, so we can assume that these data and all generated Type-II unified PHC data sets from it follow Pareto distribution at a 0.05% level of significance.

Based on the Type-II unified PHCS and two different choices IP and NIP priors, the ML and Bayesian estimates for the unknown parameters λ and θ are presented in Tables 7 and 8. Moreover, the 95% and 99% asymptotic confidence intervals and the credible intervals are presented in Tables 9 and 10. Finally, Tables 11 and 12 present the point predictor with 95% and 99% Bayesian prediction bounds of $Y_{s:\ell:N}$ from the future progressively censored sample of size $\ell = 10$ from a sample of size $N = 20$ with progressive censoring scheme $S = (0,2,0,2,0,2,0,2,0,2)$ for four different choices of censoring schemes.

Table 12: Bayesian point predictor with 95% and 99% ET prediction intervals for $Y_{s:10}$ for $s = 1, \cdots, 10$.

Sch.	s	95%					99%				
			IP		NIP			IP		NIP	
		$\widehat{Y}_{s:10}$	LB	UB	LB	UB	$\widehat{Y}_{s:10}$	LB	UB	LB	UB
1	1	1.225	0.629	2.026	0.389	3.037	1.343	0.484	2.185	0.231	3.694
	2	1.573	0.740	3.088	0.479	5.541	2.532	0.600	3.665	0.310	8.146
	3	2.438	0.873	5.082	0.591	11.350	7.103	0.744	6.832	0.417	21.238
	4	4.613	1.018	8.538	0.720	23.780	19.710	0.906	13.182	0.548	57.920
	5	12.188	1.193	16.670	0.881	62.358	59.551	1.105	30.852	0.720	214.386
	6	32.653	1.382	34.263	1.062	174.841	151.749	1.320	77.551	0.921	878.949
	7	111.072	1.633	96.664	1.290	789.276	431.175	1.595	290.979	1.181	6816.226
	8	322.752	1.956	311.634	1.536	4.3E+03	1.0E+03	1.940	1.3E+03	1.467	6.9E+04
	9	1.4E+03	2.547	2.9E+03	1.856	4.4E+03	3.3E+03	2.570	2.2E+04	1.839	6.0E+06
	10	4.8E+03	3.582	5.6E+04	2.504	5.7E+04	8.6E+03	3.683	9.3E+05	2.497	6.2E+06
2	1	1.206	0.700	1.860	0.484	2.545	1.187	0.598	1.908	0.363	2.732
	2	1.431	0.797	2.612	0.566	4.036	1.454	0.698	2.782	0.441	4.653
	3	1.793	0.913	3.885	0.667	6.960	1.995	0.819	4.345	0.539	8.782
	4	2.373	1.040	5.853	0.780	12.137	3.163	0.954	6.914	0.653	16.897
	5	3.790	1.194	9.924	0.921	25.074	6.966	1.120	12.597	0.799	39.717
	6	7.234	1.362	17.479	1.079	54.221	17.287	1.302	24.036	0.966	99.035
	7	21.806	1.586	39.621	1.279	168.944	59.018	1.538	61.060	1.184	378.186
	8	69.039	1.873	99.508	1.502	599.893	179.077	1.833	174.902	1.430	1.7E+03
	9	427.945	2.388	591.669	1.803	7.7E+03	881.013	2.358	1.3E+03	1.766	3.3E+04
	10	2.0E+03	3.269	6.2E+03	2.135	8.0E+03	3.3E+03	3.257	1.9E+04	2.139	3.5E+04
3	1	1.200	0.764	1.733	0.565	2.238	1.180	0.686	1.743	0.467	2.303
	2	1.379	0.851	2.295	0.642	3.258	1.367	0.775	2.348	0.542	3.471
	3	1.641	0.953	3.184	0.734	5.067	1.656	0.880	3.334	0.633	5.649
	4	2.000	1.063	4.458	0.835	7.939	2.094	0.995	4.793	0.735	9.305
	5	2.660	1.195	6.877	0.959	14.269	3.082	1.133	7.660	0.863	17.860
	6	3.871	1.338	10.937	1.096	26.567	5.320	0.261	12.676	0.261	35.781
	7	7.978	1.526	21.416	1.268	66.594	14.177	0.388	26.261	0.328	99.524
	8	20.791	1.762	45.575	1.457	185.146	41.922	0.262	59.676	0.262	312.094
	9	135.939	2.175	198.062	1.710	1.5E+03	250.632	2.118	291.317	8.937	3.1E+03
	10	7.5E+02	2.857	1.4E+03	1.992	1.5E+03	1.2E+03	2.783	2.4E+03	1.970	3.2E+03
4	1	1.200	0.758	1.744	0.562	2.250	1.179	0.681	1.753	0.467	2.306
	2	1.383	0.845	2.314	0.637	3.266	1.369	0.769	2.361	0.540	3.449
	3	1.650	0.947	3.213	0.728	5.058	1.654	0.874	3.347	0.629	5.550
	4	2.010	1.059	4.500	0.830	7.878	2.063	0.989	4.797	0.730	9.016
	5	2.651	1.195	6.943	0.954	14.051	2.896	1.131	7.634	0.857	16.999
	6	3.762	1.343	11.034	1.093	25.919	4.621	1.288	12.564	1.000	33.356
	7	3.762	1.343	11.034	1.093	25.919	11.211	1.491	25.852	1.186	90.282
	8	18.076	1.791	45.946	1.468	176.052	32.499	1.742	58.240	1.398	273.941
	9	121.989	2.232	200.630	1.740	1.4E+03	212.132	2.180	281.921	1.694	2.6E+03
	10	7.2E+02	2.969	1.4E+03	2.051	1.4E+03	1.1E+03	2.906	2.2E+03	2.035	2.7E+03

Since $R_1 = 0$, then $y_1 = 1.2$ is not removed from censored data in all Type-II unified PHCS, and since $\widehat{\theta}_{ML} = y_1$ so that $\widehat{\theta}_{ML} = 1.2$ in all four Type-II unified PHCS.

9. Conclusions and Discussion

From Tables 1 and 2, we observe that the MSEs of the Bayesian estimates based on the LINEX, GE, and SE loss functions are smaller than those of the ML estimates. Furthermore, the MSEs and EBs of all estimates decrease with increasing m and k when T_1 and T_2 are fixed. Also, the MSEs and EBs of all estimates decrease with increasing T_1 and T_2 when m and k are fixed. Moreover, a comparison of the results for the informative priors with the corresponding ones for non-informative priors reveals that the former produces more precise results.

From the results in Tables 10 and 11, we notice that the point predictor of mean is between the upper and lower bounds of the prediction intervals. Additionally, as we would expect, a comparison of the results for the informative prior with the corresponding ones for non-informative prior reveals that the former produces more precise results, because the interval length in the informative prior case is short than in non-informative case. Moreover, the 95% prediction intervals seem to be more precise than the 99% prediction intervals, Finally when we use the same value of T_1 and T_2 but increasing k and m. , the Bayesian prediction bounds become tighter as expected since the duration of the life-testing experiment is longer in this case.

Data Availability

The data used to support the findings of this study are included within the article.

Conflicts of Interest

The authors declare there is no conflict of interest.

Acknowledgments

The authors acknowledge the financial support from the King Saud University Researchers Supporting Project number RSP-2022/323, King Saud University, Riyadh, Saudi Arabia.

References

[1] B. Epstein, "Truncated life tests in the exponential case," *The Annals of Mathematical Statistics*, vol. 25, no. 3, pp. 555–564, 1954.

[2] A. Childs, B. Chandrasekar, N. Balakrishnan, and D. Kundu, "Exact likelihood inference based on Type-I and Type-II hybrid censored samples from the exponential distribution," *Annals of the Institute of Statistical Mathematics*, vol. 55, no. 2, pp. 319–330, 2003.

[3] B. Chandrasekar, A. Childs, and N. Balakrishnan, "Exact likelihood inference for the exponential distribution under generalized Type-I and Type-II hybrid censoring," *Naval Research Logistics (NRL)*, vol. 51, no. 7, pp. 994–1004, 2004.

[4] N. Balakrishnan, A. Rasouli, and N. Sanjari Farsipour, "Exact likelihood inference based on an unified hybrid censored sample from the exponential distribution," *Journal of Statistical Computation and Simulation*, vol. 78, no. 5, pp. 475–488, 2008.

[5] W. T. Huang and K. C. Yang, "A new hybrid censoring scheme and some of its properties," *Tamsui Oxford Journal of Mathematical Sciences*, vol. 26, no. 4, pp. 355–367, 2010.

[6] S. Park and N. Balakrishnan, "A very flexible hybrid censoring scheme and its Fisher information," *Journal of Statistical Computation and Simulation*, vol. 82, no. 1, pp. 41–50, 2012.

[7] D. Kundu and A. Joarder, "Analysis of Type-II progressively hybrid censored data," *Computational Statistics & Data Analysis*, vol. 50, no. 10, pp. 2509–2528, 2006.

[8] A. Childs, B. Chandrasekar, and N. Balakrishnan, "Exact Likelihood Inference for an Exponential Parameter under Progressive Hybrid Censoring Schemes," in *Statistical models and methods for biomedical and technical systems*, pp. 319–330, Birkhuser Boston, 2008.

[9] S. K. Tomer and M. S. Panwar, "Estimation procedures for Maxwell distribution under type-I progressive hybrid censoring scheme," *Journal of Statistical Computation and Simulation*, vol. 85, no. 2, pp. 339–356, 2015.

[10] H. Panahi, "Estimation methods for the generalized inverted exponential distribution under type ii progressively hybrid censoring with application to spreading of micro-drops data," *Communications in Mathematics and Statistics*, vol. 5, no. 2, pp. 159–174, 2017.

[11] A. M. Almarashi, A. Algarni, H. Okasha, and M. Nassar, "On reliability estimation of Nadarajah–Haghighi distribution under adaptive type-I progressive hybrid censoring scheme," *Quality and Reliability Engineering International*, vol. 38, no. 2, pp. 817–833, 2022.

[12] M. M. El-Din, A. R. Shafay, and M. Nagy, "Statistical inference under adaptive progressive censoring scheme," *Computational Statistics*, vol. 33, no. 1, pp. 31–74, 2018.

[13] M. M. El-Din, M. Nagy, and M. H. Abu-Moussa, "Estimation and prediction for Gompertz distribution under the generalized progressive hybrid censored data," *Annals of Data Science*, vol. 6, no. 4, pp. 673–705, 2019.

[14] Y. Cho, H. Sun, and K. Lee, "Exact likelihood inference for an exponential parameter under generalized progressive hybrid censoring scheme," *Statistical Methodology*, vol. 23, pp. 18–34, 2015.

[15] K. Lee, H. Sun, and Y. Cho, "Exact likelihood inference of the exponential parameter under generalized Type II progressive hybrid censoring," *Journal of the Korean Statistical Society*, vol. 45, no. 1, pp. 123–136, 2016.

[16] M. M. El-Din and M. Nagy, "Estimation for inverse Weibull distribution under generalized progressive hybrid censoring scheme," *Journal of Statistics Applications & Probability Letters*, vol. 4, pp. 1–11, 2017.

[17] M. Nagy, K. S. Sultan, and M. H. Abu-Moussa, "Analysis of the generalized progressive hybrid censoring from Burr Type-XII lifetime model," *AIMS Mathematics*, vol. 6, no. 9, pp. 9675–9704, 2021.

[18] M. Nagy, M. E. Bakr, and A. F. Alrasheedi, "Analysis with applications of the generalized Type-II progressive hybrid censoring sample from Burr Type-XII model," *Mathematical Problems in Engineering*, vol. 2022, Article ID 1241303, 21 pages, 2022.

[19] M. Nagy, A. F. Alrasheedi, and Department of Statistics and Operation Research, Faculty of Science, King Saud University, KSA, "The lifetime analysis of the Weibull model based on Generalized Type-I progressive hybrid censoring schemes," *Mathematical Biosciences and Engineering*, vol. 19, no. 3, pp. 2330–2354, 2022.

[20] J. Górny and E. Cramer, "Modularization of hybrid censoring schemes and its application to unified progressive hybrid censoring," *Metrika*, vol. 81, no. 2, pp. 173–210, 2018.

[21] J. Górny and E. Cramer, "Exact inference for a new flexible hybrid censoring scheme," *Journal of the Indian Society for Probability and Statistics*, vol. 19, no. 1, pp. 169–199, 2018.

[22] J. Kim and K. Lee, "Estimation of the Weibull distribution under unified progressive hybrid censored data," *Journal of the Korean Data Analysis Society*, vol. 20, no. 5, pp. 2189–2199, 2018.

[23] V. Pareto, *Cours d'Economie Politique*, Rouge et Cie, Paris, 1897.

[24] T. Lwin, "Estimation of the tail of the Paretian law," *Scandinavian Actuarial Journal*, vol. 1972, no. 2, pp. 170–178, 1972.

[25] B. C. Arnold and S. J. Press, "Bayesian estimation and prediction for Pareto data," *Journal of the American Statistical Association*, vol. 84, no. 408, pp. 1079–1084, 1989.

[26] I. Basak, P. Basak, and N. Balakrishnan, "On some predictors of times to failure of censored items in progressively censored samples," *Computational Statistics & Data Analysis*, vol. 50, no. 5, pp. 1313–1337, 2006.

[27] N. Balakrishnan, A. Childs, and B. Chandrasekar, "An efficient computational method for moments of order statistics under progressive censoring," *Statistics & Probability Letters*, vol. 60, no. 4, pp. 359–365, 2002.

[28] N. Balakrishnan and R. Aggarwala, *Progressive Censoring: Theory, Methods, and Applications*, Springer Science & Business Media, 2000.

[29] H. K. T. Ng, D. Kundu, and P. S. Chan, "Statistical analysis of exponential lifetimes under an adaptive Type-II progressive censoring scheme," *Naval Research Logistics (NRL)*, vol. 56, no. 8, pp. 687–698, 2009.

[30] L. J. Bain and M. Engelhardt, *Statistical Analysis of Reliability and Life-Testing Models: Theory and Methods*, Routledge, 2017.

[31] L. Guo and W. Gui, "Bayesian and classical estimation of the inverse Pareto distribution and its application to strength-stress models," *American Journal of Mathematical and Management Sciences*, vol. 37, no. 1, pp. 80–92, 2018.

Hindawi
Applied Bionics and Biomechanics
Volume 2022, Article ID 2801719, 18 pages
https://doi.org/10.1155/2022/2801719

Research Article

Generalized Multiphase Dynamic Modeling and Precision Interaction Force Control of a Walking Lower Limb Hydraulic Exoskeleton

Shan Chen,[1,2] **Muye Lu**,[1,2] **Fangfang Dong**,[1,3] **Haijun Liu**,[1,2] **Xiaoqing Tian**,[1,2] **and Jiang Han**[1,2]

[1]*School of Mechanical Engineering, Hefei University of Technology, Hefei 230009, China*
[2]*Anhui Engineering Laboratory of Intelligent CNC Technology and Equipment, Hefei 230009, China*
[3]*HMB Research Institute of Automation and Intelligent Equipment, Ma'anshan 243131, China*

Correspondence should be addressed to Shan Chen; cs0305@hfut.edu.cn

Received 20 January 2022; Accepted 10 March 2022; Published 7 April 2022

Academic Editor: Songyuan Zhang

Wearable lower limb hydraulic exoskeletons can be used to augment the human performance in heavy load transportation. Nonlinear and walking phase-dependent dynamics make the lower limb hydraulic exoskeleton become difficult to be modeled. This paper presents a generalized multiphase dynamic modeling method in which the dynamic model of each walking phase can all be solved based on a general higher dimensional dynamic model and different holonomic constraints. Compared to traditional lower limb exoskeleton modeling methods where the modeling of each walking phase is done independently, the proposed method is simple and applicable to arbitrary walking phases, especially for double leg support phase (closed-chain dynamics). Based on the established dynamic models, MIMO adaptive robust cascade force controllers (ARCFC) are designed both for double leg support phase and single leg support phase to effectively address high-order nonlinearities and various modeling uncertainties in hydraulic exoskeletons. An additional torque allocation method is proposed to deal with the overactuated characteristic in double leg support. Comparative simulations are conducted to verify the excellent human-machine interaction force control performance of the proposed scheme.

1. Introduction

Wearable lower limb exoskeletons are intelligent human-machine integrated devices used to augment the performance of the wearer in heavy load transportation [1, 2], such as soldier marching, earthquake rescue, and construction site. Thanks to the large ratio of power-to-weight, it is suitable to adopt hydraulic actuators in developing such systems which need to be a small size while providing large force. In hydraulic lower limb exoskeleton, the wearer provides motion commands, while hydraulic actuators supply enough actuation force to support heavy loads. When the exoskeleton tracks the human motion precisely, little load force can be felt by the wearer. Since the human-machine interaction force is closely related to the trajectory tracking error between the wearer and exoskeleton, the control objective can finally be transformed into minimizing the human-machine interaction force.

As for the interaction force controller design of a walking hydraulic lower limb exoskeleton system, a number of challenging issues exist. First, different from 1-DOF or single leg exoskeleton, there exist multiple walking phases in the walking lower limb exoskeleton, such single leg support phase, double leg support phase, and subphases during double leg support (like toe off and heel strike). Moreover, for double leg support phase and its subphases, the two feet

are landing the ground at the same time leading to a closed-chain mechanism. Also overactuated conditions exist in closed chain dynamics. All these make the dynamic modeling and controller design of lower limb exoskeleton become more difficult. Besides, as a nondesired force output source, high-order nonlinearities and various model uncertainties exist in hydraulic actuators which make the controller design of hydraulic lower limb exoskeleton more challenging than that of motor-driven system.

As for the multiphase dynamic modeling of lower limb exoskeletons, usually the dynamic model of each walking phase is established separately. For single leg support phase, since it is a serial-chain mechanism, the dynamic model is usually obtained straightforwardly using Lagrangian equations. In [3], the lower limb exoskeleton in single leg support is described as serial chain of 7 segments. Using Lagrangian equations of the second kind, the planar model of single leg support is obtained. In [4], the Lagrange equations of the second kind is adopted to model the single leg support phase of 6-link biped robot. For double leg support phase or its subphases (such as toe off and heel strike), since it is a closed-chain mechanism with overactuation, the Lagrangian of the second kind cannot be applied directly. In [3], the lower limb exoskeleton in double leg support is partitioned into two 3-DOF serial manipulators. Lagrangian equations of the second kind are used to model the dynamics of each 3-DOF manipulator, while Newtonian mechanics is adopted to describe the relationship of the two parts. In [4], the Lagrange formulation of the first kind using Lagrange multipliers is adopted for dynamic modeling of biped robot in double leg support. However, all these methods focus on the dynamic modeling of each walking phase independently in which different general coordinates needed to be established and different Lagrangian modeling process need to be conducted for each walking phase. This obviously leads to a complicated modeling process when there exist various walking phases. Also, the joint positions may become discontinuous due to the role switching of the swing and support leg [5].

As for the human-machine interaction force controller design, various control schemes are proposed [6]. One method is to design the exoskeleton controller without measuring the human-machine interaction force. In [7], an inverse dynamics-based positive feedback controller is designed for the Berkeley lower extremity exoskeleton so that the sensitivity to the human force can be increased. In [8], first the inverse dynamics of the exoskeleton is adopted to estimate the joint torque, and then, a fictitious gain is designed to increase the sensitivity of the human body. However, these methods ignore the model uncertainties in computing the inverse dynamics leading to a poor robust performances. Another line of thought is to design a cascade force controller based on the measured human-machine interaction force. Model-free PID controller [9], admittance controller [10], and human-machine cooperation controller [9] are often used in the high-level control algorithm design to generate the desired motion command, while PID [11] or dynamic model compensation are often used in the low-level controller design to achieve the motion tracking. In these cascade force control schemes, the human motion intent is inferred from the fixed dynamic model or human data which cannot be generalized to different wearers. Also, the proposed low-level motion tracking algorithm cannot guarantee the fast response and accurate tracking of human motion in the presence of strongly coupled nonlinearities and various model uncertainties. Other control methods have considered the model uncertainties in the controller design, such as the adaptive impedance control [12], neural network control [13], sliding mode controller [14, 15], and robust output feedback-assistive control [16]. However, these methods are mainly focused on the controller design of motor-driven exoskeletons which cannot be easily extended to the control of hydraulic exoskeletons. The reason is that the order of hydraulic exoskeleton dynamics is higher (it is a three-order dynamics for hydraulic exoskeleton in this paper, while it is usually a two-order dynamics for motor-driven exoskeleton systems). Also, various model uncertainties exist in the hydraulic actuators, like the load change, hydraulic parameters variation (e.g., bulk modulus), external disturbances, and leakage.

Recently, an adaptive robust cascade force control algorithm is proposed for 1-DOF and 3-DOF hydraulic exoskeleton system [17, 18]. Robust interaction force control performance to various model uncertainties is guaranteed. In this paper, the problem is extended to a walking lower limb exoskeleton. Compared to the 3-DOF single leg exoskeleton, multiple walking phases exist when two legs move, which makes the human motion intent inference method of lower limb exoskeleton different from that of single leg exoskeleton. Moreover, the closed-chain dynamics and overactuated characteristic in double leg support and its subphases make the interaction force controller design become more challenged.

This paper presents a generalized multiphase dynamic modeling method and a robust interaction force control scheme for hydraulic lower limb exoskeleton. The principal contributions can be summarized as follows:

(1) A generalized multiphase dynamic modeling method is proposed for lower limb exoskeleton which is applicable to arbitrary walking phase, especially for double leg support phase (closed-chain dynamics). Since the generalized coordinates are the same and the Lagrangian modeling process will only be done once, the multiphase dynamics modeling process of a walking lower limb exoskeleton becomes simple

(2) Multiphase adaptive robust interaction force controllers are designed to effectively deal with overactuated characteristic, negative effect of high-order nonlinearities of hydraulic system, various parameter uncertainties, and modeling errors. Robust interaction force control performance is achieved

2. Physical Modeling

Since human dynamics is very complicated and may not be conveniently applied for exoskeleton controller design, in

our modeling, we do not establish the human model, and the humans are just regarded to provide a desired motion trajectory. Then, a human-machine interface dynamic model is established to describe the relationship between interaction force and human-exoskeleton motion tracking error. The whole dynamic model of hydraulic lower limb exoskeleton includes three parts: rigid body dynamics of lower limb exoskeleton, hydraulic actuator dynamics, and human-machine interface dynamics.

2.1. Rigid Body Dynamics

2.1.1. General Higher Dimensional Dynamic Model. In this article, a walking lower limb hydraulic exoskeleton in the sagittal plane with six fully actuated revolute joints is considered. During the walking process, there are five typical walking phases, which are left leg support phase, right heel strike phase, double leg support phase, left toe off phase, and right leg support phase, as shown in Figure 1.

For a floating exoskeleton in which positions of the two exoskeleton feet can be changed, as shown in Figure 2, we can define nine generalized coordinates to completely describe the positions of such system. Denote

$$\begin{aligned} q &= [x_l \quad y_l \quad q_l \quad q_1 \quad q_2 \quad q_3 \quad q_4 \quad q_5 \quad q_6]^T, \\ T_{act} &= [\tau_1 \quad \tau_2 \quad \tau_3 \quad \tau_4 \quad \tau_5 \quad \tau_6]^T, \\ F_L &= [F_{xl} \quad F_{yl} \quad T_l]^T, \\ F_R &= [F_{xr} \quad F_{yr} \quad T_r]^T, \end{aligned} \tag{1}$$

where x_l, y_l, and q_l represent the left foot positions in the Cartesian coordinate frame, $q_1 \sim q_6$ represent the joint positions in the left leg and the right leg, $\tau_1 \sim \tau_6$ represent the joint torque from the actuators, and F_L and F_R represent ground contact force at the left and right foot.

Using Lagrangian equations, the dynamic model of the above floating exoskeleton can be described as

$$M(q)\ddot{q} + C(q,\dot{q})\dot{q} + G(q) = B_a T_{\text{act}} + J_L^T F_L + J_R^T F_R, \tag{2}$$

where $M(q)$, $C(q,\dot{q})$, and $G(q)$ represent the system matrices and gravity force, B_a represents the joint-torque projection matrix, and J_L and J_R represent the Jacobian matrix in the left and right foot.

2.1.2. Dynamic Model for Each Walking Phase. In different walking phases, the contact condition between the exoskeleton foot and the ground is different which leads to different holonomic constraints. Combining the same general dynamic model (Equation (2)) with different holonomic constraints, we can finally solve the detailed dynamic model for each walking phase through solving amount of linear equations. It should be noted that the generalized coordinates and the general high dimensional dynamic model are the same for the modeling of each walking phase which are quite different from the traditional multiphase dynamic modeling method where the generalized coordinates will be redefined and different Lagrangian modeling process will be conducted in each walking phase.

Define the following terms:

$$\begin{aligned} q &= [q_{1p} \quad q_c]^T, \\ q_{lp} &= [x_l \quad y_l \quad q_l]^T, \\ q_{c1} &= [q_1 \quad q_2 \quad q_3]^T, \\ q_{c2} &= [q_4 \quad q_5 \quad q_6]^T, \\ q_c &= [q_{c1} \quad q_{c2}]^T, \\ U_1 &= [I_{3\times3} \quad 0_{3\times6}], \\ U_2 &= [0_{6\times3} \quad I_{6\times6}], \\ U_3 &= \begin{bmatrix} I_{3\times3} \\ 0_{3\times3} \end{bmatrix}, \\ U_4 &= \begin{bmatrix} 0_{3\times3} \\ I_{3\times3} \end{bmatrix}, \\ T_1 &= [I_{2\times2} \quad 0_{2\times1}], \\ T_3 &= \begin{bmatrix} I_{4\times4} \\ 0_{2\times4} \end{bmatrix}, \\ T_4 &= \begin{bmatrix} 0_{4\times2} \\ I_{2\times2} \end{bmatrix}, \\ J_{Rq} &= -\left(J_R U_1^T\right)^{-1} J_R U_2^T, \\ J_{Rq1} &= J_R U_2^T U_3, \\ J_{Rq2} &= J_R U_2^T U_4, \\ J_{Rh1} &= T_1 J_R U_2^T T_3, \\ J_{Rh2} &= T_1 J_R U_2^T T_4. \end{aligned} \tag{3}$$

(1) Left Leg Support Dynamics. For left leg support, as shown in Figure 1(a), the positions and the rotation angle of the left foot are fixed. Thus, the following holonomic constraints exist

$$\begin{aligned} x_l &= C_{xl}, \\ y_l &= C_{yl}, \\ q_l &= C_{ql}, \end{aligned} \tag{4}$$

where C_{xl}, C_{yl}, and C_{ql} are constant values. Besides, since the right leg is the swing one, there is no ground contact force in the right foot, namely

$$F_R = [0 \quad 0 \quad 0]^T. \tag{5}$$

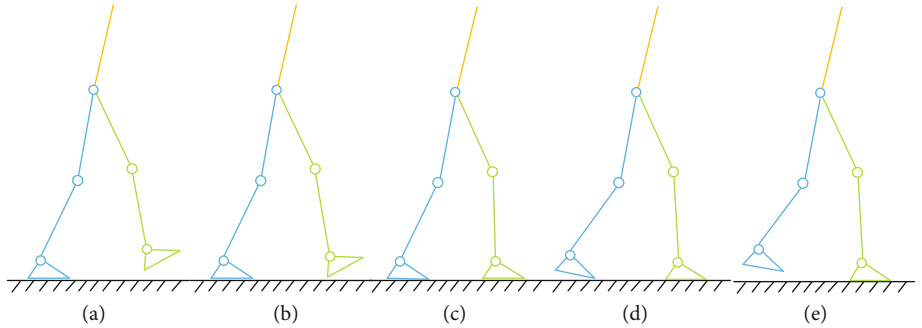

Figure 1: Multiple walking phases. (a) Left leg support. (b) Right heel strike. (c) Double leg support. (d) Left toe off. (e) Right leg support.

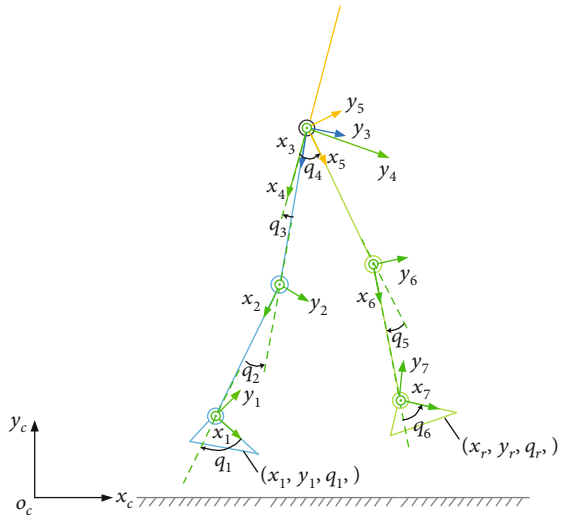

Figure 2: Coordinate frames for a floating exoskeleton (with positions of the exoskeleton feet changed). (x_l, y_l, q_l) and (x_r, y_r, q_r) represent the positions of the left foot and right foot in the Cartesian coordinate frame, receptively.

Differentiating (4) while noting (2) and (5), we can obtain

$$\begin{aligned} M\ddot{q} + C\dot{q} + G &= B_a T_{\text{act}} + J_L^T F_L + J_R^T F_R, \\ \ddot{q}_{lp} &= [0 \quad 0 \quad 0]^T, \\ F_R &= [0 \quad 0 \quad 0]^T. \end{aligned} \tag{6}$$

Here, there are 15 unknown variables ($\ddot{q}$, F_L, and F_R) and 15 equations (Equation (6)). Using T_{act} as input, $\ddot{q}$, F_L, and F_R can be solved. Finally, the dynamics can be obtained as

$$\ddot{q}_c = M_{\text{Lsp}}^{-1}\left(T_{\text{act}} - C_{\text{Lsp}}\dot{q}_c - G_{\text{Lsp}}\right), \tag{7}$$

where M_{Lsp}, C_{Lsp}, and G_{Lsp} are matrices computed from M, C, and G, as follows:

$$\begin{aligned} M_{\text{Lsp}} &= U_2 M U_2^T, \\ C_{\text{Lsp}} &= U_2 C U_2^T, \\ G_{\text{Lsp}} &= U_2 G. \end{aligned} \tag{8}$$

(2) Right Leg Support Dynamics. For right leg support, the positions of the right foot are fixed. Thus, the following holonomic constraints exist:

$$\begin{aligned} x_r &= C_{xr}, \\ y_r &= C_{yr}, \\ q_r &= C_{qr}, \end{aligned} \tag{9}$$

where C_{xr}, C_{yr}, and C_{qr} are constant values. Besides, since the left leg is the swing one, there is no ground contact force in the left foot, namely

$$F_L = [0 \quad 0 \quad 0]^T. \tag{10}$$

Since $[\dot{x}_r \quad \dot{y}_r \quad \dot{q}_r]^T = J_R\dot{q}$, it can be transformed into

$$[\dot{x}_r \quad \dot{y}_r \quad \dot{q}_r]^T = \begin{bmatrix} J_R U_1^T & J_R U_2^T \end{bmatrix} \begin{bmatrix} \dot{q}_{lp} \\ \dot{q}_c \end{bmatrix}. \tag{11}$$

Differentiating (9) while noting (11) and (2), we can obtain

$$\begin{aligned} M\ddot{q} + C\dot{q} + G &= B_a T_{act} + J_L^T F_L + J_R^T F_R, \\ \ddot{q}_{lp} &= \dot{J}_{Rq}\dot{q}_c + J_{Rq}\ddot{q}_c, \\ F_L &= [0 \quad 0 \quad 0]^T. \end{aligned} \tag{12}$$

Here, there are 15 unknown variables ($\ddot{q}$, F_L, and F_R) and 15 equations (Equation (12)). Treating T_{act} as input, $\ddot{q}$, F_L, and F_R can be computed. Finally, the dynamics can be obtained as

$$\ddot{q}_c = M_{\text{Rsp}}^{-1}\left(T_{\text{act}} - C_{\text{Rsp}}\dot{q}_c - G_{\text{Rsp}}\right), \tag{13}$$

where M_{Rsp}, C_{Rsp}, G_{Rsp}, M_{Rsp2}, C_{Rsp2}, and G_{Rsp2} are matrices computed from M, C, and G, as follows:

$$M_{Rsp} = U_2 M U_2^T + J_{Rq}^T U_1 M U_1^T J_{Rq} + U_2 M U_1^T J_{Rq} + J_{Rq}^T U_1 M U_2^T,$$

$$\begin{aligned} C_{Rsp} = {} & U_2 C U_2^T + J_{Rq}^T U_1 C U_1^T J_{Rq} + U_2 M U_1^T \dot{J}_{Rq} + U_2 C U_1^T J_{Rq} \\ & + J_{Rq}^T U_1 M U_1^T \dot{J}_{Rq} + J_{Rq}^T U_1 C U_2^T, \end{aligned}$$

$$G_{Rsp} = U_2 G + J_{Rq}^T U_1 G. \tag{14}$$

(3) Double Leg Support Dynamics. For double leg support, both the positions of the right foot and the left foot are fixed. Thus, the following holonomic constraints exist:

$$\begin{aligned} x_l &= C_{xl}, \\ y_l &= C_{yl}, \\ q_l &= C_{ql}, \\ x_r &= C_{xr}, \\ y_r &= C_{yr}, \\ q_r &= C_{qr}. \end{aligned} \tag{15}$$

Differentiating (15) while noting (11) and (2), we can obtain

$$\begin{aligned} M\ddot{q} + C\dot{q} + G &= B_a T_{\text{act}} + J_L^T F_L + J_R^T F_R, \\ \ddot{q}_{lp} &= [\,0 \quad 0 \quad 0\,]^T, \\ \ddot{q}_{lp} &= \dot{J}_{Rq}\dot{q}_c + J_{Rq}\ddot{q}_c. \end{aligned} \tag{16}$$

Here, we have 15 unknown variables ($\ddot{q}$, F_L, and F_R) and 15 equations (Equation (16)). Treating T_{act} as input, $\ddot{q}$, F_L, and F_R can be computed.

Finally, the dynamics can be obtained as

$$\ddot{q}_{c1} = M_{\text{Dsp}}^{-1}\left(B_{\text{Dsp}} T_{\text{act}} - C_{\text{Dsp}}\dot{q}_{c1} - G_{\text{Dsp}}\right), \tag{17}$$

where all the new matrices in (17) can be computed from M, C, and G.

Define the following terms:

$$\begin{aligned} A_1 &= U_3 - U_4 J_{Rq2}^{-1} J_{Rq1}, \\ A_2 &= -U_4^T + U_4^T U_2 J_R^T \left(U_3^T U_2 J_R^T\right)^{-1} U_3^T, \\ A_3 &= U_4\left(-J_{Rq2}^{-1}\dot{J}_{Rq1} + J_{Rq2}^{-1}\dot{J}_{Rq2}J_{Rq2}^{-1}J_{Rq1}\right). \end{aligned} \tag{18}$$

M_{Dsp}, C_{Dsp}, G_{Dsp} can be computed as follows:

$$\begin{aligned} M_{Dsp} &= -A_1^T U_4 A_2 U_2 M U_2^T A_1, \\ C_{Dsp} &= -A_1^T U_4 A_2\left(U_2 M U_2^T A_3 + U_2 C U_2^T A_1\right), \\ G_{Dsp} &= -A_1^T U_4 A_2 U_2 G, \\ B_{Dsp} &= -A_1^T U_4 A_2. \end{aligned} \tag{19}$$

(4) Right Heel Strike Dynamics. For right heel strike walking phase, as shown in Figure 1(b), the positions and the rotation angle of the left foot are fixed. Also, the positions of the right foot heel are fixed. Thus, the following holonomic constraints exist:

$$\begin{aligned} x_l &= C_{xl}, \\ y_l &= C_{yl}, \\ q_l &= C_{ql}, \\ x_r &= C_{xr}, \\ y_r &= C_{yr}, \end{aligned} \tag{20}$$

where C_{xr} and C_{yr} are constant values. Besides, since the right leg contact the ground on a point, there is no ground contact torque in the right foot, namely

$$T_r = 0. \tag{21}$$

Differentiating (20) while noting (2) and (11), we can obtain

$$\begin{aligned} M\ddot{q} + C\dot{q} + G &= B_a T_{act} + J_L^T F_L + J_R^T F_R, \\ \ddot{q}_{lp} &= [\,0 \quad 0 \quad 0\,]^T, \\ \ddot{x}_r &= 0, \\ \ddot{y}_r &= 0. \end{aligned} \tag{22}$$

Here, there are 15 unknown variables ($\ddot{q}$, F_L, and F_R) and 15 equations (Equation (22)). Treating T_{act} as input, $\ddot{q}$, F_L, and F_R can be solved.

Denote

$$\begin{aligned} q_{h1} &= [\,q_1 \quad q_2 \quad q_3 \quad q_4\,]^T, \\ q_{h2} &= [\,q_5 \quad q_6\,]^T. \end{aligned} \tag{23}$$

Finally, the dynamics can be obtained as

$$\ddot{q}_{h1} = M_{Hs}^{-1}(B_{Hs} T_{\text{act}} - C_{Hs}\dot{q}_{h1} - G_{Hs}), \tag{24}$$

where all the new matrices in (24) can be computed from M, C, and G.

Define the following terms:

$$\begin{aligned} H_1 &= T_3 - T_4 J_{Rh2}^{-1} J_{Rh1}, \\ H_2 &= -T_4^T + T_4^T U_2 J_R^T \left(T_3^T U_2 J_R^T\right)^{-1} T_3^T, \\ H_3 &= T_4\left(-J_{Rh2}^{-1}\dot{J}_{Rh1} + J_{Rh2}^{-1}\dot{J}_{Rh2}J_{Rh2}^{-1}J_{Rh1}\right). \end{aligned} \tag{25}$$

M_{Hs}, C_{Hs}, and G_{Hs} can be computed as follows:

$$\begin{aligned} M_{Hs} &= -H_1^T U_4 H_2 U_2 M U_2^T H_1, \\ C_{Hs} &= -H_1^T U_4 H_2\left(U_2 M U_2^T H_3 + U_2 C U_2^T H_1\right), \\ G_{Hs} &= -H_1^T U_4 H_2 U_2 G, \\ B_{Hs} &= -H_1^T U_4 H_2. \end{aligned} \tag{26}$$

(5) Left Toe Off Dynamics. For left toe off walking phase, shown in Figure 3(d), the positions and the rotation angle of the right foot are fixed. Also, the positions of the left foot toe are fixed. The holonomic constraints are similar to the right heel strike walking phase. Following the same computation process as that of right heel strike walking phase, the dynamic model of toe off walking phase can be obtained. The detailed computation process is omitted here for simplicity.

2.2. Hydraulic Actuator Dynamics. The pressure and flow rate dynamics of hydraulic cylinders can be described as [18]

$$\begin{aligned}
&\frac{V_{1i}}{\beta_e}\dot{P}_{1i} = -A_{1i}\frac{\partial x_{Li}}{\partial q_i}\dot{q}_i + Q_{1i} + \tilde{D}_{31i},\\
&\frac{V_{2i}}{\beta_e}\dot{P}_{2i} = A_{2i}\frac{\partial x_{Li}}{\partial q_i}\dot{q}_i - Q_{2i} + \tilde{D}_{32i},\\
&Q_{1i} = k_{q1i}x_{vi}\sqrt{|\Delta P_{1i}|},\\
&Q_{2i} = k_{q2i}x_{vi}\sqrt{|\Delta P_{2i}|},\\
&\Delta P_{1i} = \begin{cases} P_s - P_{1i} & \text{if } x_{vi} \geq 0,\\ P_{1i} - P_r & \text{if } x_{vi} < 0,\end{cases}\\
&\Delta P_{2i} = \begin{cases} P_{2i} - P_r & \text{if } x_{vi} \geq 0,\\ P_s - P_{2i} & \text{if } x_{vi} < 0,\end{cases}\\
&x_{vi} = u_i,\\
&i = 1,\quad 2,\quad 3,\quad 4,\quad 5,\quad 6,
\end{aligned} \tag{27}$$

where the definition of all the terms can be seen in the notation list at the Appendix.

2.3. Human-Machine Interface Dynamics. The model of human-machine interaction force may be complex; for example, the model may be uncertain and/or varies. Thus, it is difficult to obtain a precise model that can describe the properties of actual human/robot attachment precisely. Also, a much precise human/robot interface dynamic model may be much complex to be used for designing the controller. Thus, in the paper, only the main property of the interface is considered. Since a belt is often adopted in connecting the robotic leg with the human leg. Thus, a spring model with unknown stiffness can describe the main compliant property of the interface. As for other unmodeled uncertainties, we put them in the lumped disturbance. In the later part, an adaptive robust control algorithm is proposed to address the modeling errors in human-machine interface dynamic model. Thus, the human-machine interface dynamic model is described as a spring with lumped disturbance and unknown stiffness:

$$F_{hm} = K(x_h - x_e) + \tilde{D}_1, \tag{28}$$

where the definition of all the terms can be seen in the notation list at the Appendix. Equation (28) is algebraic and devoid of dynamics. Using the integral of interaction force $\int_0^t F_{hm}d\tau$ in the controller design, then the following dynamic model can be obtained:

$$\frac{d}{dt}\int_0^t F_{hm}dt = K(x_h - x_e) + \tilde{D}_1. \tag{29}$$

3. Human-Machine Interaction Force Control Schemes

3.1. Control Objective. Assuming that the wearer is able to achieve balance and locomotion, the control objective of a walking lower limb exoskeleton is to design a control law according to the multi-phase dynamic models that minimizes the human-machine interaction force so that accurate human motion tracking is achieved.

3.2. Overall Control Structure. Figure 3(a) shows the overall control structure. Foot switches are mounted at the exoskeleton foot to recognize whether the exoskeleton foot contact the ground or not, which can further help us recognize which walking phase the exoskeleton lies in. Six-axis force sensors are fixed at the back and the foot of the lower limb exoskeleton to measure the interaction force at these places. For different walking phase, different interaction force components are selected for force controller design. Many control techniques have been developed for hydraulic systems [19–21]. The ARC is verified to be effective in addressing various model uncertainties through lots of practical applications [22–26], especially for multijoint hydraulic manipulator [27, 28]. Thus, it is adopted in the following controller design. Therefore, it will be adopted in our interaction force control algorithm design. For each walking phase, an adaptive robust cascade force controller (ARCFC) is designed so that a good robust force control performance can be achieved, as shown in Figure 3(b).

3.3. ARCFC Design for Double Leg Support. For the walking phase of double leg support, there are three independent degree of freedoms, which can be seen from the dynamic model (17). Thus, in double leg support, we can only control three independent human-machine interaction force components. Since the exoskeleton feet are always in flat contact with the ground and will not hinder the movement of human feet, there is no need to reduce the interaction force at the foot contact points. Finally, three human-machine interaction force components at the back are minimized. Since there are six control inputs, the system is overactuated. In the later force controller design, three independent virtual control torques are figured out first, and then, a torque allocation method is proposed to specify the desired load force for six hydraulic cylinders. Finally, six control inputs of the hydraulic valves can be figured out.

The overall system dynamics for double leg support can be described by

$$F_{\text{hmub}} = K(x_{\text{hub}} - x_{\text{eub}}) + \tilde{D}_1,$$

$$q_{c1} = invkine_{\text{ub}}(x_{\text{eub}}), q_{c2} = invkine_r(x_{\text{er}}, q_{c1}), \dot{q}_{c2} = -J_{\text{Rq2}}^{-1}J_{\text{Rq1}}\dot{q}_{c1},$$

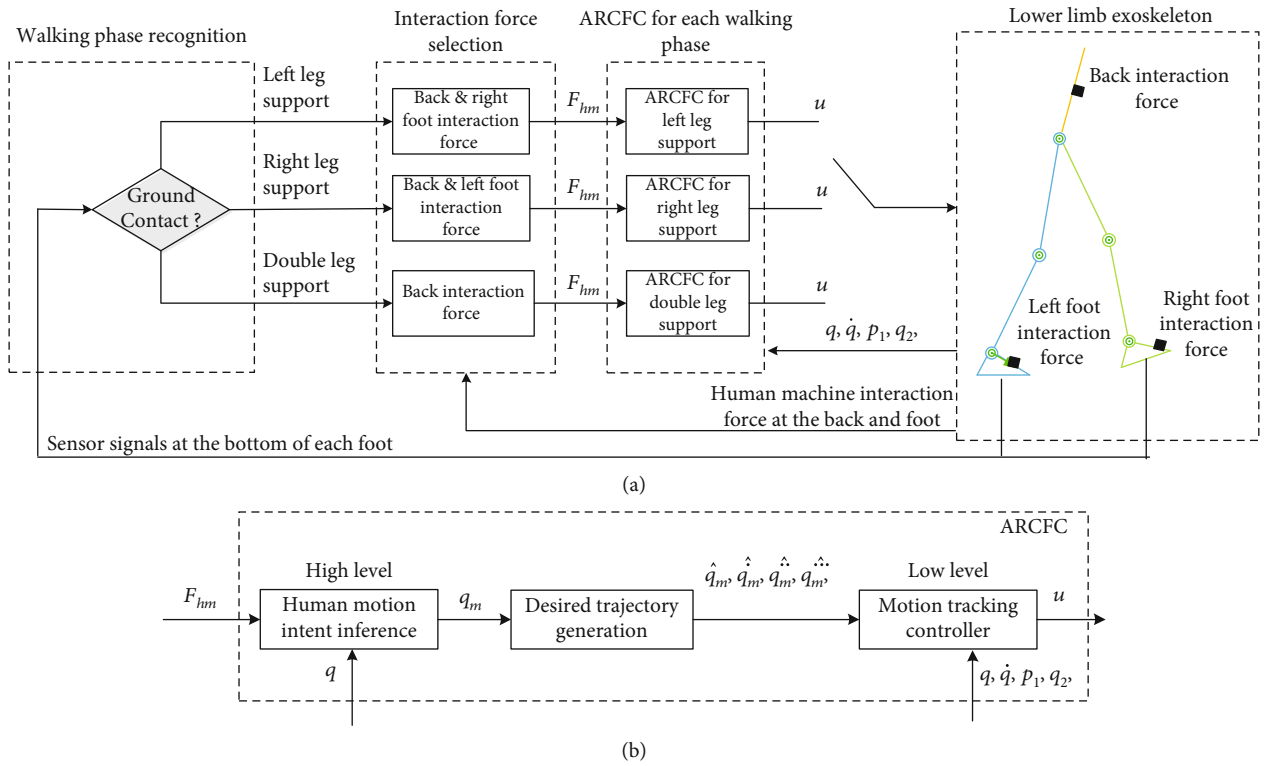

FIGURE 3: Control structure of the lower limb walking exoskeleton: (a) overall control structure and (b) structure of the adaptive robust cascade force controller (ARCFC).

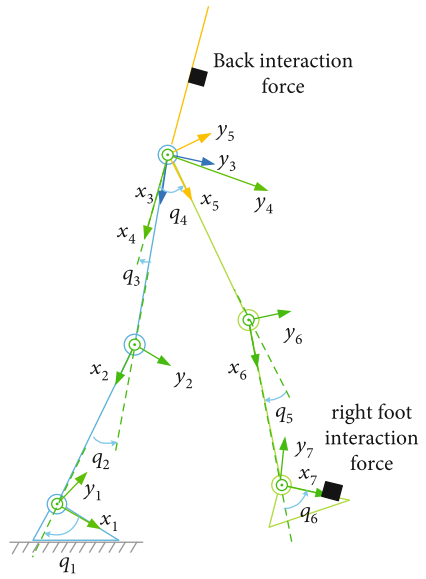

FIGURE 4: Human-machine interaction force minimized in left leg support. In this walking phase, six interaction force components at the back and right foot contact points will be minimized.

$$B_{\mathrm{Dsp}} T_{\mathrm{act}} + J_{\mathrm{ub}}^{T} F_{\mathrm{hmub}} = M_{\mathrm{Dsp}} \ddot{q}_{c1} + C_{\mathrm{Dsp}} \dot{q}_{c1} + G_{\mathrm{Dsp}} + B\dot{q}_{c1} + \tilde{D}_2,$$

$$q_c = [\, q_{c1} \quad q_{c2} \,]^T, \tau_i = (P_{1i} A_{1i} - P_{2i} A_{2i}) \frac{\partial x_{\mathrm{Li}}}{\partial q_i},$$

$$\frac{V_{1i}}{\beta_e} \dot{P}_{1i} = -A_{1i} \frac{\partial x_{\mathrm{Li}}}{\partial q_i} \dot{q}_i + Q_{1i} + \tilde{D}_{31i}, \frac{V_{2i}}{\beta_e} \dot{P}_{2i} = A_{2i} \frac{\partial x_{\mathrm{Li}}}{\partial q_i} \dot{q}_i - Q_{2i} + \tilde{D}_{32i},$$

$$Q_{1i} = k_{q1i} x_{\mathrm{vi}} \sqrt{|\Delta P_{1i}|}, Q_{2i} = k_{q2i} x_{\mathrm{vi}} \sqrt{|\Delta P_{2i}|},$$

$$\Delta P_{1i} = \begin{cases} P_s - P_{1i} & \text{if } x_{\mathrm{vi}} \geq 0, \\ P_{1i} - P_r & \text{if } x_{\mathrm{vi}} < 0, \end{cases} \Delta P_{2i} = \begin{cases} P_{2i} - P_r & \text{if } x_{\mathrm{vi}} \geq 0, \quad x_{\mathrm{vi}} = u_i, \\ P_s - P_{2i} & \text{if } x_{\mathrm{vi}} < 0, \quad i = 1 \cdots 6, \end{cases} \tag{30}$$

where $K = \mathrm{diag}\{K_{\mathrm{ubx}}, K_{\mathrm{uby}}, K_{\mathrm{ubz}}\}$ is the stiffness vector of the human-machine interface and $B = \mathrm{diag}\{B_1, B_2, B_3\}$ is the damping ratio. The definitions of all the other terms can be seen in the notation list at the Appendix.

The fifth equation of (30) has three properties:

Property 1. M_{Dsp} is a symmetric and positive definite matrix.

Property 2. $\dot{M}_{\mathrm{Dsp}} - 2C_{\mathrm{Dsp}}$ is a skew-symmetric matrix.

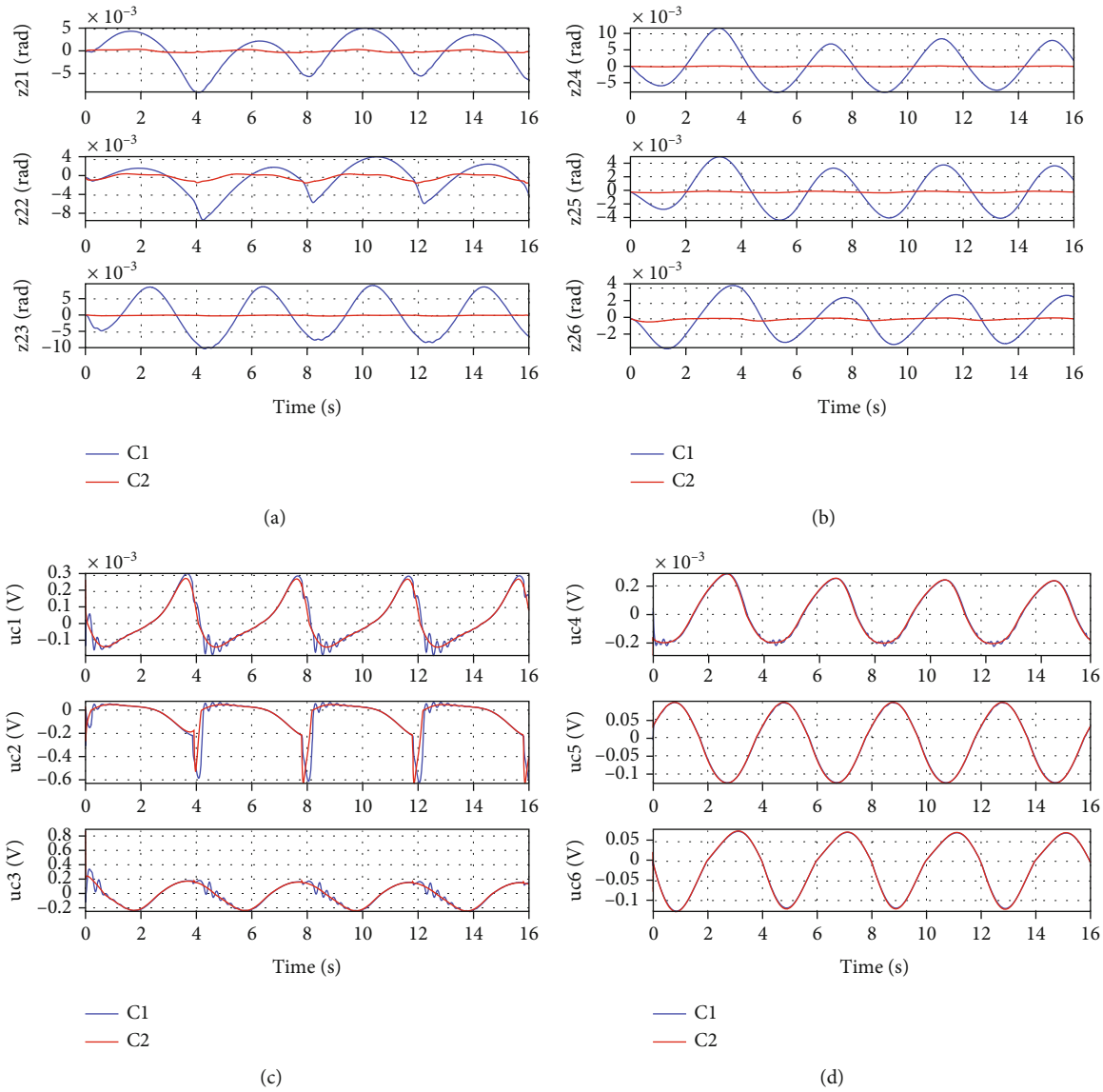

FIGURE 5: Simulation results of left leg support for Set1: (a) motion tracking error for the left leg joints, (b) motion tracking error for the right leg joints, (c) control input for the left leg joints, and (d) control input for the right leg joints.

Property 3. M_{Dsp}, C_{Dsp}, and G_{Dsp} can be linearly parameterized in term of the exoskeleton system parameters β, i.e.,

$$M_{\mathrm{Dsp}}(q_c)\ddot{q}_r + C_{\mathrm{Dsp}}(q_c, \dot{q}_c)\dot{q}_r + G_{\mathrm{Dsp}}(q_c) = f_0(q_c, \dot{q}_c, \dot{q}_r, \ddot{q}_r) + Y(q_c, \dot{q}_c, \dot{q}_r, \ddot{q}_r)\beta, \tag{31}$$

where $\dot{q}_r$ and $\ddot{q}_r$ are any vector and β is the parameter vector of the exoskeleton.

Define the following unknown parameters and lumped disturbances:

$$\tilde{\Delta}_1 = x_h + K^{-1}\tilde{D}_1,$$
$$\tilde{\Delta}_3 = -\tilde{D}_2,$$
$$\tilde{\Delta}_4 = \left[\frac{\tilde{D}_{311}\beta_e A_{11}}{V_{11}} - \frac{\tilde{D}_{321}\beta_e A_{21}}{V_{21}}, \frac{\tilde{D}_{312}\beta_e A_{12}}{V_{12}} - \frac{\tilde{D}_{322}\beta_e A_{22}}{V_{22}}, \frac{\tilde{D}_{313}\beta_e A_{13}}{V_{13}} - \frac{\tilde{D}_{323}\beta_e A_{23}}{V_{23}}, \frac{\tilde{D}_{314}\beta_e A_{14}}{V_{14}} - \frac{\tilde{D}_{324}\beta_e A_{24}}{V_{24}}, \frac{\tilde{D}_{315}\beta_e A_{15}}{V_{15}} - \frac{\tilde{D}_{325}\beta_e A_{25}}{V_{25}}, \frac{\tilde{D}_{316}\beta_e A_{16}}{V_{16}} - \frac{\tilde{D}_{326}\beta_e A_{26}}{V_{26}}\right],$$
$$\tilde{\Delta}_i = \Delta_{\mathrm{in}} + \Delta_i, \quad i = 1, 3, 4,$$
$$K_\theta = \left[1/K_{\mathrm{ubx}} \quad 1/K_{\mathrm{uby}} \quad 1/K_{\mathrm{ubz}}\right]^T,$$
$$\Delta_{1n} = \left[\Delta_{1\mathrm{ubnx}} \quad \Delta_{1\mathrm{ubny}} \quad \Delta_{1\mathrm{ubnz}}\right]^T,$$

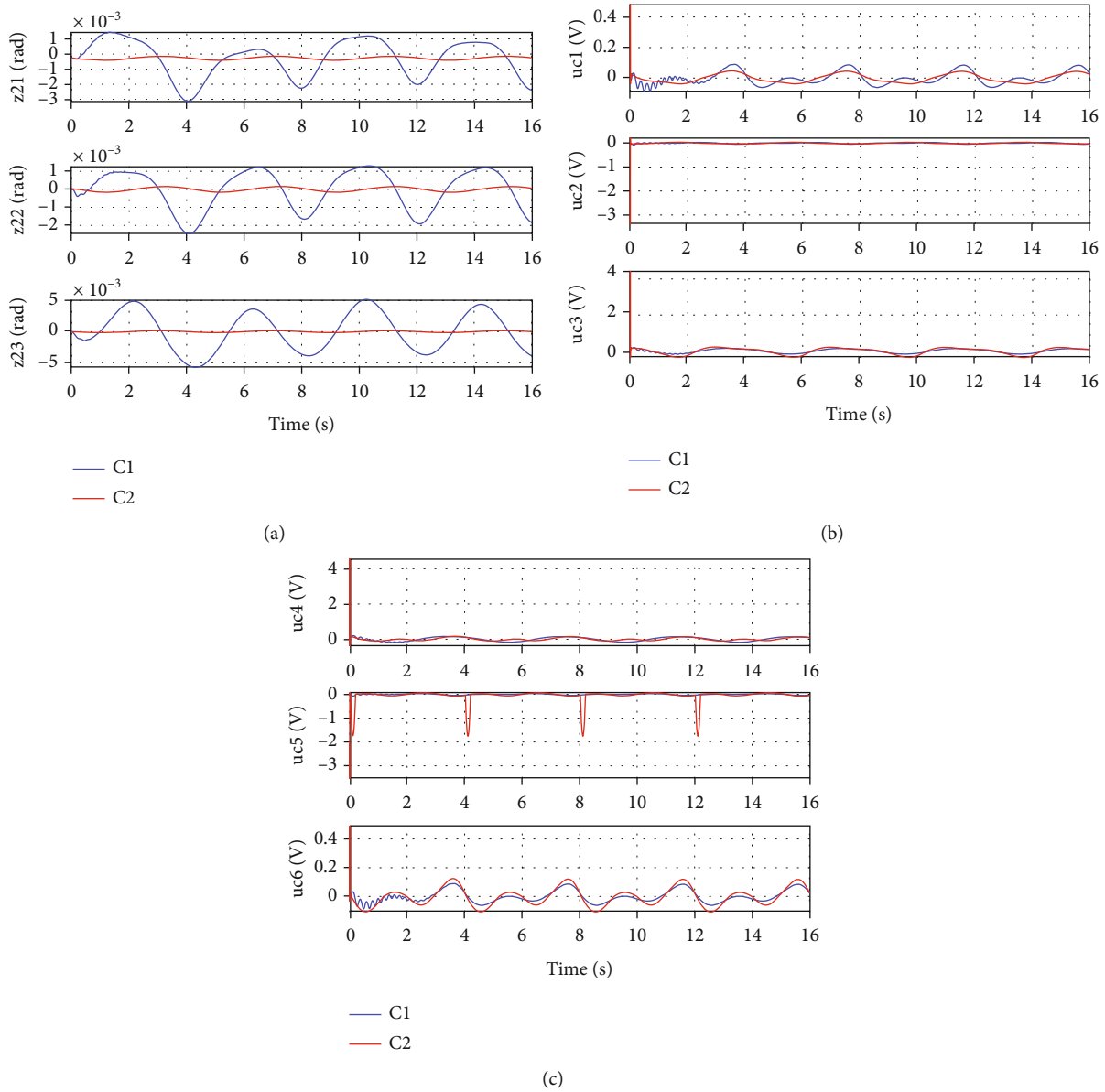

FIGURE 6: Simulation results of double leg support for Set1: (a) motion tracking error for left leg joints, (b) control input for left leg joints, (c) control input for right leg joints.

$$
\begin{aligned}
B_\theta &= [\, B_1 \quad B_2 \quad B_3 \,]^T,\\
\Delta_{3n} &= [\, \Delta_{3n1} \quad \Delta_{3n2} \quad \Delta_{3n3} \,]^T,\\
\Delta_{4n} &= [\, \Delta_{4n1} \quad \Delta_{4n2} \quad \Delta_{4n3} \quad \Delta_{4n4} \quad \Delta_{4n5} \quad \Delta_{4n6} \,]^T,\\
\theta_F &= \left[\, K_\theta^T \quad \Delta_{1n}^T \,\right]^T,\\
\theta_q &= \left[\, \beta^T \quad B_\theta^T \quad {\Delta_{3n}}^T \quad \beta_e \quad {\Delta_{4n}}^T \,\right]^T,\\
\theta &= \left[\, \theta_F^T \quad \theta_q^T \,\right]^T,
\end{aligned} \tag{32}
$$

where Δ_{in} and Δ_i are the constant and the time-varying part of $\tilde{\Delta}_i$. We assume that the bound of the uncertain parameters and disturbance is known.

Define the following states:

$$
\begin{aligned}
x_1 &= \int_0^t F_{\text{hmub}}\, dt,\\
x_2 &= [\, x_{21} \quad x_{22} \,]^T, \quad x_{21} = q_{c1}, x_{22} = q_{c2},\\
x_3 &= [\, x_{31} \quad x_{32} \,]^T, \quad x_{31} = \dot{q}_{c1}, x_{32} = \dot{q}_{c2},\\
x_4 &= P_1 = [\, P_{11} \quad P_{12} \quad P_{13} \quad P_{14} \quad P_{15} \quad P_{16} \,]^T,\\
x_5 &= P_2 = [\, P_{21} \quad P_{22} \quad P_{23} \quad P_{24} \quad P_{25} \quad P_{26} \,]^T,\\
x &= [\, x_1^T \quad {x_{21}}^T \quad {x_{31}}^T \quad {x_4}^T \quad {x_5}^T \,]^T.
\end{aligned} \tag{33}
$$

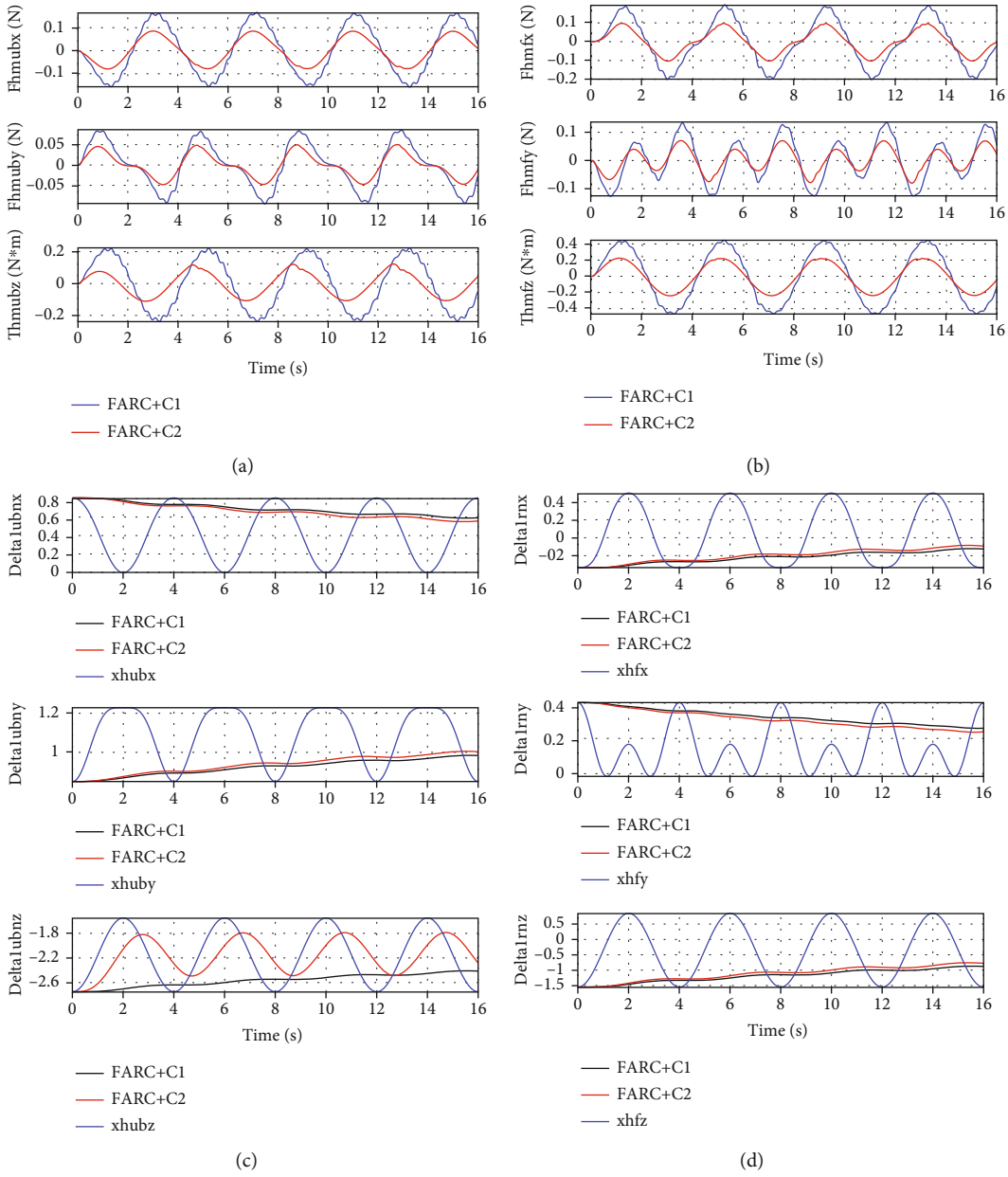

FIGURE 7: Simulation results of left leg support for Set2: (a) human-machine interaction force at the back, (b) human-machine interaction force at the right foot, (c) parameter estimation of Δ_{1n} at the back, and (d) parameter estimation of Δ_{1n} at the right foot.

The state space expression of dynamics (30) can be described as

$$\begin{aligned}
\dot{x}_1 &= -Kx_{\text{eub}} + K\Delta_{1n} + K\Delta_1,\\
x_{21} &= \text{invkine}_{\text{ub}}(x_{\text{eub}}),\\
x_{22} &= \text{invkine}_r(x_{\text{er}}, x_{21}),\\
\dot{x}_{21} &= x_{31},\\
x_{32} &= -J_{\text{Rq2}}^{-1} J_{\text{Rq1}} x_{31},\\
\dot{x}_{31} &= M_{\text{Dsp}}^{-1}\left[B_{\text{Dsp}} h P_L + J_{\text{ub}}^T F_{\text{hmub}} - C_{\text{Dsp}} x_{31} - G_{\text{Dsp}} - B x_{31} + \Delta_{3n} + \Delta_3\right],\\
\dot{P}_L &= Q_L \beta_e - q_v x_3 \beta_e + \Delta_{4n} + \Delta_4,
\end{aligned}$$

$$Q_L = K_q u, \tag{34}$$

where

$$\begin{aligned}
h &= \text{diag}\left\{\frac{\partial x_{L1}}{\partial q_1}, \frac{\partial x_{L2}}{\partial q_2}, \frac{\partial x_{L3}}{\partial q_3}, \frac{\partial x_{L4}}{\partial q_4}, \frac{\partial x_{L5}}{\partial q_5}, \frac{\partial x_{L6}}{\partial q_6}\right\},\\
A_1 &= \text{diag}\left\{A_{11}, A_{12}, A_{13}, A_{14}, A_{15}, A_{16}\right\},\\
A_2 &= \text{diag}\left\{A_{21}, \quad A_{22}, \quad A_{23}, \quad A_{24}, \quad A_{25}, A_{26}\right\}, P_L = A_1 x_4 - A_2 x_5,
\end{aligned}$$

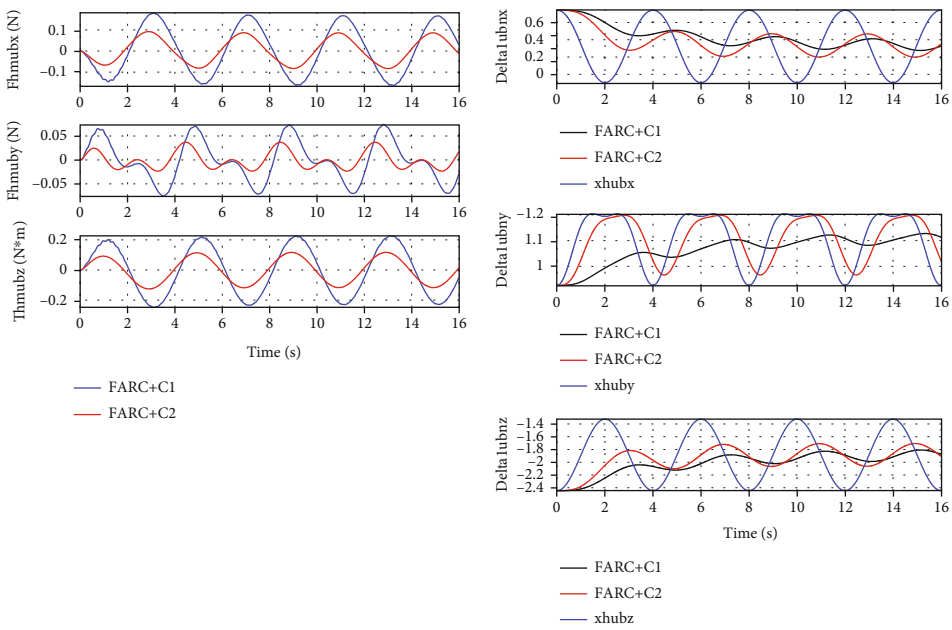

(a) (b)

FIGURE 8: Simulation results of double leg support for Set2: (a) human-machine interaction force at the back, (b) parameter estimation of Δ_{1n} at the back.

$$Q_L = \left[Q_{11}\frac{A_{11}}{V_{11}} + Q_{21}\frac{A_{21}}{V_{21}}, Q_{12}\frac{A_{12}}{V_{12}} + Q_{22}\frac{A_{22}}{V_{22}}, Q_{13}\frac{A_{13}}{V_{13}} + Q_{23}\frac{A_{23}}{V_{23}}, Q_{14}\frac{A_{14}}{V_{14}} + Q_{24}\frac{A_{24}}{V_{24}}, Q_{15}\frac{A_{15}}{V_{15}} + Q_{25}\frac{A_{25}}{V_{25}}, Q_{16}\frac{A_{16}}{V_{16}} + Q_{26}\frac{A_{26}}{V_{26}} \right]^T,$$

$$q_v = \operatorname{diag}\left\{ \left(\frac{A_{11}^2}{V_{11}} + \frac{A_{21}^2}{V_{21}}\right)\frac{\partial x_{L1}}{\partial q_1}, \left(\frac{A_{12}^2}{V_{12}} + \frac{A_{22}^2}{V_{22}}\right)\frac{\partial x_{L2}}{\partial q_2}, \cdot \left(\frac{A_{13}^2}{V_{13}} + \frac{A_{23}^2}{V_{23}}\right)\frac{\partial x_{L3}}{\partial q_3}, \left(\frac{A_{14}^2}{V_{14}} + \frac{A_{24}^2}{V_{24}}\right)\frac{\partial x_{L4}}{\partial q_4}, \cdot \left(\frac{A_{15}^2}{V_{15}} + \frac{A_{25}^2}{V_{25}}\right)\frac{\partial x_{L5}}{\partial q_5}, \left(\frac{A_{16}^2}{V_{16}} + \frac{A_{26}^2}{V_{26}}\right)\frac{\partial x_{L6}}{\partial q_6} \right\},$$

$$\begin{aligned} K_q = \operatorname{diag}\Bigg\{ & k_{q11}\frac{A_{11}}{V_{11}}\sqrt{|\Delta P_{11}|} + k_{q21}\frac{A_{21}}{V_{21}}\sqrt{|\Delta P_{21}|}, k_{q12}\frac{A_{12}}{V_{12}}\sqrt{|\Delta P_{12}|} \\ & + k_{q22}\frac{A_{22}}{V_{22}}\sqrt{|\Delta P_{22}|}, k_{q13}\frac{A_{13}}{V_{13}}\sqrt{|\Delta P_{13}|} \\ & + k_{q23}\frac{A_{23}}{V_{23}}\sqrt{|\Delta P_{23}|}, k_{q14}\frac{A_{14}}{V_{14}}\sqrt{|\Delta P_{14}|} \\ & + k_{q24}\frac{A_{24}}{V_{24}}\sqrt{|\Delta P_{24}|}, k_{q15}\frac{A_{15}}{V_{15}}\sqrt{|\Delta P_{15}|} \\ & + k_{q25}\frac{A_{25}}{V_{25}}\sqrt{|\Delta P_{25}|}, k_{q16}\frac{A_{16}}{V_{16}}\sqrt{|\Delta P_{16}|} + k_{q26}\frac{A_{26}}{V_{26}}\sqrt{|\Delta P_{26}|} \Bigg\}. \end{aligned} \tag{35}$$

The control goal is to synthesize a control input $u = [u_1 \quad u_2 \quad u_3 \quad u_4 \quad u_5 \quad u_6]^T$ based on (34) that minimizes the human-machine interaction force F_{hmub}.

3.3.1. High-Level Human Motion Intent Inference. Treating x_{eub} as virtual control input, then a control law making the integral of force tracking error $z_1 = x_1 - x_{1d}$ converge to zero or to be bounded is designed as

$$\begin{aligned} x_m &= x_{\text{ma}} + x_{\text{ms}}, \\ x_{\text{ma}} &= -\widehat{K}_f \dot{x}_{1d} + \widehat{\Delta}_{1n} = -f_{\theta_F} - Y_{\theta_F}\widehat{\theta}_F, \\ x_{\text{ms}} &= K_1 z_1 + x_{\text{msn}}, \\ \dot{\widehat{\theta}}_F &= \text{Proj}\left(-\Gamma_1 Y_{\theta_F}^T z_1\right), \end{aligned} \tag{36}$$

$$\text{Proj}_i(\bullet_i) = \begin{cases} 0 & \text{if } \widehat{\theta}_{Fi} = \theta_{F\max i} \quad \text{and} \quad \bullet_i > 0, \\ 0 & \text{if } \widehat{\theta}_{Fi} = \theta_{F\min i} \quad \text{and} \quad \bullet_i < 0, \\ \bullet_i & \text{otherwise}, \end{cases}$$

where x_{ma} is the model compensation term, x_{ms} is the robust feedback term, $K_1 = \text{diag}\{K_{11}, K_{12}, K_{13}\}$ is the linear feedback gain, $\Gamma_1 > 0$ is a diagonal adaptation rate matrix, x_{msn} is a nonlinear feedback item, $K_f = K^{-1}$, and $K_f\dot{x}_{1d} - \Delta_{1n} = f_{\theta_F} + Y_{\theta_F}\theta_F$.

We can treat x_m as inferred human motion intent, and then, the desired joint positions can be obtained as

$$q_{c1m} = \text{invkine}_{\text{ub}}(x_m). \tag{37}$$

Let $z_{2h} = \text{Kine}(x_{21}) - x_m$, where Kine means kinematics. Then, the first error dynamics is given as

$$K_f\dot{z}_1 = -K_1 z_1 - z_{2h} + \Delta_1 + Y_{\theta F}\widetilde{\theta}_F - x_{msn}. \tag{38}$$

Similar to [18], in order to obtain the desired motion trajectories ($\widehat{q}_{c1m}$, $\dot{\widehat{q}}_{c1m}$, $\ddot{\widehat{q}}_{c1m}$, and $\widehat{q}^{(3)}_{c1m}$), a output differential observer is adopted.

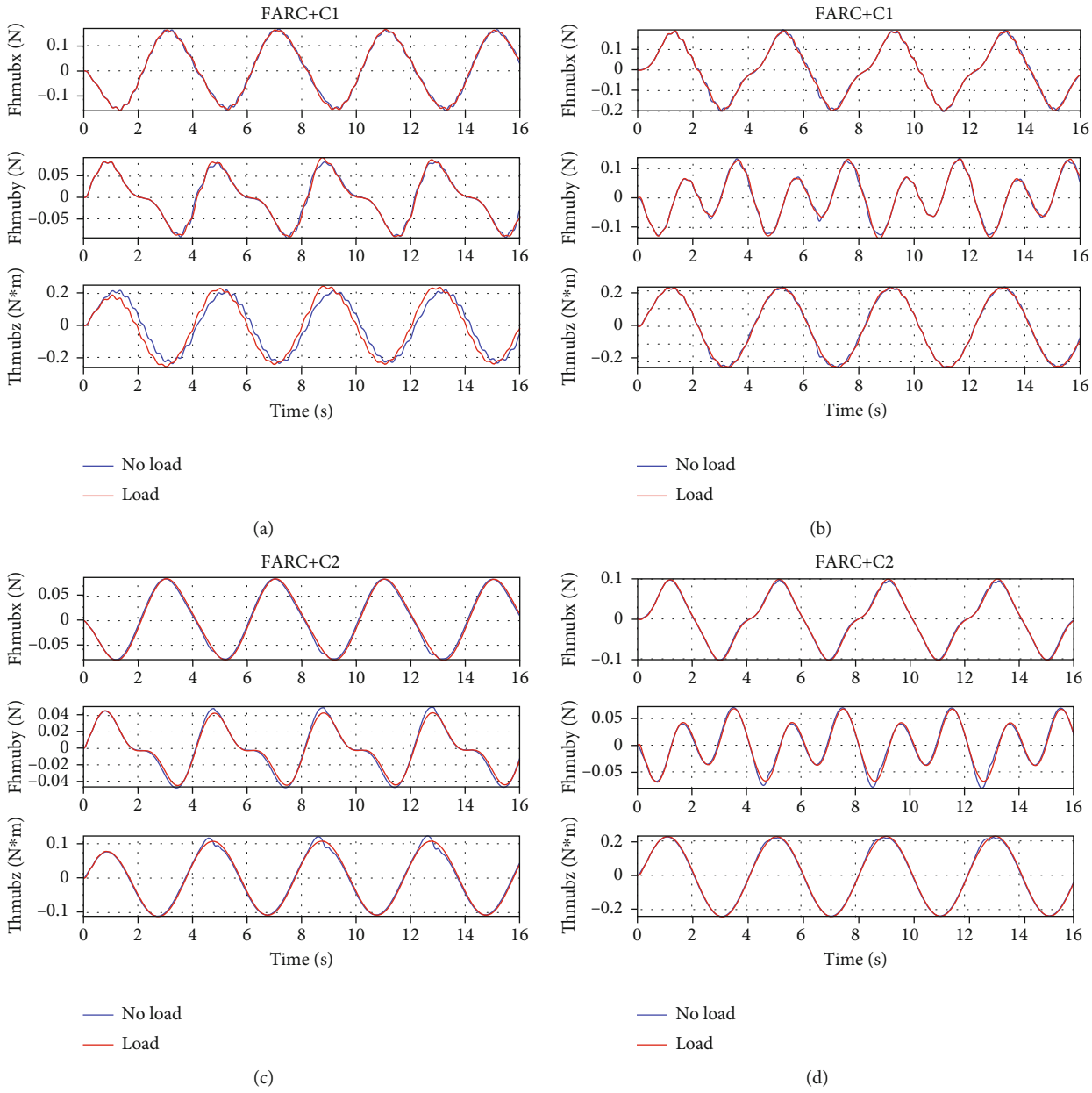

Figure 9: Human-machine interaction force of left leg support for Set3: (a) at the back for FARC+C1, (b) at the right foot for FARC+C1, (c) at the back for FARC+C2, and (d) at the right foot for FARC+C2.

3.3.2. Low-Level MIMO Motion Tracking Controller. In low-level controller design, a motion tracking control algorithm making the position tracking error $z_2 = x_{21} - \widehat{q}_{c1m}$ converge to zero or to be bounded is proposed with the following design procedures.

Step 1. Specify the desired torque τ_{actd} for $B_{\text{Dsp}}hP_L$ that achieves accurate motion tracking (i.e., $x_{21} \longrightarrow \widehat{q}_{c1m}$ if $B_{\text{Dsp}}hP_L = \tau_{actd}$).

Treating $B_{\text{Dsp}}hP_L$ as the virtual control input in this part, the control law τ_{actd} is given as

$$\begin{aligned}
\tau_{\text{actd}} &= \tau_{\text{actda}} + \tau_{\text{actds}},\\
\tau_{\text{actda}} &= f_0 + Y\widehat{\beta} + Y_B\widehat{B}_\theta - \widehat{\Delta}_{3n} - J_{\text{ub}}^T F_{\text{hmub}},\\
\tau_{\text{actds}} &= -K_{3s1}z_3 + \tau_{\text{actdsn}},\\
z_3 &= \dot{z}_2 + K_2 z_2,\\
K_{3s1} &= g_3\|\Gamma_2\phi_3\|^2 + K_3,
\end{aligned} \tag{39}$$

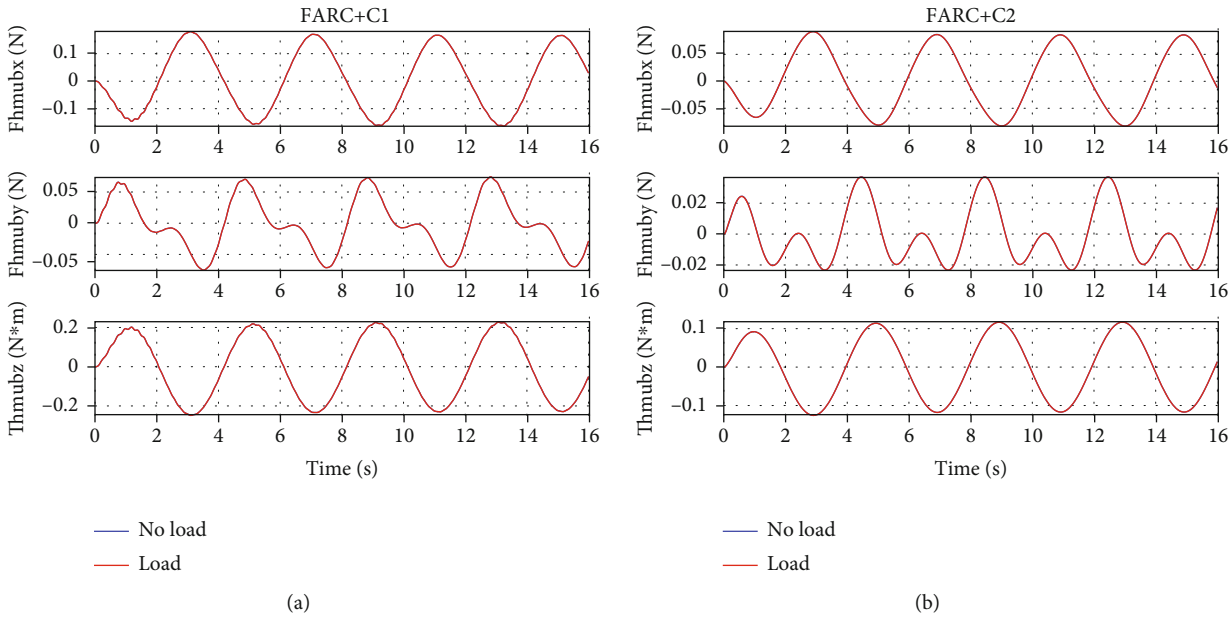

FIGURE 10: Human-machine interaction force of double leg support for Set3: (a) at the back for FARC+C1 and (b) at the back for FARC+C2.

where τ_{actda} is the term for model compensation, τ_{actds} is the robust feedback item, K_{3s1} is the gain for linear feedback, $K_3 > 0$, $g_3 > 0$, $\Gamma_2 > 0$, and τ_{actdsn} is a term for nonlinear feedback. $Bx_{31} = Y_B(x_{31})B_\theta$.

Step 2. Torque allocation (i.e., specify the desired load force P_{Ld} for each hydraulic cylinder such that $B_{\text{Dsp}}hP_{\text{Ld}} = \tau_{\text{actd}}$).

With τ_{actd} given in Step 4, the next task is to figure out the desired load force for each hydraulic cylinder such that the combined effort equals τ_{actd}. Since the system is overactuated, there is an infinite number of solutions unless additional constraints can be added. Here, an intuitive scheme inspired from the CGA data during double stance is used to allocate the operational force between the two legs without relying on computationally expensive optimization methods. It is observed that the leg with foot lying closest to the torso center of mass takes a greater portion of the load [3]. Thus, the following constraints are added:

$$\frac{J_{\text{ubL}}^{-T}\tau_L}{J_{\text{ubR}}^{-T}\tau_R} = \frac{x_{TR}}{x_{TL}}, \tag{40}$$

where J_{ubL} and J_{ubR} represent the Jacobian matrix at the back point in the left leg and in the right leg, respectively. $\tau_L = [\tau_1 \quad \tau_2 \quad \tau_3]$. $\tau_R = [\tau_6 \quad \tau_5 \quad \tau_4]$. x_{TR} and x_{TL} represent the horizontal distance from back to right ankle and the horizontal distance from back to left ankle. With (40), P_{Ld} can be solved.

Step 3. Specify the desired flowQ_{Ld} for Q_L so that the actual load force tracks the desired load force synthesized in Step 5.

The same as [18], the joint velocity and acceleration used to compute $\dot{P}_{\text{Ld}}$ for adaptive model compensation are estimated through an adaptive robust observer.

Define the observer errors as

$$\begin{aligned} e_{o1} &= x_{21} - y, \\ e_{o2} &= \dot{e}_{o1} + K_{o1}e_{o1} = x_{31} - \dot{y}_r, \\ \dot{y}_r &\triangleq \dot{y} - K_{o1}e_{o1}. \end{aligned} \tag{41}$$

Then the nonlinear observer can be designed as

$$\begin{aligned} e_{o1} &= x_{21} - y, \\ e_{o2} &= \dot{e}_{o1} + K_{o1}e_{o1} = x_{31} - \dot{y}_r, \\ \dot{y}_r &\triangleq \dot{y} - K_{o1}e_{o1}, \\ \bar{M}_{\text{Dsp}}\ddot{y}_r &= B_{\text{Dsp}}hP_L + J_{\text{ub}}^T F_{\text{hmub}} - \bar{C}_{\text{Dsp}}\dot{y}_r - \bar{G}_{\text{Dsp}} - \bar{B}\dot{y}_r + \bar{\Delta}_{3n} \\ &\quad + T_{\text{os}} + (K_{o2} + K_{o2s})e_{o2}, \\ \dot{\bar{\theta}}_q &= -\text{Proj}\left(\Gamma_o\phi_o^T e_{o2}\right), \end{aligned} \tag{42}$$

where y and $\dot{y}_r$ are the estimated joint positions and joint velocities, K_{o1} is any gain matrix, $\bar{M}_{\text{Dsp}}$, $\bar{C}_{\text{Dsp}}$, and $\bar{G}_{\text{Dsp}}$ represent the estimated matrices using new parameter estimation $\bar{\theta}_q$, K_{o2} is the gain for linear feedback, K_{o2s} is the gain for nonlinear feedback, and T_{os} is the robust feedback term.

Replacing $\dot{q}_{c1}$ with $\dot{y}_r$ in P_{Ld}, the estimated P_{Ld} can be obtained where $\hat{P}_{\text{Ld}} = P_{\text{Ld}}(q_{c1}, \dot{y}_r, \hat{\theta}_q, t)$. Let $\hat{z}_4 = P_L - \hat{P}_{\text{Ld}}$. Treating Q_L as the control input in this part, the proposed

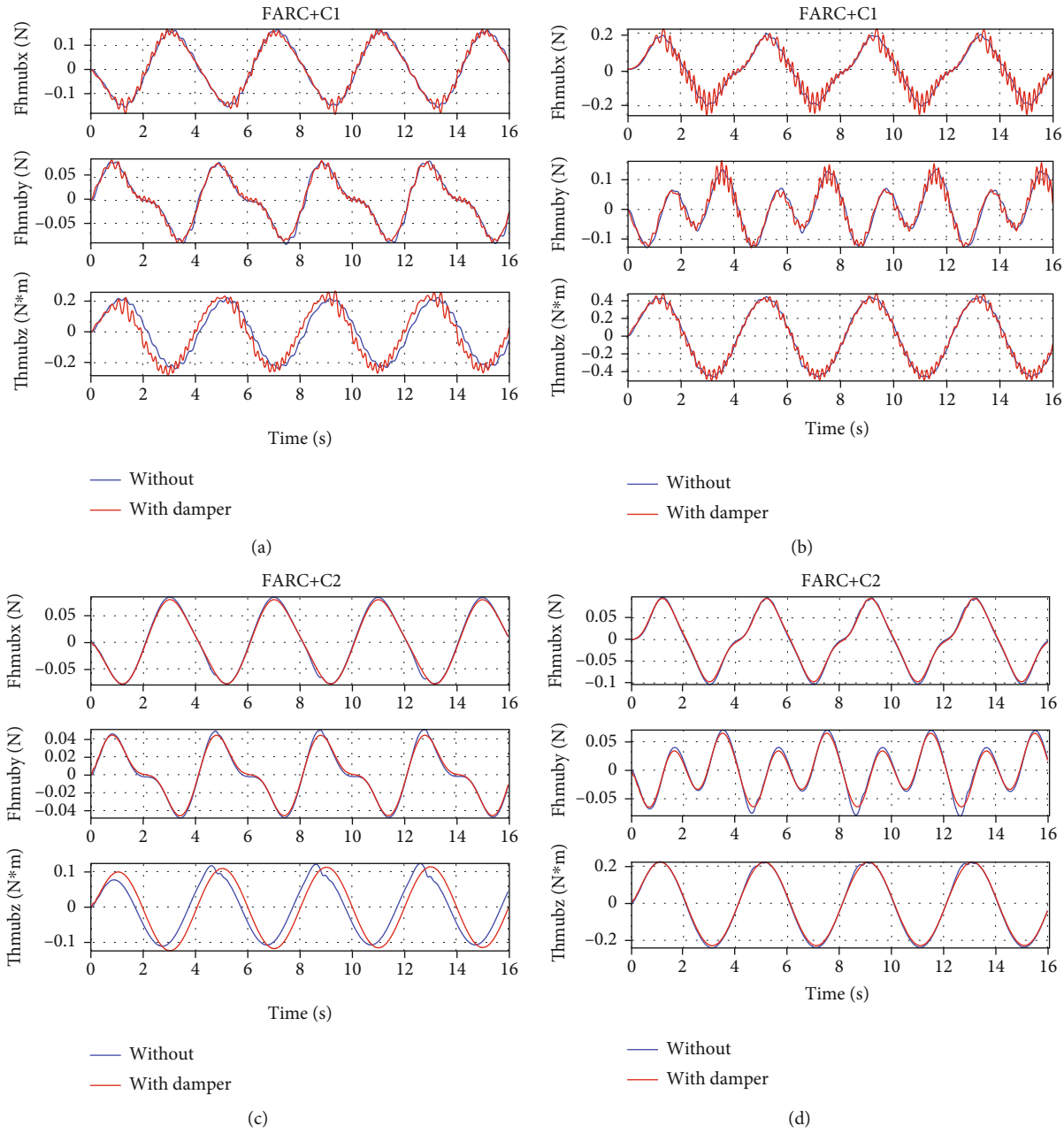

FIGURE 11: Simulation results of left leg support for Set4: (a) human-machine interaction force at the back for FARC+C1, (b) human-machine interaction force at the right foot for FARC+C2, (c) human-machine interaction force at the back for FARC+C2, and (d) human-machine interaction force at the right foot for FARC+C2.

control law making $\widehat{z}_4 = P_L - \widehat{P}_{Ld}$ converge to zero or bounded is synthesized as follows:

$$Q_{\mathrm{Ld}} = Q_{\mathrm{Lda}} + Q_{\mathrm{Lds}},$$

$$Q_{\mathrm{Lda}} = \frac{1}{\widehat{\beta}_e}\left(-\phi_{4c}^T\widehat{\theta}_q - hB_{\mathrm{Dsp}}^T z_3 + \frac{\partial \widehat{P}_{\mathrm{Ld}}}{\partial x_2}x_3 + \frac{\partial \widehat{P}_{\mathrm{Ld}}}{\partial \dot{y}_r}\ddot{y}_r + \frac{\partial \widehat{P}_{\mathrm{Ld}}}{\partial t}\right),$$

$$Q_{\mathrm{Lds}} = \frac{1}{\beta_{e\,\min}}\left(-K_{4s1}\widehat{z}_4\right) + Q_{\mathrm{Ldsn}},$$

$$K_{4s1} = g_4\|\Gamma_2\phi_4\|^2 + d_4\left\|\frac{\partial P_{Ld}}{\partial \widehat{\theta}_q}\right\|^2 + K_4, \tag{43}$$

where Q_{Lda} and Q_{Lds} are the terms for model compensation and robust feedback, respectively, $\phi_{4c} = [\phi_{4c1}\ \ \phi_{4c2}\ \ \phi_{4c3}\ \ \phi_{4c4}\ \ \phi_{4c5}]^T$ is the vector with $\phi_{4c1} = 0_{6\times16}$, $\phi_{4c2} = 0_{6\times6}$, $\phi_{4c3} = 0_{6\times6}$, $\phi_{4c4} = -q_v x_3$, and $\phi_{4c5} = I_{6\times6}$, K_{4s1} is the linear feedback gain, $K_4 > 0$, $g_3 > 0$, $d_4 > 0$, and Q_{Ldsn} is a nonlinear feedback term.

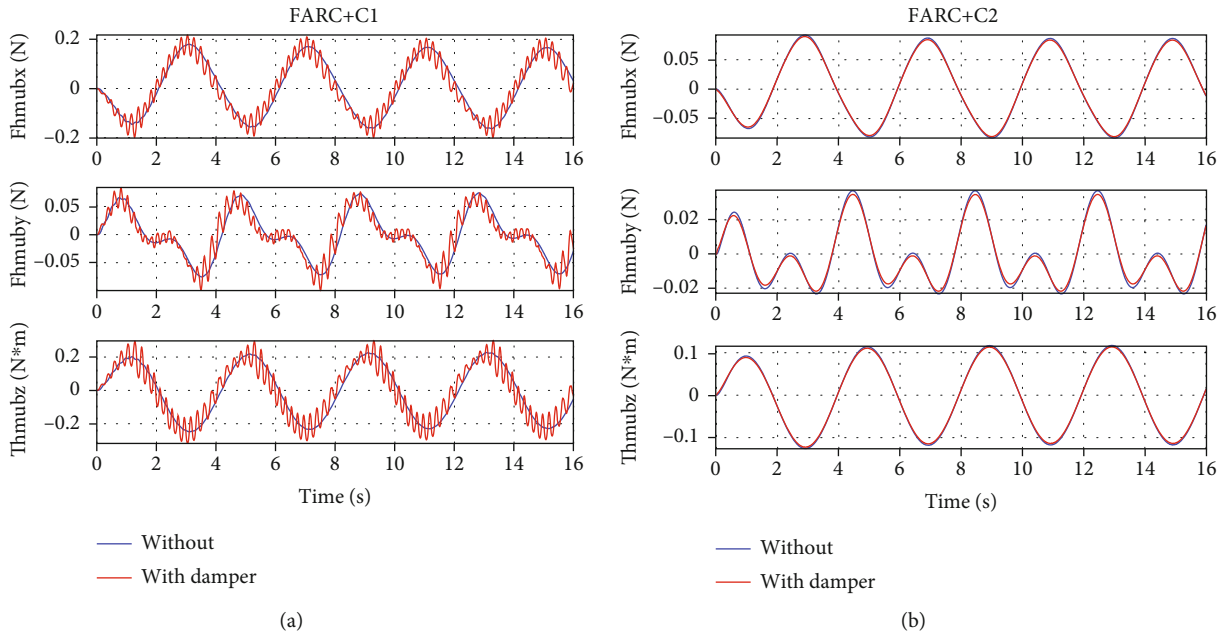

FIGURE 12: Human-machine interaction force of double leg support for Set4: (a) at the back for FARC+C1 and (b) at the back for FARC+C2.

Like $\widehat{\theta}_F$, $\widehat{\theta}_q$ is synthesized as

$$\dot{\widehat{\theta}}_q = \text{Proj}\left[\Gamma_{\theta_q}(\phi_3 z_3 + \phi_4 \widehat{z}_4)\right], \tag{44}$$

where $\Gamma_{\theta_q} > 0$ is the adaptation rate matrix.

Ultimately, we can obtain the control voltage of the valves as

$$u_i = \frac{Q_{\text{Ldi}}}{k_{q1i}(A_{1i}/V_{1i})\sqrt{\Delta P_{1i}} + k_{q2i}A_{2i}/V_{2i}\sqrt{\Delta P_{2i}}}, \quad i = \{1 \ldots 6\}. \tag{45}$$

3.4. Main Results. Furthermore, if $\Delta_i = 0$, $i = 3, 4$, after a finite time, zero final tracking error can be achieved; that is, $z_2 \longrightarrow 0$, as $t \longrightarrow \infty$.Furthermore, if $\Delta_1 = 0$ and $\dot{K}_f = 0$ after a finite time, a bounded force tracking error can be guaranteed with integral converging to zero asymptotically, i.e., $z_1 \longrightarrow 0$, as $t \longrightarrow \infty$.

Theorem 7. *For low-level motion tracking, if the control gains satisfy* $\lambda_{\min}(K_{o2}) \geq k_{o2}$, $\lambda_{\min}(K_{o2s}) \geq 1/2\sigma_e^2$, $\lambda_{\min}(K_3) \geq k_3 + 1/2$, $\lambda_{\min}(K_4) \geq k_4$, $g_3 > 2/4d_4$, *and* $g_4 > 2/4d_4$, *bounded motion tracking errors and observer errors can be guaranteed by the control law (45), which is described by*

$$V_{s4}(t) \leq \exp(-\lambda t)V_{s4}(0) + \frac{\varepsilon}{\lambda}[1 - \exp(-\lambda t)], \tag{46}$$

where

$$V_{s4} = \frac{1}{2}\left(e_{o2}^T M_{Dsp} e_{o2} + z_3^T M_{Dsp} z_3 + \widehat{z}_4^T \widehat{z}_4\right),$$

$$\lambda = 2\min\left\{\frac{\lambda_{\min}(K_3)}{\sup_t\{\lambda_{\max}(M_{Dsp}(t))\}}, \frac{\beta_e}{\beta_{e\min}}\lambda_{\min}(K_4), \frac{\lambda_{\min}(K_{o2})}{\sup_t\{\lambda_{\max}(M_{Dsp}(t))\}}\right\},$$

$$\varepsilon = \varepsilon_o + \varepsilon_3 + \varepsilon_4. \tag{47}$$

Theorem 8. *For human motion intent inference in high-level controller, if the zero tracking error* $z_{2h} = 0$ *is realized in the inner loop, a bounded human-machine interaction force tracking error can be guaranteed by the control law (36), which is described by*

$$V_{s1}(t) \leq \exp(-\lambda_1 t)V_{s1}(0) + \frac{\varepsilon_1}{\lambda_1}[1 - \exp(-\lambda_1 t)], \tag{48}$$

where

$$V_{s1} = (1/2)z_1^T K_f z_1,$$

$$\lambda_1 = 2\frac{\lambda_{\min}(K_1)}{\sup_t\{\lambda_{\max}(K_f(t))\}}. \tag{49}$$

Theorems 7 and 8 can be proved using arguments in [18]. From Theorems 7 and 8, if large controller gains are selected, the force tracking error can still be small when the desired trajectory changes.

3.5. ARCFC Design for Left Leg Support. For the walking phase of left leg support, there exist six independent degree of freedoms and six control inputs, which can be seen from the dynamic model (7). Thus, we can control six

independent human-machine interaction force components. Here, we select to minimize six interaction force components at the back and right foot, as shown in Figure 4.

The dynamics of left leg support is a serial chain one, and there is no overactuated characteristic in the system. Thus, the torque allocation is not needed in the controller design for left leg support. Other steps are almost the same as the ARCFC for double leg support except that the independent degrees of freedoms becomes six compared to three in double leg support. Here, for simplicity, the detail controller design process for left leg support is omitted in this paper.

4. Comparative Simulations

4.1. Simulation Setup. Based on the dynamic model, a simulation model is constructed in MATLAB/Simulink. The simulation parameters are the same as those in [18]. At first, the estimates of system parameters are set to be real values. The lumped disturbances are set to zero. The sampling time is selected as $t_s = 0.0001s$. The value for desired human-machine interaction force is set to zero. Considering the similarity between human body and lower limb exoskeleton, it is better to use human clinical gait analysis (CGA) data as desired joint position for simulation. However, the CGA data is different for people with different height and walking speed. Since the sinusoid curves are often used as desired trajectory for simulation of control algorithms. For a preliminary validation of the proposed controller performance, we choose the desired joint motion trajectory as sinusoid curves. The amplitude and the frequency of the sinusoid curves can be selected on the same order of magnitude as that of CGA data. In the simulation, the following control algorithms are conducted:

C1: The Low-Level PID Control with Velocity Feedforward

The control law is given by

$$u = -K_p z_2 - K_I \int_0^t z_2 dt - K_d \dot{z}_2 + V_f \dot{x}_{2id}, \tag{50}$$

In the simulation, a Z-N method with slight adjustments is used to obtain the control gains of PID controller. For left leg support, $K_p = \text{diag}\{10, 10, 10, 10, 10, 10\}$, $K_I = \text{diag}\{10, 10, 10, 10, 10, 10\}$, $K_d = \text{diag}\{30, 30, 20, 20, 15, 15\}$, and $V_f = \text{diag}\{0.1, 0.1, 0.1, 0.1, 0.1, 0.1\}$. For double leg support, $K_p = \text{diag}\{10, 10, 10, 10, 10, 10\}$, $K_I = \text{diag}\{10, 10, 10, 10, 10, 10\}$, $K_d = \text{diag}\{30, 30, 20, 20, 30, 30\}$, and $V_f = \text{diag}\{0.1, 0.1, 0.1, 0.1, 0.1, 0.1\}$.

C2: The Proposed Low-Level Motion Tracking Controller

According to the gain tuning rules described in [29], for left leg support, $K_2 = \text{diag}\{40, 40, 40, 40, 40, 40\}$, $K_3 = \text{diag}\{100, 100, 100, 100, 100, 100\}$, $K_4 = \text{diag}\{100, 100, 100, 100, 100, 100\}$, $K_{o1} = \text{diag}\{40, 40, 40, 40, 40, 40\}$, and $K_{o2} = \text{diag}\{100, 100, 100, 100, 100, 100\}$. For double leg support, $K_2 = \text{diag}\{320, 320, 320\}$, $K_3 = \text{diag}\{800, 800, 800\}$, and $K_4 = \text{diag}\{800, 800, 800, 800, 800, 800\}$, $K_{o1} = \text{diag}\{320, 320, 320\}$, $K_{o2} = \text{diag}\{800, 800, 800\}$. The adaptive rates are chosen to be zero for simplicity.

FARC: The High-Level Control Algorithms Proposed in This Paper

Different high-level controller gains are selected for different low-level controllers. In left leg support walking phase, for C1, the controller gains are $K_1 = \text{diag}\{4, 4, 4, 4, 4, 4\}$ and $\Gamma_1 = \text{diag}\{0_{1\times6}, 0.2_{1\times2}, 2, 0.2_{1\times3}\}$. For C2, the controller gains are $K_1 = \text{diag}\{8, 8, 8, 8, 8, 8\}$ and $\Gamma_1 = \text{diag}\{0_{1\times6}, 0.25_{1\times2}, 4, 0.25_{1\times3}\}$. In double leg support walking phase, for C1, the controller gains are chosen as $K_1 = \text{diag}\{4, 4, 4\}$ and $\Gamma_1 = \text{diag}\{0_{1\times3}, 1_{1\times3}\}$. For C2, the controller gains are $K_1 = \text{diag}\{8, 8, 8\}$ and $\Gamma_1 = \text{diag}\{0_{1\times3}, 4, 15, 4\}$.

To show the control performance, three sets are simulated:

Set1: motion tracking control of two low-level controllers.

Set2: nominal interaction force control.

Set3: interaction force control to load change.

Set4: interaction force control to human-machine interface modeling errors.

4.2. Simulation Results. In *Set1*, the desired motion trajectory for left leg support is selected as $x_{2d} = [-2 + 0.2\sin((\pi/2)t - \pi/2), 0.5 + 0.2\sin((\pi/2)t - \pi/2), -0.3 + 0.2\sin((\pi/2)t - \pi/2), 0.3 + 0.2\sin((\pi/2)t - \pi/2), -0.5 + 0.2\sin((\pi/2)t - \pi/2), 2 + 0.2\sin((\pi/2)t - \pi/2)]$rad. The desired motion trajectory for double leg support is selected as $x_{2d} = [-2 + 0.2\sin((\pi/2)t - \pi/2), 0.5 + 0.2\sin((\pi/2)t - \pi/2), 0.2\sin((\pi/2)t - \pi/2)]$rad. Figures 5 and 6 show the simulation results for Set1. It is seen that for both left leg support and double leg support, the proposed low-level controller (C2) achieves a smaller motion tracking error. The reason is that the controller gains of C1 can only be selected quite limitedly because of neglecting the strongly coupled dynamics in the controller design, while the controller gains of C2 can be selected as larger values due to the consideration of multi-joint coupling in the control algorithm design so as to achieve a better motion tracking performance.

For *Set2*, by passing the sinusoid curves $x_{2d} = [-2 + 0.2\sin((\pi/2)t - \pi/2), 0.5 + 0.2\sin((\pi/2)t - \pi/2), -0.3 + 0.2\sin((\pi/2)t - \pi/2), 0.3 + 0.2\sin((\pi/2)t - \pi/2), -0.5 + 0.2\sin((\pi/2)t - \pi/2), 2 + 0.2\sin((\pi/2)t - \pi/2)]$rad through the kinematics equations for left leg support and passing the sinusoid curves $x_{2d} = [-2 + 0.2\sin((\pi/2)t - \pi/2), 0.5 + 0.2\sin((\pi/2)t - \pi/2), 0.2\sin((\pi/2)t - \pi/2)]$rad through the kinematics equations for double leg support, the trajectory of human motion x_h can be finally solved. Without much performance compromised, only Δ_{1n} is selected to be adapted. With high-level controller selected as FARC, Figures 7 and 8 show that FARC+C2 achieve a smaller interaction force than that of FARC+C1. It is because a larger closed loop bandwidth can be achieved by C2 due to considering all characteristic of system dynamics, which results in larger high-level controller gains and adaptive rates. Then, better parameter estimation and force control performance

can be achieved by FARC+C2.

In *Set3*, a $2.72kg$ weight is mounted at the shank to study the performance of the proposed ARCFC to parameter variation. From Figures 9 and 10, we can see that a consistent performance can be achieved both for the proposed ARCFC (FARC+C2) and the PID cascade force controller (FARC +C1) to load variation. Since the proposed ARCFC achieves higher closed loop bandwidth and faster parameter adaptation, model uncertainties due to load variation can be compensated more quickly and accurately which leads to a smaller interaction force and more consistent force control performance load variation.

In *Set4*, the human-machine interface dynamics is described as a spring-damper model which means in Equation (28), the modeling errors is described as $\tilde{D}_1 = B_{\text{hm}}(\dot{x}_h - \dot{x}_e)$ where B_{hm} is the damping ratio at the human-machine interface. From Figures 11 and 12, it can be seen that a consistent performance can be achieved for the proposed ARCFC (FARC+C2) to human-machine interface modeling errors both in left leg support phase and double leg support phase. For PID cascade force controller (FARC +C1), when adding the damping in the human-machine interface, the human interaction force becomes chattering. The reason is that the closed loop bandwidth and parameter adaptation rate of PID cascade force controller are limited leading to a poor disturbance rejection performance.

In this paper, only simulations are carried out, and also, the human motion trajectory is generated by sinusoid curves for a preliminary validation of the proposed controller performance. In the future, comparative experiments will be conducted on a real lower limb hydraulic exoskeleton platform to further validate the performance of the proposed interaction force controller in practical applications.

5. Conclusion

In this paper, a generalized multiphase dynamic modeling method is proposed for lower limb exoskeleton in which the dynamic model of each walking phase can all be obtained based on the dynamic model of a floating lower limb exoskeleton (with positions of the exoskeleton feet changed) and different holonomic constraints, which significantly simplify the dynamic modeling process of the multiphase lower limb exoskeleton. MIMO adaptive robust interaction force controllers with high level doing human motion intent inference while low level conducting human trajectory tracking are designed both for double leg support phase and single leg support phase. A torque allocation method is proposed to deal with the overactuated characteristic in double leg support. Comparative simulations show the effectiveness and better performance of the proposed multiphase human-machine interaction force controller. In our future research, we will do the modeling and controller design of underactuated lower limb exoskeleton systems. Stability analysis of uncontrolled internal dynamics and adaptive robust force control of underactuated exoskeleton systems will be conducted.

Data Availability

The data that support the findings of this study are available from the corresponding author upon reasonable request.

Conflicts of Interest

The authors declare that they have no conflict of interest.

Acknowledgments

This work was supported by the National Natural Science Foundation of China under Grants 61803141 and 51905140 and the Fundamental Research Funds for the Central Universities of China under Grant No. PA2020GDSK0090.

Supplementary Materials

Appendix: the description of each variable in this paper is shown in the following notation list. *(Supplementary Materials)*

References

[1] C. J. Walsh, K. Endo, and H. Herr, "A quasi-passive leg exoskeleton for load-carrying augmentation," *International Journal of Humanoid Robotics*, vol. 4, no. 3, pp. 487–506, 2007.

[2] L. M. Mooney, E. J. Rouse, and H. M. Herr, "Autonomous exoskeleton reduces metabolic cost of human walking during load carriage," *Journal of Neuroengineering and Rehabilitation*, vol. 11, no. 1, p. 80, 2014.

[3] J. L. C. Racine, *Control of a Lower Extremity Exoskeleton for Human Performance Amplification*, Univ. of California, Berkeley, CA, 2003, PhD thesis.

[4] H. F. Al-Shuka, B. J. Corves, and W. H. Zhu, "Dynamic modeling of biped robot using Lagrangian and recursive Newton-Euler formulations," *International Journal of Computer Applications*, vol. 101, no. 3, 2014.

[5] G. Yan, B. Yao, and C. S. George Lee, "Exponential stabilization of fully actuated planar bipedal robotic walking with global position tracking capabilities," *Journal of Dynamic Systems, Measurement, and Control*, vol. 140, no. 5, article 051008, 2018.

[6] T. Yan, M. Cempini, C. M. Oddo, and N. Vitiello, "Review of assistive strategies in powered lower-limb orthoses and exoskeletons," *Robotics and Autonomous Systems*, vol. 64, pp. 120–136, 2015.

[7] J.-L. Hami Kazerooni, L. H. Racine, and R. Steger, "On the control of the Berkeley lower extremity exoskeleton (bleex)," in *Proceedings of the 2005 IEEE International Conference on Robotics and Automation*, pp. 4353–4360, Barcelona, Spain, 2005.

[8] K. Kong and M. Tomizuka, "Control of exoskeletons inspired by fictitious gain in human model," *IEEE/ASME Transactions on Mechatronics*, vol. 14, no. 6, pp. 689–698, 2009.

[9] H.-D. Lee, B.-K. Lee, W.-S. Kim, J.-S. Han, K.-S. Shin, and C.-S. Han, "Human–robot cooperation control based on a dynamic model of an upper limb exoskeleton for human power amplification," *Mechatronics*, vol. 24, no. 2, pp. 168–176, 2014.

[10] H. Lee, B. Lee, W. Kim, M. Gil, J. Han, and C. Han, "Human-robot cooperative control based on phri (physical human-robot interaction) of exoskeleton robot for a human upper extremity," *International Journal of Precision Engineering and Manufacturing*, vol. 13, no. 6, pp. 985–992, 2012.

[11] Y. Long, Z. J. Du, C. F. Chen et al., "Hybrid control scheme of a hydraulically actuated lower extremity exoskeleton for load-carrying," *Journal of Intelligent & Robotic Systems*, vol. 91, no. 3-4, pp. 493–500, 2018.

[12] Z. Li, Z. Huang, W. He, and S. Chun-Yi, "Adaptive impedance control for an upper limb robotic exoskeleton using biological signals," *IEEE Transactions on Industrial Electronics*, vol. 64, no. 2, pp. 1664–1674, 2017.

[13] X. Zhang, H. Wang, Y. Tian, L. Peyrodie, and X. Wang, "Model-free based neural network control with time-delay estimation for lower extremity exoskeleton," *Neurocomputing*, vol. 272, pp. 178–188, 2018.

[14] C. Jarrett and A. J. McDaid, "Robust control of a cable-driven soft exoskeleton joint for intrinsic human-robot interaction," *IEEE Transactions on Neural Systems and Rehabilitation Engineering*, vol. 25, no. 7, pp. 976–986, 2017.

[15] J. Cao, S. Q. Xie, and R. Das, "MIMO sliding mode controller for gait exoskeleton driven by pneumatic muscles," *IEEE Transactions on Control Systems Technology*, vol. 26, no. 1, pp. 274–281, 2018.

[16] I. Kardan and A. Akbarzadeh, "Robust output feedback assistive control of a compliantly actuated knee exoskeleton," *Robotics and Autonomous Systems*, vol. 98, pp. 15–29, 2017.

[17] S. Chen, Z. Chen, B. Yao et al., "Adaptive robust cascade force control of 1-dof hydraulic exoskeleton for human performance augmentation," *IEEE/ASME Transactions on Mechatronics*, vol. 22, no. 2, pp. 589–600, 2017.

[18] S. Chen, Z. Chen, and B. Yao, "Precision cascade force control of multi-dof hydraulic leg exoskeleton," *IEEE Access*, vol. 6, pp. 8574–8583, 2018.

[19] J. Yao, W. Deng, and Z. Jiao, "Adaptive control of hydraulic actuators with LuGre model based friction compensation," *IEEE Trans. Industrial Electronics*, vol. 62, no. 10, pp. 6469–6477, 2015.

[20] W. Shen and J. Wang, "An integral terminal sliding mode control scheme for speed control system using a double-variable hydraulic transformer," *ISA Transactions*, 2019.

[21] T. Lin, Y. Lin, H. Ren, H. Chen, Z. Li, and Q. Chen, "A double variable control load sensing system for electric hydraulic excavator," *Energy*, vol. 223, article 119999, 2021.

[22] B. Helian, C. Zheng, B. Yao, L. Lyu, and C. Li, "Accurate motion control of a direct-drive hydraulic system with an adaptive nonlinear pump flow compensation," *IEEE/ASME Transactions on Mechatronics*, vol. 26, no. 5, pp. 2593–2603, 2020.

[23] B. Helian, Z. Chen, and B. Yao, "Precision motion control of a servomotor-pump direct-drive electrohydraulic system with a nonlinear pump flow mapping," *IEEE Transactions on Industrial Electronics*, vol. 67, no. 10, pp. 8638–8648, 2020.

[24] L. Lyu, Z. Chen, and B. Yao, "Advanced valves and pump coordinated hydraulic control design to simultaneously achieve high accuracy and high efficiency," *IEEE Transactions on Control Systems Technology*, vol. 29, no. 1, pp. 236–248, 2021.

[25] H. Chuxiong, H. Zhipeng, Y. Zhu, and Z. Wang, "Advanced gtcf-larc contouring motion controller design for an industrial x–y linear motor stage with experimental investigation," *IEEE Transactions on Industrial Electronics*, vol. 64, no. 4, pp. 3308–3318, 2017.

[26] M. Yuan, C. Zheng, B. Yao, and X. Liu, "Fast and accurate motion tracking of a linear motor system under kinematic and dynamic constraints: an integrated planning and control approach," *IEEE Transactions on Control Systems Technology*, vol. 29, no. 2, pp. 804–811, 2019.

[27] S. Zhou, C. Shen, Y. Xia, Z. Chen, and S. Zhu, "Adaptive robust control design for underwater multi-dof hydraulic manipulator," *Ocean Engineering*, vol. 248, article 110822, 2022.

[28] B. Fanping and B. Yao, "Observer based coordinated adaptive robust control of robot manipulators driven by single-rod hydraulic actuators," in *Proceedings 2000 ICRA. Millennium Conference. IEEE International Conference on Robotics and Automation. Symposia Proceedings (Cat. No. 00CH37065)*, pp. 3034–3039, San Francisco, CA, USA, 2000.

[29] S. Chen, T. Han, F. Dong et al., "Precision interaction force control of an underactuated hydraulic stance leg exoskeleton considering the constraint from the wearer," *Machines*, vol. 9, no. 5, p. 96, 2021.

Hindawi
Applied Bionics and Biomechanics
Volume 2022, Article ID 5875004, 13 pages
https://doi.org/10.1155/2022/5875004

Research Article

Event-Triggered Finite-Time Attitude Cooperative Control for Multiple Unmanned Aerial Vehicles

Qiang Han,[1,2] **Yongshuai Zhou**,[2] **Xin Liu**,[2] **and Xianguo Tuo**[2]

[1]*Robot Technology Used for Special Environment Key Laboratory of Sichuan Province, Southwest University of Science and Techno1ogy 621010, China*
[2]*Artificial Intelligence Key Laboratory of Sichuan Province, Sichuan University of Science & Engineering, Zigong 643000, China*

Correspondence should be addressed to Xianguo Tuo; tuoxg@cdut.edu.cn

Received 5 January 2022; Revised 27 January 2022; Accepted 1 February 2022; Published 21 February 2022

Academic Editor: Songyuan Zhang

The finite-time attitude cooperative control problem for a group of multiple unmanned aerial vehicle systems with external disturbances and uncertain parameters is discussed in this paper. The dynamics of the systems is described by quaternion avoiding the singularity. Based on the attitude error and angular velocity error, a novel nonsingular terminal sliding mode surface is proposed for the controller with event-triggered scheme. The lumped disturbances are estimated by neural networks with adaptive law. The communication frequency is decreased by the proposed distributed event-triggered based sliding mode controller. Lyapunov theory is utilized to analyze the stability of the systems, and the Zeno behavior is avoided by rigorous proof. Finally, simulation examples are presented to illustrate the efficiency of the proposed control algorithm.

1. Introduction

Attitude cooperative control of multiple unmanned aerial vehicle systems (MUAVs) is significantly important in the formation flying missions. Compared to a single unmanned aerial vehicle (UAV), MUAVs can accomplish more complex and dangerous missions by collaboration, such as search and rescue, forest fire fighting, emergency rescue, low-attitude reconnaissance, and combat military missions [1–3]. Attitude cooperative control problem has been of growing interests in last several years due to its engineering and theoretical implications. Many scholars proposed different attitude control scheme to improve the accuracy and stability of the MUAVs. Variable structure control combined with decentralized communication scheme was proposed for spacecraft formation flying [4], based on the development of consensus theory, leader-follower was employed in the multiple aircrafts [5, 6]. As the amount of the MUAVs increases, the communication burden among each UAV will increase and may cause the network communication jam, and it would seriously affect the stability of the systems due to the band width is limited. It is significant to consider the network communication strategy of MUAVs when designing the attitude cooperative controller.

Even-triggered scheme is employed in the multiagent systems for considering the limited band width and energy consumption, instead of continuous control input update, the controller updates the input depending on the event-triggered function, which is relevant to the measurement error, and when the estimation error comes up to the given threshold value the update of the controller will be updated [7]. An event-triggered-based controller was proposed in first-order multiagent systems (MAS) by introducing the event-triggered mechanism, and the triggered condition was designed associated with the states of agents [8]. Distributed rendezvous problem was investigated for second-order multiagent systems with combinational measurement by event-triggered mechanism [9]. Based on the measurement error, the event triggered function was built for linear MAS, and all the states of the agents reach to consensus [10, 11]. Event-triggered scheme was employed in many system dynamical model which can be described as second-order dynamics [12]. A distributed sliding mode controller

based on event triggered finite time mechanism was designed for formation of multirobot systems [13]. The event triggered was widely used in attitude control of spacecrafts to save the communication resources [14–16]. However, the mentioned works with attitude control did not consider the uncertain parameters. Based on event-triggered strategy, time-varying formation problem was investigated for MUAVs under switching topology [17], attitude formation on SO (8) [18], and dynamical consensus formation problem which was limited by time-varying disturbances [19]. However, external disturbances and inertial matrix uncertainty cannot avoid in practical environment. The event-based formation control for MUAVs only guarantees asymptotically convergence in the aforementioned works [17–19]. Finite-time control is a useful tool which has high accuracy and robustness property, enabling the control systems to approach the stable region in finite time. Finite-time control has been extensively utilized in Euler-Lagrange systems [20–22]. Distributed attitude tracking problem of spacecrafts was proposed considering disturbances and uncertain parameters in finite time [20]. Adaptive control was introduced into the finite-time controller extended the mentioned work [20] for attitude tracking problem of spacecrafts [21]. Feedback control was employed in formation control for finite time convergence of nonholonomic wheeled mobile robots [22]. Distributed finite-time control (FTC) problem was studied for multiple quadrotor formation with the information of leader not available to all the followers [23]. However, no external disturbances were considered. The disturbance was estimated by the observer, and FTC was investigated for a single quadrotor [24, 25]. However, attitude cooperative problem was not considered. There is less work associated with the finite-time attitude cooperative or formation control with event-triggered mechanism for MUAVs. Most recently, FTC based on event-triggered was investigated for quadrotor flying control [26, 27]. However, attitude tracking problem was not considered, and the controller designed was limited to the specific UAV. So, attitude cooperative control with FTC theory and event-triggered mechanism is more interesting.

Motivated by the aforementioned works and analysis, finite-time attitude cooperative control problem of MUAVs with event-triggered mechanism is investigated, and the network communication resources are reduced. The contribution of this paper is illustrated in the following aspects: (1) external disturbances and uncertain parameters are considered in the attitude dynamics, and the attitude cooperative problem is described by the quaternion avoiding the singularity. The attitude tracking consensus errors are measured by employing a positive error function, a novel integral sliding mode surface is proposed, the FTC is designed for the closed loop systems, and neural network is utilized to estimate the lumped uncertainties. (2) The communication frequency of the controller among the followers is reduced due to the event-triggered strategy which is employed in the controller, so the proposed novel event-triggered function saves the communication burden and energy of each UAV. The deduced lower bound between triggering intervals guarantee no Zeno behavior occurs. (3) Fast terminal sliding mode control is utilized in control law which guarantees that the attitude achieves the desired value in finite time.

The rest of this paper is organized as follows. In Section 2, preliminaries of graph theory, quaternion-based attitude dynamics of MUAVs, and some useful lemmas are given, and Section 3 gives main results. The performance of the controller is proved by numerical simulation examples in Section 4. Finally, conclusion is given in Section 5.

2. Preliminaries and Problem Formulation

2.1. Notations. The following convenience notations are adopted throughout the paper: R^n denotes $n \times 1$ real column vector, $I_n = [1, \ldots 1]^T$ denotes $n \times 1$ column vector with each element being, and I_n denotes a $n \times n$ dimensional identity matrix. $\otimes$ stands for Kronecker product. $\|.\|$ stands for the induced matrix 2-norm or the Euclidean vector norm. In addition, for a given vector $x \in R_n$, x_i denotes the ith element of the vector x, $sig^r(x) = \text{sgn}\,(x)|x|^r$.

Graph theory is utilized to describe the communication flow among the MUAVs. Let $G = (\nu, \xi)$ denotes the graph, in which, $\nu = \{\nu_1, \nu_2, \cdots, \nu_n\}$ is a nonempty set containing a group number of nodes which denotes the UAV, and $\xi \subseteq \nu \times \nu$ is called edge which is a set of nodes. If there any two nodes could communicate with each other, the graph G is called connected graph. $A = [a_{ij}]_{N\times N} \in R^{n\times n}$ is weighted adjacency matrix representing the communication between each node, in which, $a_{ii} = 0$, otherwise, $a_{ij} = a_{ji} \geq 0$. $D = \text{diag}\,\{d_1, d_2, \cdots, n\}$ denotes the degree matrix of associated with weighted graph, the elements of the degree matrix are $d_i = \sum_{j=1}^{n} a_{ij}$. The Laplacian matrix of the weighted graph is denoted by $L = D - A$, and L is symmetric matrix.

Throughout this paper, leader-follower MUAVs are considered which contains one leader and n followers. The followers are marked as $i(i = 1, \cdots, n)$, and the leader is marked as 0. Let $\bar{G}$ denotes the topology graph associated with MUAVs containing one leader and n followers. A diagonal matrix $B = \text{diag}\,\{b_1, \cdots, b_n\}$ is utilized to denote the communication between the follower UAV and the leader UAV. If $b_i > 0$ means that the ith follower can obtain the communication flow of the leader, otherwise, $b_i = 0$.

Assumption 1. Consider the MUAVs consisting of N followers and one leader, the topology of the MUAVs is described by $\bar{G}$, and $\bar{G}$ is directed connected graph.

Based on Assumption 1 and graph theory, we define a matrix $C = L + B$.

Lemma 2 (see [28]). *If Assumption 1 holds, then, matrix C is invertible.*

Lemma 3 (see [29]). *Consider a system modeled as* $\dot{z} = f(z)$, $f(0) = 0, x \in \mathbb{R}^n$, *a continuous function* $V(z) \in \mathbb{C}^1$ *which is defined on a neighbourhood of the origin. If the function* $V(z)$ *satisfies that it is positive definite and* $\dot{V}(z) \leq -\nabla_1 V^{\partial}(z)$, *where* $\partial \in (0, 1)$, ∇_1 *is positive parameters. The systems*

converge to the origin in finite-time, the converge time T which depends on the initial state of z(0):

$$T(z(0)) \le \frac{V^{1-\partial}(z(0))}{\nabla_1(1-\partial)}. \tag{1}$$

Lemma 4 (see [30]). *If there is a real number $x_i \in \mathbb{R}$, $i = 1, \cdots, n$, $\alpha \in (0, 1]$, then*

$$\left(\sum_{i=1}^{n} | x_i |\right)^{\alpha} \le \sum_{i=1}^{n} |x_i|^{\alpha} \le n^{1-\alpha}\left(\sum_{i=1}^{n} | x_i |\right)^{\alpha}. \tag{2}$$

For $x \in \mathbb{R}^n$, $|\alpha| \in (0, 1)$, then

$$\|x^{\alpha}\| \le n^{1-\alpha}\|x\|^{\alpha}. \tag{3}$$

2.2. Attitude Dynamics Model of MUAVs. Throughout this paper, the attitude dynamics of UAV is described by quaternion which could avoid singular problem and analyze conveniently [31].

$$\begin{aligned} J_i\dot{\omega}_i &= u_i - S(\omega_i)J_i\omega_i + \vartheta_i, \\ \dot{Q}_i &= \frac{1}{2}\phi(Q_i)\omega_i, \end{aligned} \tag{4}$$

where $Q_i = [q_i\ q_{i0}]^T$ represents the attitude of the ith UAV, $q_i \in \mathbb{R}^3$, $q_{i0} \in \mathbb{R}$, $Q_i \in \mathbb{R}^4$, $Q_i \in \mathbb{R}^4$, $|Q_i| = 1$, and $\omega_i \in \mathbb{R}^3$ is the angular velocity. J_i denotes the inertia matrix of the ith UAV and is positive definite; u_i denotes the control torque of the ith UAV; ϑ_i denotes the external disturbances. $\phi(Q_i)$ is given by

$$\phi(Q_i) = \begin{pmatrix} q_{i0}I_3 + S(q_i) \\ -q_i{}^T \end{pmatrix}. \tag{5}$$

For a vector given as $n = [n_1, n_2, n_3]^T \in R^{3\times1}$, $S(n)$ is defined as

$$S(n) = \begin{pmatrix} 0 & -n_3 & n_2 \\ n_3 & 0 & -n_1 \\ -n_2 & n_1 & 0 \end{pmatrix}. \tag{6}$$

Let $R(Q_i)$ denote the rotation matrix which is given as $R(Q_i) = (2q_{i0}{}^2 - 1)I_3 + 2q_iq_i{}^T - 2q_{i0}\Pi(q_i)$, $Q_i = [q_i\ q_{i0}]^T$ for the attitude control of UAV, the rotation matrix denotes the inertial frame of the ith UAV into the body frame. The multiplication between two unit quarternions is given by

$$Q_1 \odot Q_2 = \begin{pmatrix} q_{10}q_2 + q_{20}q_1 + S(q_1)q_2 \\ q_{10}q_{20} - q_1^T q_2 \end{pmatrix}, \tag{7}$$

where $Q_1 = [q_1 \quad q_{10}]^T$ and $Q_2 = [q_2 \quad q_{20}]^T$.

In the leader-following MUAVs, the followers adjust itself attitude to be consistent with the attitude of the leader. The attitude tracking errors and angular velocity errors of the ith UAV are given as follows

$$\tilde{Q}_i = Q_i^{-1} \odot Q_d, \tag{8}$$

$$\tilde{\omega}_i = \omega_i - R\left(\tilde{Q}_i\right)\omega_d, \tag{9}$$

where $Q_d \triangleq [q_d, \eta_d]^T$ denotes the desired attitude which is given $Q_d \triangleq [q_d, \eta_d]^T$, and the desired angular velocity is denoted by ω_d. Based on the definition of the tracking errors, $\tilde{\omega}_i$ and $\tilde{Q}_i$ represent the attitude velocity tracking error and angular tracking errors, respectively.

The attitude tracking error systems can be obtained,

$$J_{\mathrm{i}}\dot{\tilde{\omega}}_{\mathrm{i}} = -\omega_{\mathrm{i}}{}^{\times} \cdot J_{\mathrm{i}}\omega_{\mathrm{i}} + u_{\mathrm{i}} + T_{\mathrm{i}} \cdot [\Pi(\tilde{\omega}_{\mathrm{i}}) \cdot R(Q_{\mathrm{id}}) \cdot \omega_d - R(Q_{\mathrm{id}}) \cdot \dot{\omega}_d], \tag{10}$$

$$\dot{\tilde{Q}}_i = \frac{1}{2}\phi\left(\tilde{Q}_{\mathrm{i}}\right) \cdot \tilde{\omega}_{\mathrm{i}}. \tag{11}$$

Assumption 5. Three positive constants d_m, σ_1, σ_2 exist and are satisfying $|d_i| \le d_m$, $|\omega_i| \le \sigma_1$, and $|\dot{\omega}_i| \le \sigma_2$, respectively.

Assumption 6. The inertia matrix $\bar{J}_i$ is known and nonsingular. ΔJ denotes the uncertainties and is bounded.

Lemma 7 (see [32]). *Considering the system formulated as eqs. (10) and (11), for sliding mode surface $\kappa_i = \tilde{\omega}_i + r_1q_i + r_2q_i^c$, where $0 < c < 1$, $r_1 > 0$, $r_2 > 0$, for $i = 1, \cdots, n$. If the sliding mode surface reaches zero, then, $\tilde{\omega}_i = 0, q_{0,i} = 1$ and $q_i = 0$ can be reached in finite time, respectively.*

3. Main Results

3.1. Event-Triggered Finite-Time Control Design. In this section, the control objective is to design a finite-time control law such that the angular velocity errors $\tilde{\omega}_i$ and the error quaternions $\tilde{Q}_i$ of the closed-loop system (10) and (11) can converge to small regions in finite time, respectively.

First, the sliding mode surface $\bar{s}_i$ is defined as

$$\bar{s}_i = \bar{J}_i[\tilde{\omega}_i + k_1\tilde{q}_i + k_2T_i(\tilde{q}_i)], \tag{12}$$

with $T_i(\tilde{q}_i)(\tilde{q}_i) = [T_{i1}(\tilde{q}_{i1}), T_{i2}(\tilde{q}_{i2}), T_{i3}(\tilde{q}_{i3})]^T \in R^{3\times1}$,

$$T_{ij}\left(\tilde{q}_{ij}\right) = \begin{cases} \mathrm{sig}^{\ell}\left(\tilde{q}_{ij}\right), \text{if } s_{ij}^* = 0 \text{ or } s_{ij}^* \ne 0, \left|\tilde{q}_{ij}\right| > \Upsilon, \\ \varpi_1\tilde{q}_{ij} + \varpi_2\mathrm{sig}^2\left(\tilde{q}_{ij}\right), \text{if } s_{ij}^* \ne 0, \left|\tilde{q}_{ij}\right| \le \Upsilon \end{cases} \tag{13}$$

where $i = 1, \cdots, n$, $j = 1, 2, 3$, $s_i^* = [s_{i1}^*, s_{i2}^*, s_{i3}^*]^T$, and $s_i^* = \tilde{\omega}_i + k_1\tilde{q}_i + k_2\mathrm{sig}^r(\tilde{q}_i)$, where k_1 and k_2 are positive constants. Define $\mathrm{sig}^{\iota}(\tilde{q}_i) = [\mathrm{sig}^{\iota}(\tilde{q}_{i1}), \mathrm{sig}^{\iota}(\tilde{q}_{i2}), \mathrm{sig}^{\iota}(\tilde{q}_{i3})]^T$, $\iota \in (0, 1)$, $\varpi_1 = (2 - r)\Upsilon^{r-1}$, $\varpi_2 = (r - 1)\Upsilon^{r-2}$, Υ is a small positive constant.

To develop the control law, the following equations are derived from (10) and (11):

$$\bar{J}_i\left(\dot{\tilde{w}}_i + k_1\dot{\tilde{q}}_i + k_2\dot{T}_i(\tilde{q}_i)\right) = z_i + \delta_i + u_i, \tag{14}$$

where

$$\begin{aligned} z_i = &-S(w_i)\bar{J}_i w_i + \bar{J}_i\left(S(\tilde{w}_i)R\left(\tilde{Q}_i\right)w_d - R\left(\tilde{Q}_i\right)\dot{w}_d\right) \\ &+ k_1\bar{J}_i\dot{\tilde{q}}_i + k_2\bar{J}_i\dot{\alpha}_i(\tilde{q}_i), \end{aligned} \tag{15}$$

$$\dot{\alpha}_i(\tilde{q}_i) = \begin{cases} r\ \mathrm{diag}\left(\left|\tilde{q}_{ij}\right|^{r-1}\right)\tilde{q}_i, & \text{if} \quad s_{ij}^* = 0 \quad \text{or} \quad s_{ij}^* \neq 0, \quad \left|\tilde{q}_{ij}\right| > \phi, \\ l_1\dot{\tilde{q}}_i + 2l_2\tilde{q}_i\ \mathrm{sgn}\ (\tilde{q}_i)\dot{\tilde{q}}_i, & \text{if} \quad s_{ij}^* \neq 0, \quad \left|\tilde{q}_{ij}\right| \leq \phi, \end{cases} \tag{16}$$

$$\delta_i = \vartheta_i - \tilde{J}_i\dot{\tilde{w}}_i - S(w_i)\tilde{J}_i w_i + \tilde{J}_i\left[S(\tilde{\omega}_i)R\left(\tilde{Q}_i\right)\omega_d - R\left(\tilde{Q}_i\right)\dot{\omega}_d\right]. \tag{17}$$

δ_i is the lumped disturbances containing model uncertainty and external disturbances.

By (12) and (14), we can obtain

$$\dot{\bar{s}}_i = z_i + \delta_i + u_i. \tag{18}$$

Based on the sliding mode surface $\bar{s}_i = \bar{J}_i[\tilde{\omega}_i + k_1\tilde{q}_i + k_2 T_i(\tilde{q}_i)]$, a novel integral sliding mode surface is proposed which is given as follows

$$s_i = \bar{s}_i - \int_0^t x_i^\eta dt, \tag{19}$$

where $x_i = -\sum_{j\in N_i} a_{ij}(\bar{s}_i - \bar{s}_j) + b_i\bar{s}_i$, and $\eta \in (0.5, 1)$ is strictly the ratio of positive odd numbers. The derivative of (19) is

$$\dot{s}_i = \dot{\bar{s}}_i - x_i^\eta. \tag{20}$$

An event-triggered finite-time sliding mode consensus controller is designed as follows

$$u_i(t) = x_i^\eta\left(t_k^i\right) - k_3\ \mathrm{sign}\ \left(s_i\left(t_k^i\right)\right) - k_4 s_i\left(t_k^i\right) - z_i\left(t_k^i\right) - \widehat{\delta}_i\left(t_k^i\right), \tag{21}$$

where k_3 and k_4 are positive constants, respectively. For $t \in [t_k^i, t_{k+1}^i)$, t_k^i is the latest event-triggered time for the ith UAV, and the UAV only updates the control protocol at its own event-triggered time.

An adaptive radial basis function neural networks (RBFNNs) scheme is proposed for the unknown disturbance δ_i, as RBFNNs can estimate the unknown continuous functions δ_i and ensure tracking error ultimately converges to an adequately small compact. Illustrated in Figure 1, the adaptive RBFNNs can be written as

$$\widehat{\delta}_i = \widehat{W}_i^T H_i(X_{\mathrm{in}}), \tag{22}$$

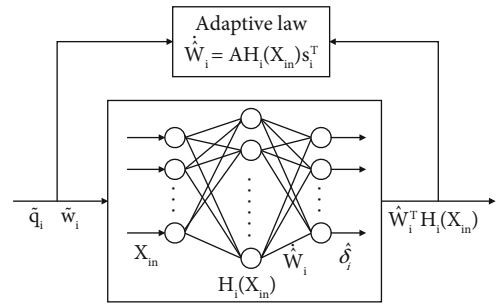

Figure 1: Adaptive RBFNN control.

where $\widehat{\delta}_i \in \mathbb{R}^3$ is the RBFNNs output vector, $X_{\mathrm{in}} = [\tilde{q}_i^T, \tilde{w}_i^T]^T \in \mathbb{R}^6$ is the input vector of the RBFNNs, $\widehat{W}_i \in \mathbb{R}^{J\times 3}$ is the weight vector, $J > 1$ is the nodes number of middle hidden layer, $H_i = [h_{i1}, \cdots, h_{iJ}]^T \in \mathbb{R}^J$ is the basis function vector, and h_{ij} is being the commonly used Gaussian functions, which is simplified as

$$h_{ij}(X_{\mathrm{in}}) = \exp\left(-\frac{\left\|X_{\mathrm{in}} - c_{iJ}\right\|^2}{\sigma_{iJ}}\right), \tag{23}$$

where c_{iJ} is the center of the receptive field, and σ_{iJ} is the width of the Gaussian function. There exists an optimal vector W_i^* such that

$$\delta_i = W_i^{*T} H_i(X_{\mathrm{in}}) + \varepsilon_i, \tag{24}$$

where ε_m^i denotes the maximum value of the RBFNNs estimation error $\|\varepsilon_i\|$.

Let $\tilde{W}_i = W_i^* - \widehat{W}_i$ denotes the vector of weight errors, and the adaptive weight update law are designed as

$$\dot{\widehat{W}}_i = AH_i(X_{\mathrm{in}})s_i^T, \tag{25}$$

where A is a positive-definite symmetric matrix of gains.

The measurement error of the event-triggered mechanism is defined as

$$\begin{aligned} e_i(t) = &\ x_i^\eta\left(t_k^i\right) - x_i^\eta(t) - k_3\ \mathrm{sign}\ \left(s_i\left(t_k^i\right)\right) + k_3\ \mathrm{sign}\ (s_i(t)) \\ &- k_4 s_i\left(t_k^i\right) + k_4 s_i(t) - z_i\left(t_k^i\right) + z_i(t) - \widehat{\delta}_i\left(t_k^i\right) + \widehat{\delta}_i(t). \end{aligned} \tag{26}$$

3.2. Stability Analysis. In the following, the stability of the attitude cooperative under event-triggered adaptive RBFNNs control law is analyzed in detail.

Theorem 8. *On the basis of Assumptions 1, and considering that the system (10) and (11) under the action of the controller (21) and the adaptive weight update law (25), the following event-triggered function is given as follows*

$$Y(t) = \|e_i\| - k_3 - k_4\|s_i\| + \rho_i, \tag{27}$$

where $\varepsilon_m^i < \rho_i < k_3$, and when the event-triggered function $Y(t) > 0$, that is, $\|e_i\| > k_3 + k_4\|s_i\| - \rho_i$, the event is triggered. The ith UAV performs information interaction and update the control protocol at its own event-triggered time. And the system can achieve finite-time consensus under this action.

Proof. First, selecting the Lyapunov function as follows

$$V_1 = \frac{1}{2}s_i^T s_i + \frac{1}{2}\mathrm{tr}\left(\tilde{W}_i^T A^{-1}\tilde{W}_i\right). \tag{28}$$

Taking the derivative of (28), substituting (21) and (26) into the derivative, we can obtain

$$\begin{aligned}\dot{V}_1 &= s_i^T\left(e_i - k_3\,\mathrm{sign}\,(s_i) - k_4 s_i + \delta_i - \hat{\delta}_i\right) + \mathrm{tr}\left(-\tilde{W}_i^T A^{-1}\dot{\hat{W}}_i\right)\\ &\le \|s_i\|\|e_i\| - k_3\|s_i\| - k_4\|s_i\|^2 + s_i^T\left(\tilde{W}_i^T H_i + \varepsilon_i\right)\\ &\quad + \mathrm{tr}\left(-\tilde{W}_i^T A^{-1}\dot{\hat{W}}_i\right) \le \|s_i\|\left(\|e_i\| - k_3 - k_4\|s_i\| + \varepsilon_m^i\right)\\ &\quad + \mathrm{tr}\left(\tilde{W}_i^T H_i s_i^T\right) + \mathrm{tr}\left(-\tilde{W}_i^T A^{-1}\dot{\hat{W}}_i\right).\end{aligned} \tag{29}$$

By the adaptive weight update law (25), it is obtained that

$$\dot{V}_1 \le \|s_i\|\left(\|e_i\| - k_3 - k_4\|s_i\| + \varepsilon_m^i\right). \tag{30}$$

When the event-triggered function $Y(t) \le 0$, $\|e_i\| \le k_3 + k_4\|s_i\| - \rho_i$,

$$\dot{V}_1 \le -\|s_i\|\left(\rho_i - \varepsilon_m^i\right) < 0. \tag{31}$$

According to the Lyapunov stability theory, it can be seen that under the action of the controller (21), the adaptive weight update law (25), and the event-triggered function (27), the sliding mode surface s_i can realize $s_i = 0$ and $\dot{s}_i = 0$. By lemma 2, the reaching time is given as follows

$$t_r = \frac{\sqrt{2}V_1^{1/2}(0)}{\rho_i - \varepsilon_m^i}. \tag{32}$$

Then, select the Lyapunov function as

$$V_2 = \frac{1}{2}\bar{S}^T[(L+B)\otimes I_3]^T[(L+B)\otimes I_3]\bar{S}, \tag{33}$$

where $\bar{S} = [\bar{s}_1{}^T, \cdots, \bar{s}_n{}^T]^T$.

Define

$$\begin{aligned}p_i &= \sum_{j\in n_i} a_{ij}\left(\bar{s}_i - \bar{s}_j\right) + b_i\bar{s}_i,\\ P &= \left[p_1^T, \cdots, p_n^T\right]^T = (L+B)\otimes I_3\cdot\bar{S}.\end{aligned} \tag{34}$$

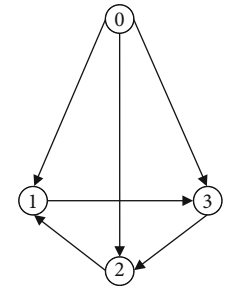

Figure 2: Communication topology.

Then, we can get

$$V_2 = \frac{1}{2}P^T P. \tag{35}$$

Let $S = [s_1{}^T, \cdots, s_n{}^T]^T$, when $\dot{s}_i = 0$, we know $\dot{\bar{s}}_i = x_i^\eta$, then $\dot{\bar{S}} = -[(L+B)\otimes I_3\cdot\bar{S}]^\eta$.

Under Assumption 1 and Lemma 2, it can be obtained that $\lambda_{\min}(L+B) > 0$. And taking the derivative of (35), we can obtain

$$\begin{aligned}\dot{V}_2 &= -P^T[(L+B)\otimes I_3]\left[(L+B)\otimes I_3\cdot\bar{S}\right]^\eta\\ &= -P^T[(L+B)\otimes I_3]P^\eta \le -\lambda_{\min}(L+B)P^T P^\eta,\end{aligned} \tag{36}$$

Since the positive odd ratio parameter $\eta \in (0.5, 1)$, and combined with Lemma 3, we can find

$$\begin{aligned}\dot{V}_2 &\le -\lambda_{\min}(L+B)\left(\sum_{i=1}^{3n}|p_i|^{1+\eta}\right) \le -\lambda_{\min}(L+B)\left(\|P\|^2\right)^{1+\eta/2}\\ &\le -2^{1+\eta/2}\lambda_{\min}(L+B)V_2^{1+\eta/2}.\end{aligned} \tag{37}$$

According to Lemma 1, under the action of the controller (21), the state of the system can reach and remain on the sliding mode surface $\bar{S} = 0$ within finite time. The settling time is t_f.

$$t_f = \frac{V_2^{1-\eta/2}}{2^{1+\eta/2}\lambda_{\min}(L+B)(1-\eta/2)}. \tag{38}$$

When $\bar{S} = 0$, then $\bar{s}_i = \bar{J}_i[\tilde{\omega}_i + k_1\tilde{q}_i + k_2\alpha_i(\tilde{q}_i)] = 0$, so $\tilde{\omega}_i + k_1\tilde{q}_i + k_2\alpha_i(\tilde{q}_i) = 0$. According to Lemma 4, we know $\tilde{\omega}_i \longrightarrow 0$, $\tilde{q}_i \longrightarrow 0$ in finite time will be satisfied.

Next, we need to analyze whether the system has a minimum event-triggered time interval strictly greater than zero, which means that there is no Zeno behavior. When the event-triggered function (27) satisfies $Y(t) > 0$, the event is triggered. Combining (26), we can see that between any two adjacent event-triggered moments, $\|e_i\|$ increases from zero to $k_3 + k_4\|s_i\| - \rho_i$, therefore, when the growth rate is the fastest, the event-triggered time interval is the smallest. In this case, when the minimum time interval is a value

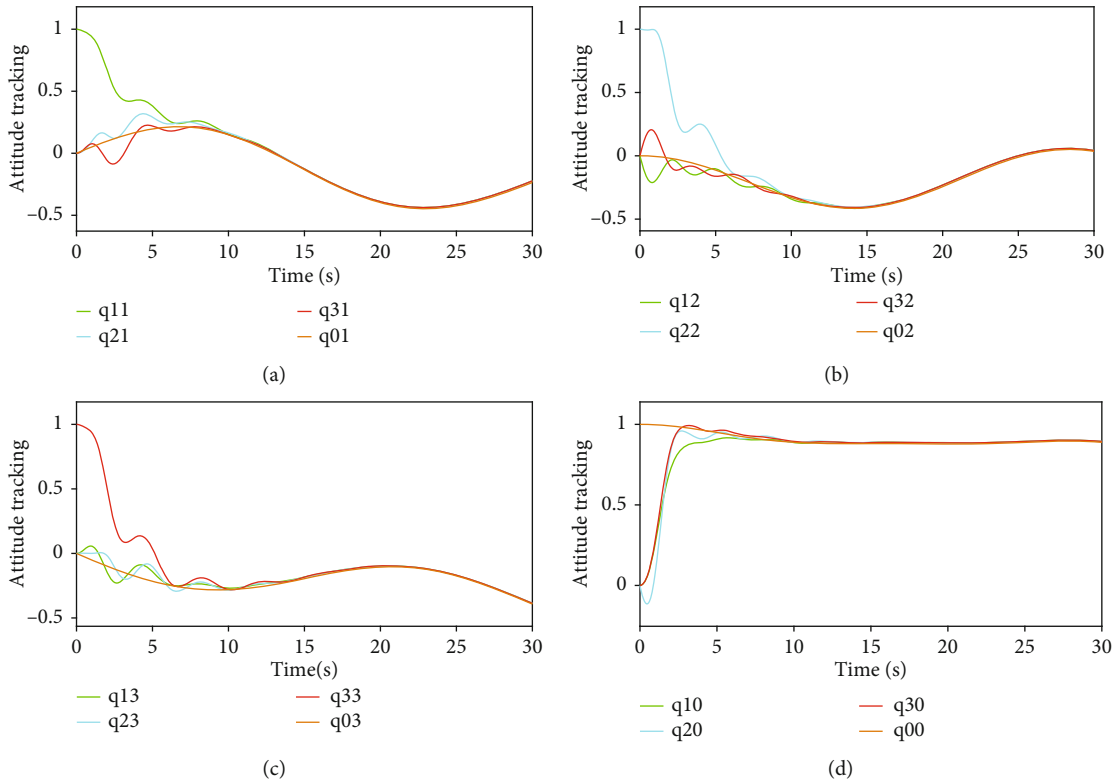

Figure 3: Attitude tracking.

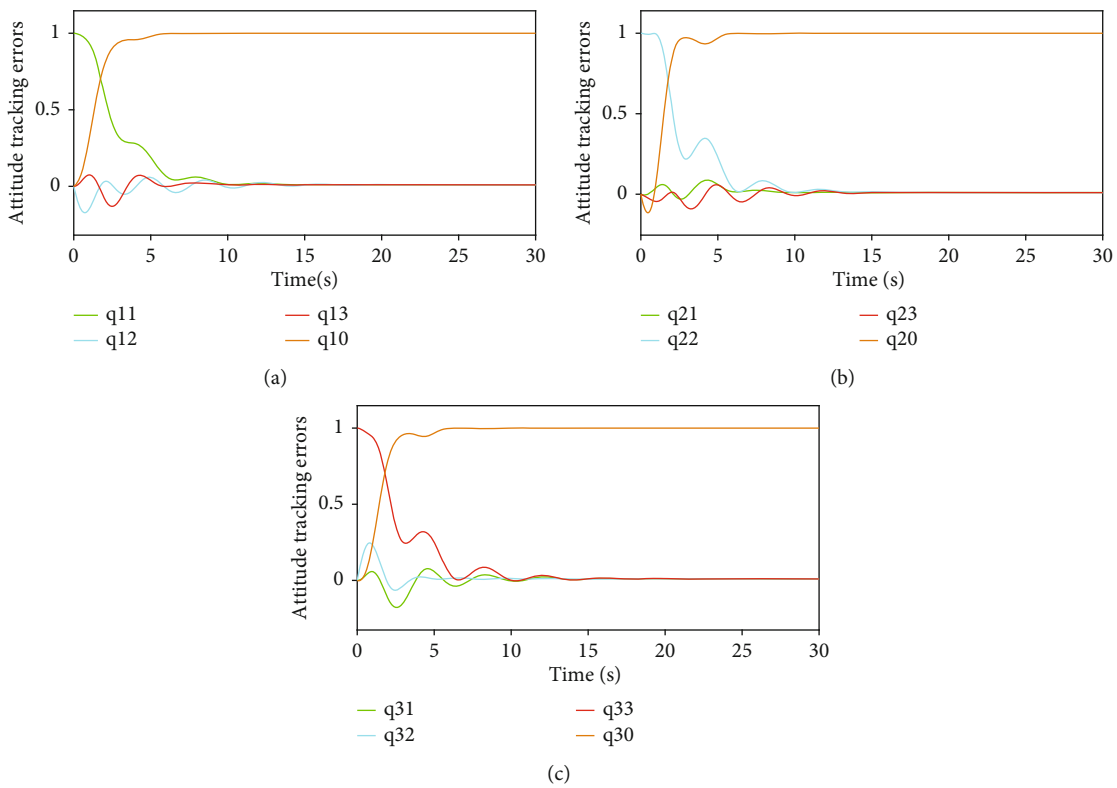

Figure 4: Attitude tracking errors.

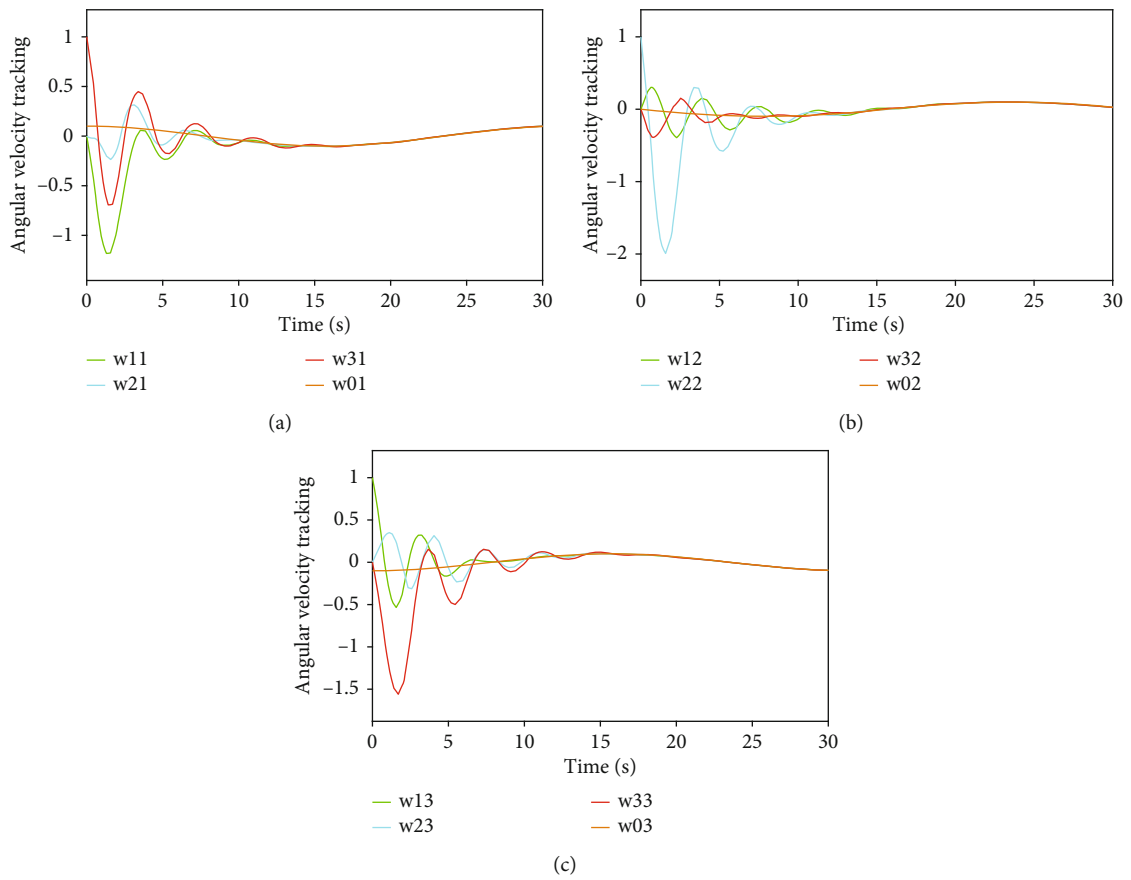

Figure 5: Angular velocity tracking.

greater than zero, it can be guaranteed that there is no Zeno behavior.□ □

Theorem 9. *Based on Assumption 1, the system (10) and (11) under the action of the controller (21), the adaptive weight update law (25), and the event-triggered function (27), the system does not have Zeno behavior under any initial conditions.*

Proof. Let $\beta_i(t) = k_3 \operatorname{sign}(s_i(t)) + k_4 s_i(t) + z_i(t) + \widehat{\delta}_i(t)$, since the system (10) and (11) can achieve consensus under the action of the controller (21), the adaptive weight update law (25), and the event-triggered function (27), $\|\dot{\beta}_i(t)\|$ have upper bounds, which are taken as $\|\dot{\beta}_i(t)\|_{\max}$. And combining (26) to derive $\|e_i\|$ as follows

$$\begin{aligned}\frac{d\|e_i\|}{dt} &\le \left\|\frac{de_i}{dt}\right\| \le \left\|\frac{d\left[-x_i^{\eta}(t) + \beta_i(t)\right]}{dt}\right\| \le \left\|\frac{d}{dt}x_i^{\eta}(t)\right\| + \left\|\dot{\beta}_i(t)\right\| \\ &\le \eta\left\|x_i^{\eta-1}\right\|\|\dot{x}_i\| + \left\|\dot{\beta}_i(t)\right\|_{\max}.\end{aligned} \tag{39}$$

Let $X = [x_1^T, \cdots, x_n^T]^T$, we can obtain $\dot{X} = -(L+B) \otimes I_3 \cdot \dot{\bar{S}}$. When $\dot{S} = 0$, $\bar{S} = X^{\eta}$ will be satisfied, so $\dot{X} = -(L+B) \otimes I_3 \cdot X^{\eta}$. And according to Lemma 3, we know

$$\begin{aligned}\left\|x_i^{\eta-1}\right\| &\le \left\|X^{\eta-1}\right\| \le (3n)^{2-\eta}\|X\|^{\eta-1}, \\ \|\dot{x}_i\| \le \left\|\dot{X}\right\| &\le \|(L+B) \otimes I_3 \cdot X^{\eta}\| \le \|L+B\|\|X^{\eta}\| \\ &\le (3n)^{1-\eta}\|L+B\|\|X\|^{\eta}.\end{aligned} \tag{40}$$

By (38) and (39), we can obtain

$$\frac{d\|e_i\|}{dt} \le \eta(3n)^{3-2\eta}\|L+B\|\|X\|^{2\eta-1} + \left\|\dot{\beta}_i(t)\right\|_{\max}. \tag{41}$$

Due to $X = -P$ and $\|P\| = \sqrt{2}V_2^{1/2}(t) \le \sqrt{2}V_2^{1/2}(0)$, we have

$$\frac{d\|e_i\|}{dt} \le 2^{2\eta-1/2}\eta(3n)^{3-2\eta}\|L+B\|V_2^{2\eta-1/2}(0) + \left\|\dot{\beta}_i(t)\right\|_{\max}. \tag{42}$$

For any $t \in [t_k^i, t_{k+1}^i)$, t_k^i is the latest event-triggered time for the ith UAV, the time interval $T_m^i = t_{k+1}^i - t_k^i$, and $\|e_i(t_k^i)\| = 0$ at the event-triggered moment, and let $\lambda_i = 2^{2\eta-1/2}\eta$

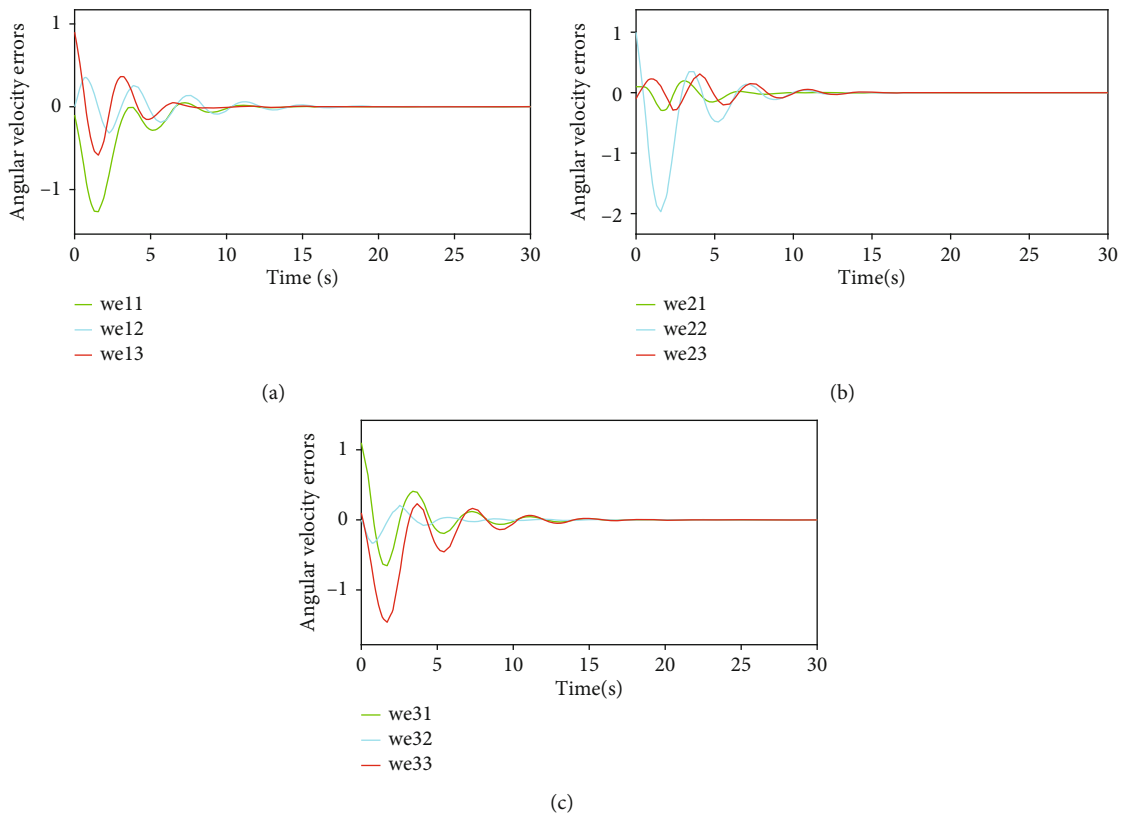

Figure 6: Angular velocity errors.

$(3n)^{3-2\eta}\|L+B\|V_2^{2\eta-1/2}(0)+\|\dot{\beta}_i(t)\|_{\max}$, we can obtain

$$\|e_i(t)\|-\left\|e_i\left(t_k^i\right)\right\|=\|e_i(t)\|\le\left(t-t_k^i\right)\lambda_i\le T_m^i\lambda_i. \tag{43}$$

When the event-triggered function (27) satisfies $Y(t)>0$, the event is triggered, we have

$$\|e_i(t)\|>k_3+k_4\|s_i\|-\rho_i>k_3-\rho_i. \tag{44}$$

Combining (41) and (42), we can know

$$T_m^i>\frac{k_3-\rho_i}{\lambda_i}. \tag{45}$$

It can be concluded from (43) that the event-triggered time interval is strictly greater than zero, so there is no Zeno behavior.□ □

4. Example Simulation

Considering the system composed of four UAVs includes three follower UAVs and one leader UAV, and the leader node is marked as 0. The directed communication topology is shown in Figure 2. Hence, we have

$$L=\begin{bmatrix}1&-1&0\\0&1&-1\\-1&0&1\end{bmatrix}\quad B=\begin{bmatrix}1&0&0\\0&1&0\\0&0&1\end{bmatrix}. \tag{46}$$

The actual inertia matrices are assumed to be

$$J_1=\begin{bmatrix}15&1&1\\2&16&0.5\\0&0.5&14\end{bmatrix}\quad J_2=\begin{bmatrix}13&0.5&0\\1&15&0.5\\0&1.5&14\end{bmatrix}\quad J_3=\begin{bmatrix}14&1&2\\0&13&0\\2&1&15\end{bmatrix}. \tag{47}$$

With the existence of model uncertainties and external disturbances, the nominal inertia matrices of the UAV are given by $\bar{J}_1=\bar{J}_2=\bar{J}_3=\mathrm{diag}\left([20\ 20\ 20]^T\right)$. Take the disturbances as

$$\begin{aligned}d_1&=[0.1\sin(t),0.2\cos(0.5t),0.15\cos(0.7t)]^T,\\d_2&=[0.1\cos(t),0.2\sin(0.5t),0.15\sin(0.7t)]^T,\\d_3&=[0.1\cos(t),0.2\cos(0.5t),0.15\sin(0.7t)]^T.\end{aligned} \tag{48}$$

The initial quaternions of the follower UAVs are selected as $Q_1(0)=[1,0,0,0]^T$, $Q_2(0)=[0,1,0,0]^T$, and $Q_3(0)=[0,0,1,0]^T$, the initial angular velocities of the follower

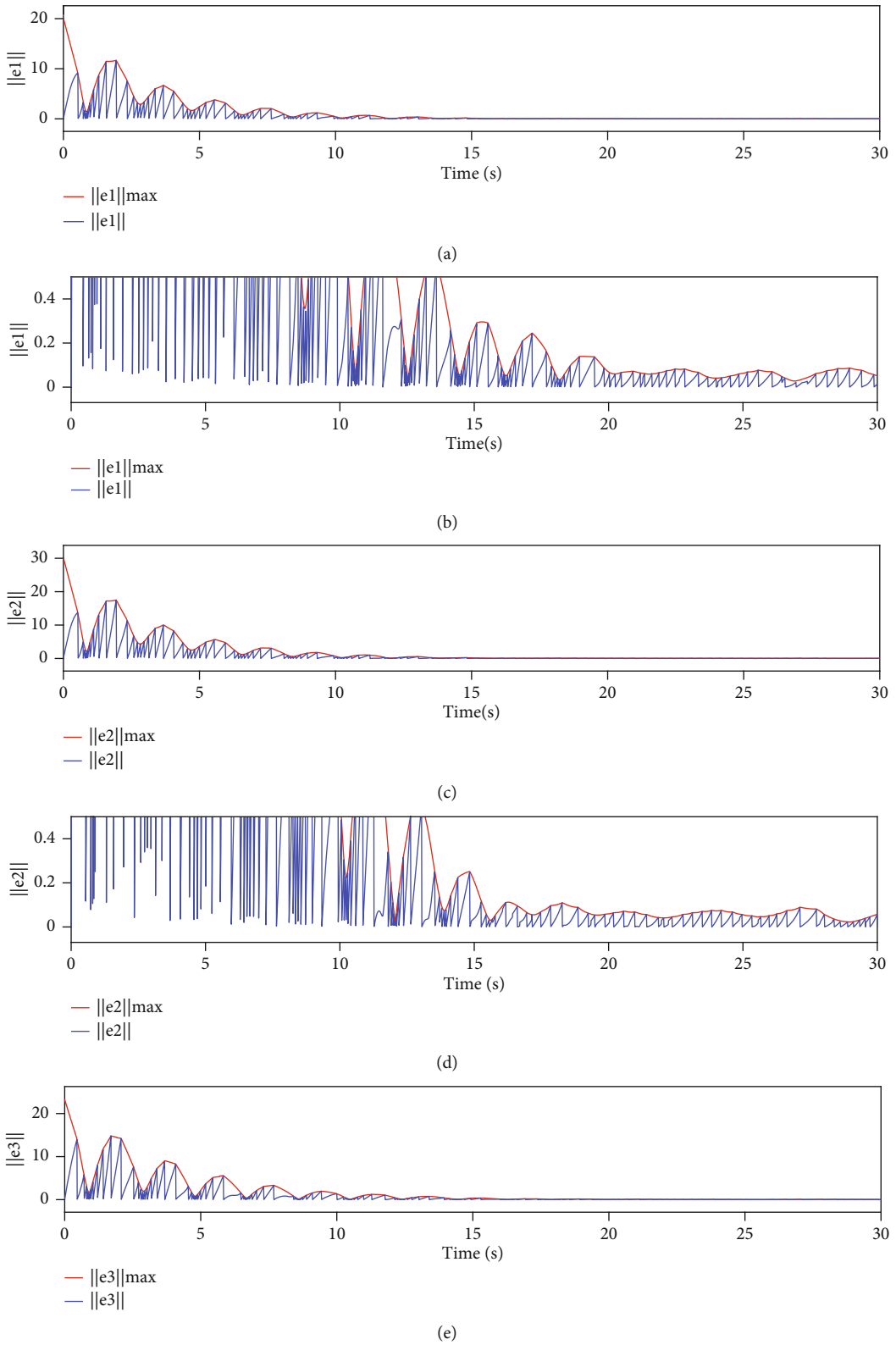

Figure 7: Continued.

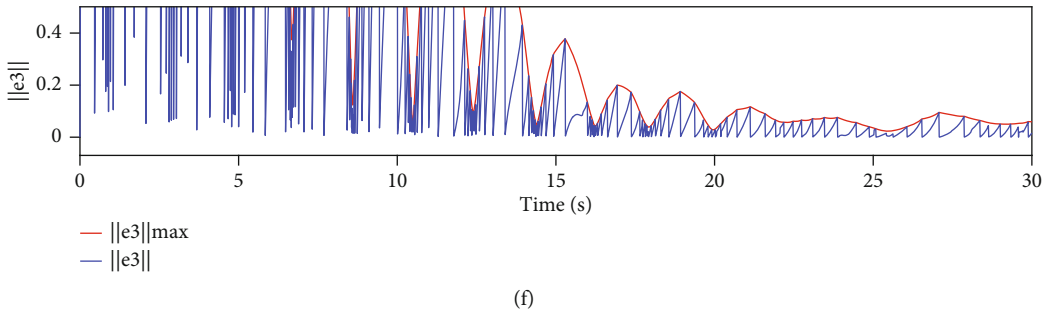

(f)

Figure 7: Variation trend of measurement error norm $\|e_i\|$ and threshold$\|e_i\|_{\max}$.

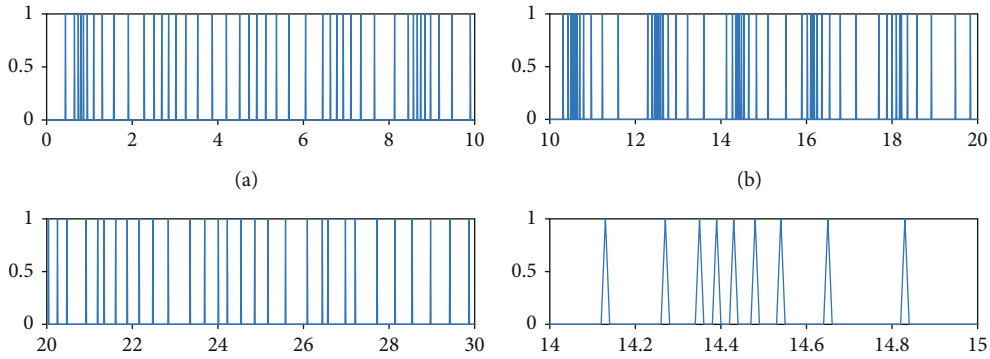

Figure 8: Event-triggered time for UAV1.

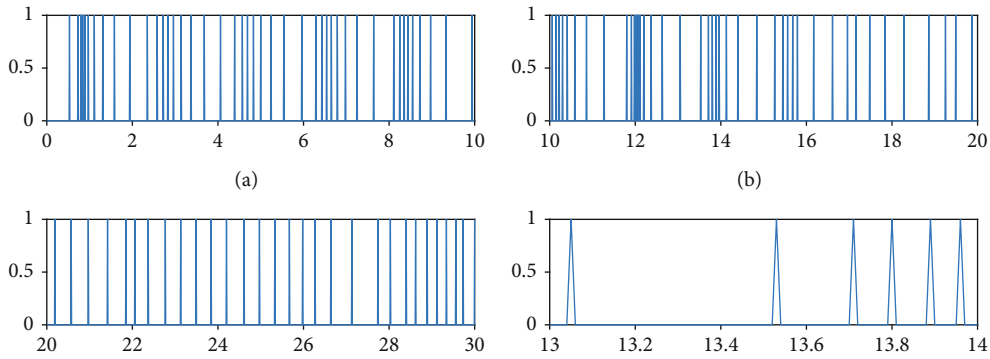

Figure 9: Event-triggered time for UAV2.

UAVs are selected as $w_1(0) = [0, 0, 1]^T$, $w_2(0) = [0, 0, 1]^T$, and $w_3(0) = [0, 0, 1]^T$. The initial quaternion of the leader UAV is selected as $Q_0(0) = [0, 0, 0, 1]^T$, and the angular velocity of the leader UAV is given as$w_0(t) = [0.1 \cos(0.2t), -0.1 \sin(0.2t), -0.1 \cos(0.2t)]^T$.

The controller parameters are chosen with $k_1 = 1$, $k_2 = 0.001$, $k_3 = 0.01$, $k_4 = 1$, $r = 0.6$, $\phi = 0.1$, $\eta = 0.1$, and $\rho_i = 0.009$. The adaptive RBFNN controller parameters are adjusted as $J = 7$, $c_i = [-1.5, -1, -0.5, 0, 0.5, 1, 1.5]$, $\sigma_i = 5$, and $A = \text{diag}([0.5\,0.5\,0.5]^T)$.

Figures 3 and 4, respectively, show the attitude tracking Q_i and the attitude tracking errors $\tilde{Q}_i$ of the ith UAV,$i = 1, 2, 3$.

Figures 5 and 6, respectively, show the angular velocity tracking w_i and the attitude tracking errors $\tilde{w}_i$ of the ith UAV. From Figures 3–6, it can be seen that the attitude and the angular velocity of all follower UAVs can accurately track the leader UAV over time under the action of the controller (17) and the event-triggered function (23).

Figure 7 shows the evolution process of the measurement error norm of the system, where threshold $\|e_i\|_{\max} = k_3 + k_4\|$

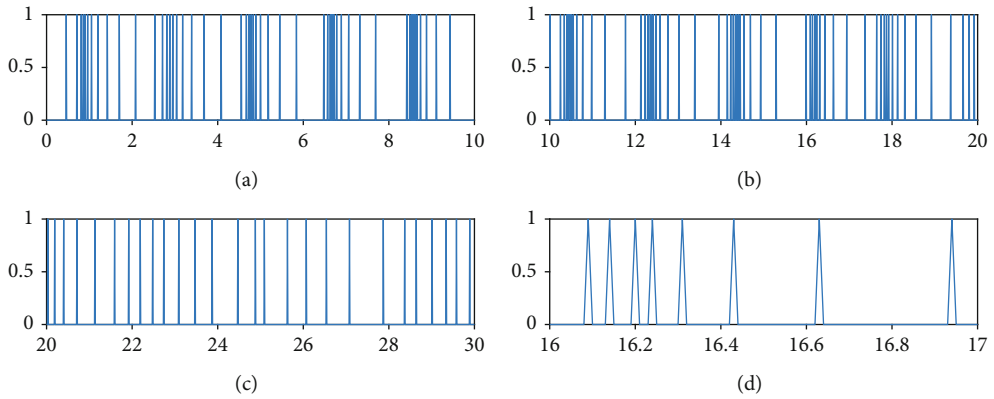

Figure 10: Event-triggered time for UAV3.

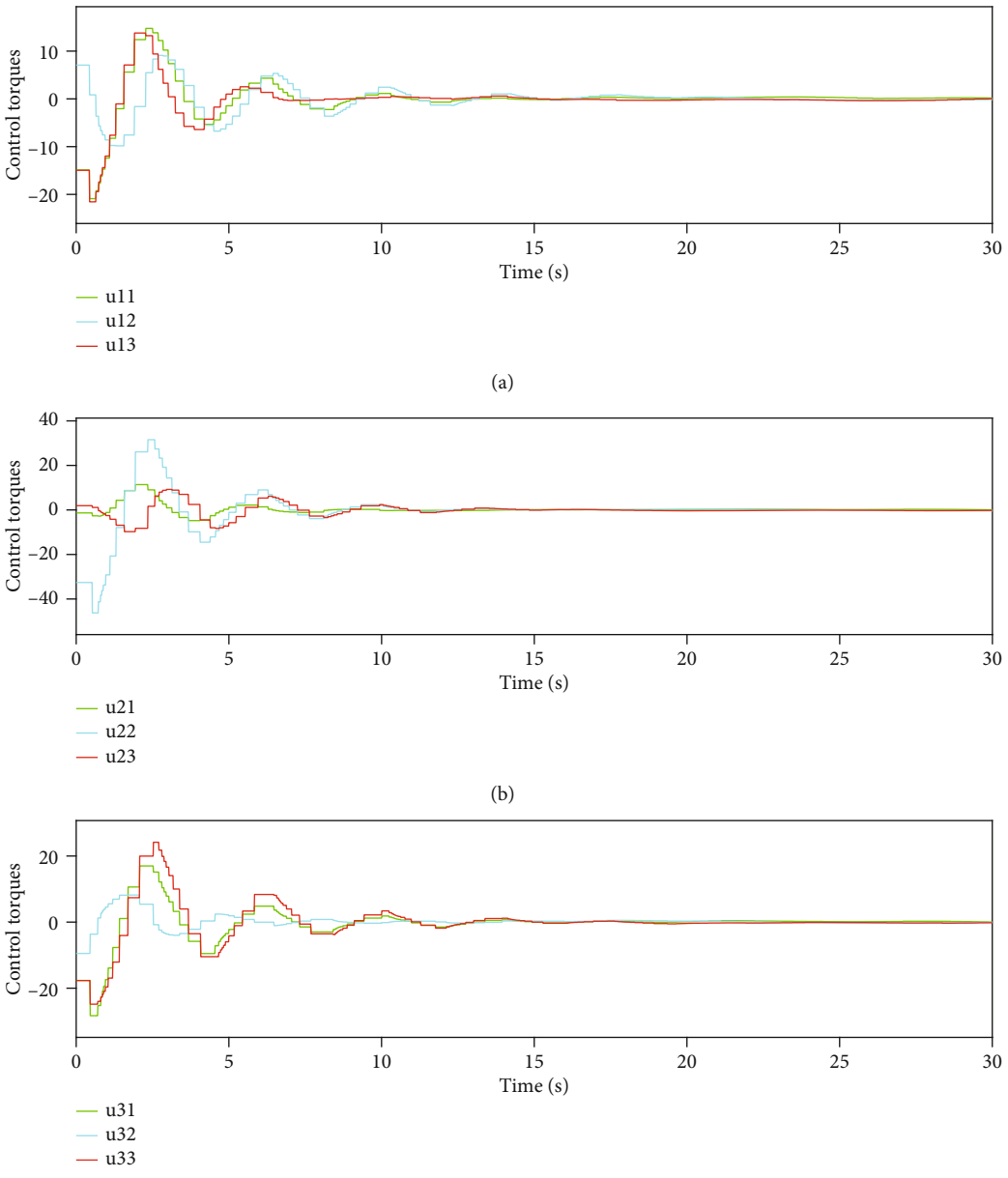

Figure 11: Control torques.

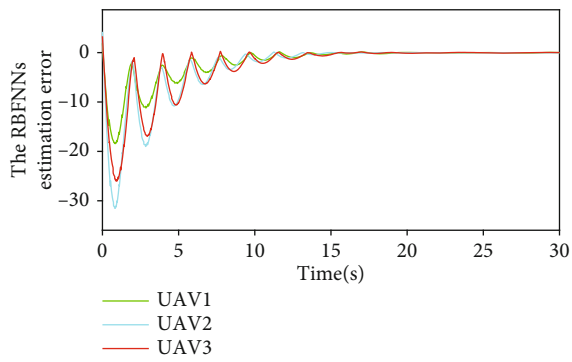

Figure 12: The RBFNN estimation error $\|\varepsilon_i\|$.

$s_i\| - \rho_i$. When the value of $\|e_i\|$ increases from zero to $\|e_i\|_{\max}$, the event is triggered.

Figures 8–10 show the event-triggered time of the UAV i, $i = 1, 2, 3$, and the denser part marked by the rectangular box is enlarged. At the event-triggered time of the UAV i, the UAV i interacts with information and updates the controller. Figure 11 shows the control torque u_i of the UAV i.

From Figures 7–11, it can be seen that the superior performance of the proposed event-triggered control strategy in reducing the energy dissipation of the system and the update frequency of the controller.

The approximation error $\|\varepsilon_i\|$ of the RBFNNs to unknown lumped disturbance δ_i is shown in Figure 12. It can be seen that the RBFNNs can approach δ_i at a faster speed under the action of the adaptive weight update law (23).

5. Conclusions

In this paper, a distributed finite time event-triggered control strategy with RBFNNs is proposed for attitude cooperative control of MUAVs. Under the leader-following framework, the tracking errors of attitude converge to zero in finite time, the communication resources is saved and the Zeno behavior is excluded by utilizing the event-triggered scheme. Finally, theory and numerical simulation proof is given for the proposed control law. In the future, we will consider actuator saturation problem by fault-tolerant technology and self-triggered scheme to be used in finite-time control.

Data Availability

We have no data to share for this paper.

Conflicts of Interest

The authors declare that they have no conflicts of interest.

Acknowledgments

This research was jointly supported by National Natural Science Foundation of China (41874213), Robot Technology Used for Special Environment Key Laboratory of Sichuan Province (17kftk05), and Science and Technology project of Sichuan Province (2021YFS0339).

References

[1] M. Mozaffari, W. Saad, M. Bennis, and M. Debbah, "Efficient deployment of multiple unmanned aerial vehicles for optimal wireless coverage," *IEEE Communications Letters*, vol. 20, no. 8, pp. 1647–1650, 2016.

[2] E. T. Alotaibi, S. S. Alqefari, and A. Koubaa, "LSAR: multi-UAV collaboration for search and rescue missions," *Access*, vol. 7, pp. 55817–55832, 2019.

[3] B. Alzahrani, O. S. Oubbati, A. Barnawi, M. Atiquzzaman, and D. Alghazzawi, "UAV assistance paradigm: state-of-the-art in applications and challenges," *Journal of Network and Computer Applications*, vol. 166, article 102706, 2020.

[4] E. Jin, X. Jiang, and Z. Sun, "Robust decentralized attitude coordination control of spacecraft formation," *Systems & Control Letters*, vol. 57, no. 7, pp. 567–577, 2008.

[5] Y. Kuriki and T. Namerikawa, "Consensus-based cooperative control for geometric configuration of UAVs flying in formation," in *The SICE Annual Conference 2013*, pp. 1237–1242, Nagoya, Japan, 2013.

[6] W. Ren, "Consensus strategies for cooperative control of vehicle formations," *IET Control Theory & Applications*, vol. 1, no. 2, pp. 505–512, 2007.

[7] P. Tabuada, "Event-triggered real-time scheduling of stabilizing control tasks," *IEEE Transactions on Automatic Control*, vol. 52, no. 9, pp. 1680–1685, 2007.

[8] D. V. Dimarogonas, E. Frazzoli, and K. H. Johansson, "Distributed event-triggered control for multi-agent systems," *IEEE Transactions on Automatic Control*, vol. 57, no. 5, pp. 1291–1297, 2012.

[9] Y. Fan, G. Feng, Y. Wang, and C. Song, "Distributed event-triggered control of multi-agent systems with combinational measurements," *Automatica*, vol. 49, no. 2, pp. 671–675, 2013.

[10] E. Garcia, Y. Cao, and D. W. Casbeer, "Decentralized event-triggered consensus with general linear dynamics," *Automatica*, vol. 50, no. 10, pp. 2633–2640, 2014.

[11] W. Zhu, Z.-P. Jiang, and G. Feng, "Event-based consensus of multi-agent systems with general linear models," *Automatica*, vol. 50, no. 2, pp. 552–558, 2014.

[12] J. Yang, F. Xiao, and T. Chen, "Event-triggered formation tracking control of nonholonomic mobile robots without velocity measurements," *Automatica*, vol. 112, article 108671, 2020.

[13] R. R. Nair, L. Behera, and S. Kumar, "Event-triggered finite-time integral sliding mode controller for consensus-based formation of multirobot systems with disturbances," *IEEE Transactions on Control Systems Technology*, vol. 27, no. 1, pp. 39–47, 2019.

[14] S. Weng and D. Yue, "Distributed event-triggered cooperative attitude control of multiple rigid bodies with leader–follower architecture," *International Journal of Systems Science*, vol. 47, no. 3, pp. 631–643, 2016.

[15] W. Baolin, Q. Shen, and X. Cao, "Event-triggered attitude control of spacecraft," *Advances in Space Research*, vol. 61, no. 3, pp. 927–934, 2018.

[16] W. Liu, Y. Geng, W. Baolin, and D. Wang, "Neural-network-based adaptive event-triggered control for spacecraft attitude tracking," *IEEE transactions on neural networks and learning systems*, vol. 31, no. 10, pp. 4015–4024, 2020.

[17] Z. Zhou, H. Wang, and H. Zhongquan, "Event-based time varying formation control for multiple quadrotor UAVs with

Markovian switching topologies," *Complexity*, vol. 2018, Article ID 8124861, 15 pages, 2018.

[18] C. Dong, M. Ma, Q. Wang, and S. Ma, "Event-based formation control of multiple quadrotors on SO(3)," *Mathematical Problems in Engineering*, vol. 2018, Article ID 4707219, 11 pages, 2018.

[19] L. Wei, M. Chen, and T. Li, "Dynamic event-triggered cooperative formation control for UAVs subject to time-varying disturbances," *IET Control Theory & Applications*, vol. 14, no. 17, pp. 2514–2525, 2020.

[20] A. M. Zou and K. D. Kumar, "Finite-time attitude tracking control for spacecraft using terminal sliding mode and Chebyshev neural network," *IEEE Transactions on Systems, Man, and Cybernetics, Part B (Cybernetics)*, vol. 41, no. 4, pp. 950–963, 2011.

[21] L. Kunfeng and Y. Xia, "Adaptive attitude tracking control for rigid spacecraft with finite-time convergence," *Automatica*, vol. 49, no. 12, pp. 3591–3599, 2013.

[22] Y. Cheng, R. Jia, D. Haibo, G. Wen, and W. Zhu, "Robust finite-time consensus formation control for multiple nonholonomic wheeled mobile robots via output feedback," *International Journal of Robust and Nonlinear Control*, vol. 28, no. 6, pp. 2082–2096, 2018.

[23] M. F. Hassan and M. Hammuda, "Leader-follower formation control of mobile nonholonomic robots via a new observer-based controller," *International Journal of Systems Science*, vol. 51, no. 7, pp. 1243–1265, 2020.

[24] B. Tian, L. Liu, L. Hanchen, Z. Zuo, Q. Zong, and Y. Zhang, "Multivariable finite time attitude control for quadrotor UAV: theory and experimentation," *IEEE Transactions on Industrial Electronics*, vol. 65, no. 3, pp. 2567–2577, 2018.

[25] F. Wang, H. Gao, K. Wang, C. Zhou, Q. Zong, and C. Hua, "Disturbance observer-based finite-time control design for a quadrotor UAV with external disturbance," *IEEE Transactions on Aerospace and Electronic Systems*, vol. 57, no. 2, pp. 834–847, 2021.

[26] J. Duan, H. Zhang, Y. Liang, and Y. Cai, "Bipartite finite-time output consensus of heterogeneous multi-agent systems by finite-time event-triggered observer," *Neurocomputing*, vol. 365, pp. 86–93, 2019.

[27] J. Wang, C. Bi, D. Wang, Q. Kuang, and C. Wang, "Finite-time distributed event-triggered formation control for quadrotor UAVs with experimentation," *ISA Transactions*, vol. 119, 2021.

[28] Y. Hong, J. Hu, and L. Gao, "Tracking control for multi-agent consensus with an active leader and variable topology," *Automatica*, vol. 42, no. 7, pp. 1177–1182, 2006.

[29] S. P. Bhat, S. Dennis, and Bernstein, "Finite-time stability of continuous autonomous systems," *SIAM Journal on Control and Optimization*, vol. 38, no. 3, pp. 751–766, 2000.

[30] Z. Zhu, Y. Xia, and F. Mengyin, "Attitude stabilization of rigid spacecraft with finite-time convergence," *International Journal of Robust and Nonlinear Control*, vol. 21, no. 6, pp. 686–702, 2011.

[31] A. Abdessameud and A. Tayebi, *Motion Coordination for Vtol Unmanned Aerial Vehicles: Attitude Synchronisation and Formation Control*, Springer, 2013.

[32] S. Li, D. Haibo, and X. Lin, "Finite-time consensus algorithm for multi-agent systems with double-integrator dynamics," *Automatica*, vol. 47, no. 8, pp. 1706–1712, 2011.